Spring 5-15-2019

Developing nucleon self-energies to generate the ingredients for the description of nuclear reactions

Mack Charles Atkinson
Washington University in St. Louis

WASHINGTON UNIVERSITY IN ST. LOUIS

Department of Physics

Dissertation Examination Committee:
Willem Dickhoff, Chair
Mark Alford
Robert Charity
Saori Pastore
Maria Piarulli
Lee Sobotka

Developing Nucleon Self-Energies to Generate the Ingredients for the Description of Nuclear Reactions

by

Mack Atkinson

A dissertation presented to
The Graduate School
of Washington University in
partial fulfillment of the
requirements for the degree
of Doctor of Philosophy

May 2019
St. Louis, Missouri

Contents

List of Figures

List of Tables

Acknowledgements

I would first like to express my gratitude to my wonderful advisor Wim. Your guidance and dedication to mentoring led to my growth as a physicist. The wisdom that you shared with me is indispensable. Thank you Wim.

I would like to thank my committee members Mark Alford, Lee Sobotka, Bob Charity, Saori Pastore, and Maria Piarulli.

I would like to thank Hossein Mahzoon for introducing me to the DOM code. I would also like to thank Bob for his useful advice on fitting.

I would thank Louk Lapikás and Henk Blok for providing the experimental $(e, e'p)$ data.

I would like to thank Gregory Potel for hosting me at Michigan State University in the summer of 2018. Our many discussions are very enjoyable and always lead to further insights.

I would like to thank the two undergraduate students who worked in our group. I thank Michael Keim for his contribution to the fit of ^{208}Pb. I thank Blake Bordelon for generating elastic electron scattering cross sections.

Last, but certainly not least, I would like to thank my parents. Without their loving support, I would not be where I am today. A special thanks to my dad. Your passion for math is what inspired my fascination of physics. You will always be remembered with love.

This work was supported by the U. S. National Science Foundation under grants No. PHY-1304242 and No. PHY-1613362.

Mack Atkinson

Washington University in St. Louis

May 2019

ABSTRACT OF THE DISSERTATION

Developing nucleon self-energies to generate the ingredients for the description of nuclear reactions

by

Mack Atkinson

Doctor of Philosophy in Physics

Washington University in St.Louis, 2019

Professor Willem Dickhoff (Chair)

The nucleon self-energies of ^{40}Ca, ^{48}Ca, and ^{208}Pb are determined using a nonlocal dispersive optical model (DOM). By enforcing the dispersion relation connecting the real and imaginary part of the self-energy, both experimental scattering data and nuclear structure data are used to constrain these self-energies. The ability to calculate both bound and scattering states simultaneously puts these self-energies in a unique position to consistently describe exclusive knockout reactions such as $(e, e'p)$. Using the well-constrained self-energy describing ^{40}Ca, the distorted-wave impulse approximation (DWIA) description of the $(e, e'p)$ reaction is shown to be valid for outgoing proton kinetic energies around 100 MeV. This analysis also reveals the importance of high-energy proton reaction cross section data in constraining spectroscopic factors of the $(e, e'p)$ reactions. In particular, it is imperative that high-energy proton reaction cross section data are measured for ^{48}Ca in the near future so that the quenching of the spectroscopic factor in the $^{48}\mathrm{Ca}(e, e'p)^{47}\mathrm{K}$ reaction can be properly constrained using the DOM. Moreover, DOM generated spectral functions indicate that the quenching of spectroscopic factors is due not only to long-range correlations, but also partly due to the increase in the proton high-momentum content in ^{48}Ca on account

of the strong neutron-proton interaction. Single-particle momentum distributions of protons and neutrons in ^{48}Ca and ^{208}Pb calculated from these spectral functions confirm this by clearly showing that neutron excess causes a higher fraction of high-momentum protons than neutrons. In addition to proton reaction cross section data, high-energy neutron total cross section data are also shown to constrain the distribution of neutrons in these nuclei, leading to the prediction of thick neutron skins in both ^{48}Ca and ^{208}Pb. Using the DOM spectral functions, the binding energy density of each nucleus is calculated. These energy densities call into question the degree to which the equation of state for nuclear matter is constrained by the well-known empirical mass formula.

Chapter 1

Introductory Remarks

Generally speaking, low-energy nuclear physics is the study of how the properties of nuclei emerge from the interaction of their consituent particles. In 1935, Yukawa suggested that protons and neutrons, or nucleons, interact through the exchange of light mesons (pions) [1]. This simple picture of the nucleon-nucleon (NN) interaction explained how systems of protons and neutrons (nuclei) could be bound. This NN interaction also explains the strong, short-range nature of the nuclear force which is evident from the hard-sphere-like nature of NN scattering phase shifts in addition to the observation from elastic electron scattering experiments that the radius of a given nucleus scales by $A^{1/3}$ [1, 2]. Since then, enormous progress has been made in developing this phenomenological picture through parametrized NN interactions [3, 4]. More recently, the NN interaction has been calculated using a chiral effective field theory (χEFT) in which a parametrized Lagrangian contains all the symmetries of quantum chromodynamics (QCD) [5–7]. Both phenomenological and χEFT interactions are constrained by proton-proton and proton-neutron scattering data as well as the binding energy of the deuteron.

Even with these sophisticated NN interactions, there is still the many-body problem

to overcome in order to be able to describe nuclei starting from these interactions. The ground state of light systems up to ^{12}C can be directly calculated using the Green's function Monte-Carlo (GFMC) method with the NN interaction as input [8, 9]. The ground state of larger systems up to ^{16}O can be directly calculated with less accuracy using auxiliary field diffusion Monte-Carlo (AFDMC) [10]. Any *ab-initio* calculation of the structure of nuclei larger than this relies on many-body approximations that require further softening of the NN interactions [11–13]. The structure of any nucleus larger than $A \approx 48$ (with isolated exceptions such as ^{100}Sn [14]) can only be calculated using mean-field methods that rely on parametrized density functionals fit to a large set of nuclear structure data [15]. These density functionals are far removed from the NN interaction, indicating that the theoretical description of the majority of nuclei is phenomenological.

All of the properties of nuclei known today are due to experimental measurements of nuclear reactions. Thus, it is important to connect calculations of nuclear structure with these reactions. The inclusion of scattering states in the calculations mentioned in the previous paragraph is exceedingly complicated. Variational Monte-Carlo (VMC) methods have been applied to calculate low-energy neutron-alpha (n-^{4}He) [16] and no-core shell model (NCSM) methods have been applied to low-energy neutron scattering of systems up to ^{6}He [17, 18]. While considerable progress in *ab-initio* nuclear reaction calculations is being made, parametrized optical potentials have been used for decades to accurately describe nuclear reactions for a very wide range of nuclei [19].

These phenomenological optical potentials were constrained by nucleon-nucleus elastic scattering data, so they could only describe states of nuclei in the continuum. While these optical potentials are certainly sensitive to nuclear structure, their chosen functional form prevented them from describing bound-state information. Thus, there was a disjoint description of the nucleus, where the ground state was described with a mean-field calculation while the scattering states are described with an optical potential. This situation is alleviated by

making the connection that the optical potential is the irreducible self-energy in a Green's function many-body formalism. The irreducible self-energy satisfies a dispersion relation which links nuclear structure with scattering states [20, 21]. In the seminal work of Mahaux and Sartor [22], a dispersive optical model (DOM) is proposed in which a parametrized self-energy is subject to this dispersion relation. In this thesis, DOM self-energies are fit to both elastic scattering data and bound-state data in ^{40}Ca, ^{48}Ca, and ^{208}Pb. This allows for testing reaction models, $(e, e'p)$ for example, since all the ingredients needed for these models are constrained in the DOM. Furthermore, this approach can help make sense of data to be generated at the new Facility for Rare Isotope Beams (FRIB) as the typical radioactive nucleus is particularly sensitive to the interplay between bound and continuum states [23]. The results of the current DOM analysis lead to predictions of quantities such as neutron skins and energy densities that are difficult to constrain with unambiguous experiments but are closely tied to astrophysical objects such as neutron stars [24–27].

This thesis is divided into seven chapters, with this introduction being the first. The aim is to be as self-contained as possible, so the second chapter is a detailed theoretical background of the concepts used throughout all of the chapters. This chapter is also intended to be a useful reference for anyone working with the DOM. To avoid repetition, introductions to the concepts of chapters 3-6 are left to their corresponding introductory sections. The work in Chap. 3 is published in Physical Review C, see Ref. [28]. Some of the work in Chap. 4 is published in Physical Review Letters, see Ref. [29]. Chapter 7 contains some concluding remarks and an outlook for the future. There are three appendices which each contain relevant information that would otherwise detract from the general flow of the thesis.

Chapter 2

Theoretical Background

This chapter serves as an overview of theoretical concepts relevant to the DOM and its applications. In Sec. 2.1, the optical potential is derived from fundamental scattering theory. Section 2.2 not only introduces the Lagrange basis, but provides details on the R-matrix method that is used to solve scattering equations. The many-body formalism of the single-particle propagator is presented in Sec. 2.3. The formalism of all of these sections are then combined to introduce the DOM in Sec. 2.4. Finally, methods for numerically calculating the single-particle propagator are discussed in Sec. 2.5

2.1 Nucleon-Nucleus Scattering

The goal of this section is to justify using a single complex potential to describe nucleon-nucleus scattering. The interaction between the nucleon and the nucleus can be represented by a sum over the interactions between the constituent nucleons of the nucleus and the free nucleon. Consider all possible processes which can follow from the interaction of the nucleon

with the nucleus,

$$\begin{aligned} a + A &\rightarrow a + A && \text{elastic scattering} \\ &\rightarrow a + A^* && \text{inelastic scattering} \\ &\rightarrow b + B && \text{rearrangement} \\ &\text{etc.} \end{aligned} \tag{2.1}$$

where a denotes the nucleon and A is the target nucleus. The system $a + A$ is referred to as the entrance channel while $a + A^*$, $b + B$, etc. are referred to as exit channels [30]. Equation (2.1) indicates that there can be several different channels with a and A as constituents (and likewise with b and B as constituents, etc.). It is convenient to refer to these as partitions such as $\alpha = a + A$ or $\beta = b + B$.

The full Hamiltonian can be written as

$$\hat{H} = \hat{H}_\alpha + \hat{K}_\alpha + \hat{V}_\alpha, \qquad (\hat{H} - E)\Psi = 0, \tag{2.2}$$

where $\hat{H}_\alpha$ is the internal Hamiltonian of some partition α, $\hat{K}_\alpha$ is the kinetic-energy of the relative motion between a and A, and $\hat{V}_\alpha$ is the potential of interaction between a and A. (The use of α in these derivations is completely arbitrary; any partition β also satisfies $\hat{H} = \hat{H}_\beta + \hat{K}_\beta + \hat{V}_\beta$.) The internal Hamiltonian $\hat{H}_\alpha$ consists of the Hamiltonians of a and A,

$$\begin{aligned} (\hat{H}_a - E_a)\psi_a = 0 \qquad & (\hat{H}_A - E_A)\psi_A = 0 \\ \hat{H}_\alpha = \hat{H}_a + \hat{H}_A \qquad & \psi_\alpha = \psi_a \psi_A. \end{aligned}$$

The potential $\hat{V}_\alpha$ is the interaction of all the constituents of A with a,

$$\hat{V}_\alpha(\boldsymbol{r}_\alpha, x_\alpha) = \sum_{i=1}^{A+1} \hat{V}_{1i}.$$

The total wave function Ψ for the system can be expanded over any complete set of internal states ψ_α,

$$\Psi = \sum_\alpha \xi(\boldsymbol{r}_\alpha)\psi_\alpha(x_\alpha), \tag{2.3}$$

where the coefficients $\xi_\alpha(\boldsymbol{r}_\alpha)$ are channel functions that describe the relative motion of a and A. Inserting this expansion into Eq. (2.2), multiplying on the left by ψ^*_α, and integrating over x_α leads to an infinite set of coupled equations for each $\xi_\alpha(\boldsymbol{r}_\alpha)$ [31],

$$[\varepsilon_\alpha + K_\alpha + \langle\alpha|\,\hat{V}_\alpha\,|\alpha\rangle - E]\xi_\alpha(\boldsymbol{r}_\alpha) = \sum_{\alpha'\neq\alpha} \langle\alpha|\,\hat{V}_\alpha\,|\alpha'\rangle\,\xi_{\alpha'}(\boldsymbol{r}_\alpha).$$

Each channel function $\xi_\alpha(\boldsymbol{r}_\alpha)$ has the following asymptotic form (analogous to Eq. (A.5)),

$$\xi_\alpha(\boldsymbol{r}_\alpha) \sim e^{i\boldsymbol{k}_\alpha\cdot\boldsymbol{r}_\alpha}\delta_{\alpha\alpha_i} + f_{\alpha\alpha_i}(\hat{\boldsymbol{r}}_\alpha, \boldsymbol{k}_{\alpha_i})\frac{e^{ik_\alpha r_\alpha}}{r_\alpha},$$

where α_i is the entrance channel described by $e^{i\boldsymbol{k}_{\alpha_i}\cdot\boldsymbol{r}_{\alpha_i}}$ and $f_{\alpha\alpha_i}$ is the amplitude for an incoming plane wave from α_i scattering to an outgoing spherical spherical wave in the α channel.

In order to describe elastic scattering in this reaction, an infinite set of coupled equations should be solved to obtain the elastic scattering amplitude $f_{\alpha_i\alpha_i}$. The consequence of having many other open channels to scatter to is that flux is taken from the elastic scattering channel. Thus, an approximation should be made that does not involve solving for infinite channels but can still describe the loss of flux to them. This can be done by modifying

Eq. (2.3) to only include the entrance channel α_i,

$$\Psi_{\text{model}} = \xi_{\alpha_i}(r_{\alpha_i})\psi_{\alpha_i}(x_{\alpha_i}). \tag{2.4}$$

A more formal way of stating this is through projection operators [32]

$$\Psi_{\text{model}} = \hat{P}\Psi, \qquad\qquad \Psi = \hat{P}\Psi + \hat{Q}\Psi,$$

where $\hat{P}$ and $\hat{Q}$ are projection operators such that

$$\hat{P} + \hat{Q} = 1, \qquad \hat{P}^2 = \hat{P}, \qquad \hat{Q}^2 = \hat{Q}, \qquad \hat{Q}\hat{P} = \hat{P}\hat{Q} = 0. \tag{2.5}$$

The idea of these projectors is that $\hat{P}$ projects into a model space (P-space) of the most important channels (in the case of elastic scattering this is only one, the entrance channel), while the Q-space is comprised of the infinite other channels. Thus, considering only P-space makes this reaction a more tractable problem. Now, Eq. (2.2) becomes

$$(\hat{H} - E)(\hat{P}\Psi + \hat{Q}\Psi) = 0. \tag{2.6}$$

Manipulating Eq. (2.6) using the properties in Eq. (2.5) leads to a Schrödinger equation for the model wave function $\hat{P}\Psi$ [31],

$$(\hat{\mathcal{H}} - E)\hat{P}\Psi = 0, \tag{2.7}$$

where $\mathcal{H}$ is an effective Hamiltonian in P-space,

$$\hat{\mathcal{H}} = \hat{P}\hat{H}\hat{P} + \hat{P}\hat{H}\hat{Q}\frac{1}{E - \hat{Q}\hat{H}\hat{Q} + i\eta}\hat{Q}\hat{H}\hat{P}. \tag{2.8}$$

The choice of the model wave function in Eq. (2.4) leads to further simplification of Eq. (2.8),

$$\hat{\mathcal{H}} = \hat{H}_{\alpha_i} + \hat{K}_{\alpha_i} + \hat{\mathcal{V}}(r_{\alpha_i}, x_{\alpha_i}),$$

where $\hat{\mathcal{V}}$ is the effective interaction,

$$\hat{\mathcal{V}} = \hat{P}\hat{V}_{\alpha_i}\hat{P} + \hat{P}\hat{V}_{\alpha_i}\hat{Q}\frac{1}{E - \hat{Q}\hat{H}\hat{Q} + i\eta}\hat{Q}\hat{V}_{\alpha_i}\hat{P}. \tag{2.9}$$

This reformulation of the problem is advantageous since it allows one to work in the simpler model-space. Indeed, Eq. (2.7) still represents the full problem with an infinite number of channels; this fact is hidden in the effective interaction $\mathcal{V}$. The advantage of this formulation is the possibility of approximating $\mathcal{V}$ with a simpler form.

The first term in Eq. (2.9) straight-forwardly represents the interaction in P-space. The second term compensates for the coupling to all channels in Q-space. This second term merits further investigation. First, the coupling to the other channels in Q-space will result in a loss of flux from the entrance channel. This indicates that $\hat{\mathcal{H}}$ must be complex to account for this absorption, which can be explicitly seen in Eq. (2.9), provided the energy allows for zeros in the denominator. Second, Eq. (2.9) shows an explicit energy dependence. Finally, the presence of $\hat{H}$ in the denominator includes the kinetic-energy of relative motion. Since the kinetic-energy contains differential operators, $\hat{\mathcal{V}}$ will necessarily be nonlocal [31]. This nonlocality manifests as an integral operator,

$$\hat{\mathcal{V}}\Psi = \int d^3r' \mathcal{V}(\boldsymbol{r}, \boldsymbol{r}')\Psi(\boldsymbol{r}'). \tag{2.10}$$

With these properties in mind, a simpler expression for $\hat{\mathcal{V}}$ is appropriate,

$$\hat{\mathcal{V}} = \hat{P}\hat{V}_{\alpha_i}\hat{P} + \Delta\hat{V}(E).$$

It is due to these properties that $\hat{\mathcal{V}}$ is often referred to as an optical potential, since a complex potential is analogous to a complex index of refraction for the scattering of light [33]. Thus, nucleon-nucleus scattering can be calculated using the techniques detailed in App. A by using the optical potential.

2.1.1 Optical potentials

In the previous subsection, the optical potential was derived in the context of nucleon-nucleus scattering. The task is now to find a suitable form for an optical potential that can describe elastic scattering by approximating the coupling to all open channels. Typical optical potentials are parametrized such that

$$\mathcal{V}(r, E) = V(r) + iW(r; E),$$

where both V and W involve a set of parameters which are adjusted to reproduce elastic scattering data. Due to the short-range nature of the nuclear force, a Woods-Saxon function is often adopted for the radial dependence of V and W [31],

$$V(r) = \frac{-V_0}{1 + e^{(r-r_v)/a_v}},$$

where V_0, r_v, and a_v are adjustable parameters. The imaginary form has its own set of parameters W_0, r_w, and a_w. As for the energy dependence, this is usually separated from

the radial dependence in the following way,

$$W(r;E) = W(r)W_E(E).$$

Note that these potentials are local, contrary to Eq. (2.10). The reason for this is to simplify the scattering equations. To make up for the fact that the potential should be nonlocal, it can be shown that adding an energy dependence can simulate the effects of nonlocality [31, 34]. This method has issues which will be explained in Subsection (2.4.1), hence the explicit inclusion of nonlocality in the DOM of this thesis.

To account for spin-orbit coupling, a surface term (derivative of a Woods-Saxon function) is included,

$$V^{\mathrm{so}}_{\boldsymbol{\ell s}}(r) = V_{\mathrm{so}} \left(\frac{\hbar}{m_\pi}\right)^2 \frac{1}{a_0 r} \frac{-e^{(r-r_{\mathrm{so}})/a_{\mathrm{so}}}}{\left[1+e^{(r-r_{\mathrm{so}})/a_{\mathrm{so}}}\right]^2} \boldsymbol{\ell}\cdot\boldsymbol{s} = V_{\mathrm{so}}(r)\boldsymbol{\ell}\cdot\boldsymbol{s}, \tag{2.11}$$

where V_{so}, r_{so}, and a_{so} are adjustable parameters specific to this term. The chosen form is inspired by a nonrelativistic reduction of the Dirac equation [31,35]. An intuitive explanation for the surface form of Eq. (2.11) is that in nuclear matter there is no reference point for $\boldsymbol{\ell}$, so there is no significance in the direction of a particle's spin relative to $\boldsymbol{\ell}$. Now consider a finite nucleus, the uniformity of the nuclear interior indicates (crudely) that the deviation from nuclear matter occurs in the surface. Thus, the spin-orbit coupling (which is a feature only of finite nuclei) should predominantly come from the surface. Equation (2.11) can be written in a basis of good total angular momentum by noting that

$$\boldsymbol{\ell}\cdot\boldsymbol{s} = \frac{\hbar^2}{2}\left[j(j+1) - \ell(\ell+1) - \frac{3}{4}\right].$$

The optical potential in this basis is of the following form:

$$\mathcal{V}_{\ell j}(r;E) = V(r) + iW(r;E) + V_{\rm so}(r)\boldsymbol{\ell}\cdot\boldsymbol{\sigma}.$$

2.2 R-matrix theory

All scattering calculations in this thesis are done using R-matrix theory. The advantage of R-matrix theory over standard integration methods is that it allows for the use of a finite, discrete basis of square-integrable functions [36]. Note that the dimensions of the R-matrix correspond to how many channels are included in the scattering calculation. As indicated in Sec. (2.1), only the elastic channel is included, thus the R-matrix refers here to a 1×1 matrix (or equivalently just a scalar). In this case, the R-matrix is defined as [36]

$$R_{\ell j}(E) = \frac{1}{a}\frac{u_{\ell j}(a)}{u'_{\ell j}(a)}. \tag{2.12}$$

2.2.1 Calculation of the R-matrix

In R-matrix theory, the configuration space is divided at a matching radius (a) into an internal region and an external region [36]. The wave function in the external region is simply the asymptotic expression from Eq. (A.4),

$$u^{\rm ext}_{\ell j}(r) = \frac{1}{2ikr}[S_{\ell j}(k)\tilde{O}_\ell(kr) - \tilde{I}_\ell(kr)], \tag{2.13}$$

where $O_\ell(kr)$ and $I_\ell(kr)$ are linear combinations of Coulomb functions corresponding to outgoing and incoming wave functions, respectively,

$$O_\ell(kr) = G_\ell(kr) + iF_\ell(kr) \qquad\qquad I_\ell(kr) = G_\ell(kr) - iF_\ell(kr).$$

The wave function in the internal region can be expanded over some finite basis $\{\phi_n\}$ with N basis functions as

$$u^{\text{int}}_{\ell j}(r) = \sum_{n=1}^{N} c_n \phi_n(r). \tag{2.14}$$

The particular basis used in this thesis is the Lagrange basis, which will be described in Sec. (2.2.2). An issue that arises with this division is that the Hamiltonian is not Hermitian in the internal region $(0, a)$ [36]. Consider the kinetic-energy matrix element in the finite basis,

$$\langle n|\,\hat{T}\,|m\rangle = \int_0^a dr r \int_0^a dr' r' \phi_n(r) \left[\frac{-\hbar^2}{2\mu}\frac{d^2}{dr^2}\frac{\delta(r-r')}{r^2}\right]\phi_m(r'), \tag{2.15}$$

where the centrifugal part has been omitted for clarity. The condition of Hermiticity demands that

$$\langle n|\,\hat{T}\,|m\rangle = \langle m|\,\hat{T}\,|n\rangle\,, \tag{2.16}$$

which is equivalent to switching i and j in Eq. (2.15). In order to check this condition, the method of integration-by-parts [37] can be applied to the integral in Eq. (2.15), resulting in

$$\int_0^\infty dr \phi_n(r)\phi_m^{''}(r) = \phi_n(a)\phi_m^{'}(a) - \phi_n^{'}(a)\phi_m(a) + \int_0^\infty \phi_m(r)\phi_n^{''}(r). \tag{2.17}$$

The surface terms in Eq. (2.17) do not vanish because the surface is defined at $r = a$, thus the Hermiticity relation in Eq. (2.16) is violated. In order to remedy this, Claude Bloch introduced an operator (the Bloch operator) to be added to the kinetic-energy which takes

care of the surface term [38],

$$\hat{\mathcal{L}} = \frac{\hbar^2}{2\mu}\delta(r-a)\frac{d}{dr}. \tag{2.18}$$

With this addition, $\hat{H}_\ell + \hat{\mathcal{L}}$ is now Hermitian in the internal region. The Bloch operator introduces an inhomogeneity into the Schrödinger equation,

$$(\hat{H}_{\ell j} + \hat{\mathcal{L}} - E)\left|u_{\ell j}^{\rm int}\right\rangle = \hat{\mathcal{L}}\left|u_{\ell j}^{int}\right\rangle \to \hat{\mathcal{L}}\left|u_{\ell j}^{ext}\right\rangle, \tag{2.19}$$

where $|u_\ell^{int}\rangle$ can be replaced with $|u_\ell^{ext}\rangle$ on the right-hand-side owing to the nature of the Bloch operator and the continuity condition

$$u_{\ell j}^{\rm int}(a) = u_{\ell j}^{\rm ext}(a).$$

Another nice feature of the presence of the Bloch operator in Eq. (2.19) is that the continuity of the derivatives at the boundary is guaranteed [36].

Now that the problem is well-posed, Eq. (2.19) can be manipulated by inserting various complete sets in the following way

$$\sum_{m=1}^{N}\left\langle n\right|\hat{H}_{\ell j} + \hat{\mathcal{L}} - E\left|m\right\rangle\left\langle m|u_{\ell j}^{\rm int}\right\rangle = \int_0^\infty dr r^2\left\langle n\right|\hat{\mathcal{L}}\left|r\right\rangle\left\langle r|u_{\ell j}^{\rm ext}\right\rangle. \tag{2.20}$$

Noting that $\langle m|u_{\ell j}^{\rm int}\rangle$ are the expansion coefficients in Eq. (2.14), $u_{\ell j}^{\rm int}(r)$ can be found by inverting Eq. (2.20),

$$u_{\ell j}^{\rm int}(r) = \frac{\hbar^2}{2\mu}u_{\ell j}^{'\rm ext}(a)\sum_{n,m=1}^{N}\phi_n(a)(\mathcal{C}^{-1})_{nm}\phi_m(r), \tag{2.21}$$

where the symmetric matrix $\mathcal{C}$ is defined as

$$\mathcal{C}_{nm} = \langle n| \hat{H}_{\ell j} + \hat{\mathcal{L}} - E \, |m\rangle \, .$$

Evaluating Eq. (2.21) at $r = a$ and using the definition of the R-matrix in Eq. (2.12) leads to

$$R_\ell(E) = \frac{\hbar^2}{2\mu a} \sum_{n,m=1}^{N} \phi_n(a)(\mathcal{C}^{-1})_{nm}\phi_m(a). \tag{2.22}$$

Once the R-matrix is calculated using Eq. (2.22), it can be used to calculate the scattering matrix S_ℓ by inserting Eq. (2.22) into Eq (2.12) and using Eq. (2.13). This leads to the following expression,

$$S_{\ell j} = \frac{\tilde{I}_\ell(ka) - kR_{\ell j}(E)\tilde{I}'_\ell(ka)}{\tilde{O}_\ell(ka) - kR_{\ell j}(E)\tilde{O}'_\ell(ka)}.$$

This can then be used to calculate the scattering wave function using Eq. (2.21) as well as differential cross sections as explained in App. (A).

2.2.2 Lagrange Basis

The basis functions used in all calculations contained in this thesis are the Lagrange functions [39]. Lagrange functions make use of orthogonal polynomials and Gauss quadrature [39] to form a numerically efficient basis. In order to derive these basis functions, first consider a family of orthogonal polynomials $\{p_n\}$ defined over an interval (b, c) such that

$$\int_b^c dx p_n(x)p_m(x)w(x) = h_n\delta_{nm},$$

where $w(x)$ is the weight function associated with the family of orthogonal polynomials and $\sqrt{h_n}$ is their normalization [40]. A Gauss quadrature with N mesh points consists of the N

zeros of the N^{th} degree orthogonal polynomial

$$p_N(x_i) = 0$$

along with the N associated weights w_i. The Gauss quadrature approximation of an integral is then

$$\int_b^c dx f(x)w(x) \approx \sum_{i=1}^{N} w_i f(x_i). \tag{2.23}$$

The mesh points and the weights for a given family of orthogonal polynomials can be calculated using the methods detailed in Sec. 3.6 of Ref. [39]. Typically, the weight function is absorbed into $f(x)$ such that Eq. (2.23) is instead written as

$$\int_b^c dx g(x) \approx \sum_{i=1}^{N} \lambda_i g(x_i), \tag{2.24}$$

where $g(x) = w(x)f(x)$ and $\lambda_i = w_i/w(x_i)$ [39]. Comparing to typical Riemann-sum type integration methods, the number of mesh points needed to perform various integrals needed throughout this thesis is reduced by a factor of 10. This approximation is extremely efficient for functions which can be approximated by a polynomial, but one needs to be careful if the function has any divergences or discontinuities [39]. Often, the integration range desired in a calculation is not the range over which a particular family of orthogonal polynomials is defined. To account for this, the mesh can be translated and scaled to fit the range of the problem. For a scaling and translation such as $y = ax + d$, Eq. (2.24) changes in the following way,

$$\int_{b'}^{c'} g(y)dy \approx a \sum_{i=1}^{N} \lambda_i g(ax_i + d) \to \sum_{i=1}^{N} \tilde{\lambda}_i g(\tilde{x}_i), \tag{2.25}$$

where $\tilde{x}_i = ax_i + d$ and $\tilde{\lambda}_i = a\lambda_i$ represent the transformed Lagrange mesh.

Now consider a set of N functions $\{f_i(x)\}$ which are associated with the Gauss quadrature

in such a way that

$$f_i(x_j) = \frac{\delta_{ij}}{\sqrt{\lambda_i}}. \tag{2.26}$$

For a given orthogonal polynomial of degree N, this condition is satisfied with the following expression [39]

$$f_i(x) = \frac{\lambda_i^{-\frac{1}{2}}}{p_N^{'}(x_i)} \frac{p_N(x)}{x - x_i}.$$

For most problems, the Lagrange function is represented on a scaled and translated mesh represented by Eq. (2.25),

$$f_i(r) = \frac{\tilde{\lambda}_i^{-\frac{1}{2}}}{p_N^{'}(x_i)} \frac{a p_N(\frac{r-d}{a})}{r - \tilde{x}_i}, \tag{2.27}$$

where this scaled Lagrange function satisfies a scaled version of the condition in Eq. (2.26),

$$f_i(\tilde{x}_j) = \delta_{ij} \tilde{\lambda}_i^{-\frac{1}{2}}. \tag{2.28}$$

2.2.3 Lagrange-Legendre Basis

In order to calculate the R-matrix described in Sec. (2.2), Legendre polynomials [40] are employed to generate the Lagrange functions defined in Eq. (2.27). Legendre polynomials are defined for $x \in [-1, 1]$ while the internal region for scattering is defined for $r \in [0, a]$. Thus, the following transformation is required,

$$r = \frac{a}{2}(x + 1).$$

In the literature [36, 39], the transformed Legendre mesh points are only transformed to $\tilde{x}_i \in [0, 1]$,

$$\tilde{x}_i = \frac{1}{2}(x_i + 1) \qquad\qquad \tilde{\lambda}_i = \frac{1}{2}\lambda_i,$$

altering the Lagrange condition of Eq. (2.28) to

$$f_i(a\tilde{x}_j) = \delta_{ij}(a\tilde{\lambda}_i)^{-\frac{1}{2}}. \tag{2.29}$$

Furthermore, since the scattering wave function is the regular solution of Eq. (A.3) [41], it satisfies the condition that

$$u_{\ell j}^{\text{int}}(r=0) = 0.$$

In order to enforce this boundary condition, the Lagrange functions can be weighted by a factor of $\left(\frac{r}{ax_i}\right)$, leading to

$$f_i(r) = (-1)^{N+i}\left(\frac{r}{a\tilde{x}_i}\right)\sqrt{a\tilde{x}_i(1-\tilde{x}_i)}\frac{P_N(2r/a-1)}{r-a\tilde{x}_i}, \tag{2.30}$$

where $P_N(x)$ is an N^{th}-order Legendre polynomial as defined in Ref. [40]. These Lagrange-Legendre functions can now be used as basis functions for calculating $u_{\ell j}^{\text{int}}(r)$ as in Eq. (2.14).

The true advantage of using the Lagrange basis for these calculations is revealed when considering the matrix elements of the Hamiltonian. Consider first the matrix elements of the potential,

$$\langle n|\,\hat{V}_{\ell j}\,|m\rangle = \int_0^a dr \int_0^a dr' f_n(r)\mathcal{V}_{\ell j}(r,r')f_m(r'), \tag{2.31}$$

where $f_n(r) = \langle n|r\rangle$ is the basis Lagrange-Legendre basis function defined in Eq. (2.30). Note that the factors of r^2 and r'^2 for the radial integrals in Eq. (2.31) are hidden by the basis functions representing the r-weighted wave function $u(r)$ and the r-weighted potential as defined in Eq. (A.3). Using Eq. (2.25) to approximate the integrals in Eq. (2.31) leads to

$$\langle n|\,\hat{V}_{\ell j}\,|m\rangle = a^2\sum_{\alpha=1}^{N}\sum_{\beta=1}^{N}\tilde{\lambda}_\alpha\tilde{\lambda}_\beta f_n(a\tilde{x}_\alpha)\mathcal{V}_{\ell j}(a\tilde{x}_\alpha, a\tilde{x}_\beta)f_m(a\tilde{x}_\beta). \tag{2.32}$$

Since the Lagrange-Legendre functions are being evaluated at Legendre-mesh points in Eq. (2.32), the Lagrange condition in Eq. (2.29) can be employed to simplify the potential matrix element to

$$\langle n|\,\hat{V}_{\ell j}\,|m\rangle = a(\tilde{\lambda}_n\tilde{\lambda}_m)^{\frac{1}{2}}\mathcal{V}_{\ell j}(a\tilde{x}_n, a\tilde{x}_m) \tag{2.33}$$

Thus, the Lagrange basis has reduced the computation of the potential matrix element from performing a double-integral to simply evaluating the potential at the mesh points. For the case of a local potential, a similar analysis leads to

$$\langle n|\,\hat{V}^{\text{local}}_{\ell j}\,|m\rangle = V^{\text{local}}_{\ell j}(a\tilde{x}_n)\delta_{nm}.$$

The greatest advantage of this basis is the reduction of the kinetic-energy element to an analytic expression in terms of the mesh points [39]. Using the same logic that was used for the potential matrix elements, the kinetic-energy matrix element can be shown to be

$$\langle n|\,\hat{T}+\hat{\mathcal{L}}\,|m\rangle = -\frac{\hbar^2}{2\mu}\left[a^{-\frac{3}{2}}\tilde{\lambda}_n^{\frac{1}{2}}f''_m(a\tilde{x}_n) - a^{-1}f_n(a)f'_m(a)\right], \tag{2.34}$$

where the Bloch operator (Eq. (2.18)) has been included and the centrifugal term has been omitted (it is evaluated in the same way as the potentials). The expression in Eq. (2.34) can be further simplified by taking advantage of various useful properties of Legendre polynomials [39, 40]

$$\langle n|\,\hat{T}+\hat{\mathcal{L}}\,|m\rangle = \frac{\hbar^2}{2\mu}\frac{(4N^2+4N+3)\tilde{x}_n(1-\tilde{x}_n)-6\tilde{x}_n+1}{3a^2\tilde{x}_n^2(1-\tilde{x}_n)^2}$$

for $n = m$, and

$$\langle n|\,\hat{T} + \hat{\mathcal{L}}\,|m\rangle = \frac{\hbar^2}{2\mu a^2}\frac{(-1)^{n+m}}{[\tilde{x}_n\tilde{x}_m(1-\tilde{x}_n)(1-\tilde{x}_m)]^{\frac{1}{2}}} \times\left[N^2+N+1+\frac{\tilde{x}_n+\tilde{x}_m-2\tilde{x}_n\tilde{x}_m}{(\tilde{x}_n-\tilde{x}_m)^2}-\frac{1}{1-\tilde{x}_n}-\frac{1}{1-\tilde{x}_m}\right]$$

for $n \neq m$. Note that these matrix elements are symmetric, which is due to the inclusion of the Bloch operator.

2.2.4 Lagrange-Laguerre Basis

While Legendre polynomials work well for calculating positive energy phase shifts, they are not ideal for bound-state calculations because they are defined over a finite domain and require the Bloch operator to keep the Hamiltonian Hermitian. So, Laguerre polynomials are used in negative energy calculations because they are defined for $x \in [0, \infty)$ [40]. Naturally, this means that no modification is needed to satisfy the Hermiticity of the kinetic-energy matrix. Since the size of a typical nucleus is on the order of 10 fm, the Laguerre mesh points are scaled by a factor $a_L < 1$ (typically around $a_L = 0.2$) so that the potential of the nucleus is properly sampled by the mesh. The corresponding Lagrange-Laguerre basis function is

$$f_i(r) = (-1)^i r(a_L x_i)^{-1/2}\frac{L_N(r/a)}{r - a_L x_i},$$

where $L_N(x)$ is the N^{th}-order Laguerre polynomial and x_i is a Laguerre mesh point satisfying $L_N(x_i) = 0$. These basis functions also satisfy the modified Lagrange condition of Eq. (2.29), meaning that the matrix elements of the potential are equivalent to Eq. (2.33) using the corresponding Laguerre mesh. The kinetic-energy matrix element has a different form due

to the different properties of the Laguerre polynomial [39], where

$$\langle n|\hat{T}|m\rangle = -\frac{1}{12x_n^2}[x_n^2 - 2(2N+1)x_n - 4]$$

for $n = m$, and

$$\langle n|\hat{T}|m\rangle = (-1)^{n-m}\frac{x_n + x_m}{2\sqrt{x_n x_m}(x_n - x_m)^2}$$

for $n \neq m$.

With the Lagrange basis, no integrals or derivatives are necessary when calculating matrix elements. The connection between the Lagrange functions and Gauss quadrature is why the Lagrange basis is implemented in the current applications of the DOM. With the introduction of the Lagrange basis alone, the current DOM code is roughly 60 times faster than its previous implementation. Combined with the recent parallelization of the code, the overall speed of DOM fits has increased by well over two orders of magnitude.

2.3 Green's Functions

Green's functions were originally formulated to aid in solving ordinary differential equations [42]. In general, Green's function for a given differential equation is the solution to said equation with an added (or replaced) inhomogeneity of a Dirac delta function. In particular, Green's function for the three-dimensional nonlocal Schrödinger equation is defined as

$$(\frac{\hbar^2}{2\mu}\boldsymbol{\nabla}^2 + E)G(\boldsymbol{r}, \boldsymbol{r'}) - \int_{\mathcal{V}} d^3r_1 V(\boldsymbol{r}, \boldsymbol{r_1})G(\boldsymbol{r_1}, \boldsymbol{r'}) = \delta^{(3)}(\boldsymbol{r} - \boldsymbol{r'}). \tag{2.35}$$

Another common use of Green's function is in electrostatics, where it represents the potential of a unit point source:

$$\nabla^2 G(\boldsymbol{x}, \boldsymbol{x'}) = -4\pi\delta^{(3)}(\boldsymbol{x} - \boldsymbol{x'}).$$

This Green's function can then be used to find the potential of a general charge distribution, given a set of boundary conditions [33]. This is to say that the idea of a Green's function is a general one with connections throughout all of science. With this in mind, any mention of Green's functions in this section will refer to Green's function satisfying the Schrödinger equation, Eq. (2.35).

2.3.1 Single-particle propagator in a one-body system

Most texts refer to the single-particle propagator and Green's function synonymously [43]. Since the idea of Green's function has been introduced, it is natural to now introduce the concept of the propagator. Consider the time-dependent Schrödinger equation of a single particle,

$$-i\hbar\frac{\partial}{\partial t}\left|\psi, t_0; t\right\rangle + \hat{H}(\boldsymbol{r})\left|\psi, t_0; t\right\rangle = 0, \tag{2.36}$$

where the Hamiltonian is chosen to be time-independent. The solution to Eq. (2.36) is

$$\left|\psi, t_0; t\right\rangle = e^{-\frac{i}{\hbar}\hat{H}(\boldsymbol{r})(t-t_0)}\left|\psi, t_0\right\rangle.$$

The state $|\psi, t_0; t\rangle$ can be written as a wave function by projecting an eigenbra of coordinate space

$$\psi(\boldsymbol{r}, t - t_0) = \langle \boldsymbol{r}|\psi, t_0; t\rangle = \int_{\mathcal{V}} d^3r' \left\langle \boldsymbol{r}\right| e^{-\frac{i}{\hbar}\hat{H}(\boldsymbol{r})(t-t_0)}\left|\boldsymbol{r'}\right\rangle \psi(\boldsymbol{r'}, t' - t_0), \tag{2.37}$$

where a complete set ($\int d^3r' \left|\boldsymbol{r'}\right\rangle \left\langle \boldsymbol{r'}\right| = 1$) has been inserted. Equation (2.37) appears to be an application of Green's Theorem to the time-dependent Schrödinger equation with the

matrix element acting as Green's function. While Eq. (2.37) moves the state both into the future and the past, the propagator is an object that describes propagation only into the future

$$G(\boldsymbol{r},\boldsymbol{r'};t-t') = -\frac{i}{\hbar}\left\langle \boldsymbol{r}\right| e^{-\frac{i}{\hbar}\hat{H}(\boldsymbol{r})(t-t')}\left|\boldsymbol{r'}\right\rangle \theta(t-t'), \tag{2.38}$$

where the step function ensures this forward propagation. The factor of $\left(-\frac{i}{\hbar}\right)$ in Eq. (2.38) is a normalization factor so that $G(\boldsymbol{r},\boldsymbol{r'},t-t')$ satisfies the following equation

$$\left[i\hbar\frac{\partial}{\partial t} - H(\boldsymbol{r})\right] G(\boldsymbol{r},\boldsymbol{r'},t-t') = \delta(t-t')\delta(\boldsymbol{r}-\boldsymbol{r'}),$$

which is consistent with the definition of Green's function given in Sec. 2.3. The interpretation of the propagator, $G(\boldsymbol{r},\boldsymbol{r'},t-t')$, is that it represents the probability amplitude of finding the particle at position $\boldsymbol{r}$ at time t provided it originally started at position $\boldsymbol{r'}$ at time t'.

Now, consider a complete set of eigenfunctions of $\hat{H}$, $\{|\psi_n\rangle\}$, such that

$$\hat{H}\left|\psi_n\right\rangle = \varepsilon_n\left|\psi_n\right\rangle,$$

and insert into Eq. (2.38)

$$\begin{aligned} G(\boldsymbol{r},\boldsymbol{r'};t-t') &= i\hbar\theta(t-t')\sum_n \left\langle \boldsymbol{r}\right| e^{-\frac{i}{\hbar}\hat{H}(\boldsymbol{r})(t-t')}\left|\psi_n\right\rangle\left\langle\psi_n\right|\left.\boldsymbol{r'}\right\rangle \\ &= i\hbar\theta(t-t')\sum_n \psi_n(\boldsymbol{r})\psi_n(\boldsymbol{r'})e^{-\frac{i}{\hbar}\varepsilon_n(t-t')}. \end{aligned} \tag{2.39}$$

Equation (2.39) is a Fourier series, which is inspiration to look at the Fourier transform of the propagator. This will be done by rewriting Eq. (2.39) as an integral over energy. Consider

the following representation of the step function

$$\theta(t-t') = \frac{i}{2\pi} e^{\frac{i}{\hbar}E(t-t')} \int_C dz \frac{e^{-\frac{i}{\hbar}z(t-t')}}{z-E+i\eta}, \qquad \eta \to 0^+. \tag{2.40}$$

There are two cases to consider in Eq. (2.40), backward and forward time propagation. Backward time propagation means that $t < t'$, so the exponential in the integrand will decay for large, positive, imaginary values of z, meaning that the contour should be closed in the upper-half of the complex z-plane. Seeing as there are no poles in the upper-half, the contour integral vanishes. Forward time propagation means that $t > t'$, so the exponential in the integrand will decay for large, negative, imaginary values of z, meaning that the contour should be closed in the lower-half of the complex z-plane. This integral can be evaluated using the Cauchy Residue Theorem [44], resulting in the right-hand-side of Eq. (2.40) being equal to 1. The behavior of this expression exactly describes that of the step function $\theta(t-t')$.

Bringing the step function inside the sum in Eq. (2.39) and using Eq. (2.40) results in

$$\begin{aligned} G(\boldsymbol{r},\boldsymbol{r'};t-t') &= \frac{1}{2\pi\hbar}\int_C dz e^{-\frac{i}{\hbar}z(t-t')} \sum_n \frac{\psi_n(\boldsymbol{r})\psi_n^*(\boldsymbol{r'})}{z-\varepsilon_n+i\eta} \\ &= \frac{1}{2\pi\hbar}\int_{-\infty}^{\infty} dE e^{-\frac{i}{\hbar}E(t-t')} \sum_n \frac{\psi_n(\boldsymbol{r})\psi_n^*(\boldsymbol{r'})}{E-\varepsilon_n+i\eta}. \end{aligned} \tag{2.41}$$

After close inspection, the last expression in Eq. (2.41) can be recognized as the Fourier transform of the propagator in the energy domain, where

$$G(\boldsymbol{r},\boldsymbol{r'};E) = \sum_n \frac{\psi_n(\boldsymbol{r})\psi_n^*(\boldsymbol{r'})}{E-\varepsilon_n+i\eta} = \langle \boldsymbol{r}| \frac{1}{E-\hat{H}+i\eta} |\boldsymbol{r'}\rangle \,. \tag{2.42}$$

Now, apply $(E-\hat{H})$ to Eq. (2.42) and the original definition for Green's function of the Schrödinger equation, Eq. (2.35), is recovered. The simpler expression for the propagator in Eq. (2.42) is the reason that most calculations of G are done in the energy domain.

At this point, to get a handle on the propagator, it is useful to consider the case when no potential is present, i.e. $\hat{H} = \hat{T}$ where $\hat{T}$ is the kinetic-energy operator. This is referred to as the free propagator or free Green's function,

$$G^{(0)}(\boldsymbol{r}, \boldsymbol{r'}; E) = \langle \boldsymbol{r} | \, \frac{1}{E - \hat{T} + i\eta} \, | \boldsymbol{r'} \rangle \, . \tag{2.43}$$

This can be evaluated by inserting a complete set of plane waves into Eq. (2.43),

$$G^{(0)}(\boldsymbol{r}, \boldsymbol{r'}; E) = \int d^3k \, \langle \boldsymbol{r} | \, \frac{1}{E - \hat{T} + i\eta} \, | \boldsymbol{k} \rangle \, \langle \boldsymbol{k} | \boldsymbol{r'} \rangle = \frac{1}{(2\pi)^3} \int d^3k \frac{e^{i\boldsymbol{k}\cdot(\boldsymbol{r}-\boldsymbol{r'})}}{E - \frac{\hbar^2 k^2}{2m} + i\eta}. \tag{2.44}$$

The last integral in Eq. (2.44) can be calculated in spherical coordinates using contour integration for the integral over k, closing the contours in the upper/lower-half of the complex k-plane, resulting in

$$G^{(0)}(\boldsymbol{r}, \boldsymbol{r'}; E) = -\frac{m}{2\pi\hbar^2} \frac{e^{ik_0|\boldsymbol{r}-\boldsymbol{r'}|}}{|\boldsymbol{r} - \boldsymbol{r'}|}, \tag{2.45}$$

where

$$k_0 = \frac{\sqrt{2mE}}{\hbar}.$$

So the free propagator for the single-particle case is an outgoing spherical wave. This provides the boundary conditions for any single-particle propagator, since all propagators behave like a free propagator outside the range of the potential. The formalism is slightly different when the Coulomb potential is present due to its infinite range, but this does not change the fact that the propagator will act as an outgoing wave [43]. This boundary condition is a direct consequence of choosing forward propagation in time. If instead backward time propagation were enforced ($\theta(t' - t)$), the sign in the exponential in Eq. (2.45) would be flipped, corresponding to an incoming wave.

2.3.2 Single-Particle propagator in a many-body system

The previous subsection detailed the single-particle propagator in a system with only one particle. It is useful to think of the propagator in this way to get a handle on it, but the single-particle propagator of a many-body system is the relevant quantity for most nuclear calculations [20]. In second-quantization (the language of many-body physics), the single-particle propagator from the previous section can be written as

$$G(\boldsymbol{r}, \boldsymbol{r'}; t - t') = -\frac{i}{\hbar} \langle 0 | \, \hat{a}_{\boldsymbol{r}} e^{-\frac{i}{\hbar}\hat{H}(\boldsymbol{r})(t-t')} \hat{a}^{\dagger}_{\boldsymbol{r'}} \, | 0 \rangle \, \theta(t - t'), \tag{2.46}$$

where $|0\rangle$ is the vacuum state and $\hat{a}_{\boldsymbol{r}}$ and $\hat{a}^{\dagger}_{\boldsymbol{r'}}$ are annihilation and creation operators for states at $\boldsymbol{r}$ and $\boldsymbol{r'}$, respectively. This can be interpreted as a particle state propagating forward in time in the vacuum. While Eq. (2.46) is expressed in the Schrödinger picture, it can be expressed in a more compact form in the Heisenberg picture [43]

$$G(\boldsymbol{r}, \boldsymbol{r'}; t - t') = -\frac{i}{\hbar} \langle 0 | \, \hat{a}_{\boldsymbol{r}}(t) \hat{a}^{\dagger}_{\boldsymbol{r'}}(t') \, | 0 \rangle \, \theta(t - t'), \tag{2.47}$$

where

$$\hat{O}_H(t) = e^{\frac{i}{\hbar}\hat{H}t} \hat{O}_S e^{-\frac{i}{\hbar}\hat{H}t}.$$

Equation (2.47) reduces to Eq. (2.46) by noting that the vacuum is the zero-energy eigenstate of the Hamiltonian.

Moving now to a many-body system, the definition of the single-particle propagator needs to be modified to account for the presence of other particles. Instead of using the vacuum as a reference state, the ground state of the A-particle system is used. This means that

Eq. (2.47) becomes

$$G^{(p)}(\boldsymbol{r},\boldsymbol{r'};t,t') = -\frac{i}{\hbar}\left\langle \Psi_0^A \right| \hat{a}_{\boldsymbol{r}}(t)\hat{a}^\dagger_{\boldsymbol{r'}}(t') \left| \Psi_0^A \right\rangle \theta(t-t'), \tag{2.48}$$

where $|\Psi_0^A\rangle$ is the fully correlated ground-state wave function of the A-body Hamiltonian

$$\hat{H}\left|\Psi_0^A\right\rangle = E_0^A \left|\Psi_0^A\right\rangle .$$

The superscript on the propagator ($G^{(p)}$) denotes the fact that Eq. (2.48) is describing the propagation of an added particle in the presence of the ground state of the A-body system. This clarification is needed since one can also describe the propagation of a hole in the presence of the ground state of the A-body system. For this reason, $G^{(p)}$ is referred to as the "particle propagator" while $G^{(h)}$ is referred to as the "hole propagator", defined as

$$G^{(h)}(\boldsymbol{r},\boldsymbol{r'};t,t') = \frac{i}{\hbar}\left\langle \Psi_0^A \right| \hat{a}^\dagger_{\boldsymbol{r}}(t)\hat{a}_{\boldsymbol{r'}}(t') \left| \Psi_0^A \right\rangle \theta(t'-t).$$

The step function for the hole propagator corresponds to propagation of the hole backward in time. Note that the distinction between particle and hole propagators was not necessary in the previous subsection since there cannot be a hole in the vacuum ($\hat{a}_{\boldsymbol{r}}|0\rangle = 0$).

The full single-particle propagator is a combination of $G^{(p)}$ and $G^{(h)}$ in the following way

$$G(\alpha,\beta;t,t') = -\frac{i}{\hbar}\left\langle \Psi_0^A \right| \mathcal{T}[a_\alpha(t)a^\dagger_\beta(t')] \left| \Psi_0^A \right\rangle , \tag{2.49}$$

where $\mathcal{T}$ is the time-ordering operation (see Ref. [20] for details) and the symbols α and β represent a general basis. Applying the time-ordering operation and using the definition of

the Heisenberg operators, Eq. (2.49) becomes

$$\begin{aligned} G(\alpha,\beta;t,t') = -\frac{i}{\hbar}\Big[&\theta(t-\ t')e^{\frac{i}{\hbar}E_0^A(t-t')}\left\langle\Psi_0^A\right|a_\alpha e^{-\frac{i}{\hbar}\hat{H}(t-t')}a_\beta^\dagger\left|\Psi_0^A\right\rangle \\ &- \theta(t'-t)e^{\frac{i}{\hbar}E_0^A(t'-t)}\left\langle\Psi_0^A\right|a_\alpha e^{-\frac{i}{\hbar}\hat{H}(t'-t)}a_\beta^\dagger\left|\Psi_0^A\right\rangle\Big] \\ = G^{(p)}(\alpha,\beta,t,t') &+ G^{(h)}(\alpha,\beta;t,t'). \end{aligned}$$

The above expression is analogous to Eq. (2.46) with the main differences being that there is now a hole propagator and that there are additional exponentials involving the ground-state energy. Following the logic that led to Eq. (2.39), inserting complete sets of the Hamiltonian leads to

$$\begin{aligned} G(\alpha,\beta;t,t') = -\frac{i}{\hbar}\Bigg[&\theta(t-t')\sum_m e^{\frac{i}{\hbar}(E_0^A-E_m^{A+1})(t-t')}\left\langle\Psi_0^A\right|a_\alpha\left|\Psi_m^{A+1}\right\rangle\left\langle\Psi_m^{A+1}\right|a_\beta^\dagger\left|\Psi_0^A\right\rangle \\ &- \theta(t'-t)\sum_n e^{\frac{i}{\hbar}(E_0^A-E_n^{A-1})(t'-t)}\left\langle\Psi_0^A\right|a_\alpha\left|\Psi_n^{A-1}\right\rangle\left\langle\Psi_n^{A-1}\right|a_\beta^\dagger\left|\Psi_0^A\right\rangle\Bigg], \end{aligned}$$

where the complete sets are from the $A+1$ system

$$\hat{H}\left|\Psi_m^{A+1}\right\rangle = E_m^{A+1}\left|\Psi_m^{A+1}\right\rangle$$

and the $A-1$ system

$$\hat{H}\left|\Psi_n^{A-1}\right\rangle = E_n^{A-1}\left|\Psi_n^{A-1}\right\rangle.$$

Again, the Fourier transform of the single-particle propagator will be more useful in

calculations. Just as with Eq. (2.41),

$$G(\alpha,\beta;E) = \sum_m \frac{\langle \Psi_0^A | \, a_\alpha \, | \Psi_m^{A+1} \rangle \, \langle \Psi_m^{A+1} | \, a_\beta^\dagger \, | \Psi_0^A \rangle}{E - (E_m^{A+1} - E_0^A) + i\eta} + \sum_n \frac{\langle \Psi_0^A | \, a_\beta^\dagger \, | \Psi_n^{A-1} \rangle \, \langle \Psi_n^{A-1} | \, a_\alpha \, | \Psi_0^A \rangle}{E - (E_0^A - E_n^{A-1}) - i\eta}. \tag{2.50}$$

Equation (2.50) is known as the Lehmann representation [20] of the single-particle propagator. Removing the complete sets of eigenstates from Eq. (2.50) leads to

$$G(\alpha,\beta;E) = \langle \Psi_0^A | a_\alpha \frac{1}{E - (\hat{H} - E_0^A) + i\eta} a_\beta^\dagger \, | \Psi_0^A \rangle + \langle \Psi_0^A | \, a_\beta^\dagger \frac{1}{E - (E_0^A - \hat{H}) + i\eta} a_\alpha \, | \Psi_0^A \rangle \, . \tag{2.51}$$

Note again the connection to Eq. (2.41) with the main difference being the second term in Eq. (2.51), which corresponds to the propagation of a hole in the many-body ground state.

2.3.3 Aspects of the single-particle propagator

Before discussing how to calculate the single-particle propagator, it is important to illustrate the benefits that come from knowing the propagator of a many-body system. The propagator contains information that has direct connections to many experimental observables. The first feature to notice is that the denominators in Eq. (2.50) correspond to the excitation energies of the $(A+1)/(A-1)$ systems with respect to the ground state of the A-body system. Naturally, the $(A+1)$ excited states correspond to the poles of the particle propagator while the $(A-1)$ excited states correspond to the poles of the hole propagator. These hole energies are probed through particle knock-out experiments [45] while the particle energies are probed with stripping experiments [46]. The numerators of Eq. (2.50) are the transition strengths from the ground state of the A-body system to the corresponding excited states of

the $(A+1)/(A-1)$ -body systems. To extract transition strengths, it is useful to consider the propagator on the diagonal, $G(\alpha,\alpha;E)$, since this makes the numerator an absolute square,

$$G(\alpha,\alpha;E) = G(\alpha;E) = \sum_m \frac{|\langle\Psi_0^A|\, a_\alpha\, |\Psi_m^{A+1}\rangle|^2}{E-(E_m^{A+1}-E_0^A)+i\eta} + \sum_n \frac{|\langle\Psi_0^A|\, a_\beta^\dagger\, |\Psi_n^{A-1}\rangle|^2}{E-(E_0^A-E_n^{A-1})-i\eta}.$$

The numerators can be expressed with energy-dependent spectral functions, which provide the transition probability densities to excited states at any given energy. Consider Eq. (2.51) for a large system. The spacing between energy levels in a system decreases with size, therefore it is reasonable to formulate a continuous version of Eq. (2.51). The denominator of the first term in Eq. (2.51) contains the difference between excited states of the $(N+1)$ system and the ground state of the N system. This can be rewritten as

$$E_m^{N+1} - E_0^N = (E_m^{N+1} - E_0^{N+1}) + (E_0^{N+1} - E_0^N) = E_x^{N+1} + \varepsilon_f^+, \tag{2.52}$$

where E_x^{N+1} is the excitation energy of the $(N+1)$ system and ε_f^+ is the particle-addition threshold. The same can be done for the denominator of the second term,

$$E_n^N - E_0^{N-1} = (E_0^N - E_n^{N-1}) + (E_0^{N-1} - E_n^{N-1}) = \varepsilon_f^- - E_x^{N+1}, \tag{2.53}$$

where E_x^{N-1} is the excitation energy of the $(N-1)$ system and ε_f^- is the particle-removal threshold. Now, the sum in Eq. (2.51) can be changed to

$$\sum_n \to \int dn \to \int dE \frac{dn}{dE} \to \int dE.$$

This, combined with Eq. (2.52) and Eq. (2.53), leads to

$$G(\alpha;E)=\int_0^\infty dE'\left[\frac{A(\alpha;E')}{E-E'-\varepsilon_f^+ +i\eta}+\frac{B(\alpha;E')}{E+E'-\varepsilon_f^- -i\eta}\right], \tag{2.54}$$

where the integration is over the excitation energies, which explains the positive integration bounds. To analyze Eq. (2.54), the following identity can be invoked

$$\frac{1}{E\pm i\eta}=\mathcal{P}\frac{1}{E}\mp i\pi\delta(E). \tag{2.55}$$

This identity mediates the separation of the real and imaginary components of G such that

$$\mathrm{Im}G(\alpha;E)=-\pi A(\alpha;E-\varepsilon_f^+)+\pi B(\alpha;-E+\varepsilon_f^-).$$

As stated earlier, the energy-arguments of A and B are positive since they correspond to excitation energies. Therefore, ImG can be separated into three energy domains,

$$\mathrm{Im}G(\alpha;E)=\begin{cases}-\pi A(\alpha;E-\varepsilon_f^+), & E>\varepsilon_f^+\\ 0, & \varepsilon_f^-<E<\varepsilon_f^+\\ \pi B(\alpha;\varepsilon_f^- -E), & E<\varepsilon_f^-\end{cases}. \tag{2.56}$$

Using Eq. (2.55), the real part of G is

$$\mathrm{Re}G(\alpha;E)=\mathcal{P}\int_0^\infty dE'\left[\frac{A(\alpha;E')}{E-E'-\varepsilon_f^+}+\frac{B(\alpha;E')}{E+E'-\varepsilon_f^-}\right]. \tag{2.57}$$

The limits of integration in Eq. (2.57) can be massaged to make the connection to ImG more explicit,

$$\mathrm{Re}G(\alpha;E)=\mathcal{P}\int_{\varepsilon_f^+}^\infty dE'\frac{A(\alpha;E'-\varepsilon_f^+)}{E-E'}+\mathcal{P}\int_{-\infty}^{\varepsilon_f^-}dE'\frac{B(\alpha;\varepsilon_f^- -E')}{E-E'}. \tag{2.58}$$

The form of Eq. (2.58) along with Eq. (2.56) suggests the following dispersion relation,

$$\mathrm{Re}G(\alpha;E) = \frac{1}{\pi}\mathcal{P}\int_{-\infty}^{\infty} dE' \frac{\mathrm{Im}G(\alpha;E')}{E-E'}\mathrm{sgn}(\varepsilon_f^+ - E'). \tag{2.59}$$

Thus, the spectral function is simply the imaginary part of the propagator. The particle spectral function is defined as

$$\begin{aligned} S_p(\alpha;E) &= -\frac{1}{\pi}\mathrm{Im}G(\alpha,\alpha;E) \\ &= \sum_n |\left\langle \Psi_n^{A+1}\right| \hat{a}_\alpha^\dagger \left|\Psi_0^A\right\rangle|^2 \delta(E-(E_n^{A+1}-E_0^A)). \end{aligned} \tag{2.60}$$

The delta function in Eq. (2.60) indicates that the poles of the propagator when $E > \varepsilon_f^+$ correspond to the particle part, which is consistent with Eq. (2.56). The interpretation of the particle spectral function is that it is the probability density for adding a particle at energy E to an A-body system to create an $(A+1)$-body system. Equation (2.60) shows that this involves summing the probabilities of ending in each possible excited state of the $A+1$ system with an energy of $E_n^{A+1} = E_0^A + E$ as a result of adding a particle. The particle spectral function is observed experimentally through the same stripping reactions that probe the $A+1$ excited states [46].

The hole spectral function can be calculated analogously,

$$\begin{aligned} S_h(\alpha;E) &= \frac{1}{\pi}\mathrm{Im}G(\alpha,\alpha;E) \\ &= \sum_m |\left\langle \Psi_m^{A-1}\right| \hat{a}_\alpha \left|\Psi_0^A\right\rangle|^2 \delta(E-(E_0^A-E_m^{A-1})). \end{aligned} \tag{2.61}$$

Conversely to the particle case, the delta function in Eq. (2.61) indicates that the only imaginary component in the energy range of $E < \varepsilon_f^-$ comes from the hole part of the propagator. The interpretation of the hole spectral function is that it is the probability

density for removing a hole at energy E from an A-body system to create an $(A-1)$-body system. Equation (2.61) shows that this involves summing the probabilities of ending in each possible excited state of the $A-1$ system with an energy of $E_n^{A-1} = E_0^A - E$ as a result of removing a hole. The hole spectral function is observed experimentally with knockout reactions such as $(e, e'p)$ reactions [45].

Spectral functions provide a sense of how important many-body correlations are in a system. In the case of an atomic nucleus, the independent particle model (IPM) interpretation would result in hole spectral functions with delta functions only at the single-particle energy levels with transition probabilities equal to one. In reality, the atomic nucleus is a correlated system, meaning that the spectral function will consist of many delta functions with varying strengths. This implies that the hole being removed has a probability of being connected with many excited states at various energies, not just the single-particle energy calculated in the IPM. To get an idea of what this looks like, Fig. 2.1 is an excitation energy spectrum measured in an ^{40}Ca(e,e'p)^{39}K experiment [45]. This excitation spectrum corresponds to the hole spectral function (Eq. (2.61)) with a shifted energy denominator since it is plotted as a function of $E_x = E - E_0^{(^{39}K)}$. In the IPM, the $1s\frac{1}{2}$ orbital is the second least bound proton shell in ^{40}Ca. This shell is 2.5 MeV more bound than the least bound proton shell, so one would expect to see a single peak at $E_x = 2.5$ MeV with a normalization of unity. While it is true that the majority of the strength resides in the peak at $E_x = 2.5$ MeV, Fig. 2.1 shows that there is additional strength measured throughout the energy domain of the experiment.

While the spectral function is interesting on its own, it can also be used to calculate observables such as the one body density matrix, defined as

$$\rho(\alpha, \beta) = \langle \Psi_0^A | \, \hat{\rho} \, | \Psi_0^A \rangle = \langle \Psi_0^A | \, \hat{a}_\alpha^\dagger \hat{a}_\beta \, | \Psi_0^A \rangle \, . \tag{2.62}$$

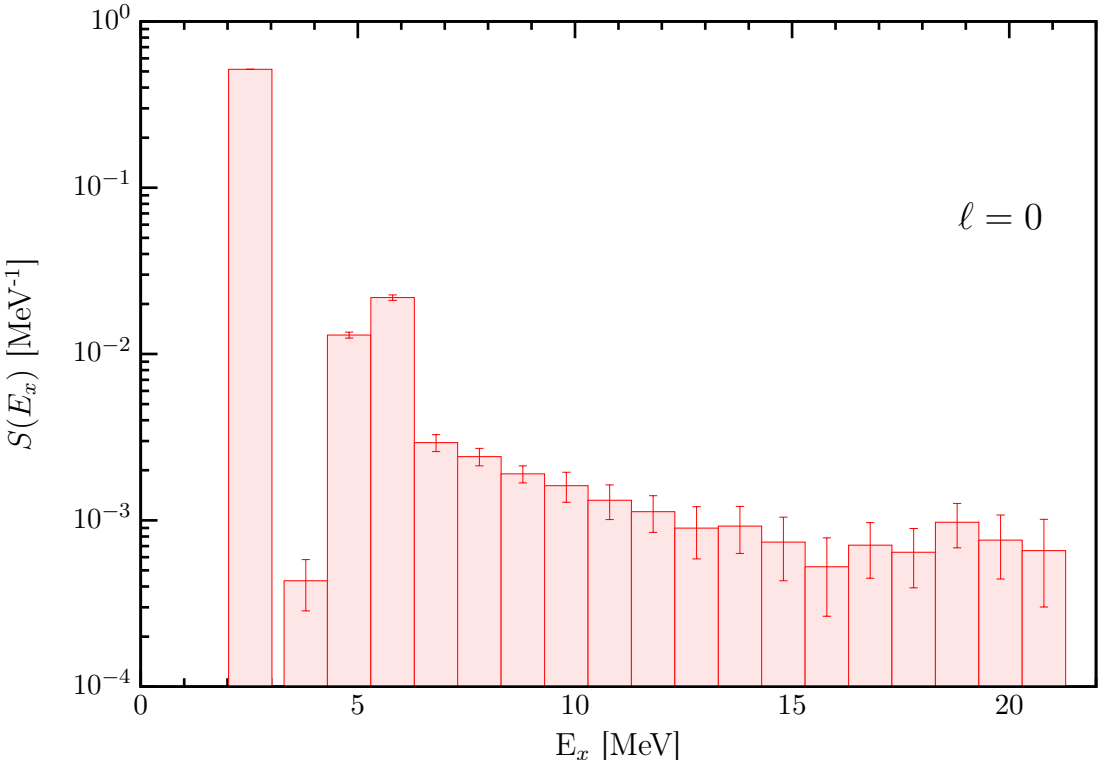

Figure 2.1: Spectral strength as a function of excitation energy for the removal of the $1s\frac{1}{2}$ orbital from ^{40}Ca and extracted from the $^{40}\mathrm{Ca}(e,e'p)^{39}\mathrm{K}$ experiment [45, 47]. E_x is the excitation energy with respect to the ground state of ^{39}K.

By inspecting Eq. (2.61), it is clear that Eq. (2.62) is obtained through an integral over energy of $S^h(\alpha,\beta;E)$,

$$\rho(\alpha,\beta) = \int_{-\infty}^{\varepsilon_F} dE S^h(\alpha,\beta;E). \tag{2.63}$$

In nuclei, the diagonal of the one-body density matrix in coordinate space can represent the matter density or the charge density,

$$\rho(\boldsymbol{r}) = \rho(\boldsymbol{r},\boldsymbol{r}).$$

The occupation of particles with quantum numbers α in a nucleus can be calculated by

integrating the diagonal elements of the one-body density matrix,

$$n_\alpha = \int d^3r \rho_\alpha(\boldsymbol{r}). \tag{2.64}$$

There is also strength above the Fermi-energy contained in the particle spectral function, which can be calculated in a similar way,

$$d_\alpha = \int d^3r \int_{\varepsilon_f}^{\infty} S^p_\alpha(\boldsymbol{r}, \boldsymbol{r}; E). \tag{2.65}$$

The occupation and depletion satisfy the following sum rule [20, 21]

$$n_\alpha + d_\alpha = 1, \tag{2.66}$$

which is a natural result, since the entire particle must be present when considering the entire energy domain. Consequences of this sum rule are explored in more detail in later chapters.

2.3.4 The Dyson equation

At this point, it should be clear that the propagator is a useful tool for studying nuclei. While the single-particle propagator is defined in Eq. (2.49), it is not obvious how to evaluate it. The propagator can be expanded in a perturbation series by introducing the Interaction picture [20,21], which then leads to the self-consistent equation for the propagator known as the Dyson equation. In order to rewrite the propagator in a perturbative way, the Gell-Mann and Low theorem can be employed [21].

Theorem 1 (Gell-Mann and Low)**.** *Let $\hat{H} = \hat{H}_0 + e^{-\varepsilon|t|}\hat{H}_1$ be the Hamiltonian of an interacting system where $\hat{H}_0$ is the non-interacting Hamiltonian such that $\hat{H}_0 |\Phi_0\rangle = E_0 |\Phi_0\rangle$ and*

$|\Phi_0\rangle$ is the nondegenerate ground state, then

$$\lim_{\varepsilon\to 0}\frac{\hat{U}_\varepsilon(0,\pm\infty)\,|\Phi_0\rangle}{\langle\Phi_0|\,\hat{U}_\varepsilon(0,\pm\infty)\,|\Phi_0\rangle}=\frac{|\Psi_0\rangle}{\langle\Phi_0|\Psi_0\rangle}$$

is an eigenstate of $\hat{H}$,

$$\hat{H}\frac{|\Psi_0\rangle}{\langle\Phi_0|\Psi_0\rangle}=E\frac{|\Psi_0\rangle}{\langle\Phi_0|\Psi_0\rangle},$$

provided $\langle\Phi_0|\Psi_0\rangle$ is non-vanishing.

Using Theorem 1 to rewrite all instances of $|\Psi_0\rangle$ in Eq. (2.49) and transforming Heisenberg operators to Interaction operators results in

$$\frac{\langle\Psi_0|\,\mathcal{T}\left[a_{\alpha H}(t)a^\dagger_{\beta H}(t')\right]|\Psi_0\rangle}{\langle\Psi_0|\Psi_0\rangle}=\lim_{\varepsilon\to 0}\frac{\langle\Phi_0|\,\mathcal{T}\left[\hat{U}_\varepsilon(\infty,t)a_{\alpha I}(t)\hat{U}_\varepsilon(t,t')a^\dagger_{\beta I}\hat{U}_\varepsilon(t',-\infty)\right]|\Phi_0\rangle}{\langle\Phi_0|\,\hat{U}_\varepsilon(\infty,0)\hat{U}_\varepsilon(0,-\infty)\,|\Phi_0\rangle},\tag{2.67}$$

where subscripts I and H denote the Interaction picture and the Heisenberg picture, respectively. The time-evolution operators in Eq. (2.67) can be expanded in the Interaction picture [20, 21] which leads to

$$G(\alpha,\beta;t,t')=\frac{\sum_{n=0}^{\infty}\left(\frac{-i}{\hbar}\right)^n\int_{-\infty}^{\infty}dt_1...\int_{-\infty}^{\infty}dt_n\,\langle\Phi_0|\,\mathcal{T}\left[\hat{H}_1(t_1)...\hat{H}_1(t_n)\hat{a}_\alpha(t)\hat{a}^\dagger_\beta\right]|\Phi_0\rangle}{\sum_{m=0}^{\infty}\left(\frac{-i}{\hbar}\right)^m\int_{-\infty}^{\infty}dt'_1...\int_{-\infty}^{\infty}dt'_m\,\langle\Phi_0|\,\mathcal{T}\left[\hat{H}_1(t'_1)...\hat{H}_1(t'_m)\right]|\Phi_0\rangle},\tag{2.68}$$

where the limit as $\varepsilon\to 0$ has been taken. It is now clear that the propagator has an infinite number of terms, and Eq. (2.68) generates the perturbation series term-by-term.

To get an idea of how each term is generated, it is useful to consider the first two terms in the perturbation series. The zeroth-order term of the series is just $G^{(0)}(\alpha,\beta,t-t')$, as expected. The first-order term is more involved to calculate. Let the interacting Hamiltonian,

$\hat{H}_1$, be a two-body interaction

$$\hat{H}_1 = \hat{V} = \frac{1}{4}\sum_{\alpha\beta\gamma\delta} \langle\alpha\beta|\, V\, |\gamma\delta\rangle\, \hat{a}^\dagger_\alpha \hat{a}^\dagger_\beta \hat{a}_\delta \hat{a}_\gamma.$$

With this form of the interacting Hamiltonian, the first-order term from the numerator of Eq. (2.68) is

$$G^{(1)}_{\text{num}}(\alpha,\beta,t-t') = \frac{-i}{\hbar}\sum_{\gamma\delta\varepsilon\theta}\int_{-\infty}^{\infty} dt_1\, \langle\gamma\delta|\, V\, |\varepsilon\theta\rangle \times \langle\Phi_0|\, \mathcal{T}\left[\hat{a}^\dagger_\gamma(t_1)\hat{a}^\dagger_\delta(t_1)\hat{a}_\theta(t_1)\hat{a}_\varepsilon(t_1)\hat{a}_\alpha(t)\hat{a}^\dagger_\beta(t')\right]|\Phi_0\rangle\,. \quad (2.69)$$

The time-ordering of the six operators in Eq. (2.69) results in six separate contributions to the first-order approximation to the propagator. Each higher order has more operators to time-order, which becomes exceedingly tedious very quickly. Luckily, Wick's theorem can be used to express the time-ordering of operators in a systematic way.

Theorem 2. *Wick' Theorem*

$$\mathcal{T}[\hat{U}\hat{V}\hat{W}...\hat{X}\hat{Y}\hat{Z}] = N(\hat{U}\hat{V}\hat{W}...\hat{X}\hat{Y}\hat{Z}) + N(\textit{sum over all possible pairs of contractions})$$

Wick's Theorem greatly simplifies the calculation of each term in the propagator, since the expectation value of any normal-ordered product (N) in the ground-state is non-zero only for fully-contracted sets of particle/hole creation/annihilation operators [20]. Furthermore, each contracted pair corresponds to a free-propagator

$$\hat{a}_\alpha(t)^\bullet \hat{a}_\beta(t')^{\dagger\bullet} = i\hbar G^{(0)}(\alpha,\beta;t-t').$$

This indicates that all contributions to the propagator can be written in terms of the free

propagator, which is known. Since each contribution is a product of free propagators and interaction terms, they can be represented diagrammatically as Feynman diagrams [21]. To illustrate, each contribution to the numerator of the first-order term is show in Fig. 2.2. The diagrams in Fig. 2.2 can be separated into two types, connected and disconnected. Diagrams (a-c) are connected while diagrams (d-f) are disconnected. It can be shown that the disconnected diagrams are exactly canceled by the denominator in Eq. (2.68) [21]. Thus, the propagator is the sum of all connected Feynman diagrams

$$G(\alpha,\beta;t-t') = \sum_{n=0}^{\infty}\left(\frac{-i}{\hbar}\right)^n \int_{-\infty}^{\infty} dt_1 ... \int_{-\infty}^{\infty} dt_n \left\langle \Phi_0 \right| \mathcal{T}\left[\hat{H}_1(t_1)...\hat{H}_1(t_n)\hat{a}_\alpha(t)\hat{a}^\dagger_\beta(t')\right] \left|\Phi_0\right\rangle_{\text{connect}} .$$

The procedure for calculating the single-particle propagator now consists of drawing all connected, topologically distinct Feynman diagrams at each order. The Feynman rules can then be used to convert each diagram to a calculable integral/sum [20].

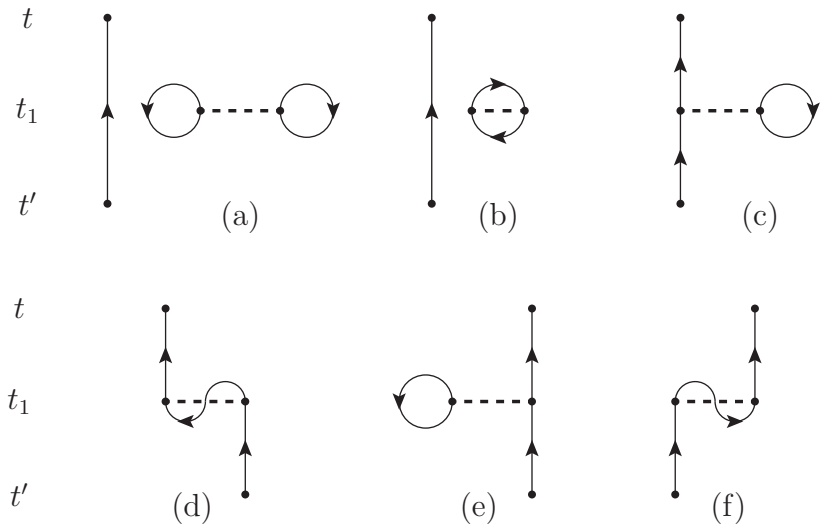

Figure 2.2: First-order contributions to the single-particle propagator. Solid lines with arrows corresponds to free propagators while dashed lines correspond to a two-body interaction.

Each term in the perturbation expansion for $G(\alpha,\beta;t-t')$ can be Fourier-transformed so that the propagator in the energy domain, $G(\alpha,\beta;E)$, is calculated term-by-term [20].

Contributions to the propagator in the energy domain can also be represented with a corresponding Feynman diagram. There is a separate set of Feynman rules for the diagrams in the energy domain [20].

After drawing diagrams of increasing order in the energy domain, it becomes clear that all connected diagrams share the same property of beginning and ending with a free propagator. Given this fact, it must be true that the propagator can be represented by the Feynman diagram in Fig. 2.3, where the double-line represents the exact single-particle propagator

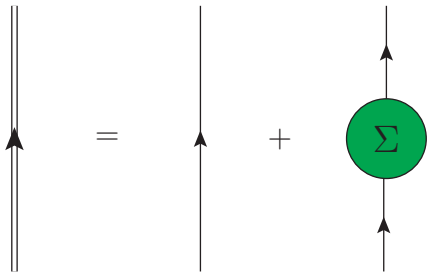

Figure 2.3: Reducible self-energy expansion

and the ball labeled Σ represents the self-energy. This defines the self-energy as the sum of all intermediate diagrams that can be drawn between the top and bottom free propagators. With some inspection, it is apparent that the self-energy can also be drawn order-by-order. To illustrate, the first- and second-order self-energy contributions are shown in Fig. 2.4.

All self-energy diagrams can be separated into two different categories, irreducible and reducible. Reducible diagrams are those which contain at least two parts that are only connected by a free propagator; Fig. 2.4(b) is an example of a reducible diagram. Conversely, irreducible diagrams are those which cannot be divided into at least two valid diagrams by "cutting" free-propagator lines. the remaining diagrams in Fig. 2.4 are examples of irreducible diagrams. The sum of all irreducible self-energy contributions provides the irreducible self-energy, Σ^*. After further analysis, it can be seen that Σ^* can generate all diagrammatic contributions to the propagator with the diagram in Fig. 2.5 . Seeing as this is an infinite sum, Fig. 2.5 can be reformulated as Fig. 2.6 by realizing that the diagrams

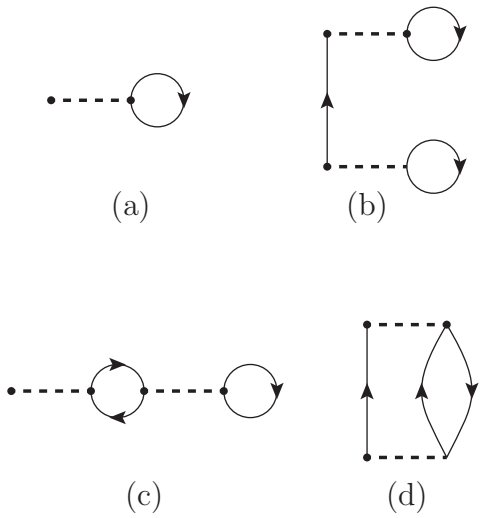

Figure 2.4: First- and second-order contributions to the self-energy

below the dashed line in Fig. 2.5 are the exact same diagrams that make up the propagator.

The equation describing Fig. 2.6 is the Dyson equation

$$G(\alpha,\beta;E) = G^{(0)}(\alpha,\beta;E) + \sum_{\gamma\delta} G^{(0)}(\alpha,\gamma;E)\Sigma^{*}(\gamma,\delta;E)G(\delta,\beta;E). \tag{2.70}$$

Given any irreducible self-energy, Eq. (2.70) will generate the corresponding propagator to all orders. So the problem of finding the single-particle propagator has been reduced to finding an appropriate irreducible self-energy. It is not possible to calculate the exact irreducible self-energy, so approximations must be made to suit the system under consideration. Rather than approximate the self-energy order-by-order, it can be generated by introducing a two-particle propagator [20]. Another method for approximating the self-energy is to parametrize it as an optical potential (see Sec. 2.1.1). This parametrization leads to the Dispersive Optical Model (DOM), which is detailed in the next section.

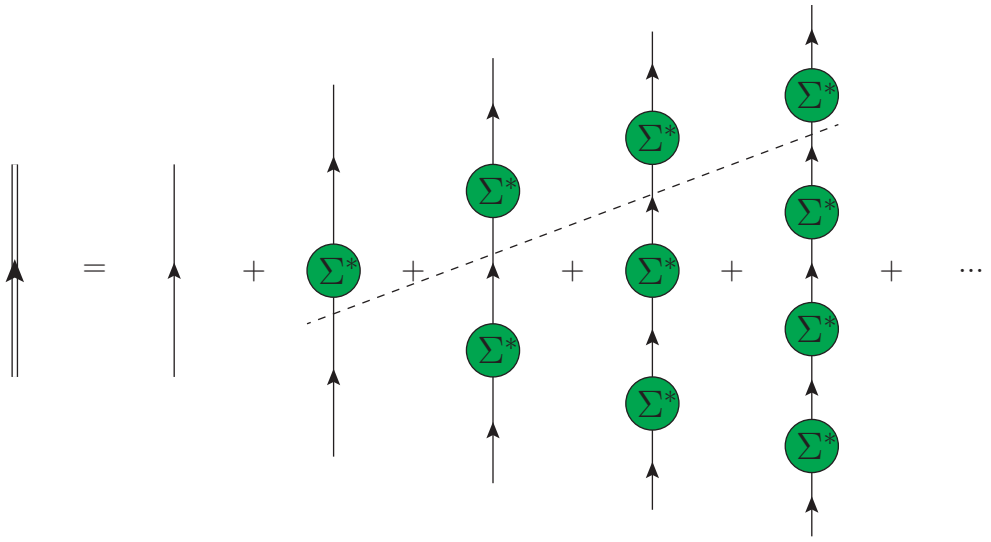

Figure 2.5: Irreducible self-energy expansion

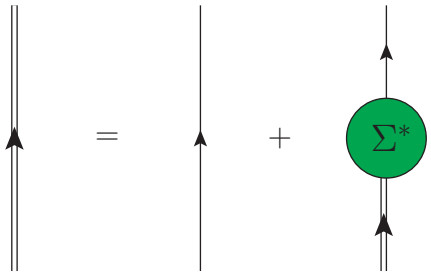

Figure 2.6: Diagrammatic Dyson Equation

2.4 The Dispersive Optical Model

The DOM, first introduced by Mahaux and Sartor [22], is a parametrized self-energy which makes use of a dispersion relation, which is obeyed by the exact self-energy, that relates the imaginary part of the potential to its real part over all energies. The parametrization is inspired by the connection between the irreducible self-energy and the optical potential, which is detailed in Subsection (2.4.2). See Ref. [48] for an in-depth review of the DOM.

2.4.1 Dispersion Relation

The irreducible self-energy can be divided into a static (energy-independent) component and a dynamic (energy-dependent) component. The static component is the Hartree-Fock term; it is real and consists only of diagrams whose free propagator lines begin and end on the same interaction. The dynamic component is comprised of all other diagrams and is in general complex,

$$\Sigma^*(\alpha,\beta;E) = \Sigma^*_{HF}(\alpha,\beta) + \Sigma^*_D(\alpha,\beta;E).$$

By its nature, Σ^*_D shares the same analytic properties as G [49]. This means that it also satisfies a dispersion relation similar to Eq. (2.59),

$$\mathrm{Re}\Sigma^*_D(\alpha,\beta;E) = \frac{1}{\pi}\mathcal{P}\int_{-\infty}^{\infty} dE' \frac{\mathrm{Im}\Sigma^*_D(\alpha,\beta;E')}{E-E'}.$$

Thus, to describe $\mathrm{Re}\Sigma^*_D$ at any energy, $\mathrm{Im}\Sigma^*_D$ must be known at all energies (positive and negative). When this constraint is enforced in an optical potential, it ensures that negative energy and positive energy observables are described simultaneously. This dispersion relation is the reason why the DOM is successful in describing nuclei.

Including the static term leads to the full dispersion relation,

$$\mathrm{Re}\Sigma^*(\alpha,\beta;E) = \Sigma^*_{HF}(\alpha,\beta) + \frac{1}{\pi}\mathcal{P}\int_{-\infty}^{\infty} dE' \frac{\mathrm{Im}\Sigma^*(\alpha,\beta;E')}{E-E'}. \tag{2.71}$$

While Eq. (2.71) would, in principle, generate a full self-energy that describes nuclei, the Σ^*_{HF} term does not provide enough binding [20]. Since the goal is to parametrize the static term, it would be more useful if the static term in Eq. (2.71) was able to provide more binding. To this end, an alternate form of Eq. (2.71) can be derived by subtracting $\mathrm{Re}\Sigma^*$ at

the Fermi energy,

$$\mathrm{Re}\Sigma^*(\alpha,\beta;E) = \mathrm{Re}\Sigma^*(\alpha,\beta;\varepsilon_F) + \frac{1}{\pi}\mathcal{P}\int_{-\infty}^{\infty} dE' \mathrm{Im}\Sigma^*(\alpha,\beta;E')\left[\frac{1}{E-E'} - \frac{1}{\varepsilon_F - E'}\right]. \quad (2.72)$$

This subtracted form is used to generate the results presented throughout this thesis. Note that since $\mathrm{Im}\Sigma^*$ is zero between the particle addition and removal thresholds (just as with G in Eq. (2.56)), the integral in Eq. (2.72) is split into two integrals corresponding to the hole and particle energy domains. These thresholds are different from those of G [20].

Equation (2.72) is a very powerful constraint that is used in the DOM to generate a proper irreducible self-energy. This dispersion relation ensures that Σ^* can be simultaneously described at positive and negative energies. This makes it possible to parametrize the irreducible self-energy at all energies. Thus, elastic-scattering data is used to constrain the self-energy at positive energies while structure information (charge density, energy levels, particle number, etc.) is simultaneously used to constrain the self-energy at negative energies. Throughout this process of adjusting parameters to describe data, Eq. (2.72) guarantees that the irreducible self-energy stays well defined [28, 29].

2.4.2 Self-Energies and optical potentials

When considering the derivations of the irreducible self-energy in Sec. 2.3.4 and the optical potential in Sec. 2.1, it is clear that these objects are related [48]. The goal of this subsection is to show that these quantities are effectively equal.

Consider an operator $\hat{H}^{(p)}$ which satisfies

$$(E - \hat{H}^{(p)}(E))\hat{G}^{(p)}(E) = 1, \quad (2.73)$$

where this defines the particle Hamiltonian as $\hat{H}^{(p)}$, and $\hat{G}_+$ is the resolvent of the particle

propagator defined in Eq. (2.48) such that

$$G^{(p)}(\boldsymbol{r}, \boldsymbol{r'}; E) = \langle \boldsymbol{r} | \, \hat{G}^{(p)}(E) \, | \boldsymbol{r'} \rangle \, . \tag{2.74}$$

Note that $\hat{H}^{(p)}(E)$ is not the same as the full many-body Hamiltonian $\hat{H}$. Since the energy domain of $\hat{G}_+(E)$ is $(\varepsilon_F^+, \infty)$, as explained in Sec. 2.3.3, this is also the energy domain of $\hat{H}^{(p)}(E)$. Thus, in this energy domain, the resolvent form of the Dyson equation can be written as

$$\hat{G}^{(p)}(E) = \hat{G}^{(0)}(E) + \hat{G}^{(0)}(E)\hat{\Sigma}^*(E)\hat{G}^{(p)}(E), \tag{2.75}$$

where $\hat{G}^{(0)}(E)$ and $\hat{\Sigma}^*(E)$ are defined in the same way as Eq. (2.74). Choosing $\hat{H}_0 = \hat{T}$ and comparing Eq. (2.75) and Eq. (2.73) leads to the following form of the particle Hamiltonian,

$$\hat{H}^{(p)}(E) = \hat{T} + \hat{\Sigma}^*(E). \tag{2.76}$$

In order to relate Eq. (2.76) to the effective Hamiltonian in Eq. (2.8), projection operators are employed. Consider the following identity,

$$\left(E - \hat{H}^{(p)}\right)\left(E - \hat{H}^{(p)}\right)^{-1} = 1 = \left(E - \hat{H}^{(p)}\right)\left(\hat{P} + \hat{Q}\right)\left(E - \hat{H}^{(p)}\right)^{-1},$$

where the properties in Eq. (2.5) have been used. The same projection operator is used that is used in Sec. 2.1, but written in second quantization,

$$\hat{P} \, |\Psi^{(A+1)}\rangle = \hat{a}_\xi^\dagger \, |\Psi_0^A\rangle \, . \tag{2.77}$$

From here, it can be shown that the relation between the particle Hamiltonian and the

effective Hamiltonian from Eq. (2.8) is [50]

$$\mathcal{H}(E) = (1 - \hat{\rho})H^{(p)}(E) + \hat{\rho}E, \tag{2.78}$$

where $\hat{\rho}$ is the one-body density operator defined in Eq. (2.62). While the Hamiltonians in Eq. (2.78) are not exactly the same, it can be shown that the scattering wave functions obtained from each are asymptotically equivalent [50].

To show this, the elastic overlap function must first be introduced,

$$|\chi_E^{(0)}\rangle = \langle \Psi_0^A | \Psi^{0(A+1)} \rangle \,, \tag{2.79}$$

where $|\Psi^{0(A+1)}\rangle$ is the scattering wave function in which the target is still in its ground state,

$$\hat{H}^{(A+1)} \, |\Psi^{(0(A+1)}\rangle = (E_0^A + E) \, |\Psi^{(0(A+1)}\rangle \,.$$

It can be shown that $|\Psi^{0(A+1)}\rangle$ satisfies an $(A+1)$-body Lippmann-Schwinger equation [50],

$$|\Psi_{\boldsymbol{k}}^{0(A+1)}\rangle = \frac{i\eta}{E_k - (\hat{H} - E_0^A) + i\eta} \hat{a}_{\boldsymbol{k}}^\dagger \, |\Psi_0^A\rangle \,. \tag{2.80}$$

Using Eq. (2.80) in Eq. (2.79) to find the elastic overlap function leads to

$$\chi_{\boldsymbol{k}}^{(0)}(\boldsymbol{r}) = \langle \Psi_0^A | \, \hat{a}_{\boldsymbol{r}} \, |\Psi_{\boldsymbol{k}}^{0(A+1)}\rangle = i\eta \, \langle \Psi_0^A | \, \hat{a}_{\boldsymbol{r}} \frac{1}{E_k - (\hat{H} - E_0^A) + i\eta} \hat{a}_{\boldsymbol{k}}^\dagger . \, |\Psi_0^A\rangle \tag{2.81}$$

The quantity on the right-hand-side of Eq. (2.81) is the particle propagator defined in Eq. (2.51) with $\alpha = \boldsymbol{r}$ and $\beta = \boldsymbol{k}$. Using the particle Hamiltonian as defined in Eq. (2.73),

the resolvent of the particle propagator can be written as

$$\hat{G}^{(p)} = \frac{1}{E_k - \hat{H}^{(p)} + i\eta}, \tag{2.82}$$

which leads to

$$\chi^{(0)}_{\boldsymbol{k}}(\boldsymbol{r}) = G^{(p)}(\boldsymbol{r}, \boldsymbol{k}; E_k) = \langle \boldsymbol{r} | \, \frac{i\eta}{E_k - \hat{H}^{(p)} + i\eta} \, | \phi_k \rangle \, .$$

This equation can be manipulated using Eq. (2.76) to produce the Lippmann-Schwinger equation for one-body scattering due to the irreducible self-energy,

$$|\chi^{(0)}_{\boldsymbol{k}}\rangle = |\phi_k\rangle + \hat{G}^{(p)}(E_k)\hat{\Sigma}^*(E_k) \, |\phi_k\rangle \, . \tag{2.83}$$

This means that $|\chi^{(0)}_{\boldsymbol{k}}\rangle$ is an eigenstate of the particle Hamiltonian,

$$\hat{H}^{(p)}(E) \, |\chi^{(0)}_E\rangle = E \, |\chi^{(0)}_E\rangle \, .$$

Thus, the elastic overlap function has been shown to truly be the elastic scattering wave function and can be calculated through single-particle scattering using the particle Hamiltonian.

To make the connection with the model wave function, compare the elastic overlap function with $|\xi\rangle$, which can be derived from Eq. (2.77),

$$\xi(\boldsymbol{r}) = \langle \boldsymbol{r} | \xi \rangle = \langle \Psi^A_0 | \, \hat{P} \, | \Psi^{A+1} \rangle \, . \tag{2.84}$$

There is a subtle but important difference between Eq. (2.79) and Eq. (2.84) which is that $|\Psi^{0(A+1)}\rangle$ is an eigenfunction of the full $A+1$ Hamiltonian while $\hat{P} \, |\Psi^{(A+1)}\rangle$ is the projection of the full $A+1$ eigenfunction to a combination of the ground state of the target nucleus

and the scattered nucleon. In order to find a relation between these similar functions, the following property of this particular projector can be invoked,

$$\langle \Psi_0^A | \, a_{\boldsymbol{r}} (1 - \hat{P}) \, | \Psi_0^{(A+1)} \rangle = 0,$$

which can be verified using Eq. (2.77). From here, it can be shown that

$$|\xi\rangle = \left(1 + \frac{\hat{\rho}}{1 - \hat{\rho}} \right) |\chi_E^{(0)}\rangle \, , \tag{2.85}$$

By inserting a complete set of natural orbitals, which are the eigenfunctions of the one-body density matrix [50], Eq. (2.85) becomes

$$\xi(\boldsymbol{r}) = \chi^{(+)}(\boldsymbol{r}) + \sum_n \psi_n(\boldsymbol{r}) \frac{n}{1 - n} \langle n | \chi_E^{(0)} \rangle \, ,$$

where $n(r)$ are natural orbitals and n are the corresponding eigenvalues. Natural orbitals are all bound states, so asymptotically,

$$\xi(\boldsymbol{r}) \sim \chi_E^{(0)}(\boldsymbol{r}).$$

Thus, the scattering wave function calculated from either the irreducible self-energy or the optical potential will yield the same elastic scattering cross section. That being said, the interior of the wave functions will not necessarily be the same. Since it was shown that the elastic overlap function calculated from the irreducible self-energy exactly represents the elastic scattering wave function, it is safe to say that self-energy interpretation of elastic scattering is more complete.

This link between the irreducible self-energy and the optical potential implies that Σ^* can be parametrized in much the same way as optical potentials have been in the past. Thus,

Woods-Saxon forms are used in a manner similar to that outlined in Sec. 2.1.1. The exact functional form and parametrization of the current implementation of the DOM is provided in App. B.

2.4.3 Properties of the DOM propagator

At first glance, it would seem that choosing $\hat{H}_0 = \hat{T}$ precludes any possibility to represent the hole propagator since this choice would make the propagator equivalent to that of a single-body system as in Sec. 2.3.1. However, it was shown in the previous subsection that the particle Hamiltonian (with the choice of $\hat{H}_0 = \hat{T}$) contains all of the information of the full Hamiltonian while being projected onto a single-body space. The same can be done for the hole propagator with the appropriately defined projection operator,

$$\hat{P}^{(h)} \left|\Psi^{(A-1)}\right\rangle = \hat{a}_{\xi^{(-)}} \left|\Psi_0^A\right\rangle .$$

This equation shows the full wave function $|\Psi^{(A-1)}\rangle$ begin projected onto the single configuration where there is a hole, $|\xi^{(-)}\rangle$, and the ground state of the A-body system. While the language for describing this situation is cumbersome compared to the particle case, the formalism is the same. Analogously, the hole Hamiltonian can be defined such that

$$(E - \hat{H}^{(h)}(E))\hat{G}^{(h)}(E) = 1,$$

where $\hat{G}_-(E)$ is the resolvent of $G^{(h)}(\alpha, \beta; E)$ defined in Eq. (2.51). Again, choosing $\hat{H}_0 = \hat{T}$ connects the Dyson equation with the hole Hamiltonian such that

$$\hat{H}^{(h)}(E) = \hat{T} + \hat{\Sigma}^*(E).$$

Thus, choosing $\hat{H}_0 = \hat{T}$ is simply projecting the many-body problem onto a one-body space, regardless of the energy domain.

With this in mind, the DOM propagator is well-defined over the entire energy domain as

$$(E - \hat{H}_{DOM}(E))\hat{G}_{DOM}(E) = 1, \tag{2.86}$$

where the DOM Hamiltonian is defined as

$$\hat{H}_{DOM}(E) = \hat{T} + \hat{\Sigma}^*_{DOM}(E),$$

and $\Sigma^*_{DOM}(\boldsymbol{r}, \boldsymbol{r}'; E)$ is detailed in App. B. Since the DOM propagator satisfies Eq. (2.86), then necessarily it satisfies Eq. (2.35). This fact is convenient, since Green's function of the Schrödinger equation has useful properties.

Consider Green's Identity, which is stated without proof [42]

Identity 1 (Green's Identity)**.** *Let $U_1(\boldsymbol{r})$ and $U_2(\boldsymbol{r})$ be "reasonable" scalar functions of position $\boldsymbol{r}$, then*

$$\oint_{\mathcal{S}} d\boldsymbol{A} \cdot [U_1(\boldsymbol{r})\boldsymbol{\nabla}U_2(\boldsymbol{r}) - U_2(\boldsymbol{r})\boldsymbol{\nabla}U_1(\boldsymbol{r})] = \int_{\mathcal{V}} d^3r[U_1(\boldsymbol{r})\boldsymbol{\nabla}^{\mathbf{2}}U_2(\boldsymbol{r}) - U_2(\boldsymbol{r})\boldsymbol{\nabla}^{\mathbf{2}}U_1(\boldsymbol{r})]. \tag{2.87}$$

Green's function of the nonlocal Schrödinger equation, Eq. (2.35), satisfies Green's Identity. One consequence of this is that Green's function is symmetric.

Proposition 1. *Let $G(\boldsymbol{r}, \boldsymbol{r'})$ be a Green's function for the nonlocal three-dimensional Schrödinger equation satisfying the boundary condition in Eq.* (2.45)*, then $G(\boldsymbol{r}, \boldsymbol{r'})$ is symmetric.*

$$G(\boldsymbol{r}, \boldsymbol{r'}) = G(\boldsymbol{r'}, \boldsymbol{r})$$

Proof. Using Green's theorem (Eq. (2.87)) with $U_1(\boldsymbol{r}) = G(\boldsymbol{r}, \boldsymbol{r_a})$ and $U_2(\boldsymbol{r}) = G(\boldsymbol{r}, \boldsymbol{r_b})$,

$$\oint_{\mathcal{S}} d\boldsymbol{A} \cdot [G(\boldsymbol{r}, \boldsymbol{r_a})\boldsymbol{\nabla} G(\boldsymbol{r}, \boldsymbol{r_b}) - G(\boldsymbol{r}, \boldsymbol{r_b})\boldsymbol{\nabla} G(\boldsymbol{r}, \boldsymbol{r_a})] \\ = \int_{\mathcal{V}} d^3r [G(\boldsymbol{r}, \boldsymbol{r_a})\boldsymbol{\nabla^2} G(\boldsymbol{r}, \boldsymbol{r_b}) - G(\boldsymbol{r}, \boldsymbol{r_b})\boldsymbol{\nabla^2} G(\boldsymbol{r}, \boldsymbol{r_b})]. \quad (2.88)$$

Taking the volume as all space, the surface integral in Eq. (2.88) vanishes

$$\oint_{\mathcal{S}} d\boldsymbol{A} \cdot [G(\boldsymbol{r}, \boldsymbol{r_a})\boldsymbol{\nabla} G(\boldsymbol{r}, \boldsymbol{r_b}) - G(\boldsymbol{r}, \boldsymbol{r_b})\boldsymbol{\nabla} G(\boldsymbol{r}, \boldsymbol{r_a})] = 0. \quad (2.89)$$

This can be seen by first noting that $G(\boldsymbol{r}, \boldsymbol{r'})$ is asymptotic to the free Green's function, Eq. (2.45), for large values of r. Thus, without loss of generality, $G^{(0)}(\boldsymbol{r}, \boldsymbol{r'})$ will be used to show the validity of Eq. (2.89). The surface element $d\boldsymbol{A}$ is in the radial direction, so

$$\boldsymbol{d\hat{A}} = \hat{\boldsymbol{r}} \implies \left[\boldsymbol{dA} \cdot G^{(0)}(\boldsymbol{r}, \boldsymbol{r_a})\boldsymbol{\nabla} G^{(0)}(\boldsymbol{r}, \boldsymbol{r_b})\right] = G^{(0)}(\boldsymbol{r}, \boldsymbol{r_a})\frac{\partial}{\partial r} G^{(0)}(\boldsymbol{r}, \boldsymbol{r_b}).$$

So the pieces to the integrand in Eq. (2.89) are

$$G^{(0)}(\boldsymbol{r}, \boldsymbol{r_a}) = \frac{e^{ik\mathscr{r}_a}}{4\pi\mathscr{r}_a},$$

where

$$\mathscr{r}_a = |\boldsymbol{r} - \boldsymbol{r_a}| = \sqrt{r^2 + r_a^2 - 2\boldsymbol{r} \cdot \boldsymbol{r_a}},$$

and

$$\frac{\partial}{\partial r} G^{(0)}(\boldsymbol{r}, \boldsymbol{r_a}) = \frac{e^{ik\mathscr{r}_a}}{4\pi\mathscr{r}_a^2}\left(r - r_a\cos\theta_{ra}\right)\left(ik - \frac{1}{\mathscr{r}_a}\right).$$

Now, without loss of generality, let $\hat{\boldsymbol{r}}_{\boldsymbol{a}} = \hat{\boldsymbol{z}}$. Thus, when considering the surface integral in

Eq. (2.88),

$$\theta_{ra} = \theta \qquad\qquad \theta_{rb} = \theta - \theta_b.$$

Considering that there is spherical symmetry, the surface integral becomes

$$\oint_{\mathcal{S}} \to 2\pi \lim_{r\to\infty} r^2 \int_{-1}^{1} d\cos\theta \left[\frac{e^{ik(\mathscr{r}_a+\mathscr{r}_b)}}{(4\pi)^2 \mathscr{r}_a \mathscr{r}_b^2} (r - r_b\cos(\theta-\theta_b)) \left(ik - \frac{1}{\mathscr{r}_b} \right) \right.$$
$$\left. - \frac{e^{ik(\mathscr{r}_a+\mathscr{r}_b)}}{(4\pi)^2 \mathscr{r}_b \mathscr{r}_a^2} (r - r_a\cos\theta) \left(ik - \frac{1}{\mathscr{r}_a} \right) \right]. \quad (2.90)$$

Taking the limit and keeping in mind that

$$\lim_{r\to\infty} \mathscr{r} = r,$$

the integrand of Eq. (2.90) becomes

$$\lim_{r\to\infty} \frac{e^{2ikr}}{8\pi^2 r} \left[r_a\cos\theta - r_b\cos(\theta-\theta_b) \right] = 0 \implies \oint_{\mathcal{S}} = 0$$

Now, the only thing left to address is the volume integral in Eq. (2.88). It can be evaluated by using Eq. (2.35) to substitute for terms involving $\boldsymbol{\nabla^2} G$, resulting in

$$0 = \frac{2\mu}{\hbar^2} \int_{\mathcal{V}} d^3r G(\boldsymbol{r}, \boldsymbol{r_a}) \left[\int_{\mathcal{V}} d^3r' \mathcal{V}(\boldsymbol{r}, \boldsymbol{r'}) G(\boldsymbol{r'}, \boldsymbol{r_b}) - EG(\boldsymbol{r}, \boldsymbol{r_b}) - \delta^{(3)}(\boldsymbol{r} - \boldsymbol{r_b}) \right]$$
$$- \frac{2\mu}{\hbar^2} \int_{\mathcal{V}} d^3r G(\boldsymbol{r}, \boldsymbol{r_b}) \left[\int_{\mathcal{V}} d^3r' \mathcal{V}(\boldsymbol{r}, \boldsymbol{r'}) G(\boldsymbol{r'}, \boldsymbol{r_a}) - EG(\boldsymbol{r}, \boldsymbol{r_a}) - \delta^{(3)}(\boldsymbol{r} - \boldsymbol{r_a}) \right].$$

This simplifies to

$$0 = G(\boldsymbol{r_b}, \boldsymbol{r_a}) - G(\boldsymbol{r_a}, \boldsymbol{r_b})$$
$$+ \int_{\mathcal{V}} d^3r \int_{\mathcal{V}} d^3r' \left[G(\boldsymbol{r}, \boldsymbol{r_a}) \mathcal{V}(\boldsymbol{r}, \boldsymbol{r'}) G(\boldsymbol{r'}, \boldsymbol{r_b}) - G(\boldsymbol{r}, \boldsymbol{r_b}) \mathcal{V}(\boldsymbol{r}, \boldsymbol{r'}) G(\boldsymbol{r'}, \boldsymbol{r_a}) \right]. \quad (2.91)$$

The double-integral in Eq. (2.91) is addressed by switching $\boldsymbol{r}$ and $\boldsymbol{r'}$ in the second term of Eq. (2.91), which does not change the result because both $\boldsymbol{r}$ and $\boldsymbol{r'}$ are integrated over all space

$$\int_{\mathcal{V}} d^3r \int_{\mathcal{V}} d^3r' G(\boldsymbol{r}, \boldsymbol{r_b}) \mathcal{V}(\boldsymbol{r}, \boldsymbol{r'}) G(\boldsymbol{r'}, \boldsymbol{r_a}) = \int_{\mathcal{V}} d^3r \int_{\mathcal{V}} d^3r' G(\boldsymbol{r'}, \boldsymbol{r_b}) \mathcal{V}(\boldsymbol{r'}, \boldsymbol{r}) G(\boldsymbol{r}, \boldsymbol{r_a}). \quad (2.92)$$

Since the potential is symmetric, the integrand in the right-hand-side of Eq. (2.92) is equal to the first term in the integral of Eq. (2.91). Thus, the double-integral in Eq. (2.91) vanishes, leaving

$$G(\boldsymbol{r}, \boldsymbol{r'}) = G(\boldsymbol{r'}, \boldsymbol{r}).$$

□

2.5 Methods of calculating G

This section will be addressing the radial Schrödinger equation, valid for spherically symmetric potentials. The radial Schrödinger equation is simplified when considering r-weighted Green's function (the energy dependence is suppressed for clarity)

$$\tilde{G}(r, r') \coloneqq rG(r, r')r',$$

and

$$\tilde{V}(r, r') \coloneqq rV(r, r')r'.$$

Implementing these r-weighted forms leads to the following form of the radial Schödinger equation

$$\frac{-\hbar^2}{2\mu}\frac{d^2}{dr^2}\tilde{G}(r,r') + \frac{\hbar^2\ell(\ell+1)}{2\mu r^2}\tilde{G}(r,r') + \int_0^\infty dr_1 \tilde{V}(r,r_1)\tilde{G}(r_1,r') = \delta(r-r'), \tag{2.93}$$

where μ is the reduces mass of the given nucleon-nucleus system. Note that the integral in (2.93) would normally have a factor of r_1^2 weighting the integrand, but this factor is actually absorbed in the r-weighted functions $\tilde{V}(r,r_1)$ and $\tilde{G}(r_1,r')$. This convention of using a tilde to specify that a function is weighted by r will be used throughout the remains of this chapter.

2.5.1 Local differential equation method

The first method is to directly solve the radial differential equation, Eq. (2.93), as detailed in [42]. This solution is valid when the potential is local, i.e. $\mathcal{V}(r,r') \rightarrow \frac{\delta(r-r')}{r^2}V_{loc}(r)$. The solution has the following form:

$$G(r,r') = \begin{cases} \dfrac{f(r)g(r')}{\frac{-\hbar^2}{2\mu}W(r')}, & r \leq r' \\ \dfrac{f(r')g(r)}{\frac{-\hbar^2}{2\mu}W(r')}, & r \geq r' \end{cases} \tag{2.94}$$

where $f(r)$ and $g(r)$ are the regular and irregular solutions to the homogeneous Schrödinger equation, and $W(r')$ is the Wronskian, defined as

$$W(r) = f'(r)g(r) - f(r)g'(r). \tag{2.95}$$

This solution can be verified by integrating the delta function from Eq. (2.93)

$$\lim_{\varepsilon\to 0}\int_{r'-\varepsilon}^{r'+\varepsilon} dr\left[\frac{-\hbar^2}{2\mu}\frac{d^2}{dr^2}G(r,r') + \frac{\hbar^2\ell(\ell+1)}{2\mu r^2} + V(r)G(r,r')\right] = 1$$

and finding that the derivative is the only non-zero term in the integral.

So the problem has been reduced to finding the regular and irregular solutions to the homogeneous Schrödinger equation. Equation (2.94) is a general expression for a Green's function; boundary conditions are needed to specify the particular problem for which Green's function is being used. It is vital to consider what boundary conditions to impose in order to find Green's function corresponding to the Lehmann representation. Outside the range of the potential, Green's function is identical (within a phase) to the free propagator. Therefore, considering the exact form of the free propagator (Eq. (2.45)) reveals the boundary conditions. For positive energies, k is real, so Eq. (2.45) represents an outgoing wave. Thus, the boundary conditions needed are those of an outgoing wave. At negative energies, k is imaginary, so Eq. (2.45) represents exponential decay. The procedure for finding f and g in all cases is identical other than the boundary conditions. The positive energy case will now be elucidated, so then the only information needed to solve the negative-energy case is that of the boundary conditions.

$\boldsymbol{E > 0}$

The regular solution, $f(r)$, needs to satisfy the boundary condition that

$$f(0) = 0.$$

It should be clear now that the regular solution corresponds to the scattering wave function detailed in Sec. 2.2. The irregular solution, $g(r)$, will diverge at the origin, so its boundary

condition should be imposed at the matching radius R,

$$g(R) = G_\ell(R) + iF_\ell(R).$$

Having a boundary condition at R forces the equation to be solved "backwards", meaning that the solution starts from R and propagates to the origin, resulting in $g(r)$. Just as in the case of the regular solution, $g(r)$ needs to asymptotically match with a phase-shifted free solution as it approaches the origin (rather than approaching ∞ as in the case of the regular solution). To do this, a matching radius near the origin, a_1, must be chosen such that the centrifugal term in Eq. (2.93) far outweighs the potential,

$$\frac{\hbar^2 \ell(\ell+1)}{2\mu a_1^2} \gg V(a_1).$$

The matching at a_1 is of the following form:

$$g(a_1) = \sin(\delta_\ell) F_\ell(a_1) + \cos(\delta_\ell) G_\ell(a_1).$$

The solution then follows a similar logic to that detailed in Sec. 2.2 except for the additional complication that arises from $g(r)$ diverging at the origin. This fact means that the particular Lagrange-Legendre basis used to calculate $f(r)$ cannot be used, since the basis functions are multiplied by r to enforce the boundary condition at the origin. Instead, the Lagrange basis used is defined without a factor of r,

$$\phi_i(r) = (-1)^{N+i} \sqrt{a x_i (x_i - 1)} \frac{P_N(2r/a - 1)}{r - a x_i}.$$

While this leaves the matrix elements of the potential unchanged, the kinetic-energy matrix elements have a different expression; see Ref. [36] for details. This also leads to a slightly

different expression for the internal wave function

$$u_{int}(r) = \sum_{ij} \phi_i(r) \mathbb{C}^{-1}_{ij} [\phi_j(a) u'_{ext}(a) - \phi_j(a_1) u'_{ext}(a_1)],$$

where a is the typical matching radius used in Sec. 2.2. The matrix $\mathbb{C}_{ij}$ is also altered by an additional Bloch operator at $r = a_1$,

$$\mathbb{C}_{ij} = \langle i | \, T + \mathcal{V} + \mathcal{L}(a) - \mathcal{L}(a_1) \, | j \rangle \, .$$

$E < 0$

As was stated earlier, the only difference between positive and negative energy is the boundary condition. At negative energies, Green's function is asymptotic to exponential decay. The free solutions to the homogeneous Schrödinger equation at negative energies are the regular and irregular Whittaker functions M_ℓ and W_ℓ, respectively [40], rather than Bessel (or Coulomb) functions. The regular solution, $f(r)$, satisfies the boundary condition

$$f(0) = 0,$$

and the matching

$$f(R) = M_\ell(R).$$

There is no need for a coefficient in front of M_ℓ because the normalization of the solution will be canceled in the expression for Green's function (Eq. (2.94)).

The irregular solution, $g(r)$, satisfies the boundary condition

$$g(R) = W_\ell(R),$$

and the matching

$$g(a_1) = \sin(\delta_\ell) W_\ell(a_1) + \cos(\delta_\ell) M_\ell(a_1).$$

2.5.2 Nonlocal differential equation method

Equation (2.94) is not valid for a nonlocal potential (which is the case for the nonlocal DOM). The method of varied parameters does not work when the potential is nonlocal; the integral term in Eq. (2.93) is the root of the issue. This can be seen by the fact that the Wronskian, $W(r)$, is no longer constant ($W'(r) \neq 0$). Differentiating Eq (2.95)

$$\frac{d}{dr} W(r) = f''(r) g(r) - g''(r) f(r),$$

and using Eq. (2.93) to substitute for f'' and g'' results in

$$\frac{d}{dr} W(r) = \frac{2\mu}{\hbar^2} \left(g(r) \int_0^\infty dr_1 \mathcal{V}(r, r_1) f(r_1) - f(r) \int_0^\infty dr_1 \mathcal{V}(r, r_1) g(r_1) \right) \neq 0. \tag{2.96}$$

The integrals, a consequence of nonlocality, are the reason Eq. (2.96) is not equal to zero. Because of this, $G(r, r')$ is not symmetric with respect to r and r' if it is represented by Eq. (2.94). This contradiction with Prop. (1) seems to imply that there needs to be an additional term in Eq. (2.94) to recover symmetry. This issue merits further investigation in the future.

2.5.3 Inverting the Dyson equation

Another way to calculate the propagator is by solving the Dyson equation through matrix inversion, which is used in Eq. (2.82). At positive energies, this inversion is numerically unstable due to the oscillations of the free propagator. Therefore, this method is only applied for calculations of the propagator at negative energies. It is preferable to the differential equation method since the propagator in Eq. (2.86) is symmetric. The propagator in the Lagrange-Laguerre basis is,

$$\langle m|\,\hat{G}_{\ell j}\,|n\rangle = \Big[E\delta_{n,m} - \langle n|\,\hat{T}_\ell\,|m\rangle - \langle n|\,\hat{\Sigma}^*_{\ell j}(E)\,|m\rangle\Big]^{-1}.$$

A typical calculation requires only 30 grid points to reach convergence.

2.5.4 Momentum-Space Method

In order to calculate the propagator at positive energies, the problem is cast into momentum space. This method is very similar to calculations of the $\mathcal{T}$-matrix in momentum-space using the Lippmann-Schwinger equation [43]. Using the Dyson equation, an expression for the reducible self-energy can be written as

$$\Sigma_{\ell j}(k,k';E) = \Sigma^*_{\ell j}(k,k';E) + \int_0^\infty dk_1 k_1^2 \Sigma^*_{\ell j}(k,k_1;E) G^0(k_1;E) \Sigma_{\ell j}(k_1,k';E), \tag{2.97}$$

where $\Sigma^*_{\ell j}(k,k';E)$ is by performing a double Fourier-Bessel transform,

$$\Sigma^*_{\ell j}(k,k';E) = \frac{2}{\pi}\int_0^\infty dr r^2 \int_0^\infty dr' r'^2 j_\ell(kr)\Sigma^*_{\ell j}(r,r';E) j_\ell(k'r'). \tag{2.98}$$

To deal with the pole in $G^0(k;E)$, Eq. (2.55) can be used to rewrite Eq. (2.97) as,

$$\Sigma_{\ell j}(k,k';E) = \Sigma^*_{\ell j}(k,k';E) + \frac{2\mu}{\hbar^2}\mathcal{P}\int_0^\infty dk_1 k_1^2 \frac{\Sigma^*_{\ell j}(k,k_1;E)\Sigma_{\ell j}(k_1,k';E)}{k_0^2-k_1^2} \\ -i\frac{\pi\mu k_0}{\hbar^2}\Sigma^*_{\ell j}(k,k_0;E)\Sigma_{\ell j}(k_0,k';E). \qquad (2.99)$$

The principle part in Eq. (2.99) can be evaluated by subtracting out the singularity,

$$\mathcal{P}\int_0^\infty dk_1 k_1^2 \frac{\Sigma^*_{\ell j}(k,k_1;E)\Sigma_{\ell j}(k_1,k';E)}{k_0^2-k_1^2} = \\ \int_0^\infty dk_1 k_1^2 \frac{\Sigma^*_{\ell j}(k,k_1;E)\Sigma_{\ell j}(k_1,k';E) - \Sigma^*_{\ell j}(k,k_0;E)\Sigma_{\ell j}(k_0,k';E)}{k_0^2-k_1^2}. \qquad (2.100)$$

The principle part of the subtracted term in Eq.(2.100) evaluates to zero, which is why there is an equality. Additionally, the subtracted term removes the divergence at $k_1 = k_0$, hence the lack of principle parts in the right-hand side of Eq. (2.100). Following the arguments in Ref. [51], Eq. (2.99) can be formulated into a matrix equation using a Laguerre mesh,

$$(1+\hat{\mathcal{A}})\hat{\Sigma}_{\ell j} = \hat{\Sigma}^*_{\ell j}. \qquad (2.101)$$

It is interesting to note that by comparing Eq. (2.97) with the $\mathcal{T}$-matrix derived from Eq. (2.83) that

$$\Sigma(E) = \mathcal{T}(E).$$

This leads to a way to benchmark this method by generating elastic-scattering cross sections from $\Sigma(k_0,k_0;E)$ and comparing to results obtained using the method described in App. (A). Typically, 30 Laguerre mesh points are sufficient to reach convergent results.

Thus, the reducible self-energy can be found by inverting Eq. (2.101), leading to the

single-particle propagator,

$$G_{\ell j}(k,k';E) = G^{(0)}(k;E) + G^{(0}(k;E)\Sigma_{\ell j}(k,k')G^{(0)}(k';E).$$

To transform the single-particle propagator to coordinate-space, a double Fourier-Bessel integral transform is necessary,

$$G_{\ell j}(r,r';E) = \frac{2}{\pi}\int_0^\infty dk k^2 \int_0^\infty dk' k'^2 j_\ell(kr) G_{\ell j}(k,k';E) j_\ell(k'r'). \tag{2.102}$$

Once again, to evaluate the integral in Eq. (2.102), the separation in Eq. (2.55) must be used. This results in a long expression which will be omitted here, but can be found in Ref. [52].

It is important to point out that the integral in Eq. (2.98) diverges if the irreducible self-energy includes the Coulomb potential. Therefore, this calculation is only exact for neutrons, while calculations for protons require an arbitrary exponential cutoff to be included with the Coulomb potential [53]. For this reason, it would be quite useful if the issue with the differential equation method for nonlocal potentials were resolved, since it does not involve a divergent integral.

Chapter 3

A DOM Analysis of $^{40}\mathrm{Ca}(e, e'p)^{39}\mathrm{K}$

3.1 Introduction

The shell model, in which the nucleons fill certain orbitals, is well suited to describe the structure of a nucleus. The best place to test this description is in or around (double) closed-shell nuclei. In the simplest picture, in which residual interactions are neglected, all orbitals are 100% filled up to the Fermi level according to the Pauli principle, and those above it are empty. However, due to residual interactions, there is depletion of orbitals below the Fermi energy and filling of those above it, as seen in the spectral functions of Sec. (2.3). The precise amount of this depletion/filling is still a topic under investigation. The best tool to study this experimentally is the $(e, e'p)$ reaction [45, 54–59]. The $(e, e'p)$ reaction involves an incoming electron colliding with a target nucleus and ejecting a proton alongside the outgoing electron. This process is displayed graphically in Fig. 3.1. At sufficiently high momentum transfer, the proton can be knocked out with enough energy such that a description within the distorted-wave impulse approximation (DWIA) is expected to be applicable [60–62] so that depletion (and also filling) of orbits can be studied.

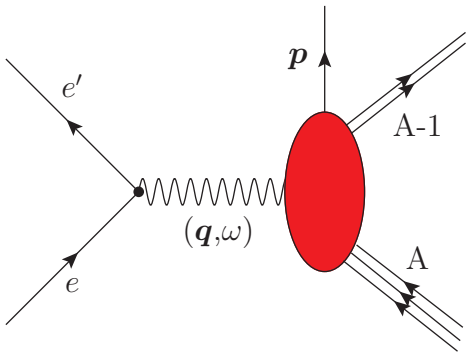

Figure 3.1: Feynam diagram of the $(e, e'p)$ reaction. The red oval represents the complex interaction of the nucleus. The electron transfers momentum $\boldsymbol{q}$ and energy ω to the ejected proton p.

The canonical analysis of this reaction, practiced by the Nikhef group [45, 54], employs a standard global optical potential for the distorted proton wave and calculates the bound-state wave function (overlap function) of the proton in a Woods-Saxon potential well, which is adjusted to describe the momentum dependence of the measured cross sections. A scaling factor of about 0.6-0.7 (relative to a completely filled orbital) is then required to describe the overall magnitude [58]. This scaling factor corresponds to the normalization of the overlap function between the target ground state and low-lying single-hole states, usually referred to as the (reduced) spectroscopic factor. Often this spectroscopic factor is reported multiplied with a factor of $(2j + 1)$ corresponding to the complete filling of a shell with angular momentum j. Furthermore, the data show that additional removal strength with essentially the same overlap function is located at nearby energies (see Fig. 2.1), providing clear evidence of the fragmentation of the single-particle strength [45, 47].

The theoretical interpretation of these experimental results, reviewed in Refs. [59,63], has mainly been concerned with the explanation of this reduction in the spectroscopic strength to 60-70% of the IPM value. Whereas the main reduction of the strength appears to be due to the coupling to low-lying surface vibrations and higher-lying giant resonances associated with long-range correlations (LRC), it has been well documented that additional short-range and tensor correlations (SRC) can be responsible for a 10-15% depletion of the IPM value [63].

The interpretation of spectroscopic factors has been questioned in the literature [64–66] as well as the possibility of measuring momentum distributions or occupation probabilities [67]. In order to address this issue, it is useful to rephrase the interpretation of the $(e, e'p)$ cross section as a question whether the DWIA is a valid reaction model for this process. It is also important to describe the data with a consistent set of ingredients. For example, in the standard Nikhef analysis, the potential used to describe the distorted proton wave is unrelated to the one that generates the overlap function and its normalization is a scaling parameter to fit the data.

It is possible to provide all the of ingredients for the DWIA from the DOM description of all available elastic nucleon scattering data as well as separation energies, particle number, total binding energy, and the nuclear charge density for ^{40}Ca. Indeed, the distorted outgoing proton wave and the overlap function with its implied normalization are all provided by the DOM to allow a consistent description of the $^{40}\mathrm{Ca}(e, e'p)^{39}\mathrm{K}$ cross section for the three available energies of 70, 100, and 135 MeV of the outgoing proton. The states analyzed for this reaction are the first two states of ^{39}K, corresponding to the $0\mathrm{d}\frac{3}{2}$ and $1\mathrm{s}\frac{1}{2}$ valence hole states in ^{40}Ca in the IPM. The three different proton energies were chosen to test the validity of the DWIA used to calculate the theoretical cross sections for this range of energies, which involves the folding of the ejected proton's bound-state wave function (overlap function with the appropriate normalization) with its outgoing distorted wave to calculate the cross section [62,68]. In the past, the spectroscopic factor was found by scaling the calculated cross sections to match the data. In the present analysis, the DOM also provides the spectroscopic factor which allows for a consistent description of the cross section and thereby an assessment of the accuracy of the DWIA description. In addition, it is possible to check the consistency between the data that determine the DOM self-energy and the $(e, e'p)$ cross sections.

3.2 Theoretical description of the $(e, e'p)$ cross section

In $(e, e'p)$ reactions, the interaction between the electron and the bound proton in the target nucleus is responsible for the removal of the proton. To describe the cross section for this process, not only is this interaction needed, but also the distortion of the incoming/outgoing electron and the outgoing proton [69]. The distinction of the roles of these interactions implies that this scattering process can be treated in the general framework of collision theory [69, 70]. Consider the process of $(e, e'p)$

$$e + A \rightarrow e' + p + B$$

describing the entrance channel α and the exit channel β. The kinematics of this can be described with

$$\boldsymbol{k} = \boldsymbol{p}_B + \boldsymbol{k}' + \boldsymbol{p}' \qquad\qquad M_A + E_e = E_B + E'_e + E'_p,$$

where $\boldsymbol{k}$ and $\boldsymbol{k}'$ are the incoming and outgoing electron momenta, $\boldsymbol{p}_B$ is the recoil momentum of the residual $A-1$ nucleus, $\boldsymbol{p}'$ is the momentum of the ejected proton, M_A is the mass of the target nucleus A, E_e and E'_e are the energies of the incoming and outgoing electron, and E'_p is the energy of the ejected proton. The convention of $c = 1$ is used throughout this thesis. Conservation of momentum at the nuclear vertex in Fig. 3.1 implies that the initial momentum of the proton inside the target nucleus A can be expressed as

$$\boldsymbol{p}_m = -\boldsymbol{p}_B = \boldsymbol{p}' - \boldsymbol{q},$$

where $\boldsymbol{q} = \boldsymbol{k} - \boldsymbol{k}'$ is the momentum transferred by the electron and $\boldsymbol{p}_m$ is labeled to indicate that this is a "missing momentum" from the target nucleus. Similarly, a missing energy can

be defined as

$$E_m = \omega - T'_p - T_B,$$

where $\omega = E_e - E'_e$ is the energy transferred by the electron, T'_p is the kinetic energy of the ejected proton, and T_B is the kinetic energy of the recoiling nucleus B. The missing energy is the separation energy of the proton from the target nucleus plus the excitation energy of the residual nucleus [45]. Thus, it is reasonable to think that the coincidence cross section (detecting the outgoing electron and proton) will depend on the probability of finding a proton of momentum $\boldsymbol{p}_m$ and energy E_m in the target nucleus of the experiments performed at Nikhef discussed here [69]. It is the goal of this section to show that this is indeed a good approximation.

The total Hamiltonian of the scattering process can be written as

$$\hat{H} = \hat{H}_\alpha + \hat{h}_\alpha + \hat{H}_I = \hat{H}_\beta + (\hat{h}_\beta + \hat{\mathcal{V}}) + \hat{H}_I,$$

where $\hat{H}_{\alpha,\beta}$ contain the internal Hamiltonians of each channel as well as the kinetic energy of relative motion (see Sec. 2.1), $\hat{h}_{\alpha,\beta}$ are the Hamiltonians describing the distortion of the electron due to the nucleus, $\hat{\mathcal{V}}$ is the potential of nucleus B distorting the outgoing proton, and $\hat{H}_I$ is the interaction responsible for the removal of the proton. The $\mathcal{T}$-matrix between α and β can then be written as (see Eq. (A.12)),

$$\mathcal{T}_{\beta,\alpha} = \langle \Psi_\beta^{(-)} | \, \hat{h}_\alpha + \hat{H}_I \, | \phi_\alpha \rangle \,, \tag{3.1}$$

where $|\phi_\alpha\rangle$ is the plane-wave stationary state of $\hat{H}_\alpha$ and $|\Psi_\beta^{(-)}\rangle$ is the solution of $\hat{H}$ having the asymptotic behavior corresponding to channel β [69]. In order to simplify Eq. (3.1), the plane wave state can be replaced with a distorted state $|\chi_\beta^{(-)}\rangle$ which satisfies the following

Lippmann-Schwinger equation [70],

$$|\chi_\beta^{(-)}\rangle = |\phi_\beta\rangle + \frac{1}{E - \hat{H}_\beta - i\eta}(\hat{\mathcal{V}} + \hat{h}_\beta)\,|\chi_\beta^{(-)}\rangle\,. \tag{3.2}$$

Equation (3.2) can be used to manipulate Eq. (3.1) in such a way that

$$\mathcal{T}_{\beta\alpha} = \langle\chi_\beta^{(-)}|\,\hat{h}_\alpha\,|\phi_\alpha\rangle + \langle\chi_\beta^{(-)}|\,\hat{H}_I\,|\Psi_\alpha^{(+)}\rangle\,, \tag{3.3}$$

where the Lippmann-Schwinger equation for $|\Psi_\alpha^{(+)}\rangle$ was also used [70]. The first term in Eq. (3.3) vanishes since the distorting potential $\hat{h}_\alpha$ cannot connect the α and β channels. The $\mathcal{T}$-matrix can be further simplified by approximating $|\Psi_\alpha^{(+)}\rangle$ with the first term in its Lippmann-Schwinger expansion (Born approximation),

$$|\Psi_\alpha^{(+)}\rangle \approx |\chi_\alpha^{(+)}\rangle\,,$$

which leads to

$$\mathcal{T}_{\beta\alpha} = \langle\chi_\beta^{(-)}|\,\hat{H}_I\,|\chi_\alpha^{(+)}\rangle\,.$$

This approximation to the $\mathcal{T}$-matrix is known as the distorted-wave Born approximation (DWBA) [31, 69]. In the calculations of $(e, e'p)$ cross sections throughout this chapter, the distorting electron interactions $\hat{h}_{\alpha,\beta}$ are approximated with an effective momentum approximation (EMA) [47], which decouples the Leptonic and Hadronic contributions to the cross section [60, 69]. With this simplification, the state associated with the α channel is a plane wave.

In order to properly describe the interaction $\hat{H}_I$, concepts from quantum field theory are borrowed. In the following derivations, various details are omitted for the sake of brevity and clarity. For a more thorough demonstration, see Ref. [69]. The interaction between the

electromagnetic field associated with the electron and the nuclear current can be expressed with the Hamiltonian density

$$\hat{\mathcal{H}}_I(x_\lambda) = -e\mathcal{A}^\mu(x_\lambda)\hat{J}_\mu(x_\lambda),$$

where x is a 4-dimensional space-time point, $\mathcal{A}^\mu(x)$ is the potential due to a free electron current, and $\hat{J}_\mu(x)$ is the nuclear current density [60, 69]. The scattering matrix (S-matrix) in the DWBA can now be expressed as [71]

$$S_{\beta\alpha} = \int d^4x_\lambda \, \langle \chi_\beta^{(-)} | \, \hat{\mathcal{H}}_I \, | \phi_\alpha \rangle \, .$$

Note that in this case, since $\alpha \neq \beta$, the S-matrix and the $\mathcal{T}$-matrix are equivalent within a scalar factor. Often, it is nicer to work with the S-matrix since it is unitary [41, 70]. The initial and final states can be represented as product states in momentum space,

$$|\phi_\alpha\rangle \equiv |kp_A\rangle \qquad\qquad |\chi_\beta^{(-)}\rangle \equiv |k'p'p_B\rangle \, ,$$

where the momenta are associated with Fig. 3.1. Enforcing translation invariance leads to a more explicit expression for the $\mathcal{T}$-matrix [69],

$$\mathcal{T}_{\beta\alpha} = \frac{e^2}{q_\lambda^2}\bar{u}(\boldsymbol{k}', \sigma')\gamma^\mu u(\boldsymbol{k}, \sigma) \, \langle p'p_B | \, \hat{J}_\mu(0) \, | p_A \rangle \, , \tag{3.4}$$

where $u(\boldsymbol{k}, \sigma)$ are Dirac spinors for free electrons and γ^μ are the Dirac matrices [69]. In order to calculate a cross section, an average over the spins of the incoming and outgoing electrons is necessary,

$$d\sigma \propto \sum_{\sigma\sigma'} |T_{\beta\alpha}|^2 \rightarrow L^{\mu\nu}W_{\mu\nu},$$

where $L^{\mu\nu}$ is the lepton tensor

$$L^{\mu\nu} \propto \sum_{\sigma\sigma'} A^{\mu} A^{\nu *}$$

and $W_{\mu\nu}$ is the hadron tensor

$$W_{\mu\nu} \propto \langle \hat{J}_{\mu} \rangle \langle \hat{J}_{\nu} \rangle .$$

Thus, to calculate the cross section, the nuclear current in Eq. (3.1) must be found. Consider the current operator in second quantization,

$$\hat{J}_{\lambda}(0) = \sum_{\sigma\sigma''} \int \frac{d^3p}{2p_0(2\pi)^3} \int \frac{d^3p''}{2p_0''(2\pi)^3} \hat{a}^{\dagger}_{\sigma''}(\boldsymbol{p}'') \langle \boldsymbol{p}''\sigma'' | \hat{J}^f_{\lambda}(0) | \boldsymbol{p}\sigma \rangle \hat{a}_{\sigma}(\boldsymbol{p}),$$

where $\langle \boldsymbol{p}'\sigma' | \hat{J}^f_{\lambda}(0) | \boldsymbol{p}\sigma \rangle$ is the matrix element of the nucleon current density operator between free nucleons [69]. The matrix element of the current operator in Eq. (3.4) can now be expressed as

$$\begin{aligned} \langle p' p_B | \hat{J}_{\lambda}(0) | p_A \rangle = \sum_{\sigma\sigma''} \int \frac{d^3p}{2p_0(2\pi)^3} \int \frac{d^3p''}{2p_0''(2\pi)^3} \\ \times \langle \boldsymbol{p}\sigma'' \boldsymbol{p}_B \sigma_B | \hat{a}^{\dagger}_{\sigma''}(\boldsymbol{p}'') \hat{a}_{\sigma}(\boldsymbol{p}) | \boldsymbol{p}_A \sigma_A \rangle \langle \boldsymbol{p}'\sigma' | \hat{J}^f_{\lambda}(0) | \boldsymbol{p}\sigma \rangle . \end{aligned} \tag{3.5}$$

In what follows, the impulse approximation (IA) will be implemented to simplify the description of the $(e, e'p)$ cross section. The assumptions under the IA are that the virtual photon is absorbed by a single nucleon, and it is this very same nucleon that is detected in coincidence with the outgoing electron [69]. To better understand how the calculation proceeds, it is useful to first consider a plane-wave impulse approximation (PWIA) which corresponds to ignoring $\mathcal{V}$, the distorting potential of the outgoing proton. With this ap-

proximation, Eq. (3.5) can be simplified by noting that

$$\hat{a}_{\sigma''}(\boldsymbol{p}'')\,|\boldsymbol{p}'\sigma'\boldsymbol{p}_B\sigma_B\rangle = 2p_0''(2\pi)^3\delta(\boldsymbol{p}''-\boldsymbol{p}')\delta_{\sigma''\sigma'}\,|\boldsymbol{p}_B\sigma_B\rangle\,. \tag{3.6}$$

Using Eq. (3.6) and momentum conservation reduces Eq. (3.5) to [69]

$$\langle p'p_B|\,\hat{J}_\lambda(0)\,|p_A\rangle = \sum_\sigma \frac{1}{2p_0(2\pi)^3}\,\langle \boldsymbol{p}_B\sigma_B|\,\hat{a}_\sigma(\boldsymbol{p})\,|\boldsymbol{p}_A\sigma_A\rangle\,\langle \boldsymbol{p}'\sigma'|\,\hat{J}^f_\lambda(0)\,|\boldsymbol{p}\sigma\rangle\,. \tag{3.7}$$

With a bit of algebra, it can be shown that the hadron tensor can be factorized into a component from the off-shell free-nucleon current and a nuclear structure component,

$$W_{\mu\nu} \propto \sum_{\sigma_A\sigma_B\sigma} |\,\langle \boldsymbol{p}_B\sigma_B|\,\hat{a}_\sigma(\boldsymbol{p})\,|\boldsymbol{p}_A\sigma_A\rangle\,|^2 \times \sum_{\sigma\sigma'} \langle \boldsymbol{p}\sigma|\,\hat{J}^{f*}_\lambda(0)\,|\boldsymbol{p}'\sigma'\rangle\,\langle \boldsymbol{p}'\sigma'|\,\hat{J}^f_\lambda(0)\,|\boldsymbol{p}\sigma\rangle\,. \tag{3.8}$$

The first sum in Eq. (3.8) is the hole spectral function in momentum space $S^{(h)}(\boldsymbol{p};E)$ (see Sec. (2.3.3)). Thus, when Eq. (3.8) is contracted with the lepton tensor, only the second sum in Eq. (3.8) will combine with $L^{\mu\nu}$ to become the off-shell electron-proton cross section [60,69] resulting in

$$\frac{d^6\sigma}{dk'_0dp'_0d\omega_{k'}d\omega_{p'}} \propto \sigma^{\rm off}_{ep}S(\boldsymbol{p};E). \tag{3.9}$$

In Eq. (3.9), $\sigma^{\rm off}_{ep}$ is not extremely well defined in the sense that it is calculated in a variety of differing ways [69, 72]. The off-shell nature of the electron-proton cross section is due to the fact that the proton is bound in a nucleus, and is explicitly stated by

$$E_m \neq (\boldsymbol{p}_m^2 + m_p^2)^{1/2}. \tag{3.10}$$

All calculations presented in this chapter are done using the proposed off-shell cross section $\sigma^{\rm cc}_1$ from Ref. [72]. The basic idea is to extrapolate from the free on-shell nucleon current by accounting for the energy difference in Eq. (3.10).

While the factorization of the cross section in Eq. (3.9) is a nice result, the PWIA is not close to reality. In order to reasonably describe the $(e, e'p)$ cross section, the potential distorting the ejected proton, $\mathcal{V}$, cannot be ignored (DWIA). The distorting potential alters Eq. (3.6) such that the delta function is replaced by a distorted wave

$$a_{\sigma''} \left| \boldsymbol{p}' \boldsymbol{p}_B \sigma_B \right\rangle = 2p_0''(2\pi)^3 \chi^{(-)}_{\sigma'\sigma''}(\boldsymbol{p}', \boldsymbol{p}'') \left| (\boldsymbol{p}_A - \boldsymbol{p}) \sigma_B \right\rangle , \tag{3.11}$$

where

$$\chi^{(-)}_{\sigma'\sigma''}(\boldsymbol{p}', \boldsymbol{p}'') = \frac{1}{(2\pi)^{3/2}} \int d^3r \chi^{(-)}_{\boldsymbol{p}'\sigma'}(\boldsymbol{r}) \eta^*_{\sigma''} e^{-i\boldsymbol{p}''\cdot\boldsymbol{r}}$$

is the Fourier transform of the distorted wave function in configuration space, and $\eta_{\sigma''}$ is a Pauli spinor [31, 69]. The nonlocality of the distorted wave in Eq. (3.11) alters the matrix elements of the current operator from Eq. (3.7), leading to a nontrivial mixing of the nuclear structure component and the electron-proton currents [69]. A consequence of this mixing is that the six-fold cross section can no longer be factorized into a product of the off-shell electron-proton cross section and the spectral function of the proton in the target nucleus. Even so, experimental momentum distributions are typically divided by the off-shell electron-proton cross section [45, 47, 60, 69, 73]

$$S^{(\mathrm{DWIA})}(\boldsymbol{p}_m; E_m) = \frac{1}{k\sigma^{\mathrm{off}}_{ep}} \frac{d^6\sigma}{dE_{k'_0} d\Omega_{k'} dp'_0 \Omega'_p}, \tag{3.12}$$

where the superscript explicitly indicates that this is not the true spectral function as defined in Sec. (2.3.3). This distinction will be made clear in Sec. (3.5) with figures of both $S(\boldsymbol{p}_m; E_m)$ and $S^{(DWIA)}(\boldsymbol{p}_m; E_m)$. While Eq. (3.12) is not exactly the spectral function, its calculation involves the hole spectral function of the target nucleus as well as the distorted wave of the ejected proton due to the $(A-1)$ residual nucleus. Thus, comparing calculations of $S^{DWIA}(\boldsymbol{p}_m, E_m)$ with $(e, e'p)$ experiments simultaneously probes both bound and scattering

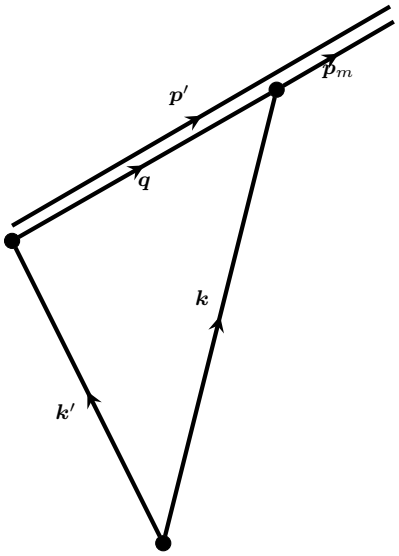

Figure 3.2: Parallel kinematics of (e,e'p) experiment

states.

The treatment of the electrons as non-interacting plane waves in the DWIA is not sufficient [45, 47]. The proper treatment would involve using solutions of the Dirac equation with the distorting potentials $h_{\alpha,\beta}$ [69]. Instead, for nuclei with up to about 20 protons, an approximation of the distortion effects is made using the EMA [47]. Since the distortion is primarily caused by the Coulomb potential, an effective momentum accounting for this can be written as

$$\boldsymbol{k}^{\text{eff}} = \boldsymbol{k} + \hat{\boldsymbol{k}} \int d^3r V_c(\boldsymbol{r}) \phi^2_{\ell j}(\boldsymbol{r}),$$

where $V_c(\boldsymbol{r})$ is the Coulomb potential of the distorting nucleus [47, 60, 74]. The EMA is used in all calculations of $(e, e'p)$ cross sections throughout this thesis.

It has been demonstrated that the IA is suitable for large momentum transfer on medium to heavy mass nuclei [45, 60, 69]. In the IA, all higher-body terms of the nuclear current operator (such as meson-exchange terms) are neglected [60]. The contributions of various meson-exchange currents have the most strength in the transverse and interference structure

functions of the cross section. In the past, $(e, e'p)$ cross sections obtained at Nikhef have been successfully described by utilizing the DWIA [45]. The Nikhef group was able to choose conditions in which the removed proton carried momentum parallel or antiparallel to the momentum of the virtual photon. This configuration is referred to as parallel kinematics and is shown in Fig. 3.2. Under these conditions, the transverse structure functions are suppressed and the interference structure functions vanish [47,60,69]. Therefore, the process can be interpreted as requiring an accurate description of the transition amplitude connecting the resulting excited state to the ground state by a known one-body operator. This transition amplitude is contained in the polarization propagator which can be analyzed with a many-body description involving linear response [20]. Such an analysis demonstrates that the polarization propagator contains two contributions. The first term involves the propagation of a particle and a hole dressed by their interaction with the medium, but not each other. The other term involves their interaction. The latter term will dominate at low energy when the proton that absorbs the photon participates in collective excitations like surface modes and giant resonances. When the proton receives on the order of 100 MeV, it is expected that the excited state that is created can be well approximated by the dressed particle and dressed hole excitation [75]. In fact, when strong transitions are considered, like in the present work, two-step processes have only minor influence [45, 76], further justifying the IA. When supplying the DWIA with the appropriate ingredients in the past, the distorted wave was typically obtained from a standard local global optical potential such as the one from Ref. [77] for ^{40}Ca. The overlap function (used for the spectral function) was obtained by adjusting the radius of a local Woods-Saxon potential to the shape of the $^{40}\mathrm{Ca}(e, e'p)^{39}\mathrm{K}$ cross section while adjusting its depth to the separation energy of the quasihole. Its normalization was obtained by adjusting the calculated DWIA cross section to the actual data [58]. Standard nonlocality corrections were applied to both the outgoing and removed proton wave functions [78], in practice making the bound-state wave function the solution of a nonlocal potential.

3.3 DOM fit of ^{40}Ca

The DOM is capable of describing both scattering and bound-state quantities, as has been explained in Sec. (2.4). Thus, the nonlocal DOM is particularly well suited for a DWIA analysis of the $(e, e'p)$ cross section as detailed in the previous section. In order to use the DOM self-energy for predictions, the parameters are fit through a weighted χ^2 minimization of available elastic differential cross section data ($\frac{d\sigma}{d\Omega}$), analyzing power data (A_θ), reaction cross sections (σ_r), total cross sections (σ_t), charge density ($\rho_{\rm ch}$), energy levels ($\varepsilon_{\ell j}$), particle number, and root-mean-square charge radius ($r_{\rm rms}$). In order to minimize the χ^2, the Powell method is used to search through the parameter space [79]. All of the parameters of the DOM are presented in App. B together with the chosen functional forms. One advantage of the Powell method is that it does not require the calculation of a gradient in parameter space, which is computationally expensive.

As noted in Sec. 2.2, all scattering data are calculated using R-matrix theory in combination with a Lagrange-Legendre basis. For specific details of the calculation of phase shifts, see App. A. The nonlocal DOM description of ^{40}Ca data was presented in Ref. [80]. In the mean time, additional experimental higher-energy proton reaction cross sections [81] have been incorporated which caused some adjustments of the DOM parameters compared to Ref. [80]. The resulting change to the proton reaction cross section (Eq. (A.8)) is shown in Fig. 3.3. The remaining observables of the fit are described in a similar way as in the previous fit. The neutron total cross section (Eq. (A.7)) is shown in Fig. 3.4. The elastic differential cross sections (Eq. (A.6)) at energies up to 200 MeV for protons and neutrons are shown in Fig. 3.5. The analyzing powers (Eq. (A.19)) for neutrons and protons are shown in Fig. 3.6.

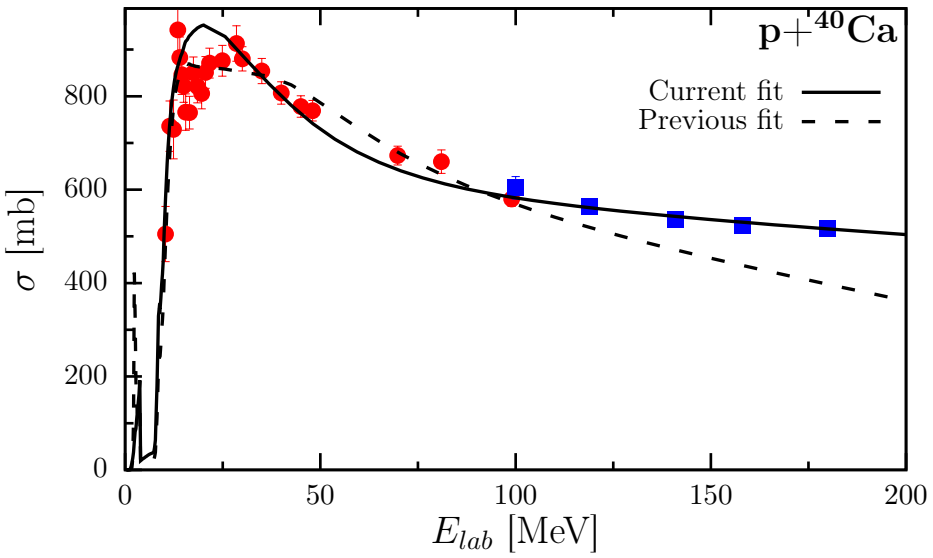

Figure 3.3: The proton reaction cross section for ^{40}Ca. The solid line represents the current fit, while the dashed line depicts the previous fit [80]. The circular data points [82] were included in the previous fit, while the square data points [81] have been added in the current fit.

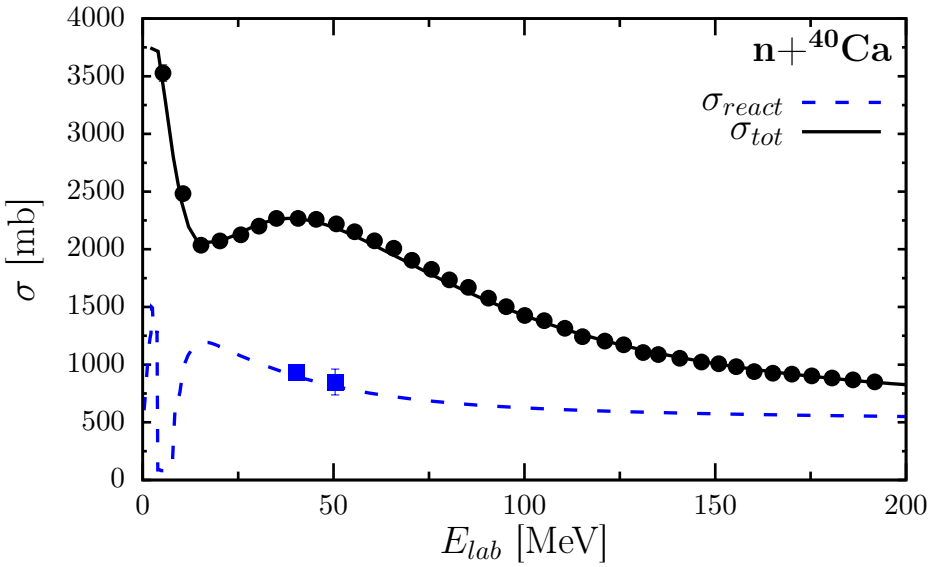

Figure 3.4: Neutron total cross section (solid line) and reaction cross section (dashed line) generated from the DOM self-energy. The circles represent measured total cross sections and the squares measured reaction cross sections. References to the data are given in Ref. [82].

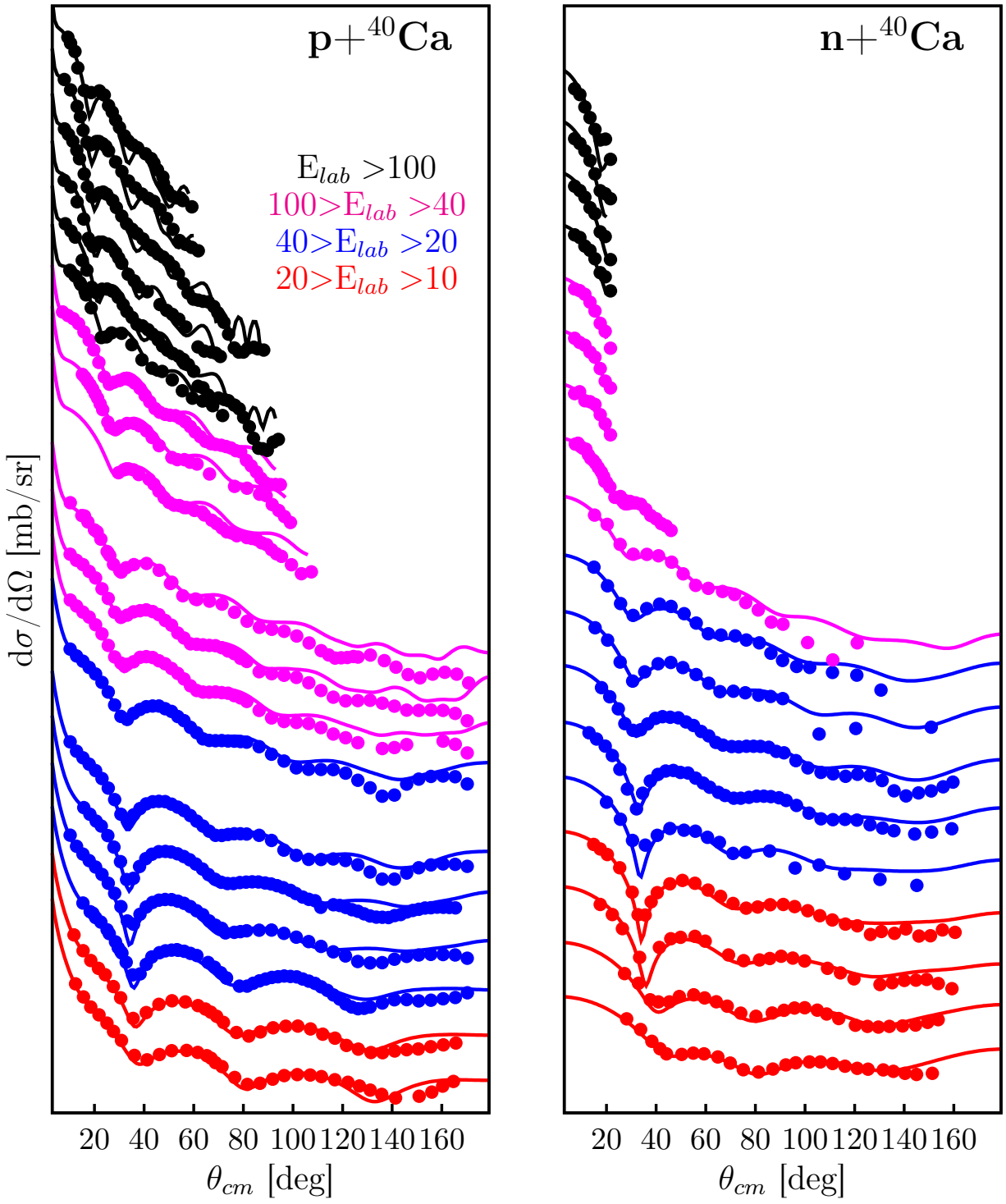

Figure 3.5: Calculated and experimental proton and neutron elastic-scattering angular distributions of the differential cross section $\frac{d\sigma}{d\Omega}$. The data at each energy is offset by factors of ten to help visualize all of the data at once. References to the data are given in Ref. [82].

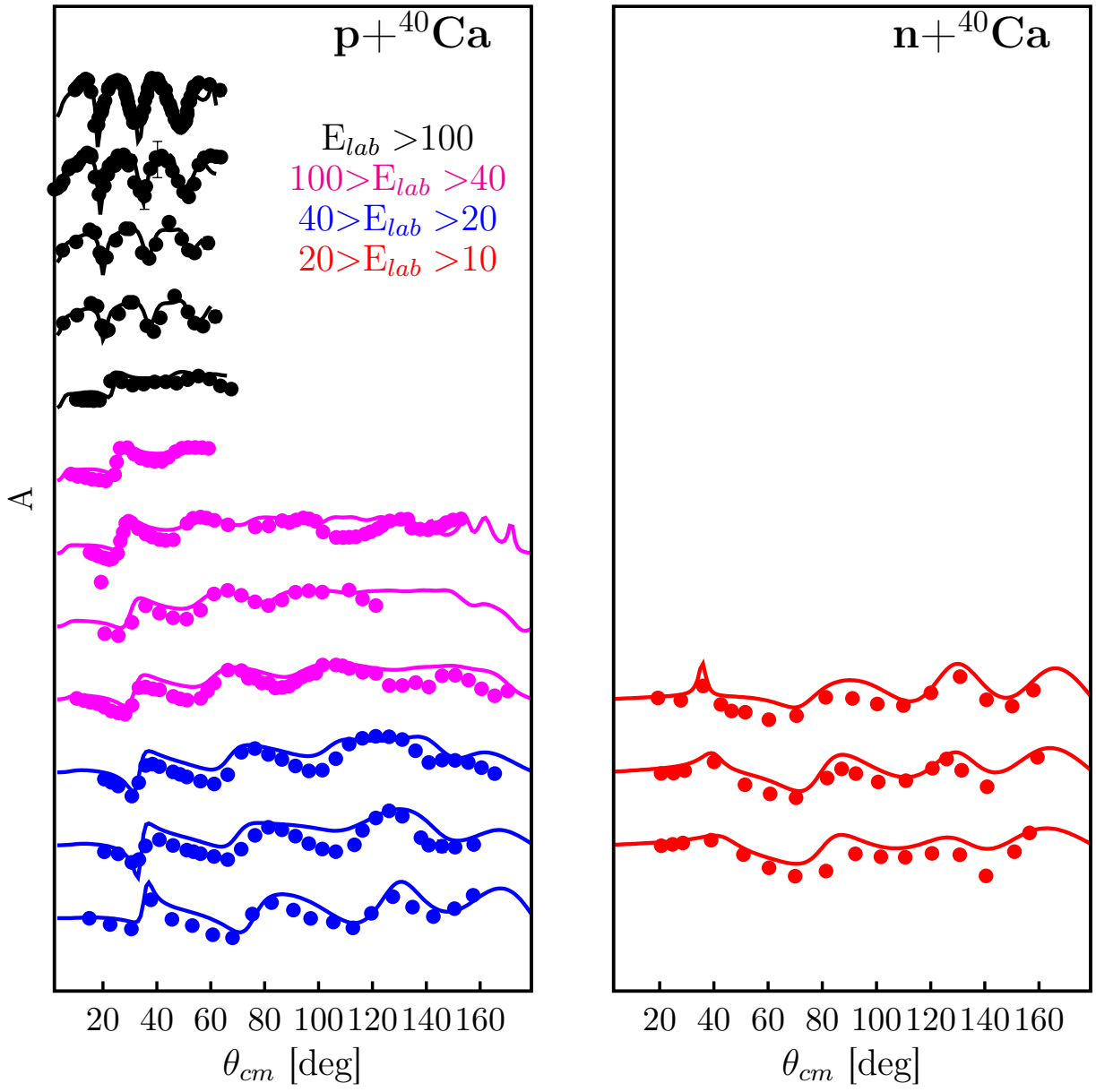

Figure 3.6: Results for proton and neutron analyzing power generated from the DOM self-energy. References to the data are given in Ref. [82].

In order to provide the structure information as well, it is important that the DOM also describe bound-state data. Since the DOM is represented in a basis of good total angular momentum, the single-particle propagator for a given ℓj can be found from the corresponding

Dyson equation of Eq. (2.70) by explicitly inserting the basis

$$\alpha \to \alpha_r \ell j \qquad\qquad \beta \to \beta_r \ell j,$$

where α_r and β_r correspond to a Lagrange-Laguerre basis (see Sec. 2.2.2), resulting in $G_{\ell j}(\alpha_r, \beta_r)$. The point-density distribution for each orbital, $\rho_{\ell j}(\alpha_r)$, can then be calculated using Eq. (2.62). The occupation of each orbital can be found by applying Eq. (2.64) to $\rho_{\ell j}(\alpha_r)$. Summing these distributions over angular momentum leads to the total point distribution for protons or neutrons,

$$\rho^{N,Z}(\alpha_r) = \frac{1}{4\pi} \sum_{\ell j} (2j+1) \rho^{N,Z}_{\ell j}(\alpha_r), \tag{3.13}$$

where the superscripts N and Z refer to neutrons and protons. While in principle, the sum in Eq. (3.13) includes all values of $\ell \to \infty$, in practice this sum is performed up to some $\ell_{\max}$ such that contributions from higher ℓ are negligible. For ^{40}Ca, convergence is reached for $\ell_{\max} = 10$. The number of neutrons and protons in ^{40}Ca is calculated by summing $\rho^{N,Z}(\alpha_r)$ over α_r. The parametrization of the ^{40}Ca self-energy in this thesis results in $Z = 19.8$ and $N = 19.7$. As 20 is the experimental number, this allows for small contributions from higher ℓ-values [28]. The point distribution in Eq. (3.13) can be transformed to configuration space using the Lagrange-Laguerre basis functions introduced in Sec. 2.2.2. The charge density is then obtained by folding in the charge distribution of the proton and the neutron with their respective point distributions $\rho^Z(r)$ and $\rho^N(r)$ (see App. C), resulting in Fig. 3.7. The experimental charge density in Fig. 3.7 is extracted from elastic electron scattering cross sections using the parametrized sum of Gaussians from Ref. [83].

In calculating the spectral functions needed for the charge density, each ℓj contribution having a corresponding bound level in the IPM has a peak roughly at the position of the

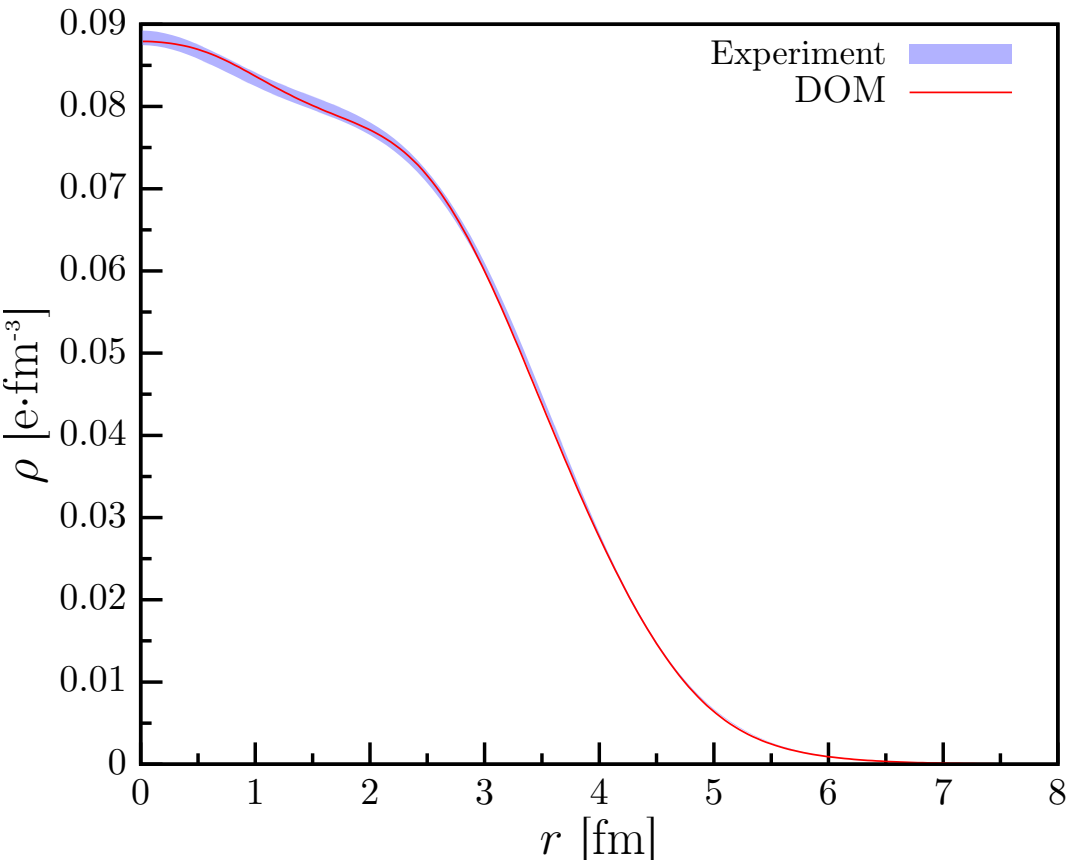

Figure 3.7: Experimental and fitted ^{40}Ca charge density. The solid line is calculated using Eq. (3.13) with a center-of-mass correction and folding with the proton charge distribution. The experimental band represents the 1% error associated with the extracted charge density from elastic electron scattering experiments [83, 84].

corresponding occupied single-particle orbit [20]. The contribution of each ℓj shell at energy E is represented by the spectral strength $S_{\ell j}(E)$,

$$S_{\ell j}(E) = \sum_{\alpha_r} S_{\ell j}(\alpha_r, \alpha_r; E). \tag{3.14}$$

This contribution to $S_{\ell j}(E)$ from particular quasihole orbitals $\phi^n \ell j$ can be calculated as

$$S^{n-}_{\ell j}(E) = \sum_{\alpha_r, \beta_r} [\phi^n_{\ell j}(\alpha_r)]^* S^h_{\ell j}(\alpha_r, \beta_r; E) \phi^n_{\ell j}(\beta_r).$$

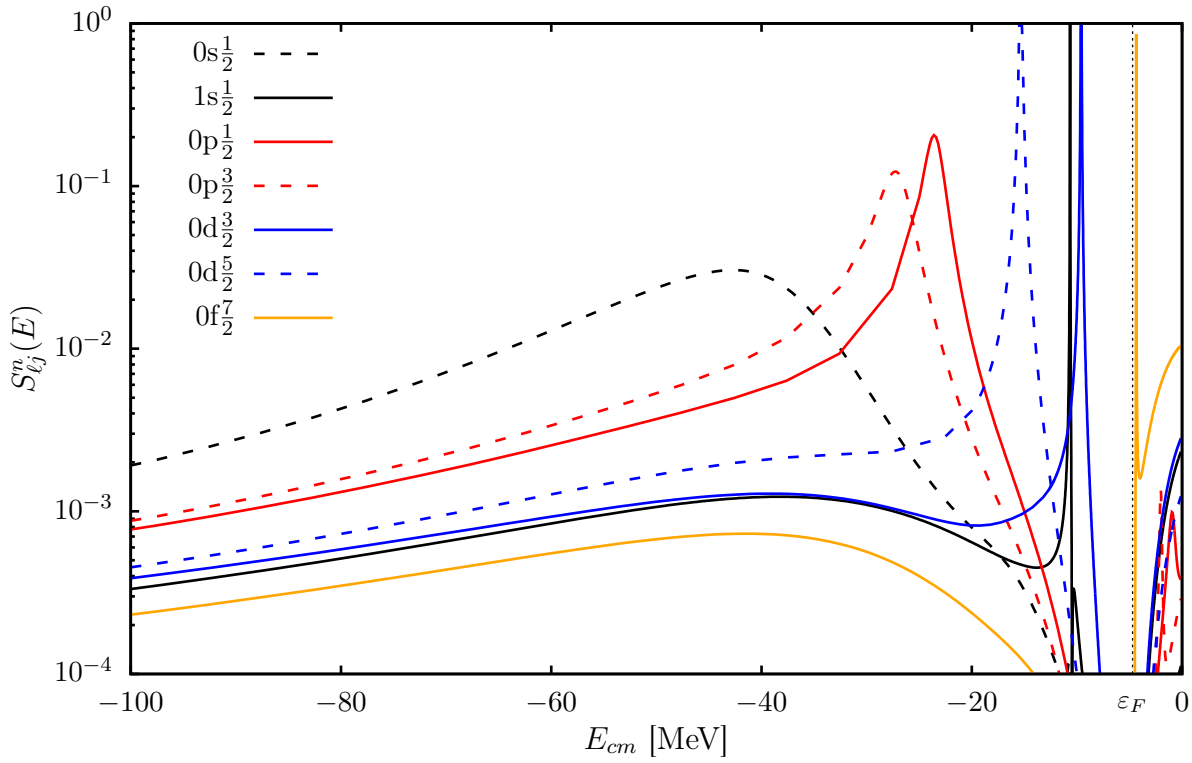

Figure 3.8: Proton spectral functions of the IPM orbitals in ^{40}Ca. The location of the peaks correspond to the binding energies of the corresponding quasihole, see Table 3.1.

The spectral strengths of the IPM orbitals of ^{40}Ca are shown in Fig. 3.8, which demonstrates how the quasihole peaks get narrower as the levels approach ε_F. This is a consequence of the imaginary part of the irreducible self-energy decreasing when approaching ε_F. In fact, the two least bound proton levels in Fig. 3.8 ($1s\frac{1}{2}$ and $0d\frac{3}{2}$) have spectral functions that are essentially delta functions peaked at their respective energy levels, where the imaginary part of the self-energy vanishes. For these orbitals, the spectral function is dominated by a single term from the sum in Eq. (2.61),

$$S^n_{\ell j}(\alpha_r, \beta_r; E) = \langle \Phi^A_0 | \, \hat{a}^\dagger_{\alpha_r n\ell j} \, | \Phi^{A-1}_m \rangle \, \langle \Phi^{A-1}_m | \, \hat{a}_{\beta_r n\ell j} \, | \Phi^A_0 \rangle \, \delta(E - \varepsilon_{n\ell j}), \tag{3.15}$$

where $|\Phi^{A-1}_m\rangle$ is the discrete excited state with total angular momentum and parity consistent

with the quasihole state described by principal quantum number n and angular momenta ℓj which has an energy of $\varepsilon^n_{\ell j}$. These overlap functions are related to quasihole wave functions, $\phi^n_{\ell j}(\alpha_r)$, which are the solutions to the Schrödinger-like equation derived from the Dyson equation, Eq. (A.3). This relation is

$$\langle \Phi^{A-1}_m | \, \hat{a}_{\beta_r n \ell j} \, | \Phi^A_0 \rangle = \sqrt{\mathcal{Z}^n_{\ell j}} \phi^n_{\ell j}(\alpha_r),$$

where $\mathcal{Z}^n_{\ell j}$ is the normalization of the quasihole wave function, known as the spectroscopic factor [20]. This spectroscopic factor is the very same factor that has been interpreted as a scaling factor for knockout reactions [28, 47]. At energies close to ε_F, where the imaginary part of the self-energy vanishes, the spectroscopic factor can be derived from the Dyson equation,

$$\mathcal{Z}^n_{\ell j} = \left(1 - \left. \frac{\partial \Sigma^*_{\ell j}(\alpha_{qh}, \alpha_{qh}; E)}{\partial E} \right|_{\varepsilon^n_{\ell j}} \right)^{-1},$$

where α_{qh} corresponds to the quasihole state that solves Eq. (A.3) [20]. This is interpreted as the spectral strength at the quasihole energy $\varepsilon^n_{\ell j}$, represented by a delta function. Note that because of the presence of imaginary parts of the self-energy at other energies, there is also strength located there, thus the spectroscopic factor will be less than 1 and also less than the occupation probability.

Not only are the spectral functions generated by these quasihole wave functions important in producing the correct charge density, but the quasihole energies can be directly measured as excitation energies of the discrete excited states of the $(A-1)$ nucleus [28]. For bound levels above ε_F ($0f^7_2$ for protons, see Fig. 3.8), these energies correspond to the excited states of the $(A+1)$ nucleus after a particle is added. Table (3.1) shows a comparison of the DOM energy levels for protons and neutrons with the experimental values in ^{40}Ca.

Table 3.1: Comparison of experimental and fitted mean energies for various proton and neutron orbitals for ^{40}Ca.

Protons	**DOM** [MeV]	**Exp.** [MeV]	**Neutrons**	**DOM** [MeV]	**Exp.** [MeV]
$\mathbf{0d_{3/2}}$	-8.13	-8.3	$\mathbf{0d_{3/2}}$	-15.4	-15.6
$\mathbf{0d_{5/2}}$	-14.4	-14.3	$\mathbf{0d_{5/2}}$	-21.72	-22.3
$\mathbf{1s_{1/2}}$	-9.19	-10.8	$\mathbf{1s_{1/2}}$	-16.5	-18.3
$\mathbf{0f_{7/2}}$	-2.85	-1.09	$\mathbf{0f_{7/2}}$	-9.80	-8.36

It should now be clear that the DOM can accurately generate all ingredients needed for the DWIA calculation of the ^{40}Ca$(e,e'p)^{39}$K cross section. The scattering results show that the DOM distorted waves at proton energies of 70, 100, and 135 MeV are accurate. The reproduction of the charge density and excitation energies indicate that the hole spectral functions of the $0d^3_2$ and $1s^1_2$ orbitals are also accurate. The distribution of single-particle strength for the two relevant proton orbits to the ^{40}Ca$(e,e'p)^{39}$K will be discussed in Sec. 3.5. It reveals that the strength for these orbits is fragmented over all energies, positive and negative, rather than concentrated at one energy as in the IPM. Note that the distribution at positive energies is constrained by elastic-scattering data, emphasizing the relevance of correlations beyond the IPM [85]. Since the DOM has so far been limited to 200 MeV positive energy, a few percent of the sum rule in Eq. (2.66) has been found above this energy [85].

3.4 Experimental $(e,e'p)$ cross section

The experimental data for the ^{40}Ca$(e,e'p)^{39}$K reaction that are presented in this thesis were obtained with the electron beam from the Medium Energy Accelerator (MEA) at Nikhef in Amsterdam with natural calcium targets. For further details of the experiment, see Ref. [28]. An example of the quality of the data is displayed in Fig. 3.9, demonstrating the fragmentation of the strength for T_p=100 MeV, p_m=140 MeV/c. Different spin-parity

identifications are displayed when known from other experiments.

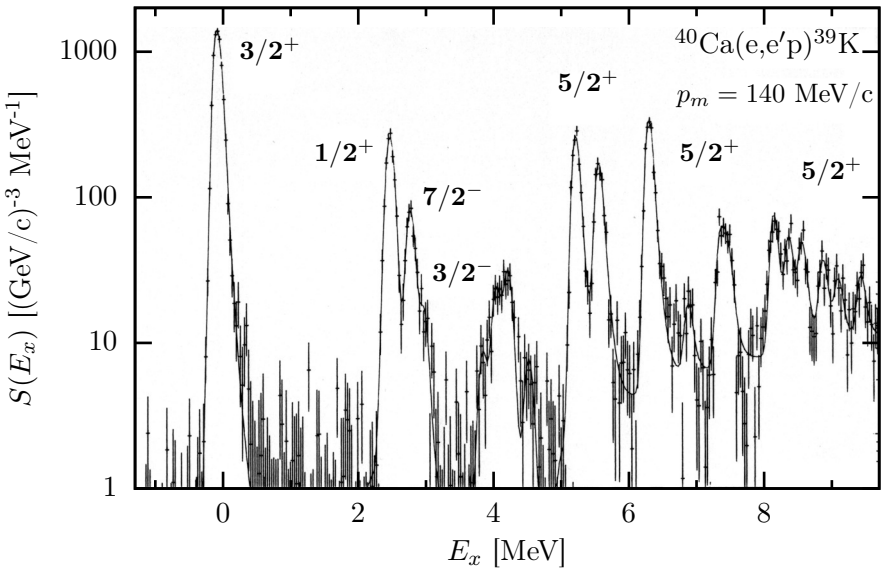

Figure 3.9: ^{40}Ca$(e,e'p)$ at missing momentum 140 MeV/c radiatively unfolded excitation-energy spectrum for the reaction ^{40}Ca$(e,e'p)$ at missing momentum 140 MeV/c, showing the well resolved transitions to the $J^\pi = 3/2^+$ ground state and $1/2^+$ first excited state in ^{39}K. Above $E_x = 5$ MeV several transitions to states with mostly $J^\pi = 5/2^+$ are identified. The peak at $E_x \approx 4$ MeV results from the reaction ^{16}O$(e,e'p)^{15}$N$_{g.s.}$ due to oxygen contamination in the target. The curve is a multiple Gaussian fit to the data.

The T_p=100 MeV data were analyzed previously in Ref. [45] with bound-state wave functions calculated in a Woods-Saxon well (free parameters: well radius and spectroscopic factor) and distorted outgoing proton wave functions calculated in a global energy-dependent optical-model potential described by Schwandt *et al.* [77]. For this purpose, the well-resolved transitions to the ground state ($3/2^+$) and first excited state ($1/2^+$) at 2.522 MeV in ^{39}K were selected. In order to facilitate the comparison, the reduced cross sections $\sigma^{exp}(p_m, E_i^0, \theta_i)$ in each data set A, B, and C were transformed to the highest-employed beam energy E_h^0 in that set according to

$$\sigma_{tr}^{exp}(p_m, E_h^0, \theta_h) = \frac{\sigma^{th}(p_m, E_h^0, \theta_h)}{\sigma^{th}(p_m, E_i^0, \theta_i)} \sigma^{exp}(p_m, E_i^0, \theta_i),$$

where in parallel kinematics the scattered electron angle θ_h follows directly from momentum and energy conservation given the fixed value of T'_p. This transformation assumes that the factorization of the cross section between the off-shell electron-proton cross section and the spectral function is reasonable (see Sec. (3.2)). The model dependence of such a transformation was found to be less than 1%, as derived from a comparison of the transformed cross section obtained with the Schwandt optical potential [77] (th=Schwandt) and the present DOM potential (th=DOM), respectively.

3.5 Results

The calculations of the $(e, e'p)$ cross sections in this thesis were performed by employing DOM ingredients that were constrained by other experimental data, as explained in Sec. (3.3). Appropriate distorted waves and overlap functions with their normalization were thus generated that allow for a DWIA description of the exclusive $(e, e'p)$ cross section for valence holes in ^{40}Ca. Agreement with cross sections therefore supports the description of the reaction in a DWIA framework, but also confirms the overall consistency of the DOM approach including its interpretation of the normalization of the overlap functions as spectroscopic factors that can be confronted with data.

The higher-energy proton reaction cross section data incorporated in the current fit dictate that the proton reaction cross section stay flat for energies in the region around 150 MeV, as shown in Fig. 3.3. This means there is more absorption at higher energies than in the previous fit, leading to increased strength in the imaginary part of the self-energy. Due to the dispersion relation of the self-energy, Eq. (2.72), this increases the spectral strength at positive energies when the Dyson equation is solved. The sum rule pertaining to the integral over all energies of the strength of the valence holes then implies that strength is transferred from below the Fermi energy to the energies with an increased imaginary self-energy. This

resulting loss of strength below the Fermi energy reduces the spectroscopic factors by about 0.05 compared to the results reported in Ref. [80].

The present DOM self-energy leads to the spectral strength distributions in Fig. 3.10. The experimental bars are the results of an angular-momentum decomposition of the experimental spectral function at $T_p = 100$ MeV as described in Ref. [47]. The experimental distributions for $\ell = 0, 2$ clearly show that the strength is already strongly fragmented at low energies. The main peak in each case represents the valence hole transition of interest in this thesis. The DOM strength is plotted as a continuous function employing the imaginary part of the self-energy, which is very small near the Fermi energy, to clarify that only one peak is generated in the present implementation. The DOM therefore does not yet include the details of the low-energy fragmentation of the valence hole states which requires the introduction of pole structure in the self-energy [63].

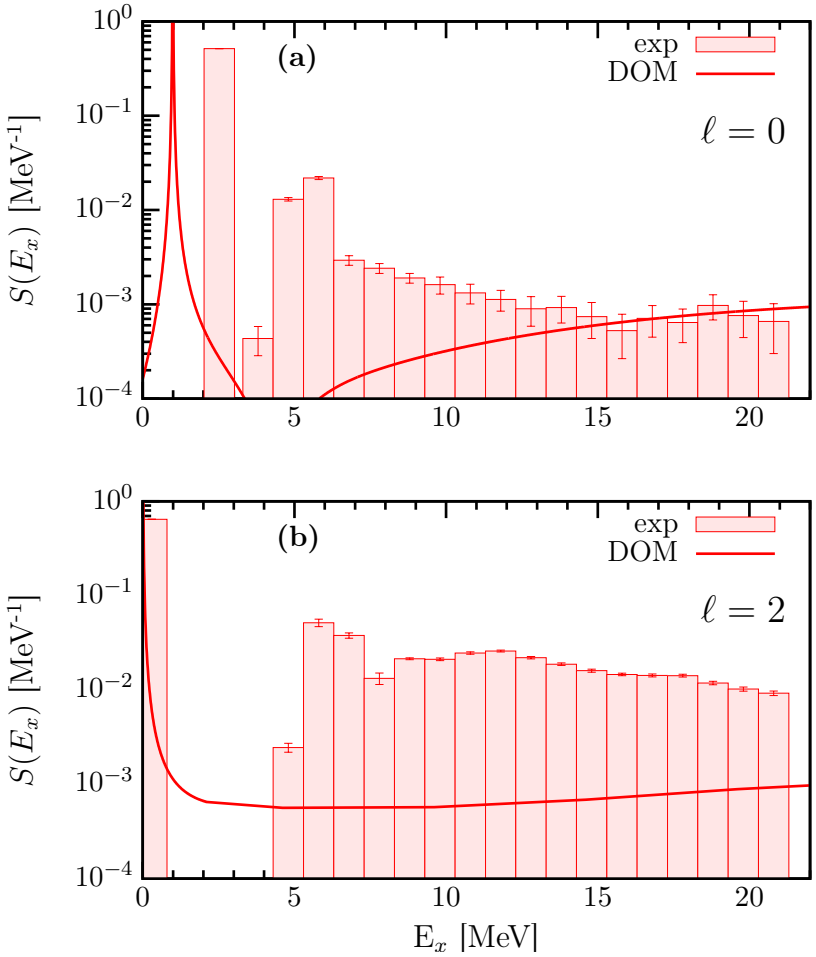

Figure 3.10: Spectral strength as a function of excitation energy for (a) the $1s\frac{1}{2}$ and (b) the $0d\frac{3}{2}$ proton orbitals, calculated from the DOM using Eq. (2.61) and extracted from the ^{40}Ca$(e, e'p)^{39}$K experiment [45, 47]. The peaks in the DOM curves and experimental data correspond to the quasihole energies of the protons in ^{40}Ca. The DOM peak in (a) does not exactly match the experiment (see Ref. [80]). The distance between the quasihole peak and the smaller contributions is substantially larger in (b) than in (a). Note that the experimental fragments in (b) above 4 MeV mostly correspond to $0d\frac{5}{2}$ strength.

The spectroscopic factor of Eq. (3.3) corresponds to the main peak of each distribution shown in Fig. 3.10. It is calculated directly from the ^{40}Ca DOM self-energy resulting in values of 0.71 and 0.74 for the $0d\frac{3}{2}$ and $1s\frac{1}{2}$ peaks, respectively. The results are probed in more detail by analyzing the momentum distributions of the ^{40}Ca$(e, e'p)^{39}$K reaction.

In the past, the DWIA calculations by the Nikhef group have been performed using the

DWEEPY code [68]. For the present work, the momentum distributions are calculated by adapting a recent version of the DWEEPY code [61] to use the DOM bound-states, distorted waves, and spectroscopic factors as inputs. Before confronting the DOM calculations with the experimental cross sections it is necessary to consider the consequences of the low-energy fragmentation as shown in Fig. 3.10. For the $0d\frac{3}{2}$ ground-state transition, there is a clear separation with higher-lying fragments, most of which cannot be distinguished from $0d\frac{5}{2}$ contributions as the experiments were not able to provide the necessary polarization information. In addition, these higher-lying fragments appear to carry little $0d\frac{3}{2}$ strength [73]. Therefore, the DOM spectroscopic factor can be directly used to calculate the cross section of the ground-state peak. The situation is different for the $1s\frac{1}{2}$ distribution which, while dominated by the large fragment at 2.522 MeV, exhibits substantial nearby strength as shown in Fig. 3.10a. These contributions come from other discrete poles in the propagator, reflecting the mixing of the $1s\frac{1}{2}$ orbit to more complicated excitations nearby in energy. Currently the origin of these additional discrete poles is not explicitly included in the DOM, although there is a smooth energy-dependent imaginary term in the self-energy to approximate their effect on the spectral strength [20]. This approximation is sufficient when discussing integrated values such as the charge density and particle number, but falls short when considering details of the low-energy fragmentation into discrete energies as in the present situation. The calculated DOM spectroscopic factor therefore includes strength in the neighborhood of the quasihole energy, resulting in an inflated value. This effect is only noticeable in the $\ell = 0$ case because there is a non-negligible amount of strength in the region near the peak. The experimental data can be used to account for this effect by enforcing that the ratio between the strength of the peak to the total spectral strength shown in the energy domain of Fig. 3.10 is the same between the data as for the DOM,

$$\frac{\mathcal{Z}_F^{\mathrm{DOM}}}{\int dE\ S^{\mathrm{DOM}}(E)} = \frac{\mathcal{Z}_F^{\mathrm{exp}}}{\int dE\ S^{\mathrm{exp}}(E)}. \tag{3.16}$$

Accounting for the contributions to the momentum distribution from different energies by scaling the DOM spectroscopic factor is justified by observing that the shape of the momentum distribution calculated at similar energies is identical, with the strength being the only difference [45]. The scaling of the spectroscopic factor leads to a reduction from 0.74 to 0.60. As mentioned, no correction is needed for the $0d\frac{3}{2}$ spectroscopic factor. The resulting momentum distributions are shown in Figs. 3.11-3.13. The previous analysis of the Nikhef group at $T_p = 100$ MeV [45] produced a comparable reproduction of the data with somewhat smaller spectroscopic factors, as shown in Table 3.2.

In order to estimate the uncertainty for the DOM spectroscopic factors, we followed the bootstrap method from Ref. [86] which was also employed in Ref. [29] to assess the uncertainty for the neutron skin in ^{48}Ca. New modified data sets were created from the original data by randomly renormalizing each angular distribution or excitation function within the experimental error to incorporate fluctuations from the systematic errors. Twenty such modified data sets were generated and refit. The resulting uncertainties are listed in Table 3.2.

Table 3.2: Comparison of spectroscopic factors in ^{40}Ca deduced from the previous analysis [45] using the Schwandt optical potential [77] to the normalization of the corresponding overlap functions obtained in the present analysis from the DOM including an error estimate as described in the main text.

$\mathcal{Z}$	$0d\frac{3}{2}$	$1s\frac{1}{2}$
Ref. [45]	0.65 ± 0.06	0.51 ± 0.05
DOM	0.71 ± 0.04	0.60 ± 0.03

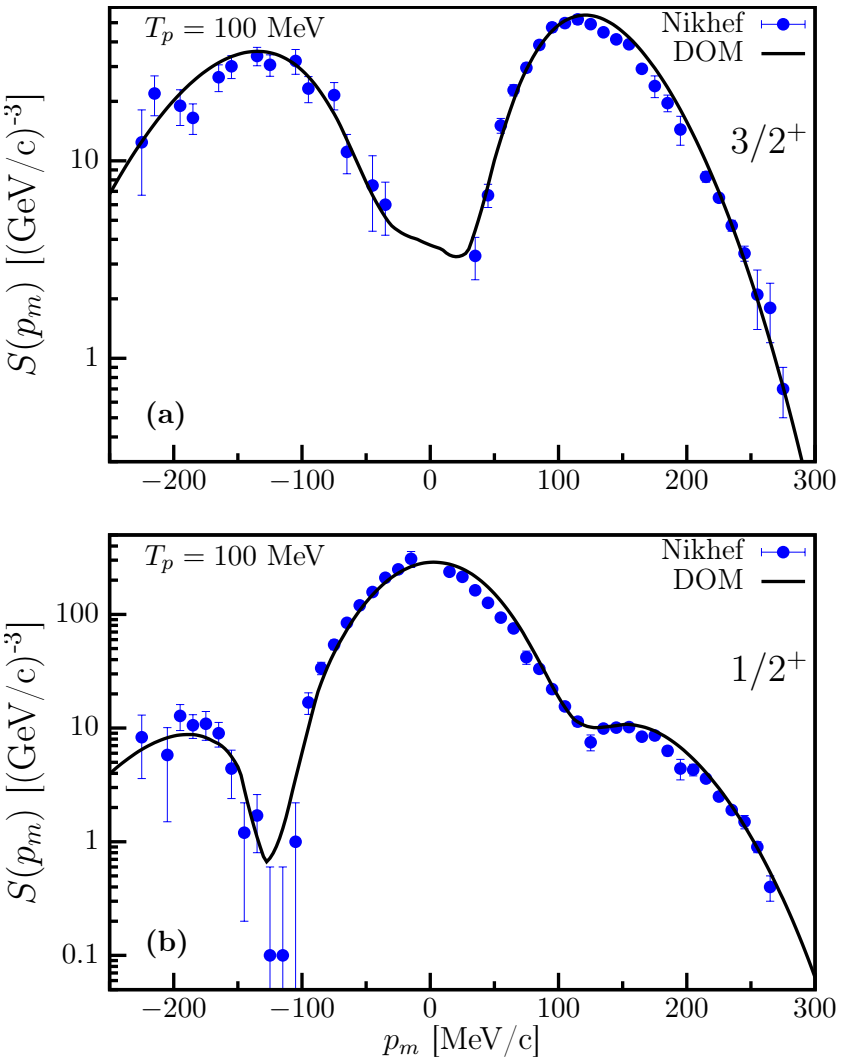

Figure 3.11: ^{40}Ca$(e, e'p)^{39}$K spectral functions in parallel kinematics at an outgoing proton kinetic energy of 100 MeV. The solid line is the calculation using the DOM ingredients, while the points are from the experiment detailed in [45]. (a) Distribution for the removal of the $0d\frac{3}{2}$. The curve contains the DWIA for the $3/2^+$ ground state including a spectroscopic factor of 0.71. (b) Distribution for the removal of the $1s\frac{1}{2}$ proton with a spectroscopic factor of 0.60 for the $1/2^+$ excited state at 2.522 MeV.

The DOM results yield at least as good agreement with the data as the standard analysis of Ref. [45] for the 100 MeV outgoing protons. The main difference in the description can be pinpointed to the use of nonlocal potentials to describe the distorted waves. Nonlocal potentials tend to somewhat suppress interior wave functions of scattering states and introduce an

additional ℓ dependence as compared to local potentials. The current consistent treatment clarifies that spectroscopic factors will be larger by about 0.05 when the proper nonlocal dispersive potentials are employed. The DOM treatment of experimental data associated with both the particle and hole aspects of the single-particle propagator furthermore allows for a positive assessment of the quality of the DWIA to describe exclusive $(e, e'p)$ cross sections with outgoing proton energies around 100 MeV.

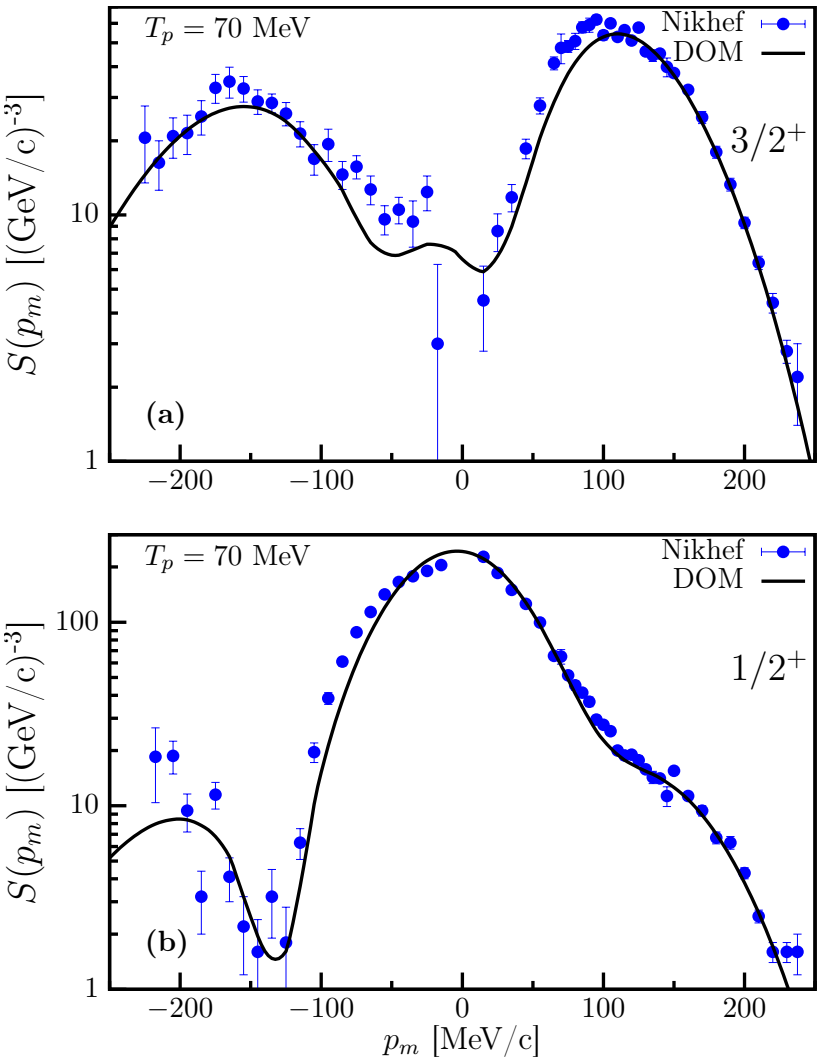

Figure 3.12: As for Fig. 3.11, but for an outgoing proton energy of 70 MeV.

It is therefore fortunate that additional data have been obtained at 70 and 135 MeV to

further delineate the domain of validity for the DWIA description of the reaction. Figure 3.12 displays the results when DOM ingredients are employed at this lower energy for the two valence hole states in ^{39}K. The only difference in the DOM calculations for these cases is the use of a different proton energy, yielding different outgoing proton waves. The overlap function and the spectroscopic factors remain the same. In Fig. 3.12 the results are shown for $T_p = 70$ MeV. The description is of similar quality as the 100 MeV case.

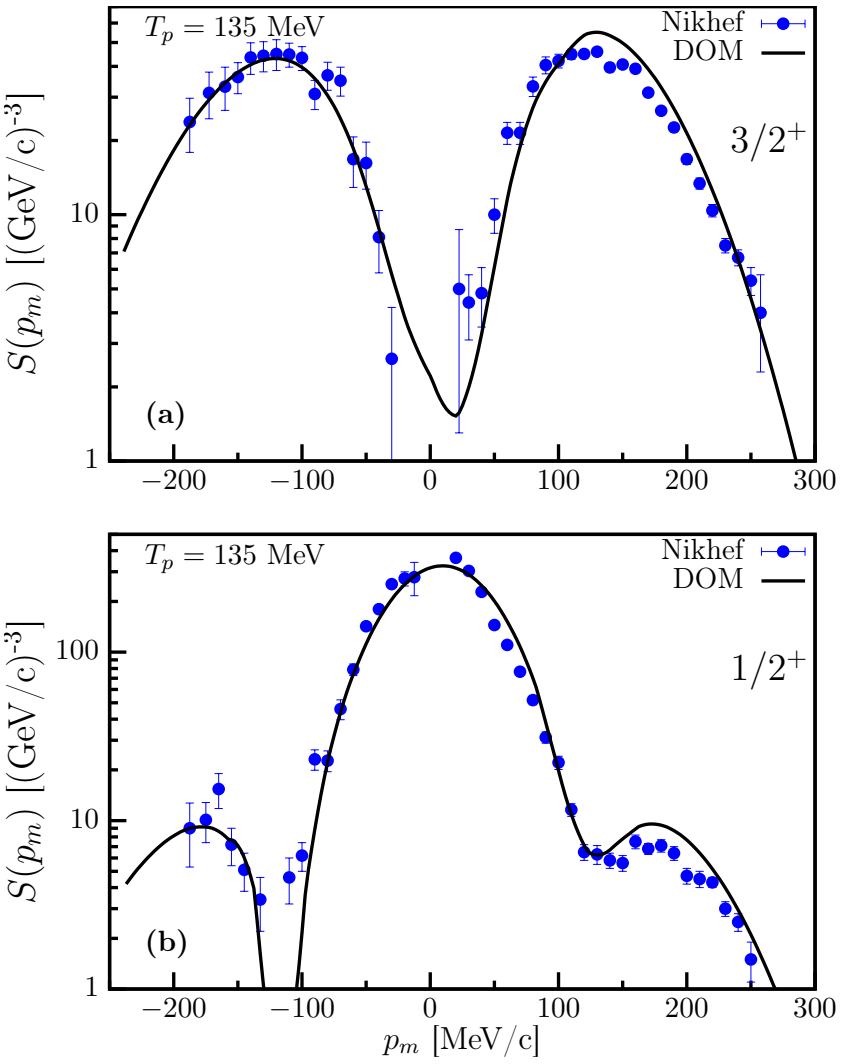

Figure 3.13: As for Fig. 3.11, but for an outgoing proton energy of 135 MeV.

The agreement with the data at 135 MeV shown in Fig. 3.13 is slightly worse but still

acceptable. At this energy (and corresponding value of the electron three-momentum transfer) the contribution of the transverse component of the excitation operator, where other mechanisms contribute in addition to those included in the present operator, will be larger. Two-body current contributions are more relevant at this energy, causing the IA to breakdown. In particular, 135 MeV is right at the pion-production threshold, which will certainly affect the $(e, e'p)$ cross section [60, 69]. Given these results, it seems that parallel kinematics, in which the longitudinal part of the operator dominates, and a proton energy around 100 MeV, as chosen by the Nikhef group, is optimal for probing the removal probability of valence protons. This can only be achieved when an analysis is conducted in which all ingredients are provided by a nucleon self-energy that is constrained by all relevant available data as in the DOM. The excellent agreement found here therefore supports the validity of the DOM approach as it is able to automatically account for the DWIA cross section in the domain where this approximation is expected to be valid.

The DOM results also generate the complete spectral distribution for the $0d\frac{3}{2}$ and $1s\frac{1}{2}$ orbits according to Eqs. (2.60) and (2.61). These distributions are displayed in Fig. 3.14 from -100 to 100 MeV. The energy axis refers to the $(A-1)$ system below the Fermi energy and the $(A+1)$ system above. For plotting purposes, the small imaginary part near the Fermi energy was employed giving the peaks a small width. The occupation probabilities are obtained from Eq. (2.64) and correspond to 0.80 and 0.82 for the $0d\frac{3}{2}$ and $1s\frac{1}{2}$ orbits, respectively. The strength at negative energy not residing in the DOM peak therefore corresponds to 9 and 7%, respectively. This information is constrained by the proton particle number and the charge density. The strength above the Fermi energy is constrained by the elastic-scattering data and generates 0.17 and 0.15 for the $0d\frac{3}{2}$ and $1s\frac{1}{2}$ orbits, respectively, when Eq. (2.65) is employed up to 200 MeV. The sum rule given by Eq. (2.66) therefore suggests that an additional 3% of the strength resides above 200 MeV, similar to what was found in Ref. [85]. Strength above the energy where surface physics dominates can be ascribed to the effects of

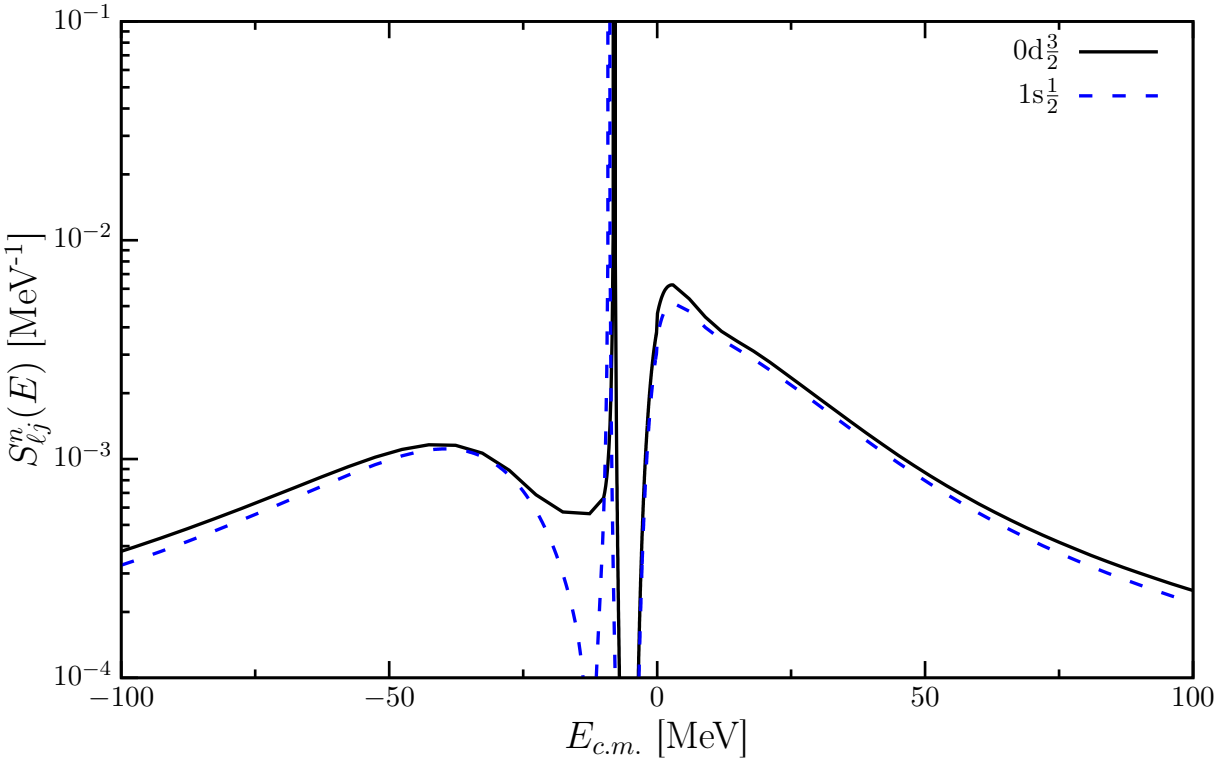

Figure 3.14: Spectral distribution of the $0d\frac{3}{2}$ and $1s\frac{1}{2}$ orbits as a function of energy. Additional strength outside this domain is not shown.

short-range and tensor correlations. The main characterizations of the strength distribution shown in Fig. 55 of Ref. [63] are therefore confirmed for ^{40}Ca. The present results thus suggest that it is possible to generate a consistent picture of the strength distributions of these orbits employing all the available experimental constraints. Therefore, it is indeed quite meaningful to employ concepts like spectroscopic factors and occupation probabilities when discussing correlations in nuclei.

3.6 Conclusions

The main conclusion of this chapter is that a consistent description of all available experimental data that are unambiguously related to the nucleon single-particle propagator is essential in providing accurate ingredients for a DWIA description of the $(e, e'p)$ reaction.

This description is provided by the DOM when it is implemented with nonlocal potentials up to at least 200 MeV in the elastic-scattering domain. The availability of $(e, e'p)$ data at 70, 100, and 135 MeV of proton outgoing energy also delineates a window in which the DWIA provides an accurate description of the exclusive cross section with energies around 100 MeV appearing to be optimal. It is important to note that it is also essential to consider the kinematics that favor the longitudinal part of the excitation operator which is dominated by a one-body component. This analysis therefore confirms the general conclusions reached in the past by the Nikhef group [58].

The confrontation of the DOM ingredients with the $(e, e'p)$ cross sections also demonstrates a necessary avenue for its further improvement. It is fortunate that a rather complete experimental picture of the $\ell = 0$ fragmentation at low energy has also been determined utilizing the $(e, e'p)$ reaction [47]. Using the experimental strength distribution without relying on their absolute values, it is possible to determine the fraction carried by the largest fragment at 2.522 MeV. Since the DOM does not yet provide the details of this low-energy fragmentation, it was possible to identify the fraction of the DOM strength to be compared to the experimental cross section for the 2.522 MeV transition using this experimental information. The resulting cross sections for both the ground state and 2.522 MeV state are then accurately described by the DWIA employing the DOM results. Nevertheless, the DOM requires further improvement to incorporate more details on the low-energy fragmentation leading possibly to additional state dependence. This improvement is particularly relevant for the description of strength distributions of weakly or deeply bound nucleons as they occur in $(N - Z)$ asymmetric nuclei. See Sec. 6.3 for an analysis of the quenching of spectroscopic factors going from ^{48}Ca to ^{40}Ca. Indeed, this feature must be addressed in the ongoing discussion related to spectroscopic factors deduced from transfer [87] and knockout [88] reactions, which appear to be in contradiction with each other. As has been highlighted here, it is important to clarify the amount of spectroscopic strength in the immediate vicinity of

the main fragment. This issue will only be more critical when a continuum of one of the nucleon species is nearby [89].

The success of the DWIA for the description of the $(e, e'p)$ reaction has implications for the possibility of employing other reactions. In particular, the (p, pN) reaction above approximately 200 MeV incoming energy appears an attractive possibility [90]. The availability of a proper description of the three distorted waves and the normalized overlap function using the DOM implies that it is possible to gauge the effective nucleon-nucleon interaction for this process by comparing with the $(e, e'p)$ results. If successful, such an analysis would lend itself to an extension to rare isotopes for which this reaction is available [91,92]. The current status of transfer reactions also suggests that the DOM can provide important contributions to the extraction of spectroscopic information [46, 93]. Before a consistent description of transfer reactions utilizing the DOM can be implemented, it will be necessary to improve the description of the deuteron distorted wave to the level currently achieved for single nucleons.

Finally, the discussion of absolute spectroscopic factors can now be shifted to the level of observable $(e, e'p)$ cross sections in which the quality of the reaction description (DWIA) can be tested by a direct comparison with data. Of particular value in reaching agreement with $(e, e'p)$ cross sections within the DOM framework is the availability of reaction cross section data, including those above 100 MeV, that directly quantify the strength of the coupling of the single-particle degree of freedom to other excitations through the imaginary part of the self-energy. The values for the valence spectroscopic factors of 0.71 for the $3/2^+$ ground state in ^{39}K and 0.60 for the $1/2^+$ excited state appear to be the final answer in the quest for absolute values for ^{40}Ca. Taking into account the uncertainties associated with all the data that provide the presented self-consistent analysis, a bootstrap error analysis was employed to estimate that the accuracy in these values is ± 0.04.

Chapter 4

Neutron Skin Thickness of Asymmetric Nuclei

4.1 Introduction

A fundamental question in nuclear physics is how the constituent neutrons and protons are distributed in the nucleus. In particular, for a nucleus which has a large excess of neutrons over protons, are the extra neutrons distributed evenly over the nuclear volume or is this excess localized in the periphery of the nucleus forming a neutron skin? A quantitative measure is provided by the neutron skin, defined as the difference between neutron and proton root-mean-squared (rms) radii,

$$\Delta r_{np} = r_n - r_p,$$

where

$$r_{n,p}^2 = \frac{1}{N_{n,p}} \int_0^\infty dr r^4 \rho_{n,p}(r), \tag{4.1}$$

and $N_{n,p}$ is the normalization of the particle point-distributions $\rho_{n,p}(r)$. Note that the standard convention is to define the neutron skin with respect to the nucleon point-distributions,

thus the size of the nucleons are not taken into account in theoretical calculations (the size of the nucleons are also factored out from experimental form factors [26]). Accurate knowledge of the distribution of neutrons in nuclei is important for calculations of the nuclear matrix elements relevant to β-decay processes [94, 95]. Furthermore, the nuclear symmetry energy, which characterizes the variation of the binding energy as a function of neutron-proton asymmetry, opposes the creation of nuclear matter with excesses of either type of nucleon. The extent of the neutron skin is determined by the relative strengths of the symmetry energy between the central near-saturation and peripheral less-dense regions. Therefore, Δr_{np} is a measure of the density dependence of the symmetry energy around saturation [67, 96–98]. This dependence is very important for determining many nuclear properties, including masses, radii, fission properties, and the location of the drip lines in the chart of nuclides. Its importance extends to astrophysics for understanding supernovae and neutron stars [99, 100], and to heavy-ion reactions [101].

Given the importance of the neutron skin in these various areas of research, a large number of studies (both experimental and theoretical) have been devoted to it [102]. While the value of r_p can be determined quite accurately from electron scattering [103], the experimental determinations of r_n are typically model dependent [102]. However, the use of parity-violating electron scattering does allow for a nearly model-independent extraction of this quantity [27]. The present value for ^{208}Pb extracted with this method from the PREX collaboration at Jefferson Lab yields a skin thickness of Δr_{np}=$0.33^{+0.16}_{-0.18}$ fm [26]. Future electron-scattering measurements are expected to reduce the experimental uncertainty. In this chapter, a DOM analysis of the neutron skins of ^{48}Ca and ^{208}Pb is presented. The point distributions generated by the single-particle propagator of the DOM self-energy are constrained by both structure and scattering data. Thus, the DOM is uniquely capable of providing insight into the connection between the neutron skin and scattering processes.

4.2 ^{48}Ca

4.2.1 Neutron Skin of ^{40}Ca

Before considering the neutron skin for ^{48}Ca, it is important to benchmark this method by considering the predictions for the $N = Z$ system ^{40}Ca. In ^{40}Ca [80], the neutron and proton self-energies were assumed identical apart from the Coulomb contribution, and they were fit simultaneously to a large amount of data including the charge distribution. It is therefore not surprising that the point neutron density distribution is very similar to the proton one, see Fig 4.1. It is clear from Fig. 4.1 that the Coulomb potential reduces the proton point distribution in the interior while extending its reach. The extracted skin thickness is Δr_{np}=-0.06 fm. Indeed, a very small, but negative, value is expected as protons have an extra repulsion from the Coulomb force which forces them slightly further apart. Other theoretical predictions for this system range from Δr_{np}=-0.02 to -0.10 fm [104–106].

Given that the fitted neutron and proton self-energies are identical apart from the Coulomb potential, the DOM extracted result may be considered highly constrained. In order to test this, the neutron data alone has been refit to see if the value of Δr_{np}^{40} changes. At the same time, it is also important to obtain an error estimate arising from the uncertainties of the experimental data. The statistical uncertainties associated with the fitted scattering data sets are typically quite small, but the largest uncertainties are systematic associated with the normalization of the cross sections. In addition, the large number of elastic differential cross sections in the data sets overwhelm the total calculated χ^2, giving little sensitivity in the fits to total and reaction cross sections and bound-state data. Therefore, a weighted χ^2 fit is implemented, giving more weight to these other data sets so they properly influence the final outcome. It is thus clear that the standard χ^2 analysis, which assumes all errors are statistical, cannot be used to estimate the Δr_{np} error. Instead, following Ref. [86], a bootstrap method is employed. New modified data sets were created from

the original data by randomly renormalizing each angular distribution or excitation function within ±10% to incorporate fluctuations from the systematic errors. Forty such modified neutron data sets were generated and refit. The mean of the new fitted skin thickness is Δr_{np}=-0.065±0.008 fm. This is almost identical to the original value obtained from fitting the combined neutron and proton data.

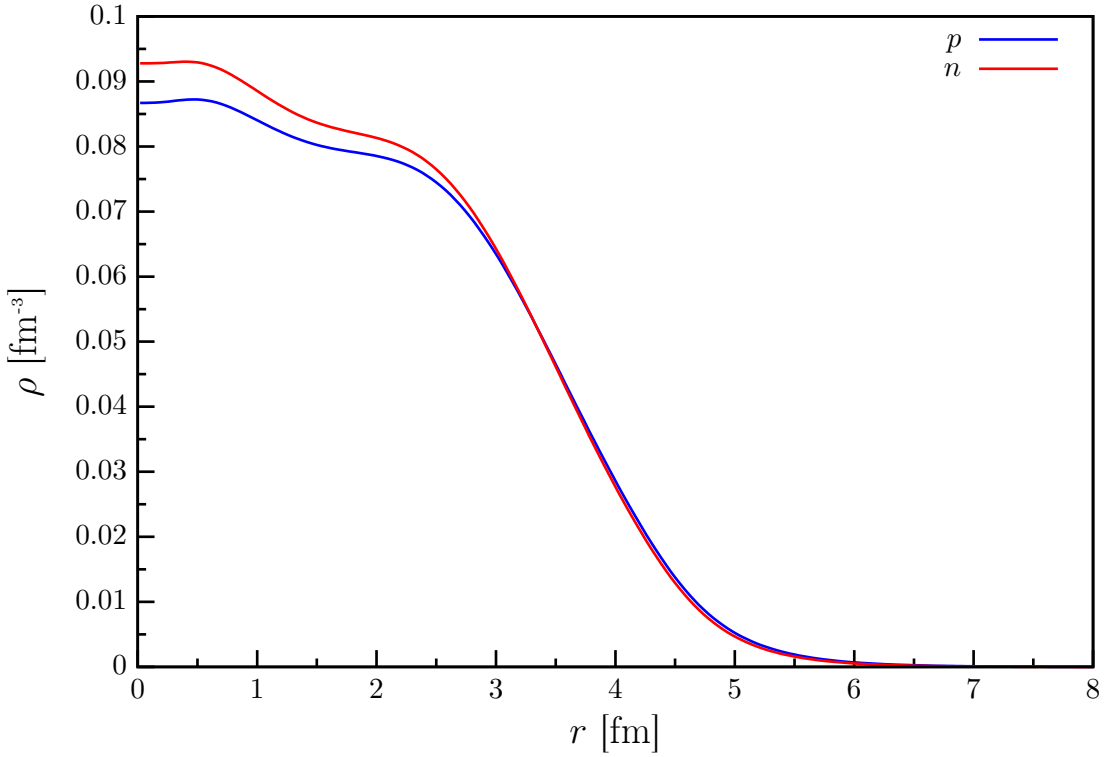

Figure 4.1: Proton (blue line) and neutron (red line) point distributions in ^{40}Ca calculated using Eq. (3.13). The neutron skin calculated with these distributions is Δr_{np}=-0.065±0.008 fm

4.2.2 Fit of ^{48}Ca

The DOM self-energy of ^{40}Ca was presented in Sec. (3.3). In order to fit a self-energy for ^{48}Ca, asymmetry parameters were added to the ^{40}Ca self-energy. Some parameters are left fixed at the values used for ^{40}Ca. Briefly, the magnitudes and radius parameters of these Woods-Saxon terms for the asymmetry contributions to the Hartree-Fock, volume, and surface

imaginary contributions are varied independently in the ^{48}Ca fits. The asymmetric Hartree-Fock component is allowed to have a different nonlocality parameter and for the main $N = Z$ component, the radius parameter is also allowed to vary. Details of the parametrization can be found in App. (B).

Previously, a fit of ^{48}Ca was published in Ref. [29, 52], quoting a neutron skin of $\Delta r_{np} = 0.249 \pm 0.023$ fm. However, just as in the case of ^{40}Ca in Sec. (3.3), the proton reaction cross section is too low at 200 MeV. While there is no experimental data for ^{48}Ca at these energies, there is data at 700 MeV [107] of the proton reaction cross section of ^{40}Ca and ^{48}Ca. Comparing the available data for $\sigma^{40}_{\text{react}}(E)$ at 200 MeV and 700 MeV reveals that the reaction cross section essentially stays flat between these energies, which is consistent with the shape of the DOM fit for ^{40}Ca in Fig. 3.3. It is reasonable to expect that $\sigma^{48}_{\text{react}}(E)$ assumes the same shape as $\sigma^{40}_{\text{react}}(E)$ at high energies. Thus, data points are extrapolated from the ^{40}Ca experimental data at energies above 100 MeV by applying the ratio that is seen in the 700 MeV data for $\sigma^{48}_{\text{react}}(E)/\sigma^{40}_{\text{react}}(E)$, see Table 4.1. The extrapolated points are shown as blue squares in Fig. 4.2 while the updated fit is represented with the solid curve.

Table 4.1: Experimental proton reaction cross section data at 700 MeV taken from Ref. [107].

Nucleus	**^{40}Ca**	**^{48}Ca**	**^{48}Ca/^{40}Ca**
$\sigma_{\mathbf{react}}(\mathbf{E})$	614 ± 38 mb	736 ± 46 mb	1.19

The remainder of the fit did not change significantly from Ref. [29], but is still shown here for completeness. Note also that the neutron skin did not change. The proton and neutron elastic differential cross sections are shown in Fig. 4.3. The proton analyzing power is shown in Fig. 4.4 (only proton analyzing powers are displayed because there are no experimental analyzing power data for neutrons). The neutron total cross section can be seen in Fig. 4.7(a). The charge density is presented in Fig. 4.5. The fit resulted in 19.8 protons and 27.9 neutrons with an $\ell_{\max} = 10$. The DOM calculated energy levels are reported in Table 4.2.

Table 4.2: Comparison of experimental and fitted mean energies for various proton and neutron orbitals for ^{48}Ca. References to the experimental levels can be found in Ref. [82].

Protons	**DOM** [MeV]	**Exp.** [MeV]	**Neutrons**	**DOM** [MeV]	**Exp.** [MeV]
$\mathbf{0d_{3/2}}$	-14.6	-12.5	$\mathbf{0d_{3/2}}$	-17.8	-16.8
$\mathbf{1s_{1/2}}$	-13.9	-12.5	$\mathbf{1s_{1/2}}$	-15.9	-17.1
$\mathbf{0f_{7/2}}$	-8.3	-9.9	$\mathbf{0f_{7/2}}$	-9.9	-9.6
$\mathbf{1p_{3/2}}$	-3.5	-5.14	$\mathbf{1p_{3/2}}$	-5.4	-6.5
$\mathbf{1p_{1/2}}$	-2.0	-3.11	$\mathbf{1p_{1/2}}$	-4.2	-3.6

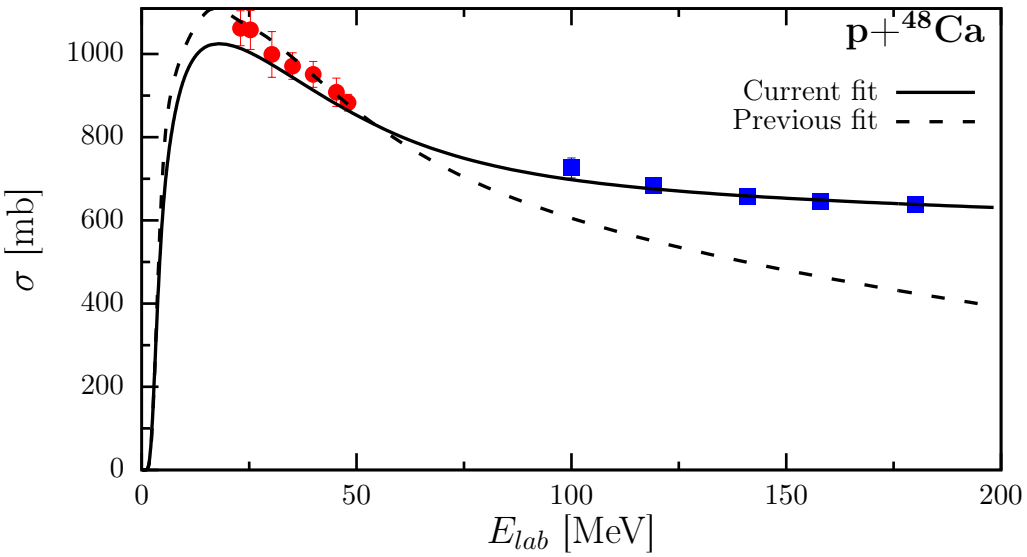

Figure 4.2: The proton reaction cross section for ^{48}Ca. The solid line represents the current fit while the dashed line depicts the previous fit [29]. The circular points are the same experimental data used in Ref. [82] and are included in the previous fit. The square points are extrapolated from the $\sigma^{40}_{\text{react}}(E)$ experimental data points at the corresponding energies. The extrapolation is explained in the main text.

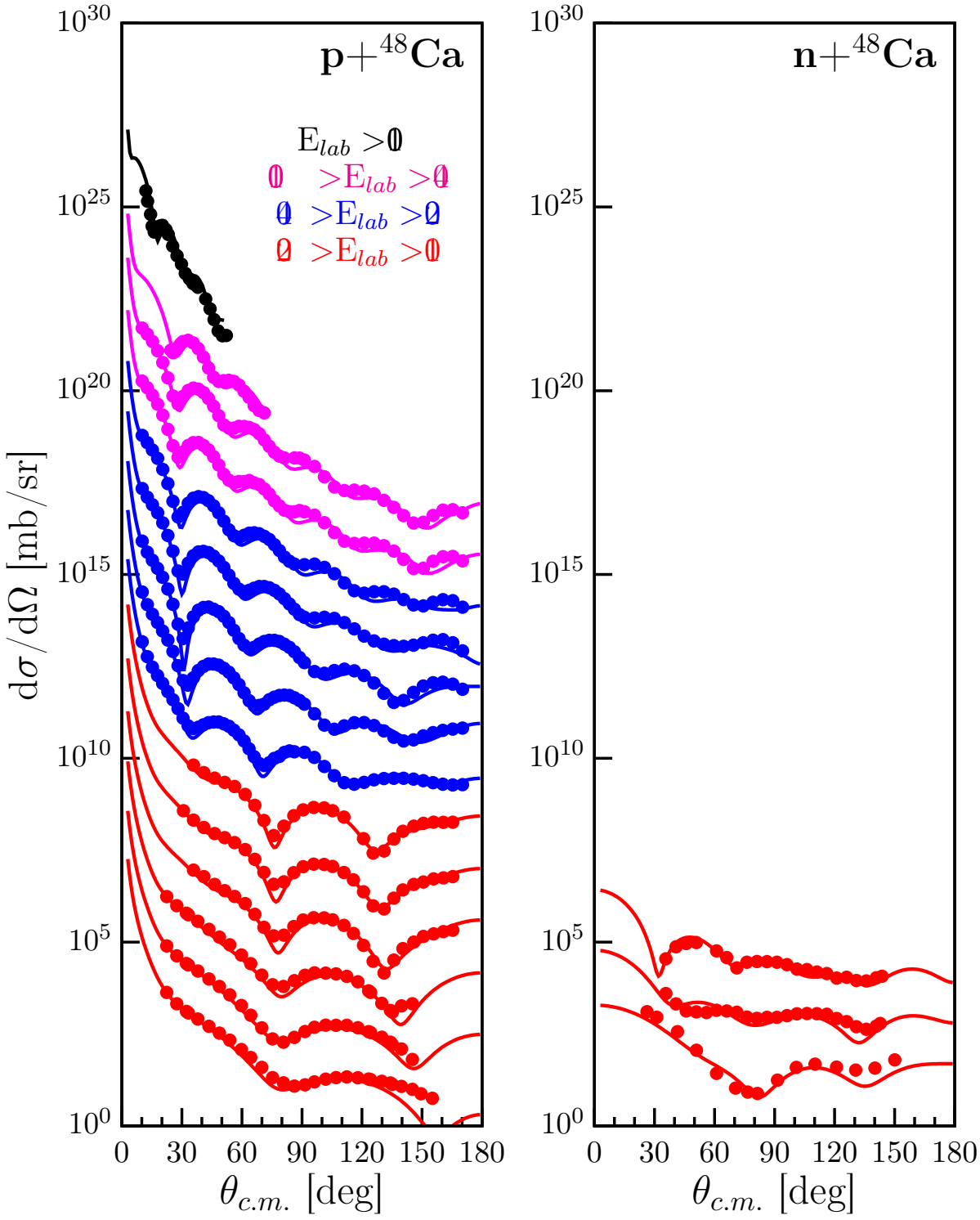

Figure 4.3: Calculated and experimental proton and neutron elastic-scattering angular distributions of the differential cross section $\frac{d\sigma}{d\Omega}$ in ^{48}Ca. The data at each energy is offset by factors of ten to help visualize all of the data at once. References to the data are given in Ref. [82].

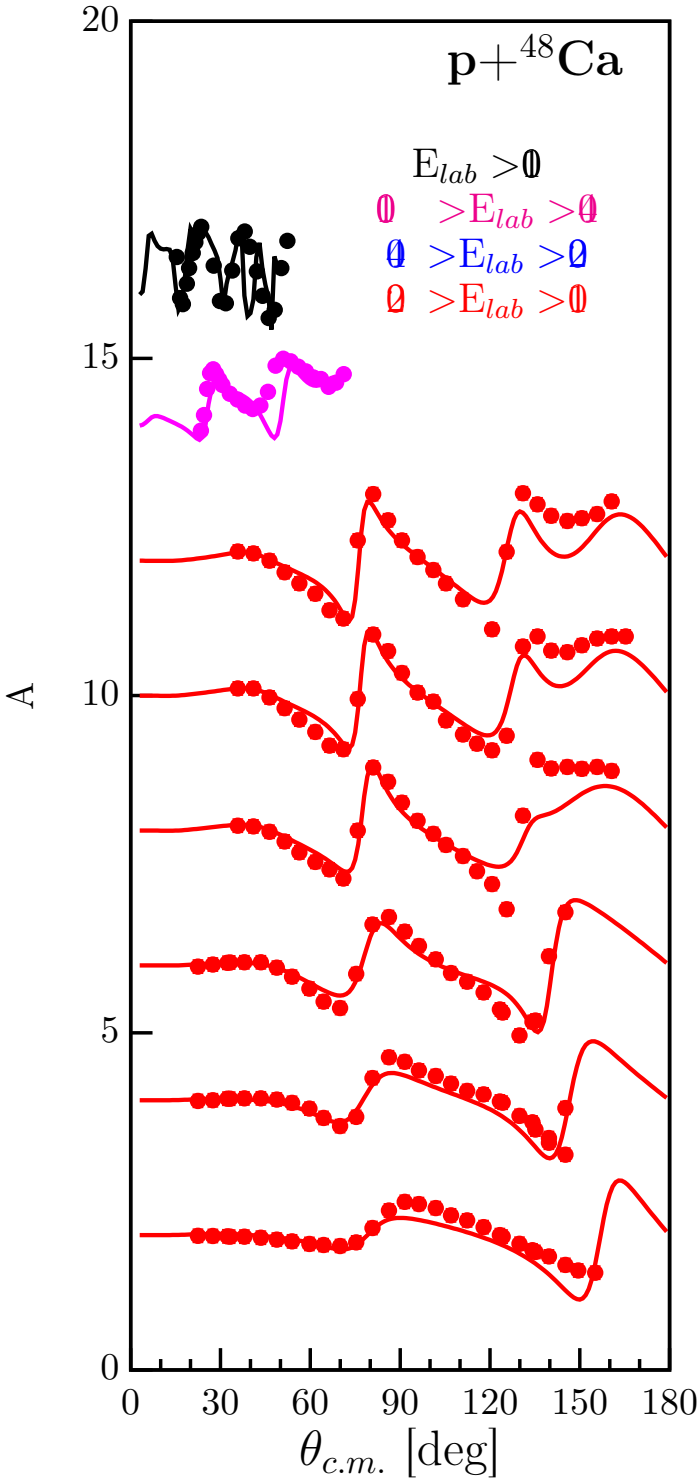

Figure 4.4: Results for proton analyzing power generated from the DOM self-energy of ^{48}Ca. The data and calculation at each energy at offset by a linear factor of 2 in order to visualize everything in a single plot. There are currently no experimental data on neutron analyzing power. References to the data are given in Ref. [82].

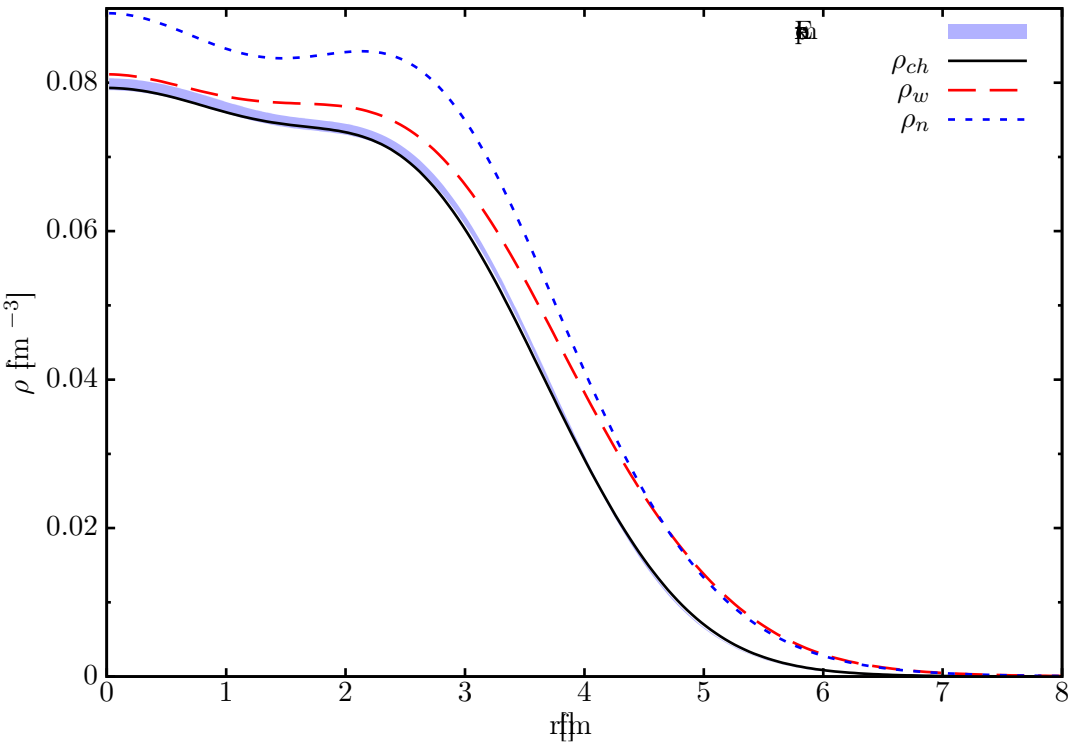

Figure 4.5: Comparison of experimental, ρ_{exp} (blue shaded region), and fitted, ρ_{ch} (solid black line), charge distribution for ^{48}Ca. The neutron matter distribution is plotted as ρ_n (blue short-dashed line), while the weak charge distribution is plotted as ρ_w (red long-dashed line). The sign of ρ_w is flipped to allow for a better comparison with the neutron and charge distributions.

4.2.3 Analysis of the neutron skin in ^{48}Ca

The experimental charge distribution is well reproduced as shown in Fig. 4.5. The neutron matter distribution clearly extends out to larger radii forming a neutron skin. The weak charge distribution, calculated by folding the weak proton and neutron form factors with their respective point distributions [26], is shown as ρ_w (the sign is flipped in order to compare with the other densities). The neutron skin of ^{48}Ca deduced from these distributions is Δr_{np}=0.249±0.023 fm, where again the bootstrap method was used to estimate the experimental uncertainty. This value overlaps with the range of values (0.12-0.26 fm) predicted with 48 reasonable nuclear energy-density functionals (EDFs) in Ref. [108], but is larger

compared to the range of 0.12-0.15 fm obtained with the coupled-cluster method [11].

To further understand which data in the fit exhibit the most sensitivity to skin thickness, additional fits were constrained where selected values of r_n are forced in the DOM calculations. This is achieved by varying the radius parameters of the main real potential (r_n^{HF} and r_n^{HFasy} in App. B) and refitting the other asymmetry dependent parameters. The weighted χ^2 as a function of the calculated r_n is plotted as the data points in Fig. 4.7(b) and the absolute minimum at r_n=3.67 fm corresponds to the skin thickness of 0.249 fm. There is some fine-scale jitter in the variation of χ^2 with r_n. To concentrate on the larger-scale variation, the data points shown in Fig. 4.7(b) are local averages with the error bars giving the range of the jitter.

The location of the *ab initio* results is also indicated at r_n ∼3.56 fm where the χ^2 is larger. The shown χ^2 has been subdivided into its contributions from its two most important components (dashed curves); from the elastic-scattering angular distributions and from the total neutron cross sections. The former has a smaller sensitivity to r_n, and its χ^2 is slightly lower for the smaller values of r_n which are more consistent with the *ab initio* result as illustrated in Fig. 4.6 where a fit with a forced value of Δr_{np}=0.132 is compared to the best DOM fit and to the data. While this new calculation improves the reproduction of these data, the deviations of both curves from the data are typical of what one sees in global optical-model fits. In addition, these experimental angular distributions only cover a small range of bombarding energies (7.97 to 16.8 MeV) and may not be typical of other energies.

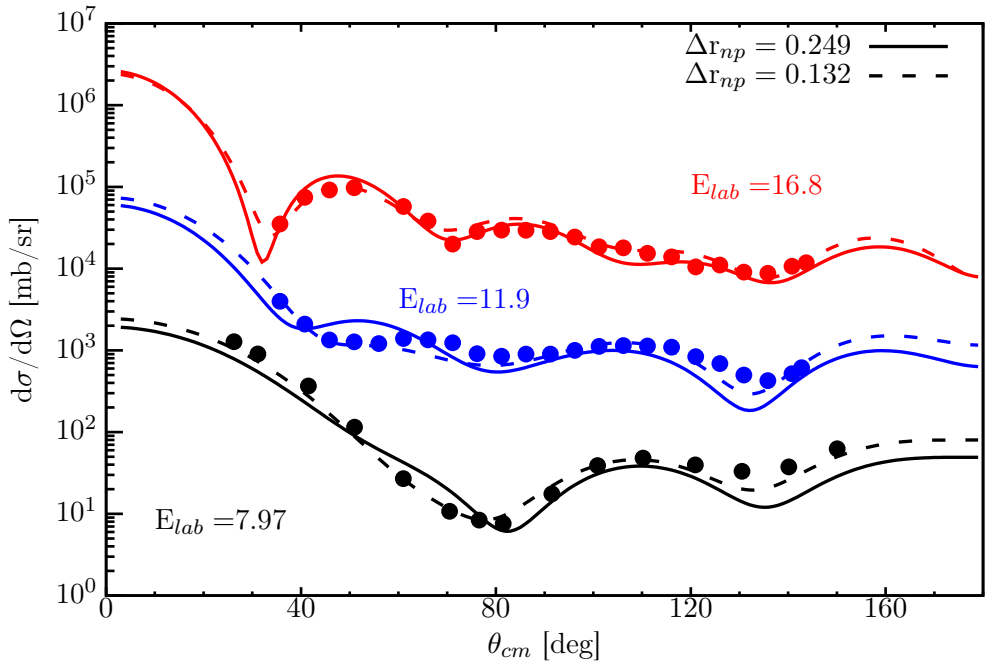

Figure 4.6: Comparison of experimental n+^{48}Ca elastic-scattering angular distributions [82, 109] to the best DOM fit of all data (solid curves) and to a constrained fit with the skin thickness forced to Δr_{np}=0.132 fm (dashed curves) which is consistent with the *ab initio* result.

The total cross section exhibits larger sensitivity and the experimental data cover a large range of neutron energies (6 to 200 MeV). Two data sets are available (circles and diamonds) but are inconsistent by ∼10% at E_{lab} ∼10 MeV, where their ranges overlap. The high-energy data set [110] (circles) was used in the DOM fit as it was obtained with ^{48}Ca metal, while the low-energy set [111] (diamonds) employed $^{48}CaCO_3$ and required a subtraction of ∼70% of the signal due to neutron absorption from the CO_3 component. Therefore, the χ^2 contribution is displayed only from the high-energy set. This χ^2 exhibits a broad minimum from r_n= 3.66 to 3.75 fm allowing values of Δr_{np} up to 0.33 fm.

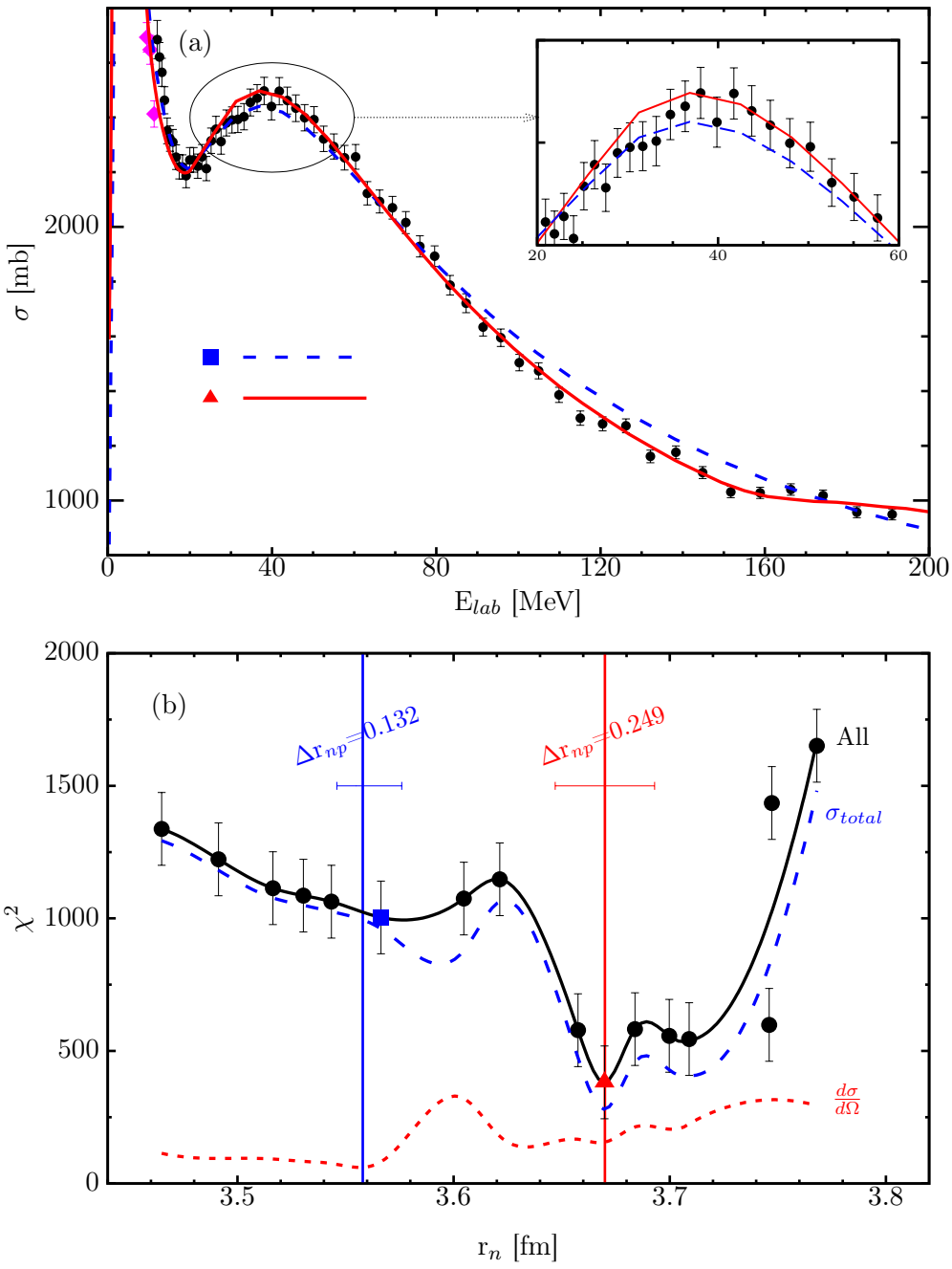

Figure 4.7: (a) Comparison of the experimental total neutron cross sections of ^{48}Ca (diamonds [111], circles [110]) to DOM fits with constrained values of r_n. The curve labeled with a triangle is for the r_n value of the DOM best fit, while the curve labeled with a square is for a value consistent with the *ab initio* result (see Fig. 4.6). (b) The χ^2 from fitting all data (solid curve) and its contribution from the elastic-scattering angular distributions and the total neutron cross section (short-dashed and long-dashed curves respectively). Each point corresponds to a fit around its value of r_n.

Figure 4.7(a) illustrates the sensitivity to r_n where the solid and dashed curves correspond to the fits indicated by triangular and square data points in Fig. 4.7(b), respectively. The former is the best fit while the latter has a skin-thickness consistent with the *ab initio* result. The latter calculation under predicts the maximum at 40 MeV while over predicting the 80-180 MeV region. These differences arise almost exclusively from the elastic-scattering contribution to the total cross section whose energy dependence displays large-scale oscillations due to the interference between transmitted and externally scattered neutrons [31] leading to a phase shift that depends on the size and depth of the real component of the neutron self-energy. Note that the results shown in Fig. 4.7 are from the previous fit of Ref. [29]. The main difference in the updated fit is the description of high-energy proton reaction cross sections, as shown in Fig. 4.2. Thus, the conclusions drawn from Fig. 4.7 are representative of the current fit as well.

To further visualize where the extra neutrons in ^{48}Ca are located, the calculated proton and neutron point distributions weighted by r^4 for both ^{40}Ca and ^{48}Ca are shown in Fig. 4.8 . The distributions are weighted by r^4 to visualize the contribution to the rms radii in Eq. (4.1). These distributions have been subdivided into the contribution from lower-ℓ orbitals ($s_{1/2}$, $p_{3/2}$, $p_{1/2}$, $d_{5/2}$, and $d_{3/2}$) and that from the remaining higher-ℓ orbitals which is dominated by the $f_{7/2}$ component. For ^{40}Ca, the proton and neutron distributions are very similar as expected given there is essentially no neutron skin. For ^{48}Ca, the contribution from the lower-ℓ orbitals, common to both neutrons and protons, is very similar to the ^{40}Ca results. Not surprisingly, the magnitude of the neutron skin comes predominately from the $f_{7/2}$ orbital, reflecting its centrifugal barrier.

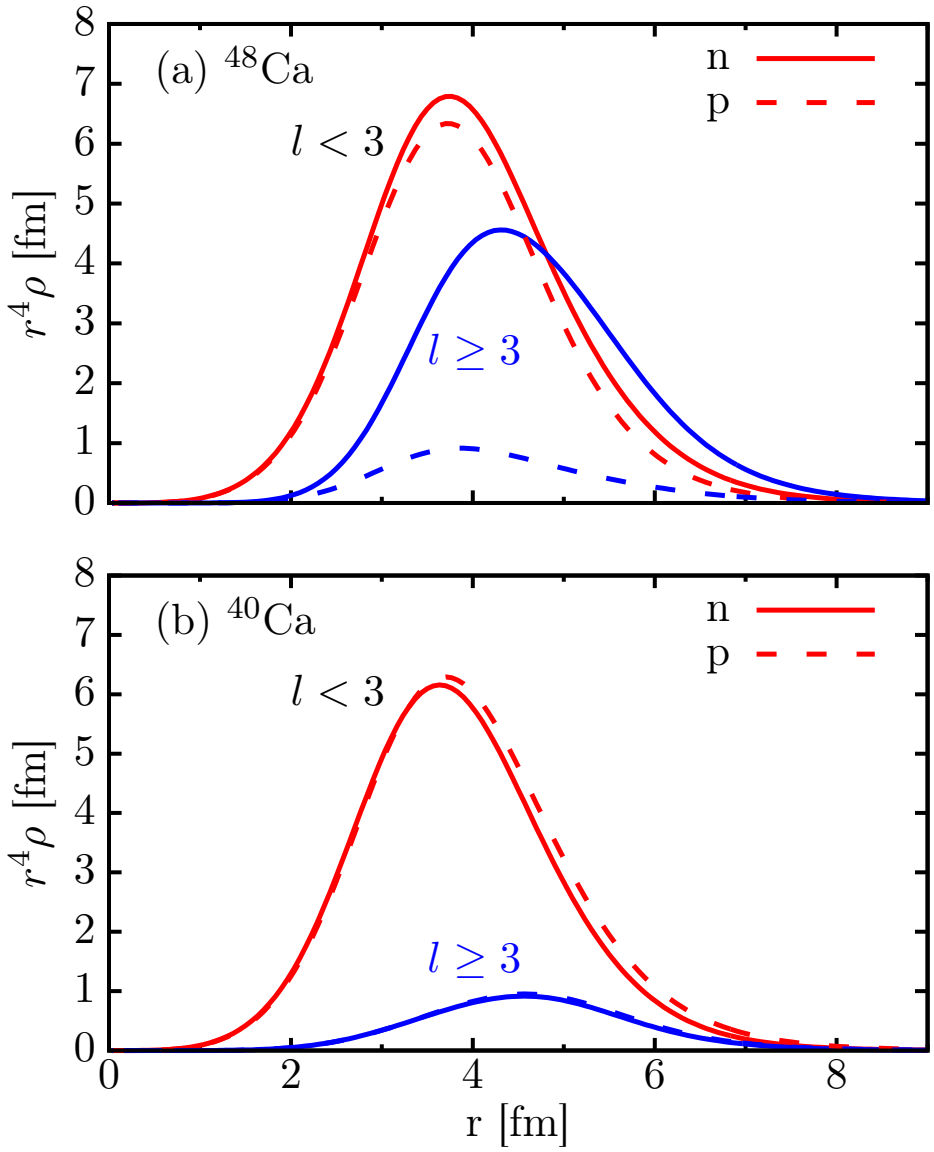

Figure 4.8: Decomposition of the r^4 weighted point densities for protons and neutrons in (a) ^{48}Ca and (b) ^{40}Ca. These are subdivided into the contribution from the lower-ℓ orbitals [$s_{1/2}$,$p_{3/2}$, $p_{1/2}$, $d_{5/2}$, and $d_{3/2}$] designated by "$\ell < 3$" and the remaining higher-ℓ orbitals "$\ell \geq 3$".

4.3 ^{208}Pb

A DOM analysis of ^{208}Pb leads to a connection with current experimental data on the neutron skin. Unfortunately, the current experimental value of the neutron skin in ^{208}Pb from the PREX experiment [26] allows for a large range of values ($\Delta r_{np}^{208} = 0.15$ fm - 0.49 fm). This error range is too large to constrain the majority of the theoretical predictions of the neutron skin from mean-field calculations [108]. Another measurement of the neutron weak form factor of ^{208}Pb is scheduled for the summer of 2019 at Jefferson Lab under the title of PREX2. This is an updated version of the original PREX experiment which is intended to provide a much narrower error bar for the neutron skin in ^{208}Pb. Thus, it is exciting to make a prediction of the neutron skin before it is measured with high precision.

4.3.1 Fit of ^{208}Pb

The functional form of the ^{208}Pb self-energy is equivalent to that of ^{48}Ca. Starting from the parameters for ^{48}Ca, the χ^2 was minimized for a similar set of experimental data for ^{208}Pb (see App. B for specific values of parameters). The neutron total cross section (Eq. (A.7)) is shown in Fig. 4.10. The elastic differential cross sections (Eq. (A.6)) at energies up to 200 MeV for protons and neutrons are shown in Fig. 4.11. The analyzing powers (Eq. (A.19)) for neutrons and protons are shown in Fig. 4.12.

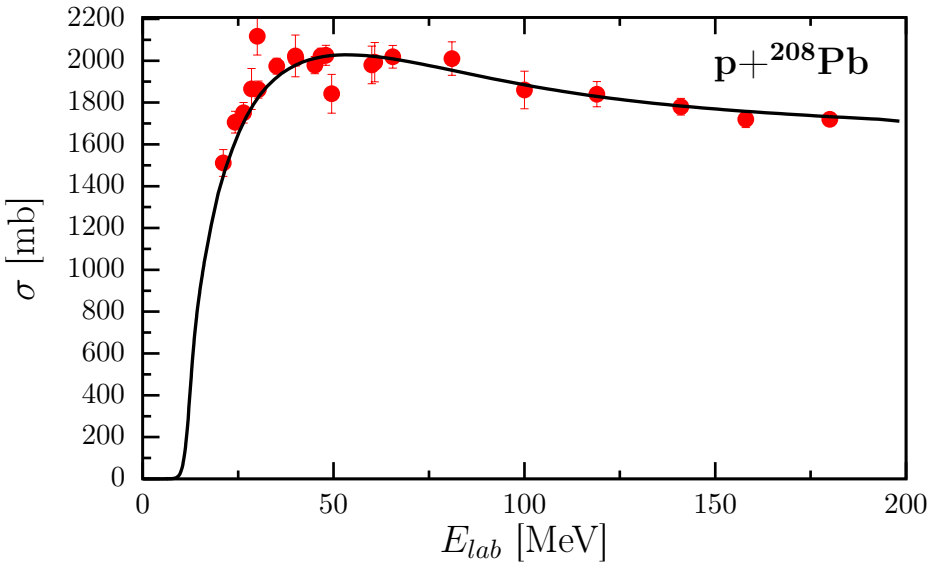

Figure 4.9: The proton reaction cross section for ^{208}Pb. References to the experimental data points can be found in Ref. [80].

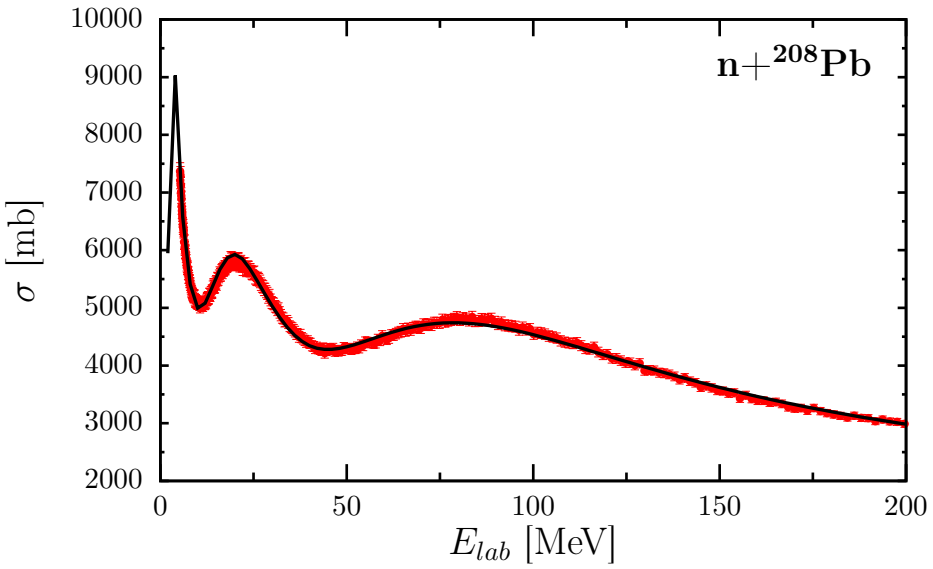

Figure 4.10: Neutron total cross section (solid line) generated from the DOM self-energy for ^{208}Pb. The circles represent measured total cross sections. References to the data are given in Ref. [82].

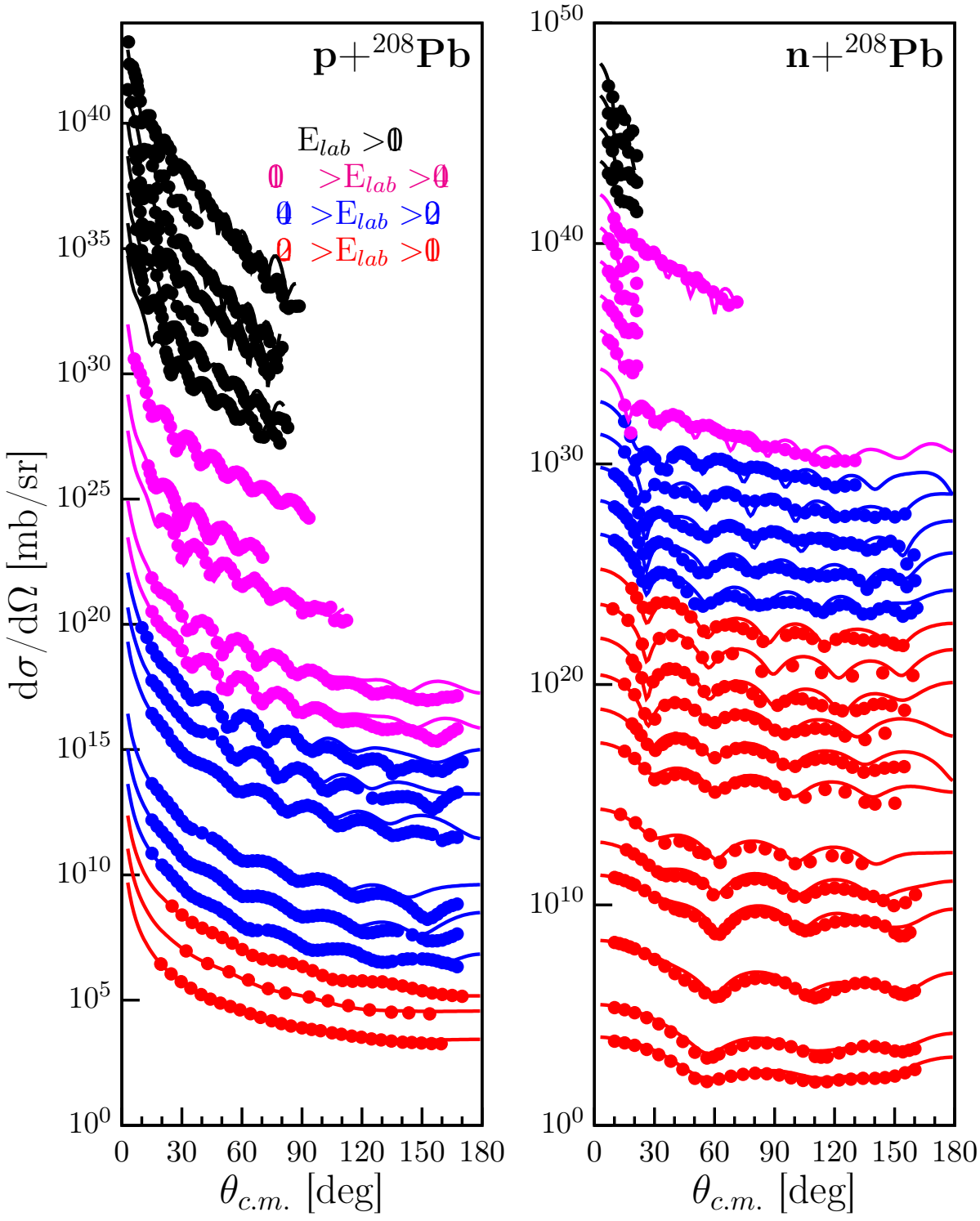

Figure 4.11: Calculated and experimental proton and neutron elastic-scattering angular distributions of the differential cross section $\frac{d\sigma}{d\Omega}$ for ^{208}Pb. The data at each energy is offset by factors of ten to help visualize all of the data at once. References to the data are given in Ref. [82].

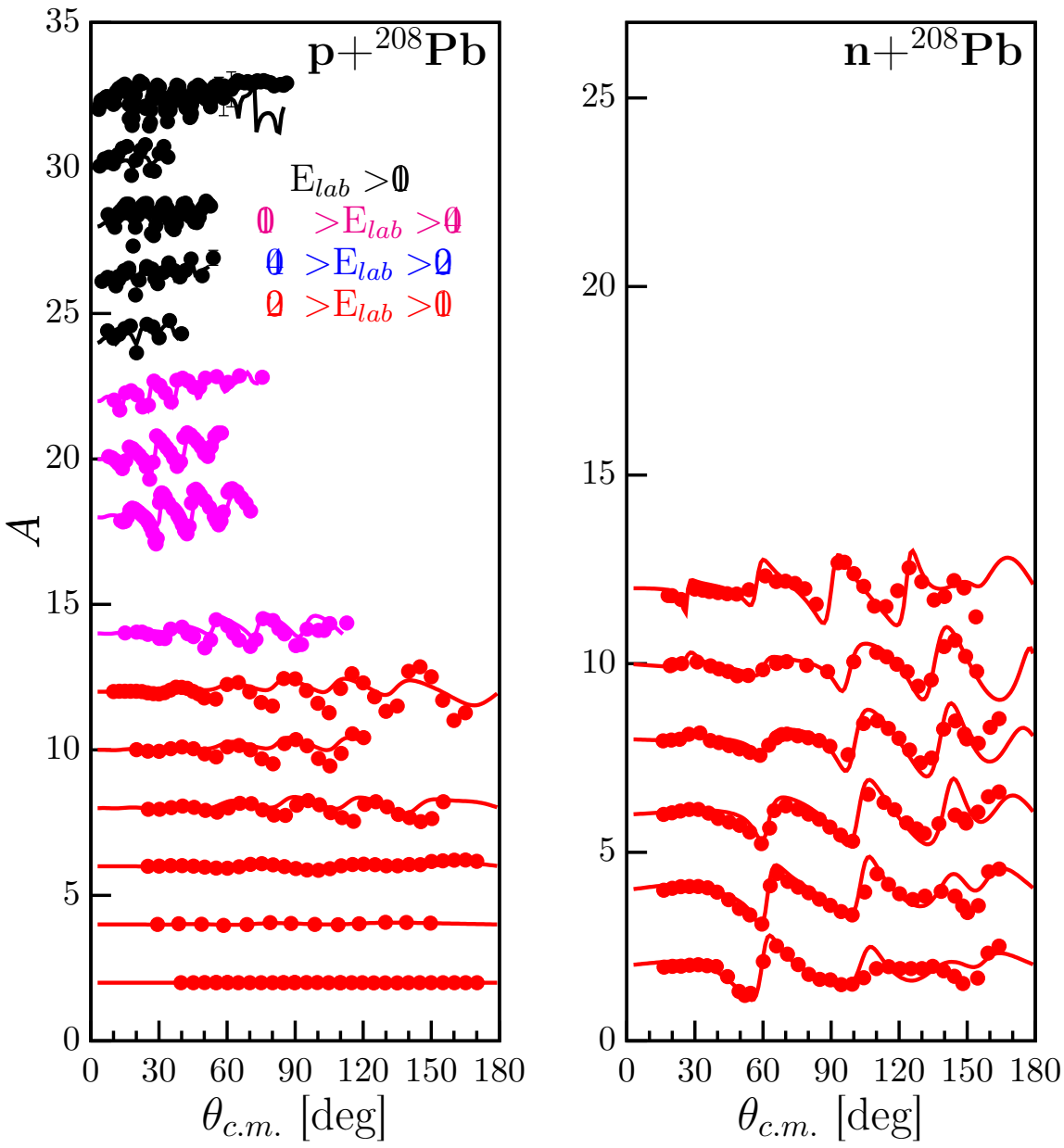

Figure 4.12: Results for proton and neutron analyzing power generated from the DOM self-energy for ^{208}Pb compared with experimental data. References to the data are given in Ref. [82].

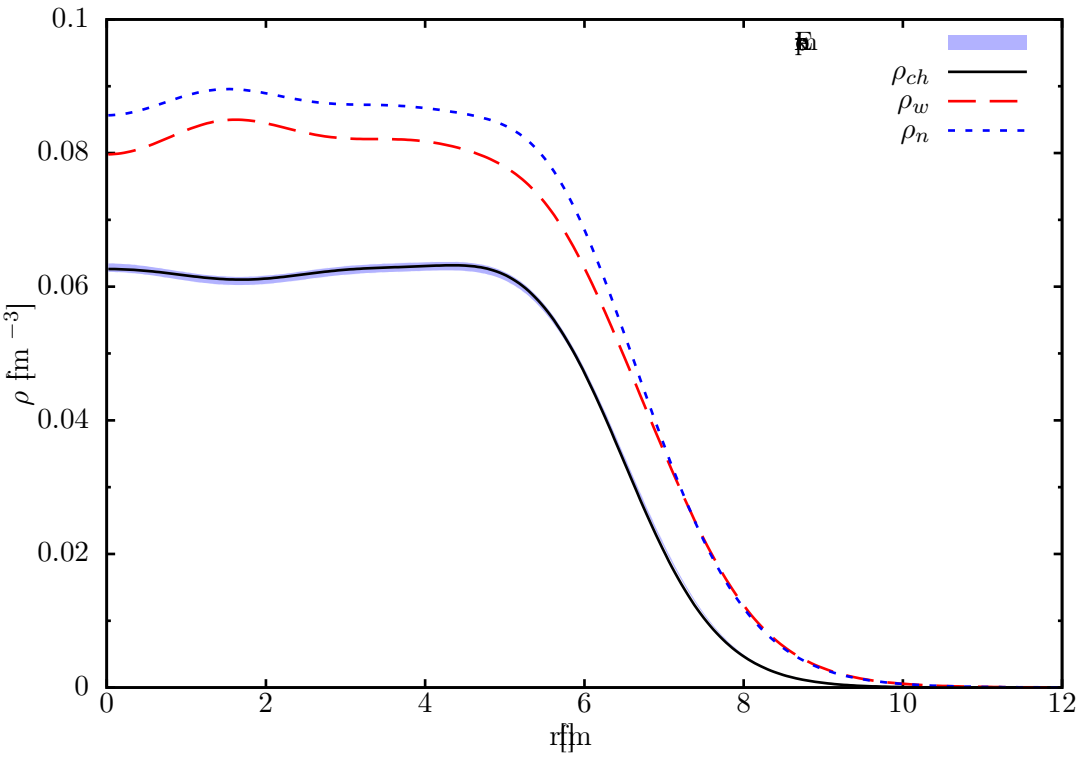

Figure 4.13: Experimental and fitted ^{208}Pb charge density. The solid black line is calculated using Eq. (3.13) and folding with the proton charge distribution (see App. C) while the experimental band represents the 1% error associated with the extracted charge density from elastic electron scattering experiments using the sum of Gaussians parametrization [83, 84]. Also shown is the weak charge distribution, ρ_w (red long-dashed line), and the neutron matter distribution, ρ_n (blue short-dashed line).

The charge density of ^{208}Pb is shown in Fig. 4.13. The experimental band is extrapolated from elastic electron scattering differential cross sections [83]. This data is well reproduced after using the DOM charge density from Fig. 4.13 as the ingredient in a relativistic elastic electron scattering code [112]. The elastic scattering cross section is shown in Fig. 4.14.

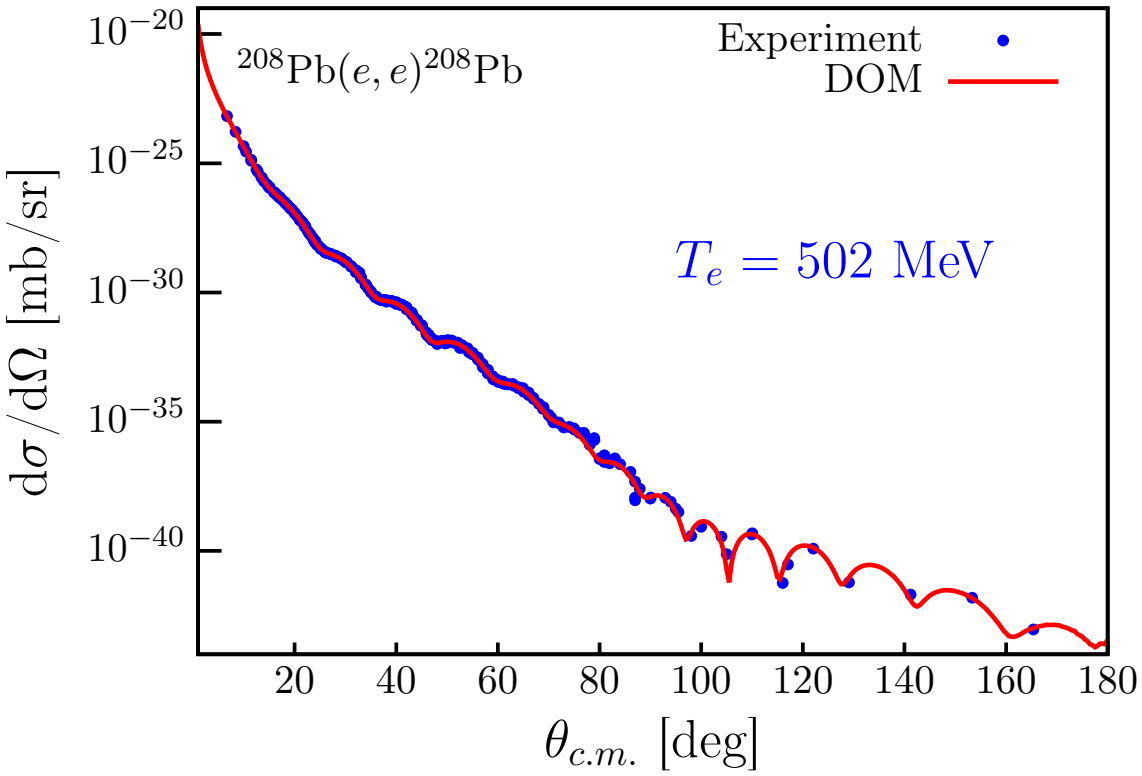

Figure 4.14: Experimental and fitted ^{208}Pb(e,e) differential cross section. The solid line is calculated using Eq. (3.13) [112] and the while the experimental data are from [83].

Table 4.3: Comparison of experimental and fitted mean energies for various proton and neutron orbitals for ^{208}Pb. References to the experimental levels can be found in Ref. [82].

Protons	DOM	Exp.
$\mathbf{2p_{1/2}}$	1.015	-0.17
$\mathbf{2p_{3/2}}$	0.2869	-0.68
$\mathbf{1f_{5/2}}$	-0.376	-0.98
$\mathbf{0i_{13/2}}$	-1.956	-2.19
$\mathbf{1f_{7/2}}$	-2.527	-2.9
$\mathbf{0h_{9/2}}$	-3.263	-3.8
$\mathbf{2s_{1/2}}$	-7.591	-8.01
$\mathbf{1d_{3/2}}$	-8.325	-8.36
$\mathbf{0h_{11/2}}$	-9.067	-9.35
$\mathbf{1d_{5/2}}$	-10.25	-9.701
$\mathbf{0g_{7/2}}$	-11.83	-11.5
$\mathbf{0g_{9/2}}$	-16.29	-15.77

Neutrons	DOM	Exp.
$\mathbf{2d_{3/2}}$	-1.097	-1.4
$\mathbf{1g_{7/2}}$	-1.385	-1.45
$\mathbf{3s_{1/2}}$	-1.324	-1.9
$\mathbf{2d_{5/2}}$	-1.775	-2.37
$\mathbf{0j_{15/2}}$	-0.368	-2.51
$\mathbf{0i_{11/2}}$	-2.565	-3.16
$\mathbf{1g_{9/2}}$	-3.195	-3.935
$\mathbf{2p_{1/2}}$	-7.126	-7.37
$\mathbf{1f_{5/2}}$	-8.099	-7.94
$\mathbf{2p_{3/2}}$	-7.727	-8.27
$\mathbf{0i_{13/2}}$	-8.326	-9
$\mathbf{1f_{7/2}}$	-9.933	-9.71
$\mathbf{0h_{9/2}}$	-10.24	-10.78

4.3.2 Analysis of ^{208}Pb Neutron Skin

The result of this DOM fit of ^{208}Pb is the prediction that $\Delta r_{np}^{208} = 0.250$. It is no surprise that this falls within the range of allowed values from the PREX experiment, but it will be interesting to compare this prediction to the updated experimental value from PREX2 in the coming year. This is also within the range of skin values (0.12 - 0.28 fm) of the 48 nuclear EDFs used in Ref. [108]. Currently, *ab-initio* calculations cannot be applied to heavy systems such as ^{208}Pb, so these mean-field results are the only other theoretical predictions of the neutron skin in ^{208}Pb.

The proton and neutron point distributions are plotted in Fig. 4.15. Unlike in ^{48}Ca, the difference in the number of protons and neutrons is quite large. In order to better visualize how the particle distributions contribute to the neutron skin, a plot of the distributions weighted by r^4 and normalized according to Eq. (4.1) is presented in Fig. 4.16. It is clear from Fig. 4.16 that the neutron distribution is more extended than the protons, resulting in

a positive neutron skin (just as with ^{48}Ca).

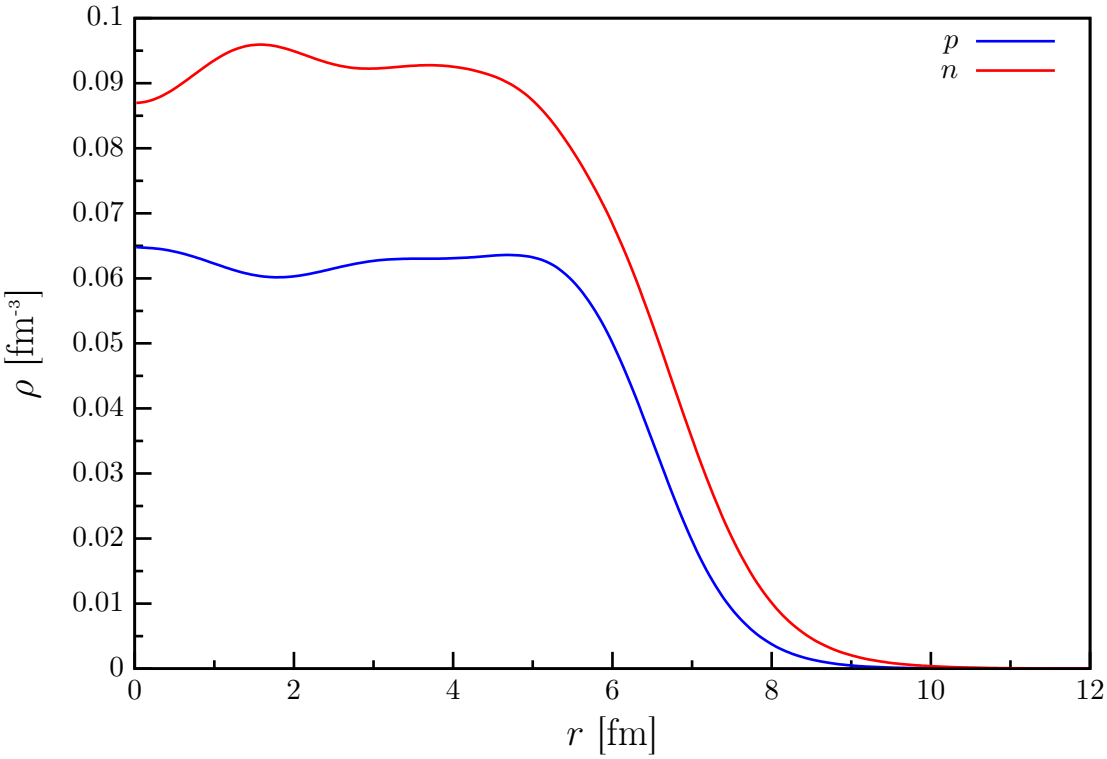

Figure 4.15: Neutron (red) and proton (blue) point distributions in ^{208}Pb. Each distribution is calculated using Eq. (3.13).

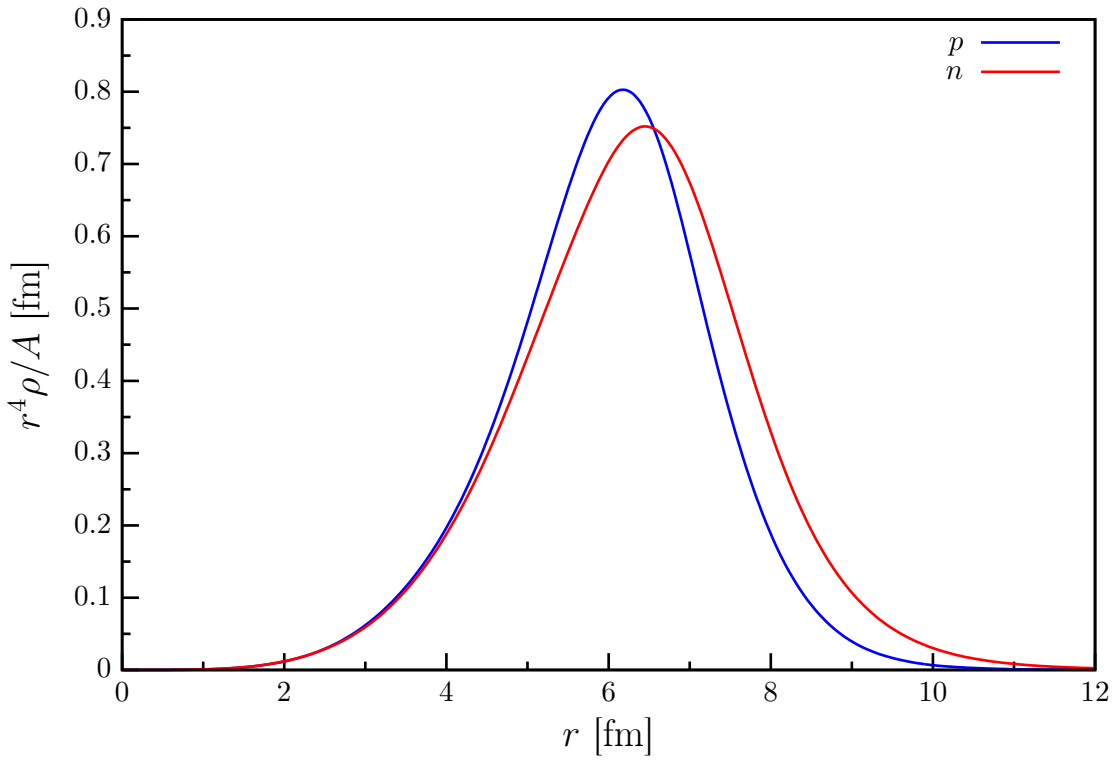

Figure 4.16: Neutron (red) and proton (blue) point distributions in ^{208}Pb weighted by r^4 and normalized according to Eq. (4.1). Each distribution is calculated using Eq. (3.13).

4.4 Conclusions

A nonlocal dispersive optical-model analysis of the asymmetric nuclei ^{48}Ca and ^{208}Pb has been performed. The neutron skins of these nuclei (along with ^{40}Ca) are shown in Table. 4.4. The neutron skins of ^{48}Ca and ^{208}Pb are quite similar. Since ^{208}Pb and ^{48}Ca have similar asymmetry parameters, indicated by α_{asy} (see App. B) in Table 4.4, it may seem reasonable that they have similar neutron skins. However, consider Fig. 4.17, which is a comparison of the neutron and proton distributions in ^{48}Ca and ^{208}Pb. Even normalized by particle number, the particle distributions in ^{208}Pb and ^{48}Ca are quite distinct due to the size difference of the nuclei. In light of this, the neutron skin of ^{208}Pb is biased to be larger by the increase in the rms radii of the proton and neutron distributions. Thus, a more interesting comparison

can be made by normalizing Δr_{np} by r_p,

$$\Delta\tilde{r}_{np} = \frac{1}{r_p}\Delta r_{np} = \frac{r_n}{r_p} - 1,$$

where $\Delta\tilde{r}_{np}$ is the normalized neutron skin thickness. This normalization serves to remove size dependence when comparing neutron skins of different nuclei. The result of this normalization is shown in Table 4.4. The difference between normalized skins of ^{208}Pb and ^{48}Ca in Table 4.4 reveals that the rms radius of the neutron distribution does not simply scale by the size of the nucleus for nuclei with similar asymmetries. While it is true that the nuclear charge radius scales roughly by $A^{1/3}$ (and by extension so does r_p), the same cannot be said about r_n. If one is to scale by the size of the nucleus, then the fact that the Coulomb repulsion (which scales with the number of protons) extends the proton distribution should be considered. Since ^{208}Pb has four times more protons than ^{48}Ca, the effect of the Coulomb repulsion on the neutron skin of ^{208}Pb could be up to four times more than the effect on the ^{48}Ca neutron skin, which can reasonably be taken from the calculated skin of -0.06 fm in ^{40}Ca. In Chap. 5, the Coulomb potential is removed from ^{208}Pb, resulting in an increased neutron skin of 0.38 fm. The results of the normalized neutrons skins with Coulomb removed are listed in Table 4.4 where it is clear that the Coulomb potential has a strong effect on the neutron skin. This points to the fact that the formation of a neutron skin cannot be explained by the asymmetry alone. Whereas the asymmetry in ^{48}Ca is primarily caused by the eight additional neutrons in the $f_{\frac{7}{2}}$ shell, there are several different additional shell fillings between the neutrons and protons in ^{208}Pb. It seems that these shell effects make it more difficult to predict the formation of the neutron skin based on macroscopic properties alone. A systematic study of more nuclei with similar asymmetry, α_{asy}, to ^{208}Pb and ^{48}Ca would help in determining the details of the formation of the neutron skin. This will lead to a better understanding of the symmetry energy of the equation of state (EOS) of nuclear

matter, which is vital to proceed in the current multi-messenger era onset by the first direct detection of a neutron star merger [25].

Table 4.4: DOM Predicted neutron skins for ^{40}Ca, ^{48}Ca, and ^{208}Pb. Also shown are the neutron skins normalized by r_p as well as neutron skins with the Coulomb potential removed from the self-energy (see Chap 5).

Nucleus	^{40}Ca	^{48}Ca	^{208}Pb
α_{asy}	0	0.167	0.211
r_p	3.47 fm	3.45 fm	5.454 fm
r_n	3.46 fm	3.70 fm	5.96 fm
Δr_{np}	-0.06 fm	0.249 ± 0.023 fm	0.250 fm
$\Delta \tilde{r}_{np}$	-0.0173 fm	0.0704 ± 0.0067 fm	0.0480 fm
Δr_{np}^{noC}	0.00 fm	0.309 ± 0.023 fm	0.380 fm
$\Delta \tilde{r}_{np}^{noC}$	0.00 fm	0.089 ± 0.0067 fm	0.070 fm

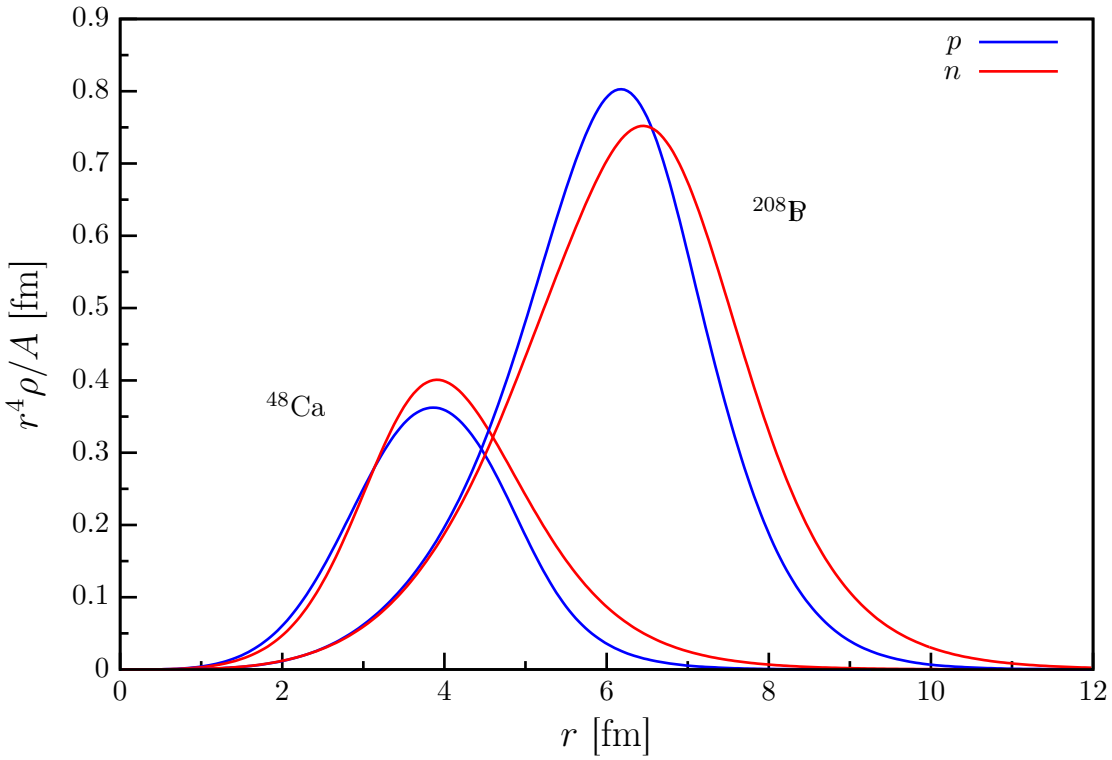

Figure 4.17: Neutron (red) and proton (blue) point distributions in ^{208}Pb weighted by r^4 and normalized according to Eq. (4.1). Each distribution is calculated using Eq. (3.13).

Chapter 5

DOM Binding Energies and Nuclear Matter

5.1 Introduction

In the DOM fits of ^{40}Ca, ^{48}Ca, and ^{208}Pb, the self-energy at negative energies was not only constrained by quasihole energies, particle numbers, and charge densities, but also by the total binding energy of each nucleus. In addition to the total binding energy, an energy density can be defined such that its volume integral is the total binding energy. These energy densities make it possible to relate the energy of these nuclei to energy calculations in infinite nuclear matter (NM) [113,114]. In particular, the link between the energy minimum at nuclear saturation and the empirical mass formula is explored in this chapter. For decades, the accepted value for the minimum energy of NM at saturation has been the empirical value around $E_0 \approx -16$ MeV [115–117]. In light of the results presented in this thesis coupled with the NM results from Ref. [113,114], the validity of the accepted value for E_0 is questioned. This in turn could change the nuclear equation of state (EOS), which is highly relevant in determining neutron-star structure [118,119].

5.2 Binding Energy in DOM Fits

The binding energy of a nucleus can be expressed as the expectation value of the Hamiltonian using the full A-body wave function,

$$E_0^A = \langle \Psi_0^A | \hat{H} | \Psi_0^A \rangle \, .$$

In second quantization, this expectation value can be written as

$$\langle \Psi_0^A | \hat{T} + \hat{V} | \Psi_0^A \rangle = \sum_{\alpha\beta} \langle \alpha | \hat{T} | \beta \rangle \, \langle \Psi_0^A | \hat{a}_\alpha^\dagger \hat{a}_\beta | \Psi_0^A \rangle + \frac{1}{4} \sum_{\alpha\beta\gamma\delta} \langle \alpha\beta | \hat{V} | \gamma\delta \rangle \, \langle \Psi_0^A | \hat{a}_\alpha^\dagger \hat{a}_\beta^\dagger \hat{a}_\delta \hat{a}_\gamma | \Psi_0^A \rangle \, , \quad (5.1)$$

where $\langle \alpha\beta | \hat{V} | \gamma\delta \rangle$ is the anti-symmetrized matrix element of the two-body nucleon-nucleon interaction [20]. The first term in Eq. (5.1) involves the density matrix, which can be directly calculated from the single-particle propagator using Eq. (2.63). The potential term in Eq. (5.1) has an indirect connection to the single-particle propagator. Consider an energy-weighted integral of the hole spectral function,

$$\int_0^{\varepsilon_F} dE E S_h(\alpha, \alpha; E) = \langle \Psi_0^A | \hat{T} | \Psi_0^A \rangle + 2 \, \langle \Psi_0^A | \hat{V} | \Psi_0^A \rangle \, . \quad (5.2)$$

The equality in Eq. (5.2) can be verified by substituting Eq. (2.61) for the spectral function and doing standard manipulations of the creation/annihilation operators to match the second quantized form of Eq. (5.1) [20, 49]. Thus, adding another factor of the expectation value of the kinetic energy to Eq. (5.2) leads to the Migdal-Galitski sum rule for the binding energy [120],

$$E_0^{N,Z} = \frac{1}{2} \sum_{\alpha\beta} \int_0^{\varepsilon_F} dE \left[\langle \alpha | \hat{T} | \beta \rangle \, S^h(\alpha, \beta; E) + \delta_{\alpha\beta} E S^h(\alpha, \alpha; E) \right] , \quad (5.3)$$

where $E_0^{N,Z}$ refers to the total binding energy of the neutrons or protons, and

$$E_0^A = E_0^N + E_0^Z.$$

It is important to note that this derivation assumes there are no three-body terms in the nucleon-nucleon interaction. While it is known that there is a three-body force, it is much weaker than the two-body force [8]. In chiral interactions, the three-body force does not even appear until next-to-next-to-leading order (NNLO) in the chiral expansion [5], but is important to generate NM saturation. With this in mind, for the purpose of the simplest DOM analysis, the energy sum rule of Eq. (5.3) is taken to be exact.

With Eq. (5.3), the binding energy of nuclei are also included in DOM fits. The particle numbers and binding energies, both calculated from sum rules, of ^{40}Ca, ^{48}Ca, and ^{208}Pb are shown in Table 5.1.

Table 5.1: Comparison of the DOM calculated particle numbers and binding energies of ^{40}Ca, ^{48}Ca, and ^{208}Pb and the corresponding experimental values.

	N	Z	DOM E_0^A/A	Exp. E_0^A/A
^{40}Ca	19.84	19.78	-8.46	-8.55
^{48}Ca	27.9	19.8	-8.84	-8.66
^{208}Pb	126.0	81.8	-7.76	-7.87

The close agreement with experiment in Table 5.1 along with the reproduction of experimental charge densities indicates that the hole spectral function is well constrained. The link between spectral functions, particle distributions, and binding energies in ^{40}Ca, ^{48}Ca, and ^{208}Pb will be explored in this chapter.

5.3 Energy Density

The energy density, $\mathcal{E}(r)$, of a nucleus can be defined such that

$$E_0^A = \int d^3r \mathcal{E}(r) = 4\pi \int_0^\infty dr r^2 \mathcal{E}(r). \tag{5.4}$$

Since the DOM is calculated in a coordinate-space basis of Lagrange functions, $\mathcal{E}(r)$ can be calculated using Eq. (5.3),

$$\begin{aligned}\mathcal{E}(r) &= \frac{1}{2}\int_0^{\varepsilon_F} dE \left[\sum_\beta \langle r|\hat{T}|\beta\rangle\, S^h(r,\beta;E) + E S^h(r,r;E)\right] \\ &= \frac{1}{2}\sum_{\alpha\gamma}\int_0^{\varepsilon_F} dE \left[\sum_\beta^N f_\alpha(r)\,\langle\alpha|\hat{T}|\beta\rangle\, S^h(\gamma,\beta;E) f_\gamma(r) + E f_\alpha(r) S^h(\alpha,\gamma;E) f_\beta(r)\right], \end{aligned} \tag{5.5}$$

where the second line comes from inserting complete sets of the Lagrange-Laguerre basis, and $f_\alpha(r)$ are the corresponding Lagrange-Laguerre basis functions of Sec. 2.2.2. The first term in Eq. (5.5) represents the kinetic energy density,

$$\mathcal{T}(r) = \sum_{\alpha\beta\gamma}^N \int_0^{\varepsilon_F} dE f_\alpha(r)\,\langle\alpha|\hat{T}|\beta\rangle\, S^h(\gamma,\beta;E) f_\gamma(r),$$

where the volume integral of $\mathcal{T}(r)$ is the total kinetic energy of the nucleus. It is now trivial to define the potential energy density as

$$\mathcal{V}(r) = \mathcal{E}(r) - \mathcal{T}(r),$$

where the volume integral of $\mathcal{V}(r)$ is the total potential energy of the nucleus. The energy density of ^{40}Ca weighted by the volume element $4\pi r^2$ is shown in Fig. 5.1. The weighting in Fig. 5.1 is chosen to emphasize the parts of the energy density that contribute to the integral in Eq. (5.4). The nucleon point-density is shown in addition to the energy densities

in Fig. 5.1 to demonstrate that the radial dependence of the energy density is very similar to that of the nucleon point-density.

Self-consistent Green's function (SCGF) calculations in NM from Ref. [114] are represented by points in Fig. 5.1. Each different shape corresponds to the use of a different NN interaction in the SCGF calculation, where the triangular points correspond to the charge-dependent Bonn (CD-Bonn) interaction [121], the circular points correspond to the Argonne v_{18} (AV18) interaction [3], and the square points correspond to the Idaho next-to-next-to-next-to-leading order (N3LO) chiral interaction [4]. The calculation in NM is for specific values of the nuclear density which are mapped to radii using the DOM matter density. These results cannot be directly compared to the energy density in finite nuclei because there is no Coulomb force included in NM. A way around this is to take advantage of isospin symmetry in $N = Z$ nuclei. Since there are an equal number of protons and neutrons in ^{40}Ca, isospin symmetry implies that the proton and neutron distributions would be the same if the Coulomb force were ignored. Thus, using twice the neutron energy density in ^{40}Ca is an effective way of removing the influence of the Coulomb force. The resulting nuclear-matter-like energy densities are represented as dashed lines in Fig. 5.1. The agreement with the NM calculations is striking provided that only SRC and tensor correlations are included [122]. This is indicative that the interior of ^{40}Ca (near saturation) acts like NM.

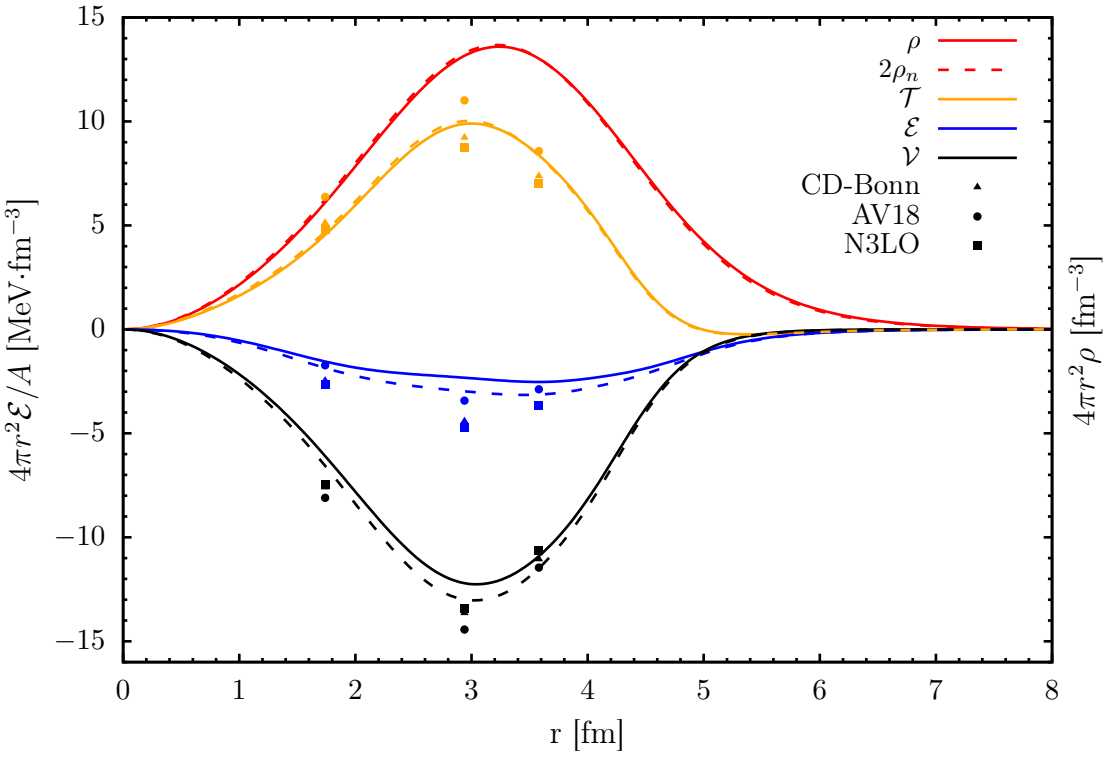

Figure 5.1: The energy density of ^{40}Ca calculated from the DOM using Eq. (5.5). The solid lines correspond to the full calculation while the dashed lines are twice the contribution from neutrons. The curves correspond to the energy density (blue lines), kinetic energy density (orange lines), potential energy density (black lines), and nucleon point-density (red lines). All curves are weighted by a volume element $4\pi r^2$. The points are taken from a SCGF calculation in NM for three different interactions based on Ref. [114].

The interaction with the best agreement with the DOM energy density in Fig. 5.1 is AV18. It is interesting that AV18 correctly predicts the nuclear saturation density, $\rho \approx 0.16$ fm [115,117], in the SCGF calculation of Ref. [113], but saturates at about -11.5 MeV. The accepted value for the energy at nuclear saturation comes from the well-known empirical mass formula (Bethe-Weizsäcker mass equation),

$$BE(A,Z) = a_V A - a_S A^{2/3} + a_C Z(Z-1)A^{-1/3} - a_A(A-2Z)^2 A^{-1} + \delta, \qquad (5.6)$$

where a_V, a_S, a_C, a_A, and δ are parameters fit to nuclear masses [1]. Ignoring the symmetry

energy at the moment, the only overlap between Eq. (5.6) and NM is the volume term, $a_V A$. Because of this, it seems natural to assume that the binding energy of NM at saturation should be $a_V = -15.85$ MeV [115, 117]. However, it is clear from Fig. 5.1 that the core of the nucleus does not contribute to the binding energy. Because the nuclear core minimally contributes to the total binding energy, there is no reason that the energy in the core should contribute to the empirical mass formula. Therefore, with the interpretation that NM is representative of the core of finite nuclei, there is no strong constraint that the binding energy of NM has to be a_V. This implies that the AV18 interaction produces consistent results for not only the density at saturation, but also the energy [113].

The fact that the binding energy density traces the nucleon density in Fig. 5.1 is not surprising when considering the decomposition of the binding energy with full A-body wave functions,

$$\begin{aligned} E_0^A = \langle \Psi_0^A | \hat{H} | \Psi_0^A \rangle = E_0^A \langle \Psi_0^A | \Psi_0^A \rangle = E_0^A \int d^3r_1 d^3r_2 ... d^3r_A \left| \Psi_0^A(\boldsymbol{r}_1, \boldsymbol{r}_2, ..., \boldsymbol{r}_A) \right|^2 \\ = E_0^A \int d^3r_1 \left[\int d^3r_2 ... d^3r_A \left| \Psi_0^A(\boldsymbol{r}_1, \boldsymbol{r}_2, ..., \boldsymbol{r}_A) \right|^2 \right], \end{aligned} \tag{5.7}$$

where the complete set $\{|\boldsymbol{r}_1 \boldsymbol{r}_1 ... \boldsymbol{r}_A\rangle\}$ has been inserted and all other quantum numbers are suppressed for clarity. Noting that the bracketed term in Eq. (5.7) is the one-body density distribution $\rho(\boldsymbol{r})$, the binding energy can be written as

$$E_0^A = \frac{E_0^A}{A} \int d^3r \rho(\boldsymbol{r}) = \int d^3r \mathcal{E}(r) \implies \mathcal{E}(r) = \left(\frac{E_0^A}{A} \right) \rho(r). \tag{5.8}$$

The exact result in Eq. (5.8) reveals that the energy density is simply the nucleon density scaled by the binding energy. While Eq. (5.8) is exact, it cannot be used as a replacement for Eq. (5.5) because there is no guarantee that the DOM propagator is equal to the exact propagator, which would be built from the exact A-body ground-state wave function using

Eq. (2.51). This is demonstrated in Fig. 5.2, which shows the energy density in ^{40}Ca calculated using both Eq. (5.5) and Eq. (5.8). The general agreement of the curves in Fig. 5.2 is quantified by the similarity of the rms radii of the energy density and the scaled matter density of 3.477 and 3.480, respectively. This reveals that the DOM description of the density is close to exact. It is not surprising that there are deviations, since the DOM fit constrains the density, which is only an indirect way of constraining the full A-body wave function. In principle, Eq. (5.8) is a good test to determine how close a given many-body approximation is to solving for the actual eigenfunction of the Hamiltonian.

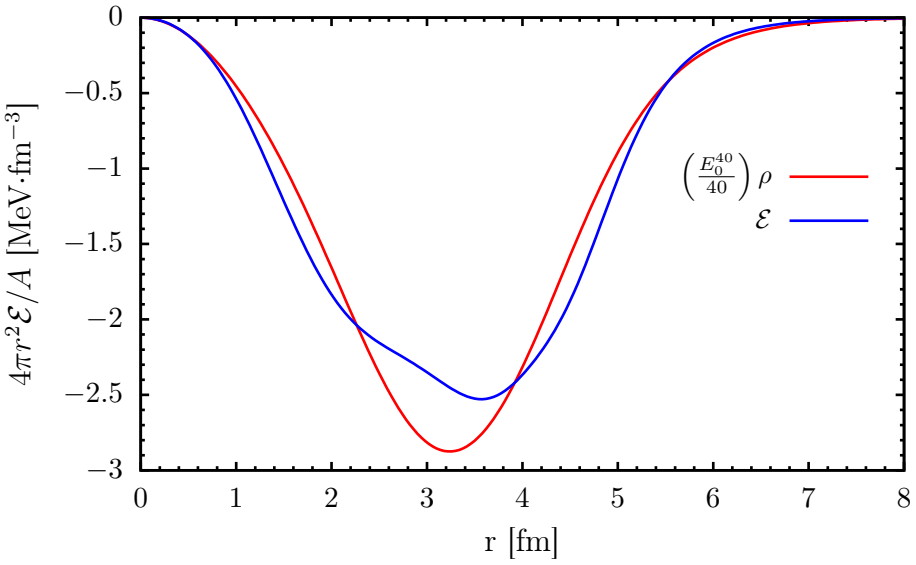

Figure 5.2: Comparison of the energy density of Eq. (5.5) (blue line) to the scaled nucleon density of Eq. (5.8) (red line) in ^{40}Ca.

In order to further explore the relationship between NM and the interior of the nucleus, the energy in the interior can be approximately calculated from the energy density using Eq. (5.8),

$$E(r) \approx \mathcal{E}(r)\left(\frac{A}{\rho}\right). \tag{5.9}$$

The approximation in Eq. (5.9) should be valid for small values of r, where the nuclear density is relatively constant and saturated (see Fig. 3.7). The energy in the interior of ^{40}Ca

is displayed in Fig. 5.3. The NM points close to $r = 2$ fm correspond to nuclear saturation. The predicted energies using CD-Bonn and N3LO interactions are close to -16 MeV (a_V) while the energy from AV18 is significantly less bound. Note that neither the CD-Bonn nor the N3LO interactions reproduce the NM saturation density in Ref. [113]. With this in mind, the DOM predicts that the energy in the interior is significantly less bound than -16 MeV, with about a 1 MeV difference from the AV18 result at saturation.

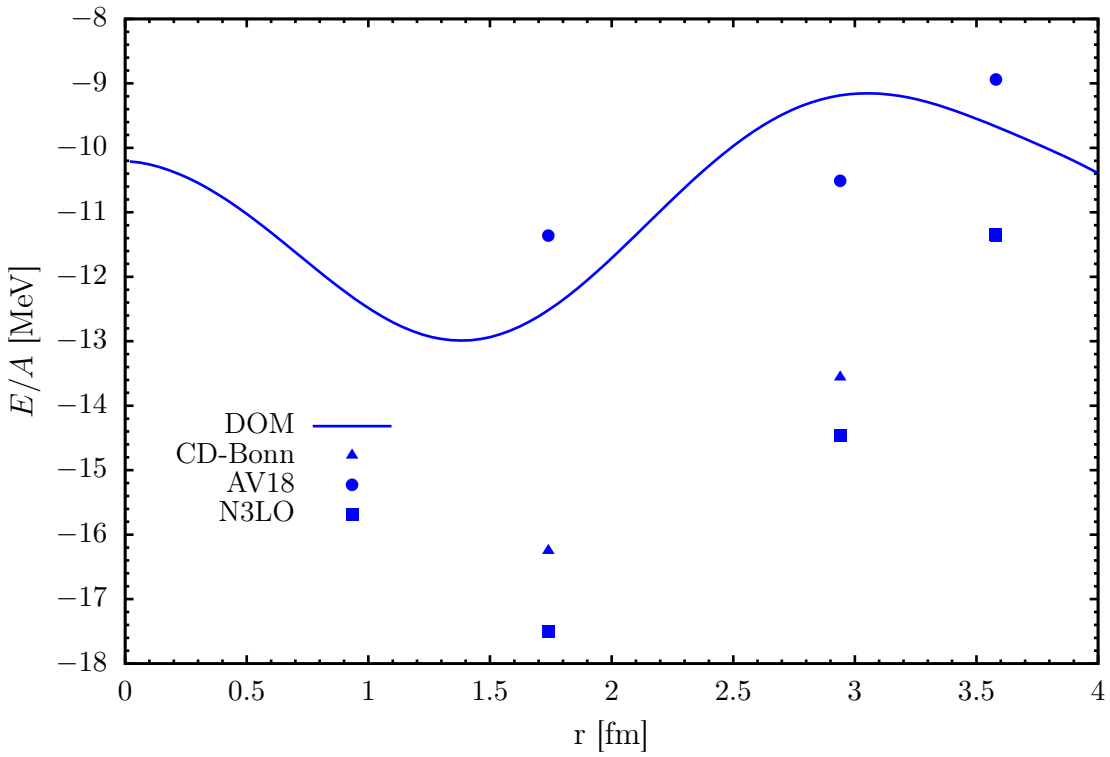

Figure 5.3: Binding energy as a function of radius in ^{40}Ca. The solid blue curve is the DOM energy. The points are SCGF NM calculations from Ref. [114].

The nuclear energy density can be further explored in ^{48}Ca and ^{208}Pb. Figure 5.4 shows the comparison of the calculated energy density (Eq. (5.5)) to the scaled energy density (Eq. (5.8)) for ^{48}Ca and ^{208}Pb, respectively. The agreement between Eq. (5.8) and Eq. (5.5) in ^{48}Ca and ^{208}Pb is comparable to that of ^{40}Ca, which is quantified with their rms radii listed in Table. 5.2. The case of ^{208}Pb is particularly interesting, because the interior is so

much larger than in ^{40}Ca and ^{48}Ca. This implies that finite-size (surface) effects are minimal in this region of ^{208}Pb, making it an ideal system to compare with NM. The trick of using isosopin symmetry to remove the effect of the Coulomb interaction on the energy density of ^{40}Ca is not valid in ^{208}Pb, since it has more neutrons than protons. Therefore, the Coulomb energy (E_C) must be explicitly subtracted from the ^{208}Pb binding energy, which can be calculated from the charge density,

$$E_C = \frac{1}{2}\int d^3r \rho_{\rm ch}(r) V_C(r), \tag{5.10}$$

where $V_C(r)$ is the Coulomb potential which is calculated from $\rho_{\rm ch}(r)$ in the usual way [33]. The Coulomb energy density, $\mathcal{E}_C(r)$, can be defined analogously to Eq (5.4). Using Eq. (5.10), $\mathcal{E}_C(r)$ can be subtracted from $\mathcal{E}(r)$ to remove the effects of the Coulomb interaction.

Table 5.2: Comparison of the rms radii of the energy densities of ^{40}Ca, ^{48}Ca, and ^{208}Pb.

	^{40}Ca	^{48}Ca	^{208}Pb
$r_{\mathcal{E}}$	3.480	3.673	5.270
r_{ρ}	3.477	3.665	5.672

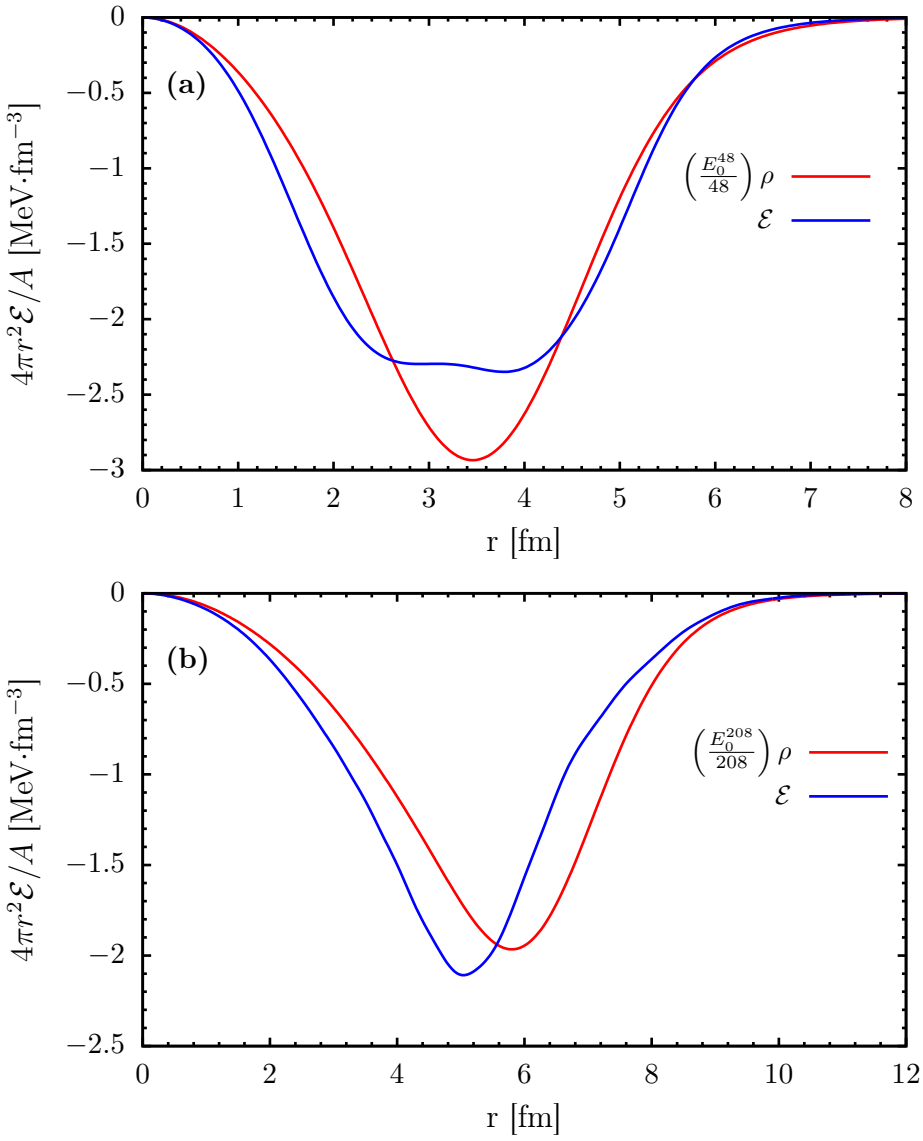

Figure 5.4: Comparison of the energy density of Eq. (5.5) (blue line) to the scaled nucleon density of Eq. (5.8) (red line) in (a) ^{48}Ca and (b) ^{208}Pb.

While removing $\mathcal{E}_C(r)$ from $\mathcal{E}(r)$ does provide a NM-like energy density, more steps need to be taken to compare with the NM calculations from Ref. [114]. An additional complication in comparing ^{208}Pb to NM is that the effect of the Coulomb potential is still reflected in the matter density of ^{208}Pb. So, the only way to truly compare to nuclear matter is to completely remove the Coulomb potential from the DOM self-energy. In doing this, the

quasihole energy levels become much more bound, which increases the number of protons. To account for this, ε_F is shifted such that it remains between the particle-hole gap of the protons in ^{208}Pb. This corresponds to a shift of 19 MeV. The resulting Coulomb-less matter distribution of ^{208}Pb is compared to the full matter distribution in Fig. 5.5. The Coulomb-less matter distribution is more concentrated in the core since there is no Coulomb repulsion. An interesting consequence of this is an increased neutron skin thickness of 0.38 fm.

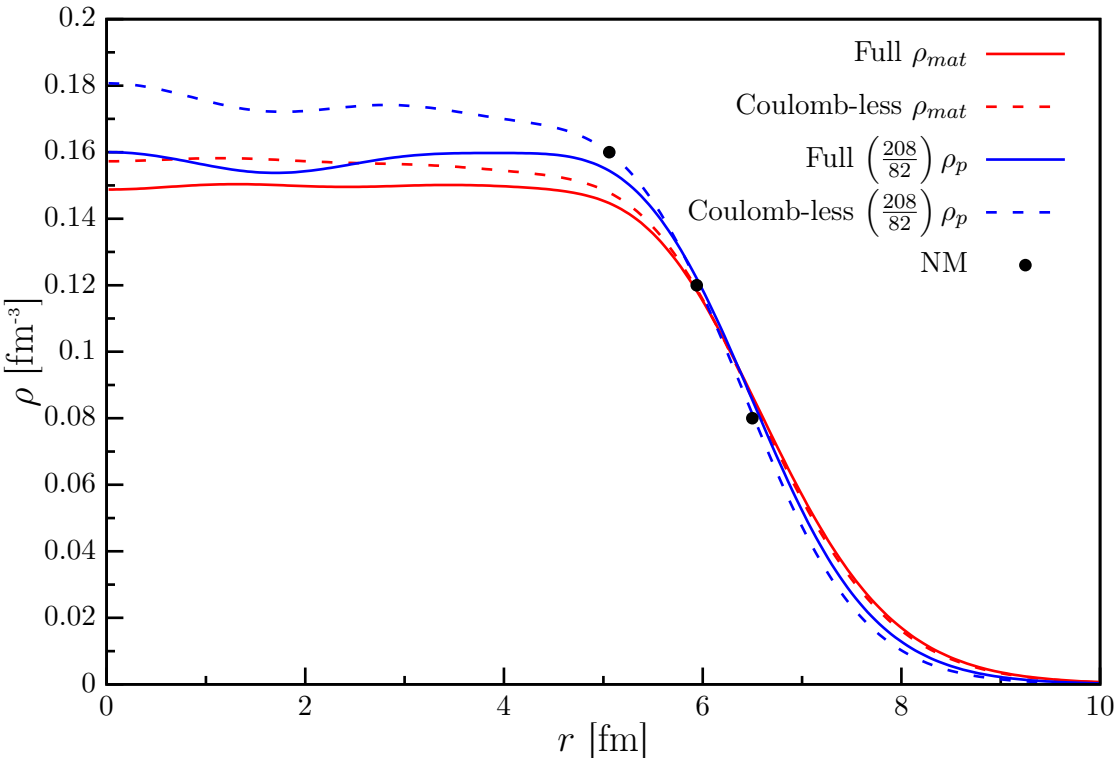

Figure 5.5: Matter distributions in ^{208}Pb. The solid red line is total matter distribution calculated from the full DOM self-energy. The dashed red line is the total matter density calculated from the DOM self-energy without the Coulomb potential. The solid blue line is the scaled proton matter distribution calculated from the full DOM self-energy. The dashed blue line is the scaled proton matter distribution calculated from the DOM self-energy without the Coulomb potential. The points indicate how the NM densities from Ref. [114] map to the Coulomb-less, scaled proton matter density.

Even with this modification, the Coulomb-less matter distribution still cannot be compared to the NM results since it never equals ρ_{sat} , as demonstrated by the dashed red curve

in Fig. 5.5. Since only the proton matter density is constrained by elastic electron scattering data, the total matter density has often been extrapolated from the proton matter density with a scaling of A/Z to account for the asymmetry [20]. This is applied to the Coulomb-less proton matter density in order to map the NM calculation from densities to coordinates. It is interesting that when Coulomb is removed, the scaled proton matter density shown in Fig. 5.5 has a value of 0.18 fm^{-3} rather than 0.16 fm^{-3} in the interior of ^{208}Pb.

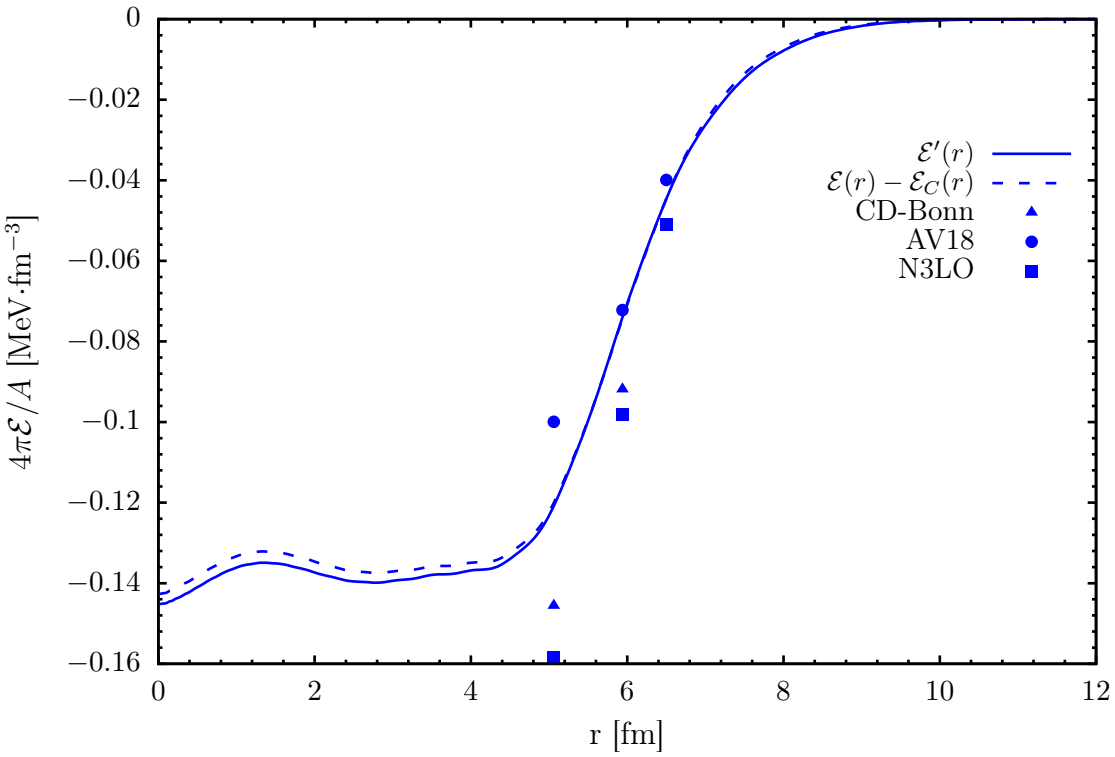

Figure 5.6: Modified energy density of ^{208}Pb. The solid blue curve is $\mathcal{E}'(r)$ calculated from the DOM self-energy with the Coulomb potential removed. The dashed blue curve is $\mathcal{E}(r)$ calculated from the full DOM self-energy with $\mathcal{E}_C(r)$ removed. The points are SCGF asymmetric NM calculations from Ref. [114].

Of course, the removal of V_C from Σ^* necessarily means that the resulting modified energy density, $\mathcal{E}'(r)$, calculated using Eq.(5.5) already has $\mathcal{E}_C(r)$ removed. This is demonstrated by the plot of $\mathcal{E}'(r)$ and $\mathcal{E}(r) - \mathcal{E}_C(r)$ in Fig. 5.6. Small differences in the two curves in Fig. 5.6 can be attributed to the differences in the matter distributions involved in calculated $\mathcal{E}(r)$

and $\mathcal{E}'(r)$. Note that the energy of ^{208}Pb is essentially constant up to 5 fm, indicative that finite-size effects are minimal in this region. Also included in Fig. 5.6 are the corresponding NM points. As seen in previous figures, the NM points calculated using AV18 are the closest to the DOM result. Even in the core of ^{208}Pb, where the larger core is a more ideal approximation of NM, the energy does not correspond to the canonical value for E_0, as shown in Fig. 5.7.

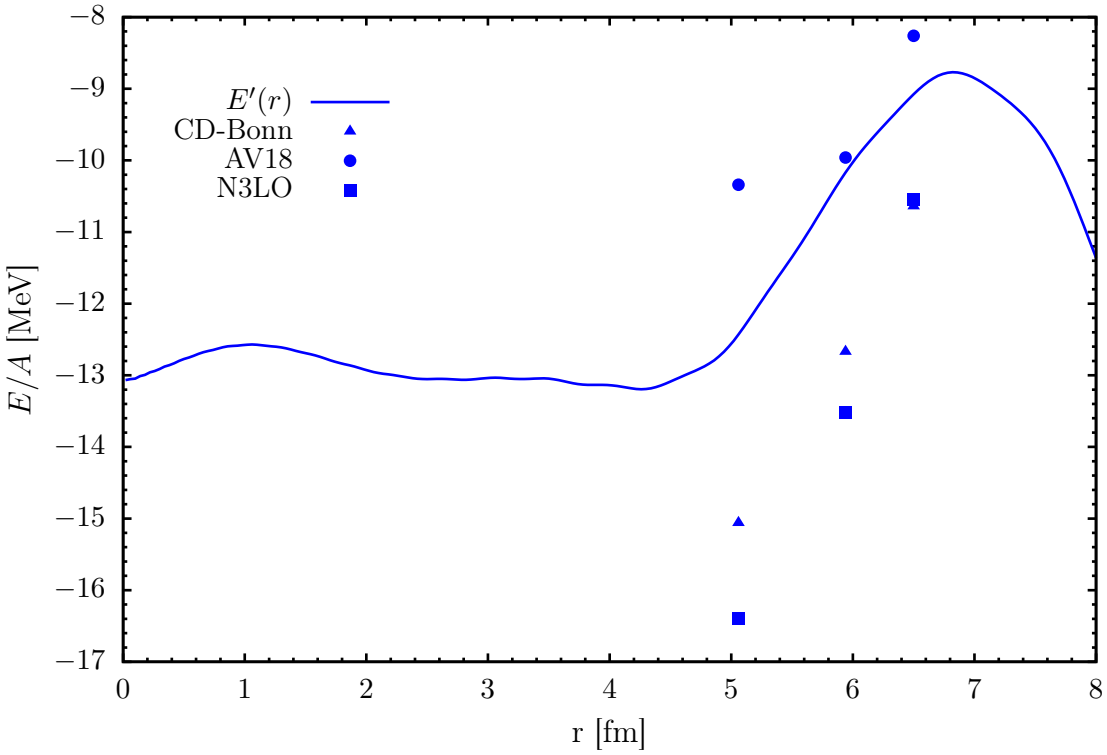

Figure 5.7: Binding energy as a function of radius in ^{208}Pb. The solid blue line is the energy of ^{208}Pb calculated using the DOM self-energy with the Coulomb potential removed. The points are SCGF asymmetric nuclear matter calculations from Ref. [114].

5.4 Conclusions

The binding energy density of ^{40}Ca, ^{48}Ca, and ^{208}Pb has been analyzed in the DOM framework. A comparison of the energy as a function of radius for all three nuclei is shown in

Fig. 5.8, where the Coulomb interaction has been removed from each nucleus. The energies in the core of each nucleus are all within 5 MeV of each other, all of which are significantly less bound than -16 MeV. Furthermore, Fig. 5.3 clearly shows that the core of the nucleus does not contribute to the total binding energy. The interpretation that the core of the nucleus is a close approximation to NM leads to the inevitable conclusion that the binding energy of NM at saturation is not necessarily -16 MeV. This is indeed puzzling when considering that the volume term is the only term in the empirical mass formula that is supposed to describe symmetric NM. Perhaps this means that the macroscopic description of nuclear binding energies in Eq. (5.6) is not a sufficient way to make a link to NM. One way to address this is to make use of the fact that the energy density tracks the matter density, as shown in Figs. 5.2, 5.4 and Eq. (5.8), and construct an alternate nuclear mass formula which depends on density and asymmetry rather than A and Z.

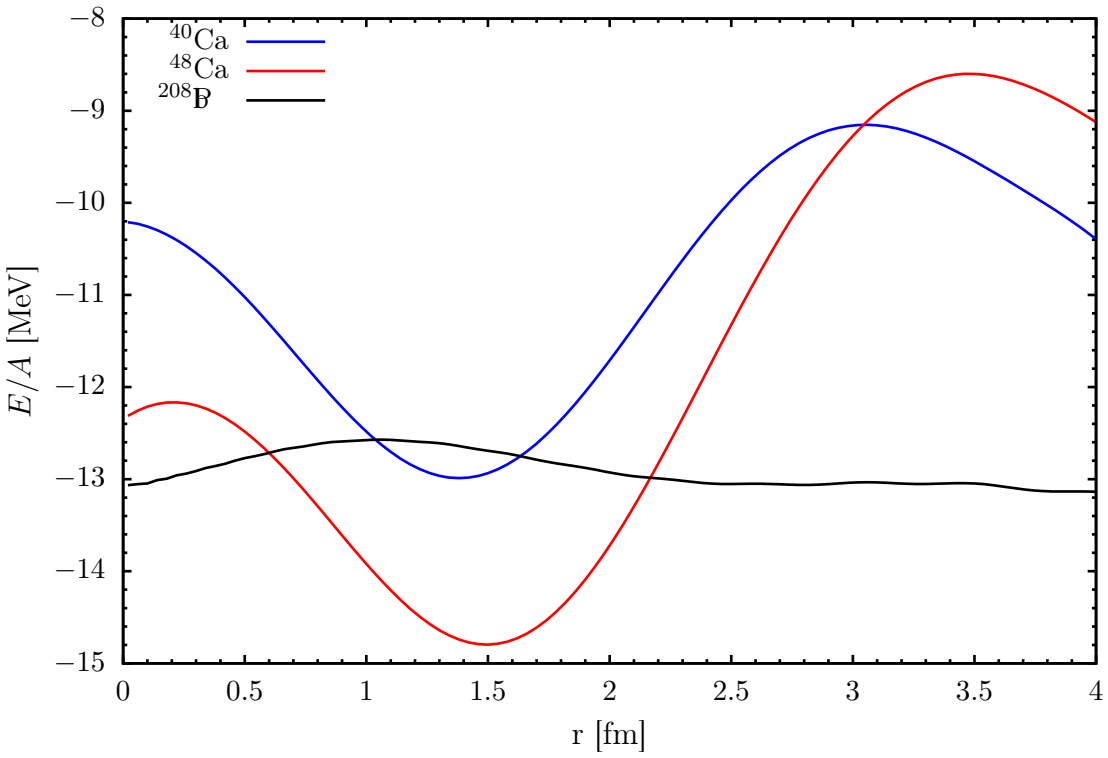

Figure 5.8: Binding energy as a function of radius in ^{40}Ca, ^{48}Ca, and ^{208}Pb.

Chapter 6

Momentum Distributions

6.1 Introduction

The mean-field description of the nucleus breaks down when the relative distance between two nucleons in the nucleus is less than 1.5 fm [123]. At these small distances, pairs of nucleons exhibit short-range correlations (SRC) due to the combination of the short-range repulsion and the attractive tensor force of the nucleon-nucleon potential. These SRCs give rise to high-momentum nucleon pairs which have been measured with inclusive (e, e') inelastic scattering by the Continuous Electron Beam Accelerator Facility (CEBAF) Large Acceptance Spectrometer (CLAS) collaboration at Jefferson Lab in ^{3}He, ^{4}He, ^{12}C, and ^{56}Fe [124]. A result of these measurements is that anywhere between $8\% - 27\%$ of nucleons in these nuclei have momenta larger than the Fermi momentum, $k_F = 1.4$ fm^{-1}. Realistic many-body calculations of low-A nuclei using variational Monte Carlo (VMC) techniques reveal that the majority of this high-momentum content comes from the tensor force in the nucleon-nucleon interaction [125]. This non-negligible fraction of high-momentum nucleons is further proof that there are correlations beyond the mean-field in nuclei. Correlations beyond the mean-

field are contained in the energy dependence of the hole spectral function, so it is natural to investigate the high-momentum content of ^{40}Ca, ^{48}Ca, and ^{208}Pb using the DOM propagator.

The momentum distribution, $n(k)$, is the diagonal part of the density matrix in momentum space, which can be calculated by Fourier transforming the one-body density matrix (Eq. (2.63)) from configuration space,

$$n(k,k') = \frac{2}{\pi}\sum_{\ell j}^{\infty}(2j+1)\int_0^\infty dr r^2 \int_0^\infty dr' r'^2 j_\ell(kr)\rho_{\ell j}(r,r')j_\ell(k'r'), \tag{6.1}$$

where the Fourier transform has been decomposed into partial waves using spherical Bessel functions. Note the importance of the off-diagonal elements of the density matrix in configuration space. An equivalent method of calculating the momentum distribution is to solve the Dyson equation in momentum space. Either way, the momentum distribution comes from an integral over energy of the hole spectral function.

6.2 High-Momentum Content of ^{40}Ca

The momentum distribution of ^{40}Ca calculated from the DOM self-energy is displayed in Fig. 6.1. The solid lines are found from the full DOM density matrix using Eq. (6.1). The dashed line corresponds to a mean-field result obtained by approximating the spectral function with the quasihole wave functions (normalized to one) for the occupied orbitals according to the IPM picture of ^{40}Ca. This Hartree-Fock-like (HF) momentum distribution has a high-momentum tail that dies very quickly for $k > k_F$, indicative that SRCs cannot be described by mean-field theories. On the other hand, the full DOM calculation has a significant high-momentum tail. The fraction of high-momentum protons and neutrons corresponds to 14.0% and 14.6% in ^{40}Ca, respectively. Since there is more high-momentum content in the DOM distribution, the HF-like distribution must be larger in the low-momentum region ($k < k_F$)

in order to conserve particle number (see Fig. 6.1).

The difference between the HF-like distribution and the DOM distribution arises from the spectral function. Specifically, the high-momentum content is caused by strength in the spectral function at energies in the continuum (far away from the quasihole energies). This can be seen in Fig. 3.8, which clearly shows non-negligible strength at energies far from the quasihole energies. Since the high-momentum content is determined by the distribution of energy in the spectral function, it is best constrained by particle number, the charge density, and the binding energy. Particle number comes from the 0^{th} energy-weighted moment of the spectral function (see Eq. (2.63)). This sum rule constrains the total strength below ε_F, but not how it is distributed over energy. The binding energy comes from the 1^{st} energy-weighted moment of the spectral function, Eq. (5.3), which is much more sensitive to the distribution of strength over energy of the spectral function. More strength at the large negative energies (continuum energies) will lead to more binding as well as more high-momentum content. Since the experimental binding energy of ^{40}Ca is well reproduced in Table 5.1, the high-momentum content is constrained to the furthest extent it can be done in the current implementation of the DOM. In order to further constrain high-momentum content, high-momentum $(e, e'p)$ data can be used as discussed in Ref. [80]. The DOM prediction for the percent of protons with high-momentum content in ^{40}Ca is roughly 14.0% and 14.6% for neutrons. While the bulk of this high-momentum content must be caused by SRCs, there is no way of distinguishing how much is due to other many-body correlations, or long-range correlations (LRC) associated with collective surface vibrations and giant resonances [63]. The small difference between the proton and neutron high-momentum content in the case of ^{40}Ca can be attributed to the Coulomb repulsion of the protons.

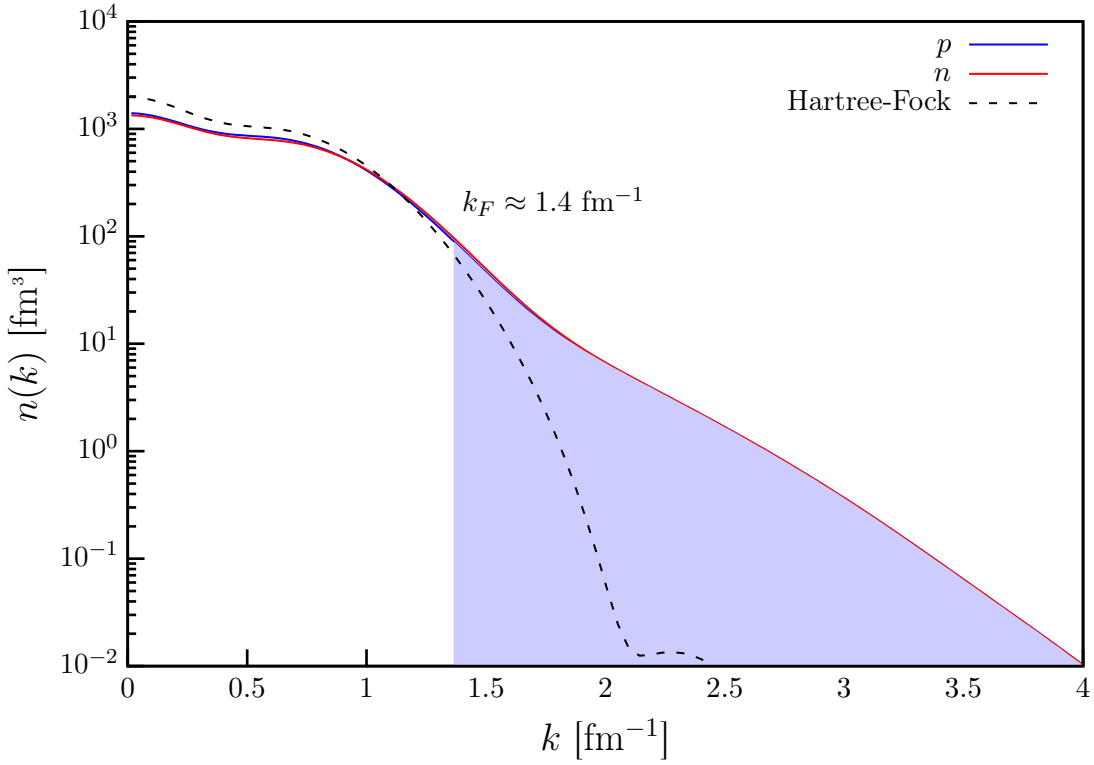

Figure 6.1: DOM calculated momentum distribution of protons (blue line) and neutrons (red line) in ^{40}Ca. The dashed line is a Hartree-Fock-like result obtained from the DOM (see main text). The blue shaded region corresponds to high-momentum content ($k > k_F$). This corresponds to 14.0% high-momentum protons and 14.6% high-momentum neutrons.

6.3 Asymmetry Dependence of High-Momentum Content

It was stated earlier that a large portion of high-momentum content is caused by the tensor force in the nucleon-nucleon interaction. In particular, the tensor force preferentially acts on pairs of neutrons and protons (np pairs) with total spin $S = 1$. This phenomenon is known as np dominance [126], and is demonstrated by a factor of 20 difference between the number of observed np SRC pairs and the number of observed pp and nn SRC pairs in exclusive $(e, e'pp)$ and $(e, e'p)$ cross section measurements of ^{12}C, ^{27}Al, ^{56}Fe, and ^{208}Pb [126].

The mechanism for this *np* dominance in nuclei can be understood by considering the bound state of the 2-body *n*-*p* system, the deuteron. The total angular momentum and parity of the deuteron has been measured to be $J^\pi = 1^+$ [126]. Positive parity means that the orbital angular momentum of the pair, L, must be even, which necessarily means that $S = 1$ and $L = 0, 2$ in order to have $J = 1$, where S is the total spin of the pair. Now that S and L are known, the total isospin of the deuteron can be determined by considering the general structure of a two-particle state. Since nucleons are fermions, a two-particle state must be antisymmetric, which implies that [20]

$$(-1)^{L+S+T} = -1, \tag{6.2}$$

where T is the total isospin of the pair. Combining what is known about S and L with the condition in Eq. (6.2) leads to the fact that $T = 0$ for the deuteron. Thus, the deuteron is a linear combination of the $L = 0$ and $L = 2$ states with $T = 0$. The corresponding spectroscopic notations [20] of these states is ${}^3S_1$ and ${}^3D_1$, respectively.

Now, the tensor force in the nucleon-nucleon interaction can be written as a scalar product of rank-2 spherical tensors

$$\hat{V}_T \propto \sqrt{24\pi}\left[[\hat{\sigma}_1 \otimes \hat{\sigma}_2]^{(2)} \otimes \hat{Y}^{(2)}\right]_0^{(0)}, \tag{6.3}$$

where $\hat{\sigma}_1$ and $\hat{\sigma}_2$ are rank-1 spherical tensors comprised of the Pauli spin matrices acting on the spin of particle 1 and 2, respectively, $[\hat{\sigma}_1 \otimes \hat{\sigma}_2]^{(2)}$ is the coupling of these rank-1 spherical tensors to a rank-2 spherical tensor, and $\hat{Y}^{(2)}$ is the 2^{nd}-order spherical harmonic acting as a rank-2 spherical tensor [1]. While $\hat{V}_T$ cannot connect two-particle states of different total angular momentum J, $Y^{(2)}$ in Eq. (6.3) can connect states with different L, differing by up to two units of L,

$$\langle TJ(LS)|\hat{V}_T|TJ(L'S)\rangle \implies \boldsymbol{L'} = \boldsymbol{L} + \boldsymbol{2},$$

keeping in mind that this is vector addition. Also noting that the nucleon-nucleon interaction conserves parity,

$$\langle TJ(LS)|\hat{V}_{NN}|TJ(L'S)\rangle \implies (-1)^L = (-1)^{L'},$$

restricts the value of L' such that

$$L' = \begin{cases} L \\ \\ L \pm 2 \end{cases}$$

This means that the tensor force couples the $^3S_1$ and the $^3D_1$ states, resulting in the binding of the deuteron [2]. The $^3D_1$ component of the deuteron wave function is responsible for the high-momentum tail of the deuteron momentum distribution [125]. Thus, without the tensor coupling between these two states in the deuteron, there would be a reduced high-momentum tail solely due to central correlations associated with the repulsive core. Pairs of nucleons within a nucleus can be analyzed in a similar manner, leading to the conclusion that the high-momentum tail onset by the tensor force coupling is dominated by nucleon pairs with $S = 1$ and $T = 0$ (np dominance) [126, 127].

The dominance of np SRC pairs would imply that that the number of high-momentum protons observed in a nucleus is dependent on how many neutrons it contains. More specifically, one would expect that the high-momentum content of protons would increase with neutron excess since there are more neutrons available to make np SRC pairs. The CLAS collaboration confirmed this asymmetry dependence by measuring the high-momentum content of protons and neutrons from $(e, e'p)$ and $(e, e'n)$ cross section measurements in ^{12}C, ^{27}Al, ^{56}Fe, and ^{208}Pb [128].

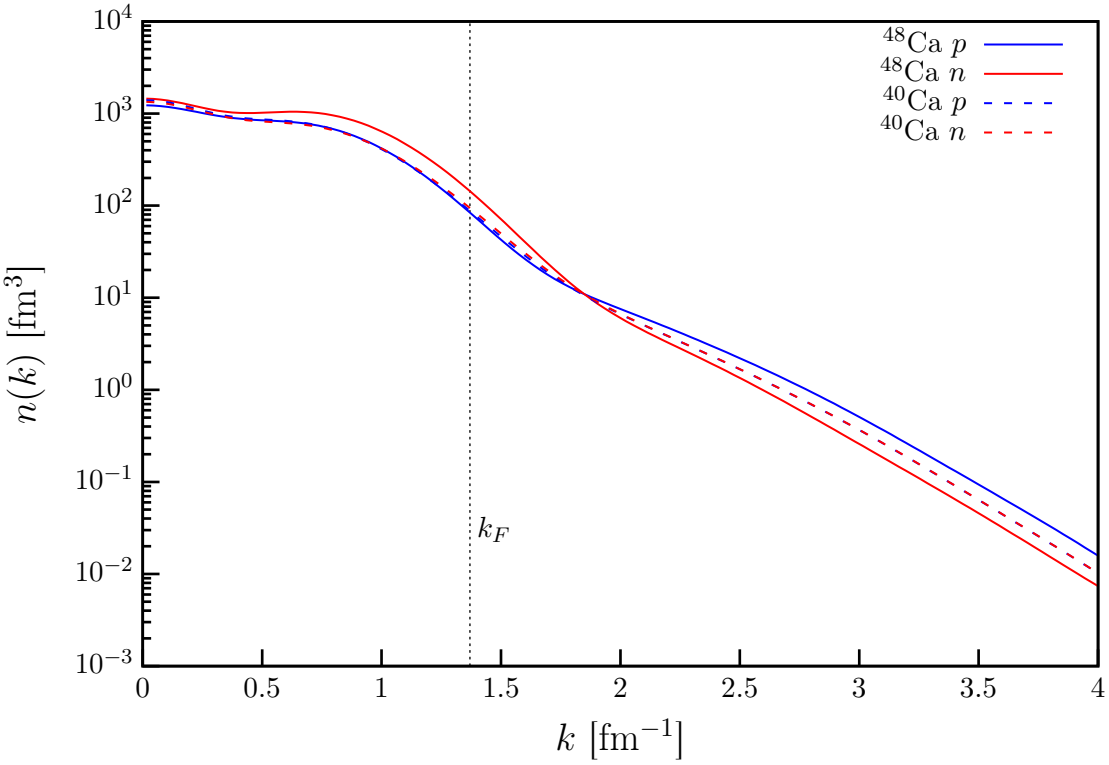

Figure 6.2: Comparison of DOM calculated momentum distributions of protons (blue) and neutrons (red) in ^{48}Ca (solid) and ^{40}Ca (dashed). The dotted line marks the location of k_F.

This effect can be studied by comparing the DOM generated momentum distributions for ^{40}Ca and ^{48}Ca, since the only difference between them is the eight additional neutrons in ^{48}Ca filling the $0f\frac{7}{2}$ shell. The momentum distributions for ^{40}Ca and ^{48}Ca are shown in Fig. 6.2. It is clear that the ^{48}Ca proton momentum distribution (solid blue line) has more high-momentum content than the ^{40}Ca proton momentum distribution (dashed blue line). Furthermore, since the number of protons does not change between ^{40}Ca and ^{48}Ca, the added high-momentum content in the tail of ^{48}Ca is accounted for by a reduction of the distribution in the $k < k_F$ region. Turning now to the neutrons in Fig. 6.2, the ^{48}Ca momentum distribution is larger in magnitude than the ^{40}Ca distribution for $k < k_F$, which is not surprising since there are now 8 more neutrons which are dominated by low-momentum content. The high-momentum content of the neutrons in ^{48}Ca decreases to 12.6% from the 14.6% of ^{40}Ca.

Thus, the effects of the asymmetry of ^{48}Ca on high-momentum content are evident in the fact that there are now significantly more high-momentum protons than neutrons. Both the increase in proton high-momentum content and the decrease in neutron high-momentum content are consistent with the CLAS measurements of neutron-rich nuclei [128] and support the *np*-dominance picture.

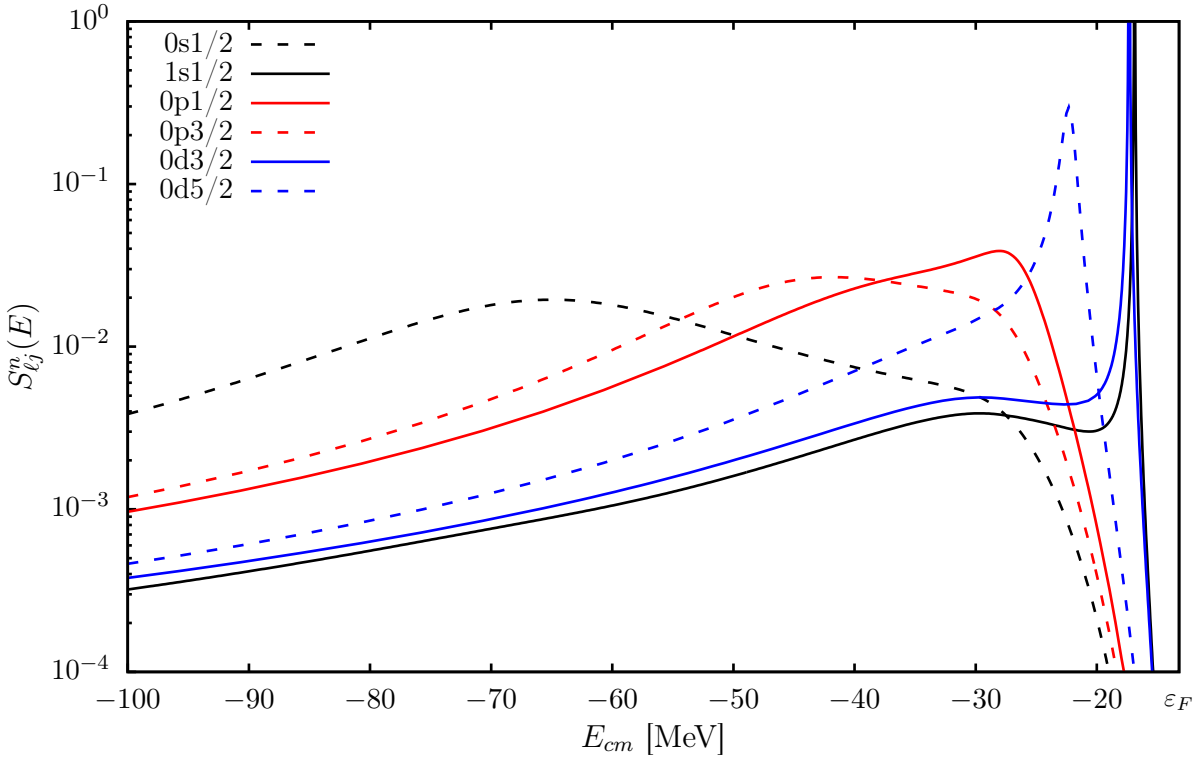

Figure 6.3: DOM generated proton spectral functions corresponding to the IPM orbitals in ^{48}Ca. Only the strength below ε_F is shown, since this is what contributes to the momentum distribution. For clarity, $S^n_{\ell j}(E)$ is shown to $E_{cm} = -100$ MeV, but the calculation goes out to $E_{cm} = -300$ MeV and follows the same trend shown here.

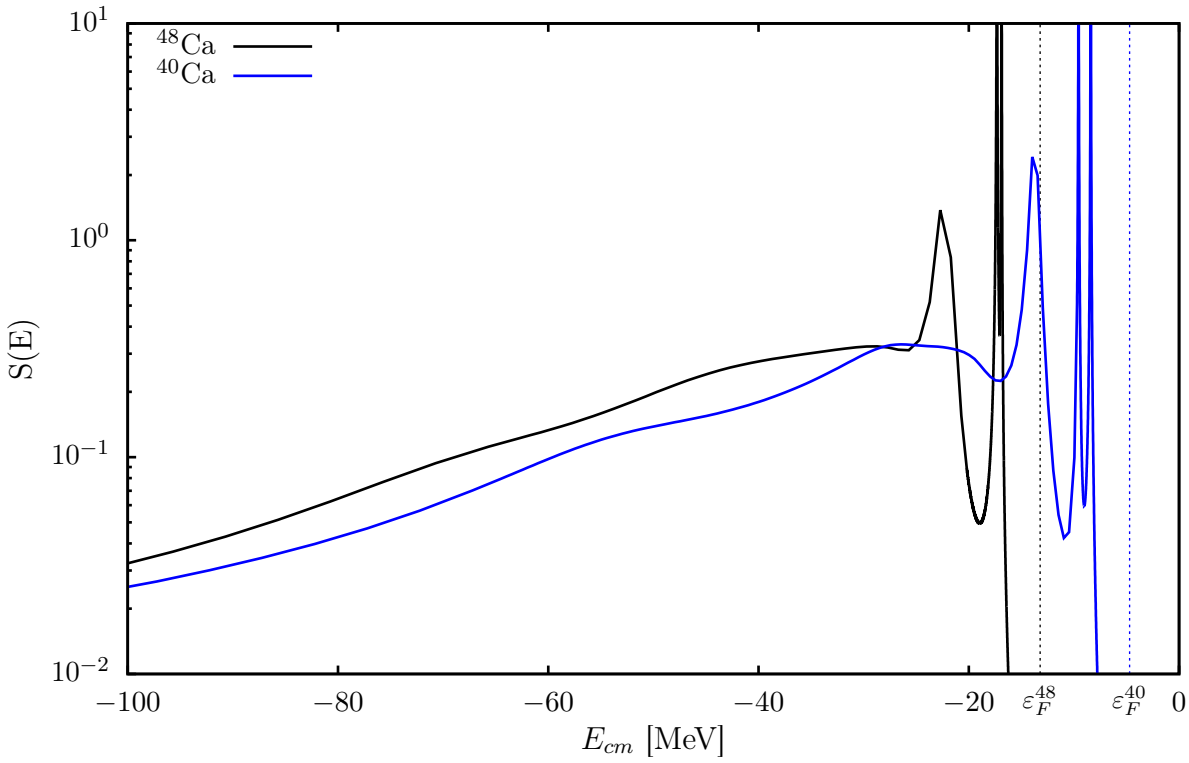

Figure 6.4: Comparison of the proton total spectral functions, calculated using Eq. (6.4), in ^{48}Ca (black line) and ^{40}Ca (blue line). The vertical dashed lines correspond to the Fermi energies for ^{48}Ca (black) and ^{40}Ca (blue). For clarity, this figure is cut at $E_{cm} = -100$ MeV, but the calculation goes out to $E_{cm} = -300$ MeV and follows the trend shown here. Only the strength below ε_F^{40} and ε_F^{48} (the contribution to the momentum distribution) is shown for $S(E)$ in ^{40}Ca and ^{48}Ca, respectively.

The increased proton high-momentum content in ^{48}Ca comes from having more strength in the continuum of the hole spectral function than in ^{40}Ca. The proton spectral functions for the mostly occupied orbitals in ^{48}Ca are shown in Fig. 6.3. Qualitatively, the spectral functions in Fig. 6.3 are very similar to the ^{40}Ca spectral functions in Fig. 3.8. To compare how strength is distributed over energy in ^{40}Ca and ^{48}Ca, the sum over all ℓj shells can be performed,

$$S(E) = \sum_{\ell j}^{\infty} (2j+1) S_{\ell j}(E), \tag{6.4}$$

where $S_{\ell j}(E)$ are defined in Eq. (3.14). The result of applying Eq. (6.4) to ^{40}Ca and ^{48}Ca

is shown in Fig. 6.4. It is clear from Fig. 6.4 that the spectral function of ^{48}Ca (black solid line) has more strength than that of ^{40}Ca at large negative energies. In order to conserve proton number, an increase in strength at continuum energies in $S(E)$ of ^{48}Ca must be compensated by a decrease in strength from energies close to the proton Fermi energy in ^{48}Ca. In particular, this manifests in the reduction of the spectroscopic factors of the $0d\frac{3}{2}$ and $1s\frac{1}{2}$ orbitals, before renormalization (see Eq. (3.16)), in ^{48}Ca from the values for ^{40}Ca to 0.60 and 0.64, respectively. This result is also qualitatively consistent with the systematic study done in Ref. [88] on spectroscopic factors obtained from various knockout reactions which showed that nuclei with larger asymmetry have quenched spectroscopic factors when compared to nuclei with less asymmetry, but not consistent with Ref. [129] and analogies of transfer reactions [19].

In order to further analyze these spectroscopic factors and explore their link with SRCs, the ^{48}Ca$(e,e'p)^{47}$K cross section is calculated following the same procedure detailed in Ch. 3 for ^{40}Ca. The experimental data of the ^{48}Ca$(e,e'p)^{47}$K reaction were obtained in parallel kinematics for outgoing proton kinetic energies of $T_p = 100$ MeV at Nikhef and previously published in Ref. [73]. Just as in Sec. 3.5, the DOM spectroscopic factors need to be renormalized by the experimental excitation spectra to account for the smearing of the DOM self-energy. The experimental excitation spectra for the $\ell = 0$ and the $\ell = 2$ excitations of ^{47}K are shown in Fig. 6.5, overlaid with the corresponding DOM spectral functions calculated from Eq. (3.15). Analogously to the ^{40}Ca calculation, the distributions in Fig. 6.5 are used to renormalize the DOM spectroscopic factors using Eq. (3.16). This scaling results in a reduction from 0.64 to 0.55 for the $1s\frac{1}{2}$ orbital and from 0.60 to 0.58 for the $0d\frac{3}{2}$ orbital. These values are in good agreement with originally published spectroscopic factors [73], as seen in Table 6.1.

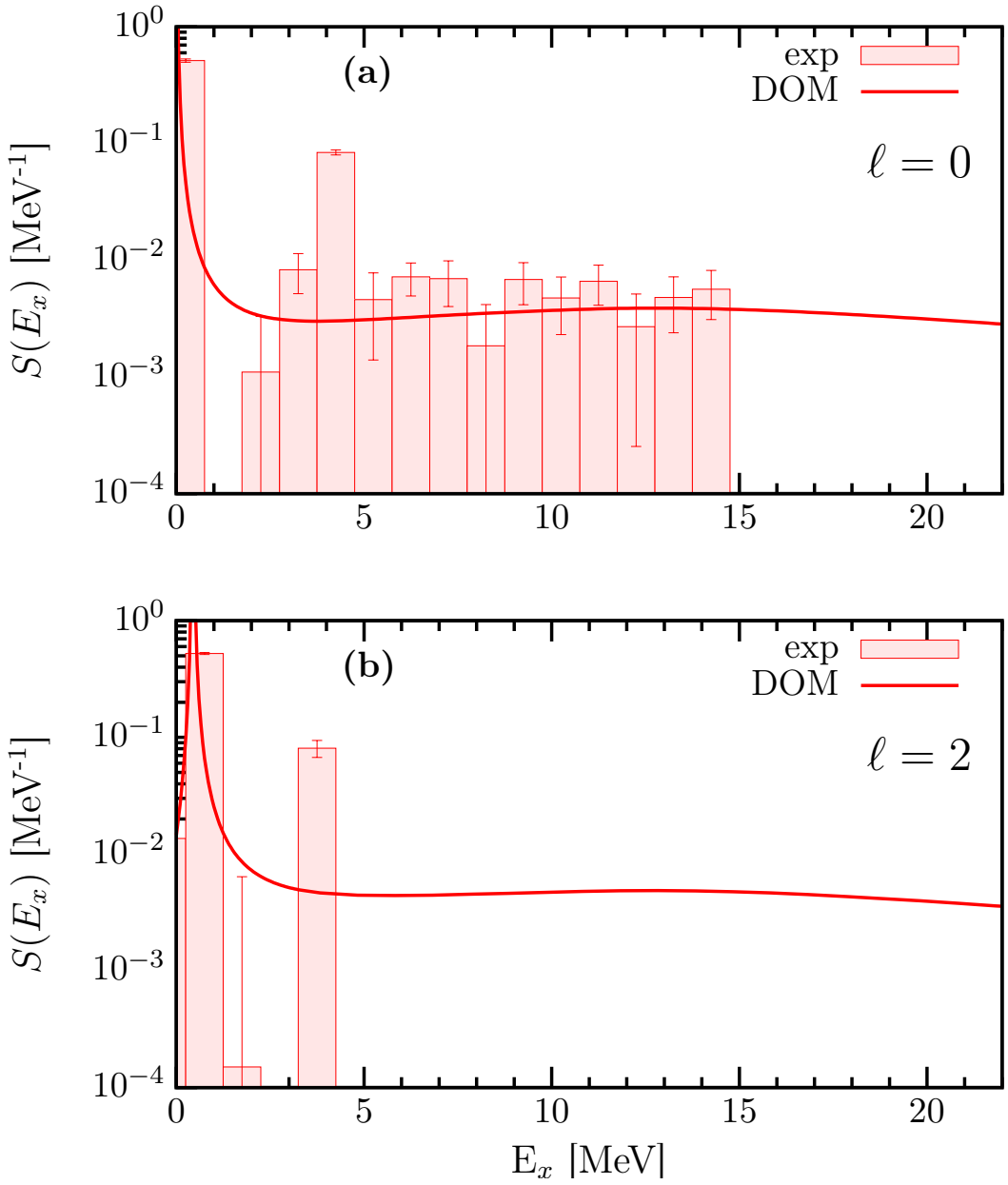

Figure 6.5: Spectral strength as a function of excitation energy in ^{48}Ca. The solid lines are DOM spectral functions for (a) the $1s\frac{1}{2}$ and (b) the $0d\frac{3}{2}$ proton orbitals. The histograms are the excitation energy spectra in ^{39}K extracted from the $^{48}\mathrm{Ca}(e,e'p)^{47}\mathrm{K}$ experiment [47, 73]. The peaks in the DOM curves and experimental data correspond to the quasihole energies of the protons in ^{40}Ca. The experimental spectrum in (b) is the isolated $0d\frac{3}{2}$ orbital.

Table 6.1: Comparison of spectroscopic factors in ^{48}Ca deduced from the previous analysis [73] using the Schwandt optical potential [77] to the normalization of the corresponding overlap functions obtained in the present analysis from the DOM including an error estimate as described in the text.

$\mathcal{Z}$	$0d\frac{3}{2}$	$1s\frac{1}{2}$
Ref. [73]	0.57 ± 0.04	0.54 ± 0.04
DOM	0.58	0.55

Using the resulting renormalized spectroscopic factors produces the momentum distributions shown in Fig. 6.6. Thus, the smaller spectroscopic factors in ^{48}Ca are consistent with the experimental cross sections of the $^{48}\mathrm{Ca}(e, e'p)^{47}\mathrm{K}$ reaction. The comparison of $\mathcal{Z}_{48}$ and $\mathcal{Z}_{40}$ in Table 6.2 reveals that while both orbitals experience a reduction, the $0d\frac{3}{2}$ shows a much larger quenching. This indicates that strength from the spectroscopic factors is pulled to the continuum in $S(E)$ when eight neutrons are added to ^{40}Ca. Thus, the quenching of the spectroscopic factor is a result of both the increased high-momentum content in ^{48}Ca, which is due to the increase in the amount of neutrons available to make np SRC pairs, and the stronger coupling to surface excitations in ^{48}Ca demonstrated by a larger proton reaction cross section in the energy range up to 50 MeV (see Figs. 3.3 and 4.2). In this way, the spectroscopic factor provides a link between these low-momentum knockout experiments done at Nikhef and the high-momentum knockout experiments done at JLAB by the CLAS collaboration. It is important to note how crucial the extrapolated high-energy proton reaction cross section data are in making these conclusions. Without them, there is no constraint for the strength of the spectral function at large positive energies, which could result in no quenching of the spectroscopic factors of ^{48}Ca due to the sum rule in Eq. (2.66).

Table 6.2: Comparison of DOM spectroscopic factors in ^{48}Ca and ^{40}Ca. These factors have been renormalized according to Eq. (3.16).

$\mathcal{Z}$	$0d\frac{3}{2}$	$1s\frac{1}{2}$
^{40}Ca	0.71 ± 0.04	0.60 ± 0.03
^{48}Ca	0.58	0.55

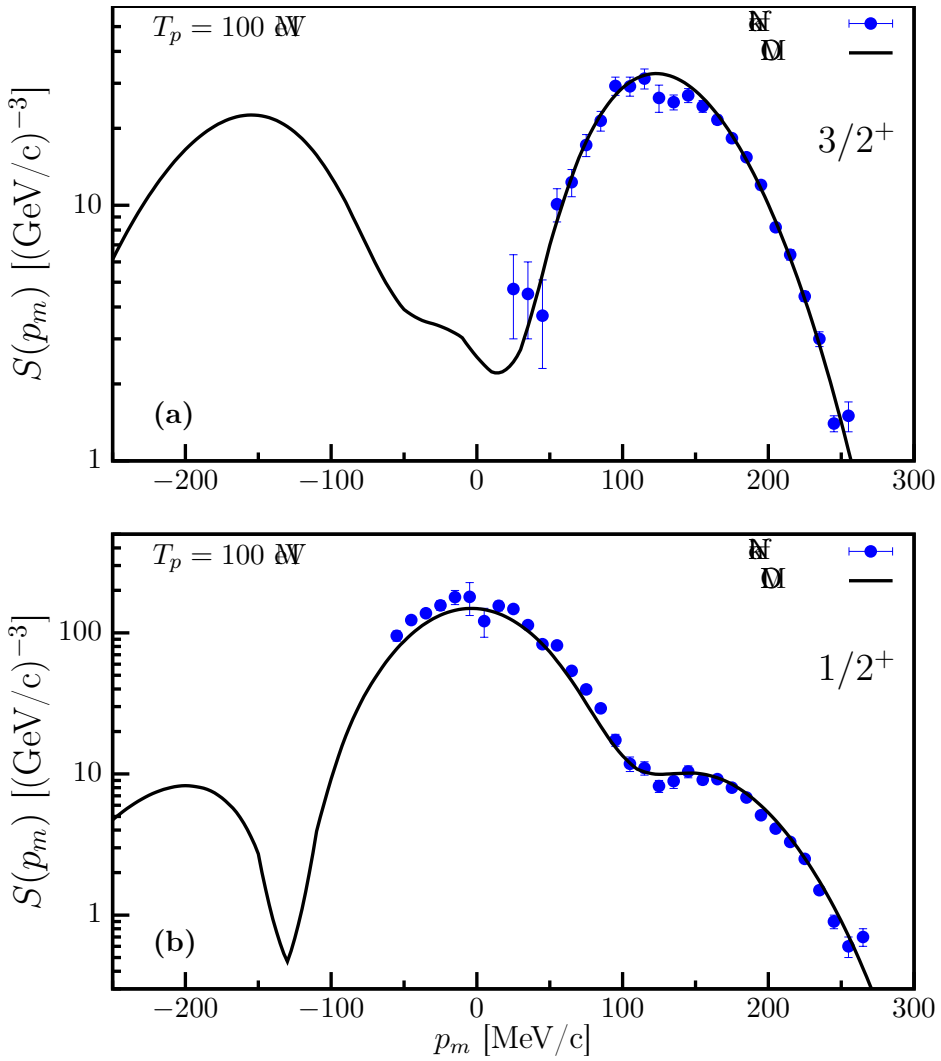

Figure 6.6: ^{48}Ca$(e,e'p)^{47}$K spectral functions in parallel kinematics at an outgoing proton kinetic energy of 100 MeV. The solid line is the calculation using the DOM ingredients, while the points are from the experiment detailed in [73]. (a) Distribution for the removal of the $0d\frac{3}{2}$. The curve contains the DWIA for the $3/2^+$ ground state including a DOM generated spectroscopic factor of 0.58. (b) Distribution for the removal of the $1s\frac{1}{2}$ proton with a DOM generated spectroscopic factor of 0.60 for the $1/2^+$ excited state at 2.522 MeV.

6.4 Conclusions

For completeness, the DOM generated momentum distributions for ^{208}Pb are shown in Fig. 6.7 with solid lines. The ^{208}Pb results in Fig. 6.7 indicate that the proton distribution (solid blue line) has more high-momentum content than the neutron distribution (solid red line). This is consistent with the ^{48}Ca results and the np dominance picture. Also included in Fig. 6.7 are the results for ^{40}Ca and ^{48}Ca. The shape of the high-momentum tail of each distribution is similar, which is consistent with the systematic study of these nuclei in Ref. [130]. This indicates that the mechanism behind SRC pairs is not strongly nucleus-dependent. The high-momentum fractions for protons and neutrons in these three nuclei are compared in Table 6.3. The fact that the high-momentum content in ^{208}Pb is less than in ^{40}Ca and ^{48}Ca points to the possibility that SRC pairs are influenced in a different way in heavier systems. It is important to remember that there is no way to separate the SRC contributions from LRC contributions to the high-momentum tail in the DOM, which could account for the reduction in ^{208}Pb. Also note that the high-momentum content is really only constrained by the DOM binding energy and particle number, so this is not a complete picture.

Table 6.3: Comparison of the DOM calculated high-momentum fraction ($k > k_F$) of ^{40}Ca, ^{48}Ca, and ^{208}Pb.

A	n_{high}	p_{high}
^{40}Ca	0.147	0.140
^{48}Ca	0.126	0.146
^{208}Pb	0.107	0.134

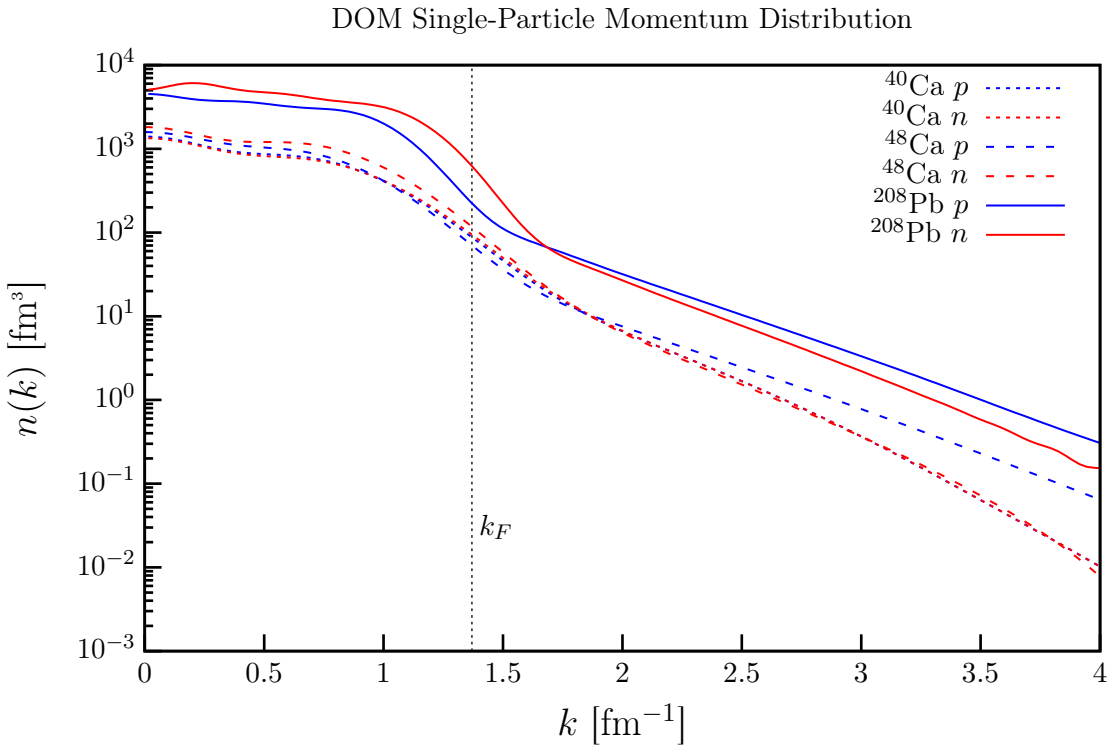

Figure 6.7: Comparison of DOM calculated momentum distributions of protons (blue) and neutrons (red) in ^{208}Pb (solid). Also included for comparison are the momentum distributions of ^{40}Ca (short-dashed lines) and ^{48}Ca (dashed lines). The dotted line marks the location of k_F.

Chapter 7

Conclusions and Outlook

Implications of fully nonlocal DOM self-energies have been presented for ^{40}Ca, ^{48}Ca, and ^{208}Pb. Constraining these self energies with experimental data at both positive and negative energies provides a complete picture of these nuclei. The distribution in strength over energy in the spectral functions of these nuclei provides insight into the many-body nature of each nucleus. The interplay between scattering states and bound states was first explored in the $^{40}\mathrm{Ca}(e, e'p)^{39}\mathrm{K}$ reaction. The ability to consistently provide the bound and scattering information for the DWIA calculation provided a platform for truly testing this approximation. This reaction mechanism is shown to be valid for outgoing proton kinetic energies around 100 MeV. The high-energy proton reaction cross section plays an important role in constraining spectroscopic factors involved in the DWIA calculation. This conclusion comes naturally in the DOM formulation, since the spectral function satisfies a sum rule (Eq. (2.66)) which links the strength of the spectral function at quasihole energies to the strength of the spectral function at energies that correspond to the high-energy proton reaction cross section. With the success of this analysis, it was natural to also calculate the $^{48}\mathrm{Ca}(e, e'p)^{47}\mathrm{K}$ cross section. The observed quenching of $\mathcal{Z}$ from ^{40}Ca to ^{48}Ca [88] is only realized in the DOM analysis

of $(e, e'p)$ if high-energy proton reaction cross section data points in ^{48}Ca are extrapolated from ^{40}Ca, since there are currently no measurements in this energy domain. This emphasizes the importance of measuring high-energy proton reaction cross section data, and in particular for ^{48}Ca which could in principle be done now with a stable ^{48}Ca target. With the construction of FRIB [23], radioactive isotope beams can be generated with energies conducive to measuring these high-energy proton reaction cross sections in inverse kinematics for more exotic nuclei. According to the conclusions from this DOM analysis, these inclusive measurements can serve to constrain more interesting exclusive reactions that are relevant in stellar processes [131].

In addition to verifying reaction mechanisms, the DOM analysis of these nuclei led to interesting conclusions about their structure. The solution of the Dyson equation (Eq. (2.70)) allows the calculation of single-particle distributions of each nucleus. Using these distributions, thick neutron skins are predicted in ^{48}Ca and ^{208}Pb. The thickness of these neutrons skins is shown to be sensitive to neutron total cross sections. This is another example of how important scattering data are for the description of nuclear structure.

Using DOM spectral functions, the binding energy density of each nucleus is calculated. These energy densities are considered well-constrained by the fact that the experimental binding energy is reproduced in the DOM fits. When viewing these energy densities, it becomes clear that the core of the nucleus does not significantly contribute to the total binding energy. Assuming that the interior of the nucleus corresponds to saturated infinite nuclear matter, this implies that the energy of nuclear matter at saturation is not necessarily constrained by the volume term of the empirical mass formula (Eq. (5.6)). The DOM prediction for the energy at nuclear saturation ranges from -10 MeV to -13 MeV, which is consistent with the SCGF calculations in NM using the well-constrained AV18 interaction [24, 113, 114]. This should bolster confidence in the APR EOS derived from the AV18 interaction since $E_0 = -12.6$ MeV [24] is an entirely reasonable value. This is evident in the

fact that predictions of neutron star structure using the APR EOS are consistent with all observations of neutron stars, including the recent neutron star merger event [24, 25].

Since these DOM generated energy densities have been shown to be consistent with nuclear matter calculations, this work will be continued with a study of the symmetry energy. In principle, with the energy densities of ^{40}Ca and ^{48}Ca, a prediction of the slope of the symmetry energy, L, could be made. This would complement the DOM predictions of the neutron skin, seeing as this density dependence gives rise to the positive neutron skin in asymmetric nuclei.

The last chapter before these conclusions addresses single-particle momentum distributions. It is the culmination of this entire thesis in that its conclusions rely on the results of all previous chapters. Correlations beyond the mean-field description of nuclei are contained in the continuum strength of the hole spectral function which manifests as a high-momentum tail of the single-particle momentum distributions. The reproduction of experimental binding energies and charge densities constrains this high-momentum tail. The DOM analysis predicts that all three nuclei have more than 10% high-momentum content. Moreover, the observation that the dominance of np SRC pairs causes an increase in proton high-momentum content in neutron-rich nuclei [128] is reproduced in the DOM single-particle momentum distributions of ^{208}Pb and ^{48}Ca. In the case of ^{48}Ca, this effect is further studied in the context of the low-momentum $^{48}\mathrm{Ca}(e, e'p)^{47}\mathrm{K}$ reaction. This analysis reveals that the quenching of spectroscopic factors is due not only to LRCs, but also to the increase in the number of np SRC pairs. A natural extension of this would be to analyze the $^{208}\mathrm{Pb}(e, e'p)^{207}\mathrm{Ti}$ reaction using the same framework.

APPENDICES

Appendix A

Scattering Theory

A.1 Elastic scattering

This section is intended to provide a brief overview of scattering from a spherically symmetric potential, for more details see [43]. The most general way to write the wave function representing the elastic scattering of a particle is

$$\psi_{\mathrm{el}}(\boldsymbol{r}) = \psi_{\mathrm{inc}}(\boldsymbol{r}) + \psi_{\mathrm{sc}}(\boldsymbol{r}),$$

where $\psi_{\mathrm{inc}}(\boldsymbol{r})$ is the incoming wave and $\psi_{\mathrm{sc}}(\boldsymbol{r})$ is the scattered wave. Now consider an incoming particle which can be described as a plane wave,

$$\psi_{\mathrm{inc}}(\boldsymbol{r}) = \phi_{\boldsymbol{k}}(\boldsymbol{r}) = e^{ikz} = \sum_{\ell=0}^{\infty}(2\ell+1)i^{\ell}j_{\ell}(kr)P_{\ell}(\cos(\theta)), \tag{A.1}$$

where the sum is over orbital angular momentum ℓ, $j_\ell(kr)$ is a spherical Bessel function, $P_\ell(\cos\theta)$ is a Legendre polynomial, and the z-direction is along the beam axis. It is useful to know the ℓ-decomposition of the plane wave in anticipation of scattering off a spherically

symmetric potential. Asymptotically, the spherical Bessel function is a superposition of incoming and outgoing spherical waves,

$$j_\ell(kr) \sim \frac{1}{2ikr}\left[e^{i(kr-\frac{1}{2}\ell\pi)} - e^{-i(kr-\frac{1}{2}\ell\pi)}\right] \qquad (r \to \infty). \tag{A.2}$$

Because total angular momentum is conserved, the scattered wave must have the same form as the incoming wave (Eq. (A.1)),

$$\psi_{\rm el}(r;k) = \sum_{\ell=0}^{\infty}(2\ell+1)i^\ell R_\ell(r;k)P_\ell(\cos\theta),$$

where $R_\ell(r;k)$ is a partial wave which solves the radial Schrödinger equation,

$$\frac{-\hbar^2}{2\mu}\frac{d^2}{dr^2}u_\ell(r) + \frac{\hbar^2\ell(\ell+1)}{2\mu r^2}u_\ell(r) + \int_0^\infty dr_1\mathcal{V}_\ell(r,r_1)u_\ell(r_1) = Eu_\ell(r), \tag{A.3}$$

where $u_\ell(r) = rR_\ell(r)$, and $\mathcal{V}_\ell(r,r_1) = rV_\ell(r,r_1)r_1$ is the potential. The incoming spherical wave cannot be changed by the interaction, but the outgoing wave can be altered. Thus, the asymptotic form of the partial wave is

$$R_\ell(r;k) \sim \frac{1}{2ikr}\left[S_\ell(k)e^{i(kr-\frac{1}{2}\ell\pi)} - e^{-i(kr-\frac{1}{2}\ell\pi)}\right] \qquad (r \to \infty), \tag{A.4}$$

where $S_\ell(k)$ is an amplitude that indicates the degree of scattering. Probability conservation implies the amplitude of the outgoing wave is less than or equal to that of the incoming wave,

$$|S_\ell(k)| \leq 1,$$

where $|S_\ell(k)| < 1$ corresponds to a loss of flux to inelastic processes. Combining Eqs. (A.4) and (A.2) leads to

$$\psi_{\rm sc}(r;k) \sim \frac{1}{2ik}\frac{e^{ikr}}{r}\sum_{\ell=0}^{\infty}(2\ell+1)i^\ell(S_\ell-1)P_\ell(\cos\theta).$$

So, the scattered outgoing wave can be expressed as an outgoing spherical wave altered by an amplitude such that

$$\psi_{\rm el}(\boldsymbol{r};k) \sim e^{ikz} + \frac{e^{ikr}}{r}f_{\rm el}(\theta;k), \tag{A.5}$$

where $f_{\rm el}$ is the elastic scattering amplitude,

$$f_{\rm el}(\theta;k) = \frac{1}{2ik}\sum_{\ell=0}^{\infty}(2\ell+1)i^\ell(S_\ell-1)P_\ell(\cos\theta).$$

The significance of $f_{\rm el}(\theta;k)$ becomes clear when considering the current density vector [41],

$$\begin{aligned}\boldsymbol{J}(\boldsymbol{r}) &= \frac{\hbar}{2mi}[\psi^*(\boldsymbol{r})\nabla\psi(\boldsymbol{r}) - (\nabla\psi(\boldsymbol{r}))^*\psi(\boldsymbol{r})] \\ &= \frac{\hbar\boldsymbol{k}}{m} + \frac{\hbar k}{m}\frac{\hat{\boldsymbol{r}}}{r^2}|f_{\rm el}(\theta;k)|^2 = \boldsymbol{J}_{\rm in} + \boldsymbol{J}_{\rm out},\end{aligned}$$

where Eq. (A.5) was inserted to find the asymptotic form of $\boldsymbol{J}(\boldsymbol{r})$. Considering that $\boldsymbol{J}_{\rm out}$ can be interpreted as the flux of scattered particles through a spherical surface element of very large radius which subtends the solid angle $(\Omega,\Omega + d\Omega)$ and $\boldsymbol{J}_{\rm in}$ is the incident flux [41], the scattering cross section can be calculated,

$$\sigma(\Omega) = \frac{\boldsymbol{J}_{\rm out}}{\boldsymbol{J}_{\rm in}} = |f_{\rm el}(\theta;k)|^2 d\Omega.$$

The elastic scattering cross section is an observable which links the formalism of quantum mechanics to experiment. Often, what is measured in experiment is the differential cross

section,

$$\frac{d\sigma}{d\Omega}(\theta) = |f_{\rm el}(\theta; k)|^2. \tag{A.6}$$

In typical scattering experiments, there are both elastic and inelastic processes. The total cross section, $\sigma_{\rm tot}$, is an experimental observable which is a measurement of scattering due to all elastic and inelastic processes. The total cross section can be calculated using the optical theorem [43],

$$\sigma_{\rm tot} = \frac{4\pi}{k}{\rm Im} f_{\rm el}(0; k). \tag{A.7}$$

Using the optical theorem, one can define the reaction cross section,

$$\sigma_{\rm react} = \sigma_{\rm tot} - \sigma_{\rm el} = \frac{\pi}{k^2}\sum_{\ell=0}^{\infty}(2\ell+1)(1-|S_\ell|^2). \tag{A.8}$$

The reaction cross section is a measure of inelastic scattering which is typically approximated by including an imaginary component to the potential to account for the loss of flux to other channels (see Sec. **??**). Note that when there is only elastic scattering, Eq. (A.8) evaluates to zero ($|S_\ell| = 1$).

The discussion up to this point has been the scattering of uncharged particles. To include charge, the Coulomb potential will be added to the scattering equation, Eq. (A.3). The Coulomb potential has infinite range [41], which changes the asymptotics of the problem. Instead of the incoming/outgoing wave functions behaving like spherical Bessel functions, they behave like Coulomb functions [43]. In fact, a more general form of the free radial Schrödinger equation can be written as

$$\frac{-\hbar^2}{2\mu}\frac{d^2}{dr^2}u_\ell(r) + \frac{\hbar^2\ell(\ell+1)}{2\mu r^2}u_\ell(r) + \frac{2k\eta}{r}u_\ell(r) = Eu_\ell(r), \tag{A.9}$$

where k is the wave number,

$$k = \frac{\sqrt{2mE}}{\hbar},$$

and η is the dimensionless Sommerfeld parameter

$$\eta = \frac{\mathrm{sgn}(Z)}{a_B k},$$

where a_B is the Bohr radius [36]. The general solutions to Eq. (A.9) are the regular and irregular Coulomb functions,

$$\tilde{F}_\ell(\eta, kr) = rF_\ell(\eta, kr) \qquad \tilde{G}_\ell(\eta, kr) = rG_\ell(\eta, kr). \tag{A.10}$$

When $\eta = 0$, Eq. (A.9) represents the scattering of a chargeless particle, and Eq. (A.10) reduces to regular and irregular Bessel functions. This changes the asymptotic form in Eq. (A.4), leading to an additional phase σ_ℓ known as the Coulomb phase, which is known analytically [43]. Not only does this change the form of the elastic scattering amplitude, but an additional Coulomb scattering amplitude must be included in the differential cross section,

$$\frac{d\sigma}{d\Omega}(\theta) = |f_C(\theta; k) + f(\theta; k)|^2.$$

For the remainder of this chapter, the Coulomb interaction will be omitted for simplicity.

For a different perspective, the Lippmann-Schwinger equation [43] can be used to show that the elastic scattering amplitude is a transition amplitude between the incoming plane wave and the stationary scattering wave function,

$$f_{\mathrm{el}}(\theta; k) = -\frac{4\mu\pi^2}{\hbar^2} \langle \phi_{\mathrm{in}} | V | \psi^{(+)} \rangle . \tag{A.11}$$

It is clear from Eq. (A.11) that $|f(\theta)|^2$ represents a transition probability which leads to the differential cross section. It is now convenient to introduce a matrix $\mathcal{T}$ such that [41]:

$$\langle \phi_{\text{in}} | \mathcal{T} | \phi_{\text{out}} \rangle \equiv \langle \phi_{\text{in}} | V | \psi^{(+)} \rangle , \tag{A.12}$$

where the plane waves ϕ_{in} and ϕ_{out} are of the same energy (on-shell). This leads to the following form of the elastic scattering amplitude,

$$f(\theta, k_0) = \frac{-4\mu\pi^2}{\hbar^2} \mathcal{T}(k_0, k_0; \theta),$$

where k_0 is used to indicate that this is an on-shell quantity. The relevance of the $\mathcal{T}$-matrix will be discussed further in Sec. 2.5.4.

A.2 Including spin

In order to describe the scattering of protons and neutrons, spin must be included in the formalism outlined in the previous subsection. As mentioned earlier, total angular momentum is conserved, so the inclusion of spin implies that the interaction of the projectile with the target can now involve spin flipping or the exchange of orbital angular momentum provided the total angular momentum remains the same [31]. The scattering analyzed in this thesis consists of nucleon-nucleus scattering where the ground state of the target nucleus is 0^+. Considering the fact that nucleons are fermions (spin-$\frac{1}{2}$), conservation of total angular momentum dictates that

$$\boldsymbol{J} = \boldsymbol{\ell} + \boldsymbol{s} = \boldsymbol{\ell}' + \boldsymbol{s}, \tag{A.13}$$

where $\boldsymbol{J}$ is the total angular momentum, $\boldsymbol{s}$ is the spin of the nucleon, and $\boldsymbol{\ell}$ and $\boldsymbol{\ell}$' are the orbital angular momenta of the nucleon before and after the collision with the nucleus. Since

nucleons are fermions (spin-$\frac{1}{2}$), Eq (A.13) allows the following values for ℓ',

$$\ell' = \begin{cases} \ell \pm 1 \\ \\ \ell \end{cases} .$$

Parity must also be conserved, therefore

$$\ell = \ell'. \tag{A.14}$$

This means that the interaction can only flip the spin of the nucleon. With this in mind, the elastic scattering amplitude in Eq. (A.5) can now be expressed as a 2×2 matrix in spin-space in the following way,

$$f_{m_s,m'_s}(k_0,\theta) = G(\theta)\mathbf{1} + H(\theta)\boldsymbol{\sigma}\cdot\hat{\boldsymbol{n}}, \tag{A.15}$$

where $\boldsymbol{\sigma} = (\sigma_x, \sigma_y, \sigma_z)$ is the Pauli spin matrix [43], and $\hat{\boldsymbol{n}}$ is the unit vector perpendicular to the scattering plane, $\boldsymbol{k} \times \boldsymbol{k'}$. It should be clear that f_{m_s,m'_s} is the amplitude for scattering from spin-state m_s to spin-state m'_s.

All calculations in this thesis are done in a total angular momentum basis. Thus, a basis transformation is necessary to get to an uncoupled basis in spin space,

$$f_{m_s,m'_s}(k_0,\theta) = \sum_{\ell m_\ell m'_\ell} \sum_{j m_j} Y_\ell^{m_\ell}(\theta,\phi) Y_\ell^{m'_\ell *}(0,0) \left\langle \ell m_\ell \frac{1}{2} m_s | j m_j \right\rangle \left\langle j m_j | \ell 0 \frac{1}{2} m'_s \right\rangle f_{\ell j}(k_0), \tag{A.16}$$

where complete sets of $|jm_j\rangle$ and $|\ell m_\ell\rangle$ have been inserted and $Y_\ell^{m_\ell}(\theta,\phi)$ is a spherical harmonic [40]. Note that the arguments leading up to Eq. (A.14) have already been applied to Eq. (A.16). Also, it is without loss of generality that the z-axis ($\theta = \phi = 0$) has been chosen for the direction of the second k_0 argument in Eq. (A.16). This is a convenient choice

since

$$Y_\ell^m(0,0) = \sqrt{\frac{2\ell+1}{4\pi}}\delta_{m,0},$$

and when combined with the rules of Clebsch-Gordan coefficients [43], simplifies Eq. (A.16) to

$$f_{m_s,m_s'}(k_0,\theta) = \frac{1}{4\pi}\sum_{\ell j}(2\ell+1)P_\ell(\cos\theta)e^{i(m_s'-m_s)\phi}\left\langle \ell(m_s'-m_s)\tfrac{1}{2}m_s \,|\, jm_s'\right\rangle \left\langle jm_s' \,|\, \ell 0\tfrac{1}{2}m_s'\right\rangle f_{\ell j}(k_0), \tag{A.17}$$

where the following identity has been used [30]:

$$Y_\ell^m(\theta,\phi) = (-1)^m\sqrt{\frac{2\ell+1}{4\pi}\frac{(\ell-m)!}{(\ell+m)!}}P_\ell^m(\cos\theta)e^{im\phi}.$$

To further simplify Eq. (A.17), noting that $j = \ell \pm \frac{1}{2}$, the relevant Clebsch-Gordan coefficients are

$$\begin{aligned}
\left\langle \ell 0\tfrac{1}{2}(\pm\tfrac{1}{2}) \,\middle|\, j\,\pm\tfrac{1}{2}\right\rangle &= \begin{cases} [(\ell+1)/(2\ell+1)]^{\frac{1}{2}}, & j = \ell+\frac{1}{2} \\ \mp[\ell/(2\ell+1)]^{\frac{1}{2}}, & j = \ell-\frac{1}{2} \end{cases} \\
\left\langle \ell\,(\pm 1)\tfrac{1}{2}(\mp\tfrac{1}{2}) \,\middle|\, j\,\pm\tfrac{1}{2}\right\rangle &= \begin{cases} [\ell/(2\ell+1)]^{\frac{1}{2}}, & j = \ell+\frac{1}{2} \\ \pm[(\ell+1)/(2\ell+1)]^{\frac{1}{2}}, & j = \ell-\frac{1}{2} \end{cases}
\end{aligned} . \tag{A.18}$$

According to Eq. (A.15), the direction of $\hat{\boldsymbol{n}}$ will affect what Pauli matrices contribute to the elastic scattering amplitude. Choosing $\boldsymbol{k}$ to be in the y-z plane will result in

$$f_{m_s,m_s'}(\theta;k_0) = \begin{pmatrix} G(\theta) & H(\theta) \\ H(\theta) & G(\theta) \end{pmatrix}.$$

From this, $G(\theta)$ and $H(\theta)$ can be calculated in the following way:

$$f_{\frac{1}{2},\frac{1}{2}}(k_0,\theta) = f_{-\frac{1}{2},-\frac{1}{2}}(k_0,\theta) = G(\theta)$$

$$f_{-\frac{1}{2},\frac{1}{2}}(k_0,\theta) = f_{\frac{1}{2},-\frac{1}{2}}(k_0,\theta) = H(\theta).$$

Plugging in the appropriate values for m_s and m_s' into Eq. (A.17), noting that $j = \ell \pm \frac{1}{2}$, and using the relations from Eq. (A.18) leads to

$$G(\theta) = \frac{i}{2k}\sum_{\ell=0}^{\infty}[(2\ell+1) - (\ell+1)S_\ell^+ - \ell S_\ell^-]P_\ell(\cos\theta)$$
$$H(\theta) = \frac{i}{2k}\sum_{\ell=1}^{\infty}(S_\ell^- - S_\ell^+)P_\ell^1(\cos\theta),$$

where the superscripts $\pm$ denote $j = \ell \pm \frac{1}{2}$. The differential cross section which does not distinguish between spin states is

$$\frac{d\sigma}{d\Omega} = \frac{1}{2s+1}\sum_{m_s m_s'}|f_{m_s m_s'}|^2 = |G(\theta)|^2 + |H(\theta)|^2.$$

The Analyzing power is

$$A_\theta = \frac{-2[f(\theta)+f_C(\theta)]g^*(\theta)}{|f(\theta)+f_C(\theta)|^2 + |g(\theta)|^2}. \tag{A.19}$$

A.3 Calculating the S-matrix

The matching radius used for ^{40}Ca is $a = 12$ fm. The scattering wave function, $u_{\ell j}(r)$, is asymptotic to phase-shifted Coulomb functions

$$u_{\ell j}(a) = C_\ell[\tilde{I}_\ell(ka) - S_{\ell j}\tilde{O}_\ell(ka)],$$

where $\tilde{O}_\ell$ is an outgoing wave multiplied by r (just like $u_{\ell j}(r)$)

$$\tilde{O}_\ell(kr) = rG_\ell(kr) + irF_\ell(kr),$$

and $\tilde{I}_\ell$ is an incoming wave multiplied by r

$$\tilde{I}_\ell(kr) = rG_\ell(kr) - irF_\ell(kr).$$

Using the definition of the R-matrix (Eq. (2.12)),

$$R_{\ell j} = \frac{u_{\ell j}(a)}{u'_{\ell j}(a)} = \frac{\tilde{I}_\ell(ka) - S_{\ell j}\tilde{O}_\ell(ka)}{\frac{d}{dr}\tilde{I}_\ell(kr)\Big|_{r=a} - S_{\ell j}\frac{d}{dr}\tilde{O}_\ell(kr)\Big|_{r=a}}. \tag{A.20}$$

Keeping in mind that

$$\frac{d}{dr}\tilde{O}_\ell(kr)\Big|_{r=a} = \frac{d(kr)}{dr}\frac{d}{d(kr)}\tilde{O}_\ell(kr)\Big|_{r=a} = \left(\frac{d(kr)}{dr}\right)\tilde{O}'_\ell\Big|_{r=a} = k\tilde{O}'_\ell(ka),$$

Eq. (A.20) becomes

$$S_{\ell j} = \frac{\tilde{I}_\ell(ka) - kR\tilde{I}'_\ell(ka)}{\tilde{O}_\ell(ka) - kR\tilde{O}'_\ell(ka)}.$$

Appendix B

Functional form and parametrization of the DOM

B.1 Symmetric Parametrization of ^{40}Ca

A detailed description of the parametrization of the proton and neutron self-energies of ^{40}Ca is presented. The functional forms of this subsection are used as the symmetric part of the self-energy for all nuclei. The forms are the same as those from the recent paper discussing $^{40}\mathrm{Ca}(e,e'p)^{39}\mathrm{K}$ [28]. With the exception of the Coulomb potential for protons, the entire DOM self-energy is nonlocal. The nonlocality for all parts of the self-energy is implemented as a Gaussian [34]. The self-energy is parametrized into the real HF term, real and imaginary spin-orbit terms, imaginary volume, and imaginary surface terms. In the following, the coulomb potential and the real spin-orbit terms are combined with the HF term,

$$\Sigma_{HF}(\boldsymbol{r},\boldsymbol{r}') = \Sigma^{nl}_{HF}(\boldsymbol{r},\boldsymbol{r}') + V^{nl}_{so}(\boldsymbol{r},\boldsymbol{r}') + \delta(\boldsymbol{r}-\boldsymbol{r}')V_C(r),$$

The Σ^{nl}_{HF} term is split into a volume and a narrower Gaussian term of opposite sign to make the final potential have a wine-bottle shape,

$$\Sigma^{nl}_{HF}\left(\boldsymbol{r},\boldsymbol{r'}\right) = -V^{vol}_{HF}\left(\boldsymbol{r},\boldsymbol{r'}\right) + V^{wb}_{HF}(\boldsymbol{r},\boldsymbol{r'}). \tag{B.1}$$

The volume term in Eq. (B.1) is given by

$$V^{vol}_{HF}\left(\boldsymbol{r},\boldsymbol{r'}\right) = V^{HF}\, f\left(\tilde{r}, r^{HF}_{(p,n)}, a^{HF}\right)\left[\frac{1}{1+x}H\left(\boldsymbol{s};\beta^{vol_1}\right) + \frac{x}{1+x}H\left(\boldsymbol{s};\beta^{vol_2}\right)\right], \tag{B.2}$$

where

$$\tilde{r} = \frac{r+r'}{2} \qquad\qquad \boldsymbol{s} = \boldsymbol{r} - \boldsymbol{r'},$$

and x is a weighting factor which allows for two different nonlocalities. With this notation, the wine-bottle (wb) potential is described by

$$V^{wb}_{HF}(\boldsymbol{r},\boldsymbol{r'}) = V^{wb}_{(p,n)}\exp\left(-\tilde{r}^2/(\rho^{wb})^2\right)H\left(\boldsymbol{s};\beta^{wb}\right), \tag{B.3}$$

where nonlocality is represented using a Gaussian,

$$H\left(\boldsymbol{s};\beta\right) = \exp\left(-\boldsymbol{s}^2/\beta^2\right)/(\pi^{3/2}\beta^3).$$

A standard Woods-Saxon radial form factor is employed,

$$f(r, r_i, a_i) = \left[1 + \exp\left(\frac{r - r_i A^{1/3}}{a_i}\right)\right]^{-1}.$$

The Coulomb term is obtained from the experimental charge density distribution for ^{40}Ca [33, 83].

The real part of the spin-orbit potential is represented as

$$V_{so}(\boldsymbol{r},\boldsymbol{r'}) = \left(\frac{\hbar}{m_\pi c}\right)^2 V^{so}\frac{1}{\tilde{r}}\frac{d}{d\tilde{r}}f(\tilde{r}, r^{so}_{(p,n)}, a^{so})\boldsymbol{\ell}\cdot\boldsymbol{\sigma}H(\boldsymbol{s};\beta^{so}), \tag{B.4}$$

where $(\hbar/m_\pi c)^2$=2.0 fm^2 as in Ref. [31, 82].

The imaginary part of the DOM self-energy has the following form,

$$\begin{aligned}\mathrm{Im}\Sigma(\boldsymbol{r},\boldsymbol{r}';E) = &-W^{vol}_{0\pm}(E)f\left(\tilde{r};r^{vol}_{\pm};a^{vol}_{\pm}\right)H\left(\boldsymbol{s};\beta^{vol}\right)\\ &+4a^{sur}W^{sur}_{\pm}(E)\,H\left(\boldsymbol{s};\beta^{sur}\right)\frac{d}{d\tilde{r}}f(\tilde{r},r^{sur}_{\pm},a^{sur}_{\pm})+\mathrm{Im}\Sigma_{so}(\boldsymbol{r},\boldsymbol{r}';E)\end{aligned} \tag{B.5}$$

Note that the parameters relating to the shape of the imaginary spin-orbit term are the same as those used for the real spin-orbit term. At energies well removed from ε_F, the form of the imaginary volume potential should not be symmetric about ε_F as indicated by the $\pm$ notation in the subscripts and superscripts [132]. While more symmetric about ε_F, a similar option is allowed for the surface absorption that is also supported by theoretical work reported in Ref. [133]. Allowing for the aforementioned asymmetry around ε_F, the following form was assumed for the depth of the volume potential [82]

$$W^{vol}_{0\pm}(E) = \Delta W^{\pm}_{NM}(E) + \begin{cases} 0 & \text{if } |E-\varepsilon_F| < \mathcal{E}^{vol} \\ A^{vol}\frac{\left(|E-\varepsilon_F|-\mathcal{E}^{vol}\right)^4}{\left(|E-\varepsilon_F|-\mathcal{E}^{vol}\right)^4+(B^{vol})^4} & \text{if } |E-\varepsilon_F| > \mathcal{E}^{vol}, \end{cases}$$

where $\Delta W^{\pm}_{NM}(E)$ is the energy-asymmetric correction modeled after nuclear matter calcu-

lations. The energy-asymmetric correction was taken as

$$\Delta W^{\pm}_{NM}(E) = \begin{cases} \alpha A^{vol}_{+}\left[\sqrt{E} + \frac{(\varepsilon_F+\mathbb{E}_+)^{3/2}}{2E} - \frac{3}{2}\sqrt{\varepsilon_F+\mathbb{E}_+}\right] & \text{for } E-\varepsilon_F > \mathbb{E}_+ \\ -A^{vol}_{-}\frac{(\varepsilon_F-E-\mathbb{E}_-)^2}{(\varepsilon_F-E-\mathbb{E}_-)^2+(\mathbb{E}_-)^2} & \text{for } E-\varepsilon_F < -\mathbb{E}_- \\ 0 & \text{otherwise.} \end{cases} \tag{B.6}$$

To describe the energy dependence of surface absorption, the form of Ref. [134] is employed,

$$W^{sur}_{\pm}(E) = \omega_4(E, A^{sur}, B^{sur_1}, 0) - \omega_2(E, A^{sur}, B^{sur_2}, C^{sur}), \tag{B.7}$$

where

$$\omega_n(E, A^{sur}, B^{sur}, C^{sur}) = A^{sur}\,\Theta(X)\,\frac{X^n}{X^n + (B^{sur})^n},$$

and $\Theta(X)$ is Heaviside's step function and $X = |E-\varepsilon_F| - C^{sur}$.

The imaginary spin-orbit term in Eq. (B.5) has the following form,

$$\mathrm{Im}\Sigma_{so}(E) = W_{so}(E)\left(\frac{\hbar}{m_\pi c}\right)^2 \frac{1}{\tilde{r}}\frac{d}{d\tilde{r}} f(\tilde{r}, r^{so}_{(p,n)}, a^{so})\frac{\boldsymbol{\ell}\cdot\boldsymbol{\sigma}}{|\boldsymbol{\ell}\cdot\boldsymbol{\sigma}|}H(\boldsymbol{s};\beta^{so}). \tag{B.8}$$

Note that the radial parameters for the imaginary component are the same as those used for the real part of the spin-orbit potential. The $\boldsymbol{\ell}\cdot\boldsymbol{\sigma}$ term is normalized in Eq. (B.8) in order to prevent $\mathrm{Im}\Sigma_{so}$ from growing with increasing ℓ. For large ℓ, this can lead to an inversion of the sign of the self-energy, which results in negative occupation. While the form of Eq. (B.8) suppresses this behavior, it is still not a proper solution. One must be careful that the magnitude of $W_{so}(E)$ does not exceed that of the volume and surface components. As the imaginary spin-orbit component is generally needed only at high energies, the form

of Ref. [82] is employed,

$$W^{so}(E) = A^{so}\frac{(E-\varepsilon_F)^4}{(E-\varepsilon_F)^4 + (B^{so})^4}. \tag{B.9}$$

All ingredients of the self energy have now been identified and their functional form described. The dynamic (energy-dependent) real part of the self-energy is then calculated using the subtracted dispersion relation in Eq. (2.72). The parameters used for the ^{40}Ca results in this thesis are displayed in Table B.1. There 30 Lagrange-Legendre and Lagrange-Laguerre grid points used in the ^{40}Ca calculations. For ^{40}Ca, the scaling parameter for the Lagrange-Laguerre mesh points is $a_L = 0.12$ (see Sec. 2.2.4). The matching radius used for scattering calculations is $a = 12$ fm (see Sec. 2.2.2).

B.2 Parametrization of Asymmetric Nuclei

The functional form for asymmetric nuclei is very similar to that of symmetric nuclei with some extensions to account for differences between protons and neutrons due asymmetry. In what follows, terms that are not changed from the corresponding symmetric nuclei are labeled with "*sym*" and are explained in Sec. B.1. Parameters which are allowed to be different for protons and neutrons will contain (n,p) terms. The new form of the Hartree-Fock term is

$$\begin{aligned} V_{HF}^{vol}(\boldsymbol{r},\boldsymbol{r}') = {} & V_{sym}^{HF} f\left(\tilde{r}, r_{(p,n)}^{HF}, a_{(p,n)}^{HF}\right)\left[\frac{1}{1+x_{sym}} H\left(\boldsymbol{s};\beta_{sym}^{vol_1}\right) + \frac{x_{sym}}{1+x_{sym}} H\left(\boldsymbol{s};\beta_{sym}^{vol_2}\right)\right] \\ & \pm V_{asy}^{HF}\frac{N-Z}{A} f\left(\tilde{r}, r_{(p,n)}^{HFaym}, a_{(p,n)}^{HFasy}\right) \\ & \times\left[\frac{1}{1+x_{sym}} H\left(\boldsymbol{s};\beta_{(p,n)}^{vol_1 asy}\right) + \frac{x_{sym}}{1+x_{sym}} H\left(\boldsymbol{s};\beta_{sym}^{vol_2 asy}\right)\right]. \end{aligned} \tag{B.10}$$

The spin-orbit term is the same as in Eq. (B.4) with some of the parameters now allowed to vary between neutrons and protons, see Table B.2.

Hartree-Fock

V^{HF} [MeV]	98.6	Eq. (B.2)
a^{HF} [fm]	0.67	Eq. (B.2)
β^{vol_1} [fm]	1.49	Eq. (B.2)
β^{vol_2} [fm]	0.73	Eq. (B.2)
x	0.91	Eq. (B.2)
V^{wb} [fm]	0.04	Eq. (B.3)
ρ^{wb} [fm]	0.69	Eq. (B.3)
β^{wb} [fm]	1.5	Eq. (B.3)

Spin-orbit

$V^{so}[MeV]$	12.9	Eq. (B.4)
a^{so} [fm]	0.75	Eq. (B.4)
β^{so} [fm]	0.79	Eq. (B.4)
A^{so} [MeV]	-1.17	Eq. (B.9)
B^{so} [MeV]	66.8	Eq. (B.9)

Volume imaginary

a_+^{vol} [fm]	0.66	Eq. (B.5)
β_+^{vol} [fm]	0.41	Eq. (B.5)
a_-^{vol} [fm]	0.26	Eq. (B.5)
β_-^{vol} [fm]	1.12	Eq. (B.5)
A_+^{vol} [MeV]	6.81	Eq. (B.1)
B_+^{vol} [MeV]	21.4	Eq. (B.1)
$\mathcal{E}_+^{vol}$ [MeV]	2.3	Eq. (B.1)
A_-^{vol} [MeV]	15.5	Eq. (B.1)
B_-^{vol} [MeV]	20.9	Eq. (B.1)
$\mathcal{E}_-^{vol}$ [MeV]	1.61	Eq. (B.1)
$\mathbb{E}_+$ [MeV]	23.3	Eq. (B.6)
$\mathbb{E}_-$ [MeV]	97.5	Eq. (B.6)
α	0.135	Eq. (B.6)

Surface imaginary

r_+^{sur} [fm]	1.10	Eq. (B.5)
a_+^{sur} [fm]	0.63	Eq. (B.5)
β_+^{sur} [fm]	1.71	Eq. (B.5)
r_-^{sur} [fm]	0.71	Eq. (B.5)
a_-^{sur} [fm]	0.74	Eq. (B.5)
β_-^{sur} [fm]	1.27	Eq. (B.5)
A_+^{sur} [MeV]	16.2	Eq. (B.7)
$B_+^{sur_1}$ [MeV]	4.52	Eq. (B.7)
$B_+^{sur_2}$ [MeV]	200	Eq. (B.7)
C_+^{sur} [MeV]	150	Eq. (B.7)
A_-^{sur} [MeV]	8.66	Eq. (B.7)
$B_-^{sur_1}$ [MeV]	14.4	Eq. (B.7)
$B_-^{sur_2}$ [MeV]	5.94	Eq. (B.7)
C_-^{sur} [MeV]	14.6	Eq. (B.7)

Table B.1: Fitted parameter values for proton and neutron potentials in ^{40}Ca. This table also lists the number of the equation that defines each individual parameter.

The imaginary self-energy now has additional asymmetric contributions,

$$\begin{aligned}\text{Im } \Sigma^{nl}(\boldsymbol{r},\boldsymbol{r}';E) = &-W_{0\pm}^{vol}(E) f\left(\tilde{r};r_{\pm(p,n)}^{vol};a_{\pm sym}^{vol}\right) H\left(\boldsymbol{s};\beta_{\pm sym}^{vol}\right) \\ &+ 4a_{sym}^{sur} W_{\pm}^{sur0}(E)\, H\left(\boldsymbol{s};\beta_{\pm sym}^{sur0}\right) \frac{d}{d\tilde{r}} f(\tilde{r},r_{\pm(p,n))}^{sur0},a_{sym}^{sur}) \\ &+ 4a_{(n,p)}^{sur} W_{\pm}^{sur}(E) H\left(\boldsymbol{s};\beta_{\pm(p,n)}^{sur}\right) \frac{d}{d\tilde{r}} f(\tilde{r},r_{\pm(p,n)}^{sur},a_{\pm(p,n)}^{sur}). \end{aligned} \tag{B.11}$$

In the energy dependence of the imaginary volume term, $A_{\pm(p,n)}^{vol}$ and $B_{\pm(p,n)}^{vol}$ from Eq. (B.1) are now allowed to vary between protons and neutrons. The energy dependence of the two surface terms in Eq. (B.11) is parametrized in the following way,

$$W_{\pm}^{sur0}(E) = \omega_4(E, A_{\pm sym}^{sur0}, B_{\pm sym}^{sur0_1}, 0) - \omega_2(E, A_{\pm sym}^{sur0}, B_{\pm sym}^{sur0_2}, C_{\pm sym}^{sur0}),$$

and

$$W_{\pm(p,n)}^{sur}(E) = \omega_4(E, A_{\pm(p,n)}^{sur}, B_{\pm(p,n)}^{sur_1}, 0) - \omega_2(E, A_{\pm(p,n)}^{sur}, B_{\pm(p,n)}^{sur_2}, C_{\pm(p,n)}^{sur}). \tag{B.12}$$

^{48}Ca Parameters

All parameters of the ^{48}Ca self-energy are listed in Table B.2. Note that the symmetric values are the same as those listed for ^{40}Ca in Table B.1. There 30 Lagrange-Legendre and Lagrange-Laguerre grid points used in the ^{48}Ca calculations. For ^{48}Ca, the scaling parameter for the Lagrange-Laguerre mesh points is $a_L = 0.15$ (see Sec. 2.2.4). The matching radius used for scattering calculations is $a = 12$ fm (see Sec. 2.2.2).

B.2.1 ^{208}Pb Parameters

The symmetric parameters are listed in Table B.2.1 while the asymmetric parameters are listed in Table B.4. There 30 Lagrange-Legendre and Lagrange-Laguerre grid points used

Table B.2: Fitted parameter values for proton and neutron potentials in ^{48}Ca. All symmetric values are taken from the ^{40}Ca values in Table B.1.

Hartree-Fock

	p	n	Eq.
V_{asy}^{HF} [MeV]	1.17	19.2	(B.10)
$r_{(p,n)}^{HF}$ [fm]	1.15	1.10	(B.10)
$r_{(p,n)}^{HFasy}$ [fm]	1.99	0.98	(B.10)
$a_{(p,n)}^{HFasy}$ [fm]	0.60	0.60	(B.10)
$\beta_{(p,n)}^{vol_1asy}$ [fm]	1.54	0.97	(B.10)
$\beta_{(p,n)}^{vol_2asy}$ [fm]	0.73	0.73	(B.10)
$V_{(p,n)}^{wb}$ [MeV]	2.58	0.04	(B.3)
$R_{(p,n)}^{wb}$ [MeV]	0.17	0.17	(B.3)
$\beta_{(p,n)}^{wb}$ [MeV]	0.62	0.62	(B.3)

Spin-orbit

$V_{(p,n)}^{so}$ [MeV]	11.5	11.5	(B.4)
$r_{(p,n)}^{so}$ [fm]	0.81	0.81	(B.4)

Volume imaginary

$V_{+(p,n)}^{vol}$ [MeV]	6.82	6.82	(B.1)
$V_{-(p,n)}^{vol}$ [MeV]	39.8	10.5	(B.1)
$B_{+(p,n)}^{vol}$ [MeV]	21.4	21.4	(B.1)
$B_{-(p,n)}^{vol}$ [MeV]	76.0	76.0	(B.1)
$r_{+(p,n)}^{vol}$ [fm]	1.36	1.36	(B.11)
$r_{-(p,n)}^{vol}$ [fm]	1.23	1.39	(B.11)
$\alpha_{(p,n)}$ [fm]	0.14	0.14	(B.11)

Surface imaginary

	p	n	Eq.
$\beta_{-(p,n)}^{sur}$ [fm]	2.38	1.27	(B.11)
$\beta_{+(p,n)}^{sur}$ [fm]	1.71	1.71	(B.11)
$A_{+(p,n)}^{sur}$ [MeV]	0.0	0.0	(B.12)
$A_{-(p,n)}^{sur}$ [MeV]	11.0	5.42	(B.12)
$B_{+(p,n)}^{sur_1}$ [MeV]	4.52	4.52	(B.12)
$B_{+(p,n)}^{sur_2}$ [MeV]	200	200	(B.12)
$C_{+(p,n)}^{sur}$ [MeV]	150	150	(B.12)
$B_{-(p,n)}^{sur_1}$ [MeV]	10.3	10.6	(B.12)
$B_{-(p,n)}^{sur_2}$ [MeV]	29.9	30.1	(B.12)
$C_{-(p,n)}^{sur}$ [MeV]	25.9	19.9	(B.12)
$r_{-(p,n)}^{sur0}$ [fm]	1.29	0.79	(B.11)
$r_{+(p,n)}^{sur0}$ [fm]	1.10	1.10	(B.11)
$r_{-(p,n)}^{sur}$ [fm]	0.54	0.51	(B.11)
$r_{+(p,n)}^{sur}$ [fm]	1.10	1.10	(B.11)
$a_{-(p,n)}^{sur}$ [fm]	0.60	0.60	(B.11)
$a_{+(p,n)}^{sur}$ [fm]	0.60	0.60	(B.11)

Hartree-Fock

V^{HF} [MeV]	94.0	Eq. (B.2)
a^{HF} [fm]	0.73	Eq. (B.2)
β^{vol_1} [fm]	1.52	Eq. (B.2)
β^{vol_2} [fm]	0.76	Eq. (B.2)
x	0.73	Eq. (B.2)
β^{wb} [fm]	0.64	Eq. (B.3)

Volume imaginary

a_+^{vol} [fm]	0.47	Eq. (B.5)
a_-^{vol} [fm]	0.23	Eq. (B.5)
$\mathcal{E}_+^{vol}$ [MeV]	16.4	Eq. (B.1)
$\mathcal{E}_-^{vol}$ [MeV]	5.24	Eq. (B.1)
$\mathbb{E}_+$ [MeV]	21.8	Eq. (B.6)
$\mathbb{E}_-$ [MeV]	81.1	Eq. (B.6)

Spin-orbit

a^{so} [fm]	0.70	Eq. (B.4)
β^{so} [fm]	0.83	Eq. (B.4)
A^{so} [MeV]	-3.65	Eq. (B.9)
B^{so} [MeV]	208	Eq. (B.9)

Surface imaginary

a_+^{sur} [fm]	0.43	Eq. (B.5)
β_+^{sur} [fm]	1.26	Eq. (B.5)
a_-^{sur} [fm]	0.55	Eq. (B.5)
β_-^{sur} [fm]	1.50	Eq. (B.5)
A_+^{sur} [MeV]	44.2	Eq. (B.7)
$B_+^{sur_1}$ [MeV]	17.4	Eq. (B.7)
$B_+^{sur_2}$ [MeV]	24.8	Eq. (B.7)
C_+^{sur} [MeV]	14.0	Eq. (B.7)
A_-^{sur} [MeV]	12.6	Eq. (B.7)
$B_-^{sur_1}$ [MeV]	15.0	Eq. (B.7)
$B_-^{sur_2}$ [MeV]	80.2	Eq. (B.7)
C_-^{sur} [MeV]	0.95	Eq. (B.7)

Table B.3: Fitted parameter values for the symmetric part of the ^{208}Pb self-energy.

in the ^{208}Pb calculations. For ^{208}Pb, the scaling parameter for the Lagrange-Laguerre mesh points is $a_L = 0.15$ (see Sec. 2.2.4). The matching radius used for scattering calculations is $a = 12$ fm (see Sec. 2.2.2).

Table B.4: Fitted parameter values for the asymmetric part of the ^{208}Pb self-energy. All symmetric values are listed in Table B.2.1.

Hartree-Fock

	p	n	Eq.
V_{asy}^{HF} [MeV]	22.7	71.1	(B.10)
$r_{(p,n)}^{HF}$ [fm]	1.18	1.20	(B.10)
$r_{(p,n)}^{HFasy}$ [fm]	1.40	1.20	(B.10)
$a_{(p,n)}^{HFasy}$ [fm]	0.39	0.80	(B.10)
$\beta_{(p,n)}^{vol_1asy}$ [fm]	0.18	1.86	(B.10)
$\beta_{(p,n)}^{vol_2asy}$ [fm]	1.52	1.52	(B.10)
$V_{(p,n)}^{wb}$ [MeV]	7.15	2.11	(B.3)
$\beta_{(p,n)}^{wb}$ [MeV]	0.64	0.64	(B.3)
$\rho_{(p,n)}^{wb}$ [MeV]	0.75	4.0	(B.3)

Spin-orbit

$V_{(p,n)}^{so}$ [MeV]	11.6	8.47	(B.4)
$r_{(p,n)}^{so}$ [fm]	1.65	0.97	(B.4)

Volume imaginary

$V_{+(p,n)}^{vol}$ [MeV]	6.93	3.01	(B.1)
$V_{-(p,n)}^{vol}$ [MeV]	57.0	60.4	(B.1)
$B_{+(p,n)}^{vol}$ [MeV]	14.4	14.4	(B.1)
$B_{-(p,n)}^{vol}$ [MeV]	84.5	84.5	(B.1)
$r_{+(p,n)}^{vol}$ [fm]	1.35	1.26	(B.11)
$r_{-(p,n)}^{vol}$ [fm]	1.35	1.00	(B.11)
$\alpha_{(p,n)}$ [fm]	0.08	0.36	(B.11)

Surface imaginary

	p	n	Eq.
$\beta_{-(p,n)}^{sur}$ [fm]	0.21	2.22	(B.11)
$\beta_{+(p,n)}^{sur}$ [fm]	1.44	2.03	(B.11)
$A_{+(p,n)}^{sur}$ [MeV]	50.0	-6.49	(B.12)
$A_{-(p,n)}^{sur}$ [MeV]	0.76	-13.0	(B.12)
$B_{+(p,n)}^{sur_1}$ [MeV]	27.7	18.1	(B.12)
$B_{+(p,n)}^{sur_2}$ [MeV]	60.5	2.40	(B.12)
$C_{+(p,n)}^{sur}$ [MeV]	200	25.1	(B.12)
$B_{-(p,n)}^{sur_1}$ [MeV]	6.18	20.2	(B.12)
$B_{-(p,n)}^{sur_2}$ [MeV]	34.3	40.0	(B.12)
$C_{-(p,n)}^{sur}$ [MeV]	22.9	1.00	(B.12)
$r_{-(p,n)}^{sur0}$ [fm]	0.97	0.95	(B.11)
$r_{+(p,n)}^{sur0}$ [fm]	1.09	1.35	(B.11)
$r_{-(p,n)}^{sur}$ [fm]	0.86	0.86	(B.11)
$r_{+(p,n)}^{sur}$ [fm]	1.20	1.63	(B.11)
$a_{-(p,n)}^{sur}$ [fm]	0.60	0.60	(B.11)
$a_{+(p,n)}^{sur}$ [fm]	0.53	0.47	(B.11)

Appendix C

Charge Density

C.1 Center of Mass Correction

The particle distributions obtained from Eq. (3.13) are relative to the center-of-mass of the A nucleons in the nucleus. In order to compare with experimental data, this relation to the center-of-mass must be removed [135],

$$\rho_{cm}(r_{cm}) \to \rho\left(\frac{A-1}{A} r_{cm}\right). \tag{C.1}$$

The effect of this transformation is to simply shift the distribution to large values of r. This is explicitly demonstrated in Fig. C.1 by $\rho\left(\frac{A-1}{A} r_{cm}\right)$, represented by the blue dashed line, extending further than $\rho(r_{cm})$, represented by the solid blue line.

The number of particles must be conserved in this transformation, thus

$$4\pi \int_0^\infty dr_{cm} r_{cm}^2 \tilde{\rho}\left(\frac{A-1}{A} r_{cm}\right) = 4\pi \int_0^\infty dr_{cm} r_{cm}^2 \rho\left(r_{cm}\right). \tag{C.2}$$

In order to satisfy Eq. (C.2), the shifted distribution needs to be normalized by the Jacobian

of the transformation,

$$\tilde{\rho}(r) = \left(\frac{A-1}{A}\right)^3 \rho\left(\frac{A-1}{A} r_{cm}\right). \tag{C.3}$$

The result of this renormalization is demonstrated by the solid red line in Fig. C.1. With Eq. (C.3), $\tilde{\rho}(r)$ is folded with the nucleon form factors (see Sec. C.2) to generate the charge densities in Figs. 3.7,4.13, and 4.5.

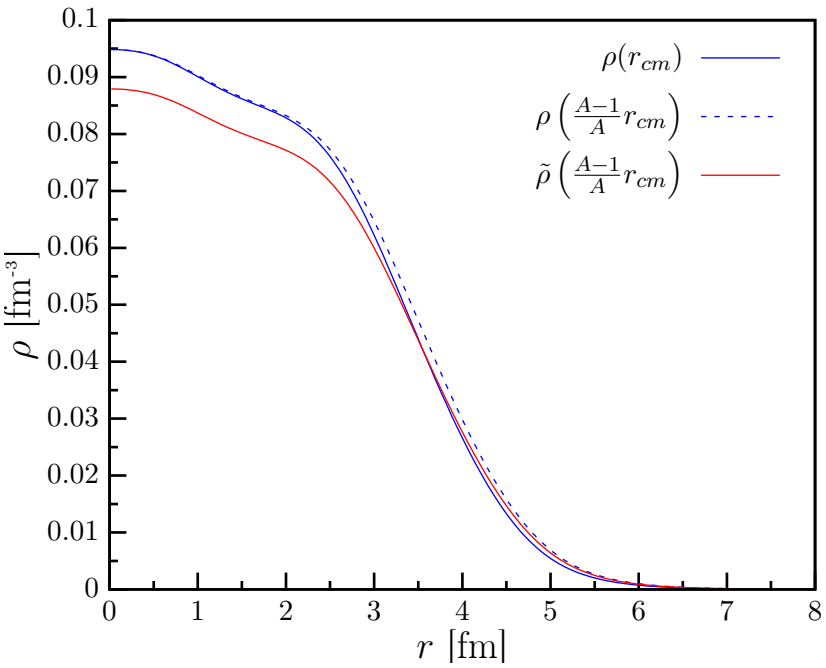

Figure C.1: The center-of-mass correction for particle distributions is shown for the specific case of ^{40}Ca. The solid red line is the corrected proton distribution which is then used to calculate the charge density to compare with electron elastic scattering results [83]. The solid blue line is the proton distribution relative to the center-of-mass, calculated directly from Eq. (3.13). The dashed blue line represents the shifted point distribution before it is renormalized, Eq. (C.1).

C.2 Folding the Nucleon Form Factors

The purpose of this section is to make explicit how the folding of the proton and neutron distributions are incorporated. There are some ambiguities in the literature that are addressed. Many papers [35,136–138] discuss how to fold the nucleon charge distributions with

point densities derived from the shell model. The nucleon distributions are parametrized as a sum of Gaussians. There is a correction claimed by these papers where the parameters r_i^2 [137,138] need to be renormalized to account for "the inclusion of the Darwin-Foldy term and the correction due to the spurious center of mass motion" [137]. This correction is of the form

$$\tilde{r}_i^2 = r_i^2 + \frac{\hbar^2}{2m^2} - \frac{b^2}{A}, \tag{C.4}$$

where b is the Harmonic-Oscillator parameter related to ω which can be roughly estimated as [35]

$$\frac{1}{Mb^2} = \omega \approx \frac{41}{A^{1/3}} \text{ MeV}.$$

The spurious center of mass motion is referring to the fact that in shell model calculations, the single-particle states are solved with a dependence on the center-of-mass location $\boldsymbol{R}$ [35]. In reality, the wave function should not depend on $\boldsymbol{R}$, so this has to be removed in some way. This is the role of the $\frac{b^2}{A}$ term in Eq. (C.4), so this term is irrelevant in the DOM.

As for the $\frac{\hbar^2}{2m^2}$ term, this can be explained by the non-relativistic reduction of the nuclear current [35]. The 4-component nuclear current for a Dirac nucleon can be written as

$$\langle J^\mu \rangle \approx \bar{u} \left[G_{E\tau} + G_{M\tau} \right] u \tag{C.5}$$

where u and $\bar{u}$ are solutions to the Dirac equation, $G_{E\tau}$ is the Sachs charge form factor for the nucleon τ (proton or neutron), and $G_{M\tau}$ is the Sachs magnetic form factor for the nucleon τ [60, 69, 72]. Most nuclear structure calculations are nonrelativistic, so in order to use the current from Eq. (C.5), a nonrelativistic version must be used. To reduce $\langle J^\mu \rangle$ to a

two-component form, substitute the following expression for u,

$$u = \left(\frac{E+m}{2E}\right)^{1/2} \begin{pmatrix} 1 \\ \frac{\boldsymbol{\sigma}\cdot\boldsymbol{P}}{E+m} \end{pmatrix} \chi,$$

where χ is a 2-component Pauli spinor [41]. This leads to the non-relativistic reduction of the current

$$\langle J^0 \rangle_{\rm nr} = \langle \rho \rangle_{\rm nr} \approx \chi^\dagger \left[\left(1 - \frac{\hbar^2 q^2}{8m^2}\right) G_{E\tau} + i\hbar^2 \frac{\boldsymbol{q}\cdot\boldsymbol{\sigma}\times\boldsymbol{P}}{4m^2}(2G_{M\tau} - G_{E\tau}) \right] \chi, \tag{C.6}$$

The first term in Eq. (C.6) is referred to as the Darwin-Foldy contribution. Ignoring the second term in Eq. (C.6) (the spin-orbit contribution), the Darwin-Foldy term can be thought of as a scaled Sachs charge form factor,

$$\tilde{G}_{E\tau}(q^2) = \left(1 - \frac{\hbar^2 q^2}{8m^2}\right) G_{E\tau}(q^2) \approx e^{\left(-\frac{1}{4}q^2 \frac{\hbar^2}{2m^2}\right)} G_{E\tau}(q^2). \tag{C.7}$$

The fully relativistic Sachs charge form factor, $G_{E\tau}(q^2)$ is parametrized as a sum of Gaussians,

$$G_{E\tau}(q^2) = \sum_{i=1}^{n} a_i e^{-q^2 r_i^2/4}$$

where a_i and r_i are parameters that are fit to relativistic electron scattering data [138]. Now use this expression for the form factor in Eq. (C.7),

$$\tilde{G}_{E\tau}(q^2) = \sum_{i=1}^{n} a_i e^{-\frac{q^2}{4}\left(r_i^2 + \frac{\hbar^2}{2m^2}\right)} = \sum_{i=1}^{n} a_i e^{-q^2 \tilde{r}_i^2/4} \tag{C.8}$$

where

$$\tilde{r}^2 = r_i^2 + \frac{\hbar^2}{2m^2}.$$

Thus, the fit parameters do need to include the $\frac{1}{2m^2}$ term.

This current is that of a single nucleon in a given nucleus. Accounting for contribution to the total density from each particle in the nucleus will roughly give the following form for the nuclear charge density (ignoring the spin-orbit term),

$$\rho_\tau^{\rm ch}(q) \approx \tilde{G}_{E\tau}(q^2)\rho_\tau^{\rm point}(q),$$

where $\rho_\tau^{\rm point}(q)$ is the point distribution calculated using $G_{\rm DOM}$. In order to get the charge density in configuration space, the inverse Fourier transform of $\rho_\tau^{\rm ch}$ results in

$$\rho_\tau^{\rm ch}(r) = \int d^3r' \rho_\tau^{\rm point}(r')\tilde{G}_{E\tau}(|\boldsymbol{r}-\boldsymbol{r'}|),$$

where $\tilde{G}_{E\tau}(|\boldsymbol{r}-\boldsymbol{r}'|)$ is nucleon charge distribution calculated by Fourier transforming Eq. (C.8) (performed using integration-by-parts and Taylor expansion),

$$\tilde{G}_{E\tau}(r) = \sum_{i=1}^{n} a_i \frac{1}{(\pi\tilde{r}_i^2)^{3/2}} e^- r^2/\tilde{r}_i^2.$$

The parameters used in the DOM fit can be found in Ref. [138].

As for the spin-orbit term in Eq. (C.6), this results in the following contribution to the charge density [138]

$$\rho_{ch}^{\ell s}(r) = -\left(\frac{\hbar}{m}\right)^2 \left(\sum_{n\ell j} \frac{1}{2} n_p \ell' \mu_p' \frac{1}{r^2}\frac{d}{dr}(r\rho_p^{n\ell j}(r)) + \sum_{n\ell j} \frac{1}{2} n_n \ell' \mu_n' \frac{1}{r^2}\frac{d}{dr}(r\rho_n^{n\ell j}(r))\right),$$

where $\mu_p' = \mu_p - \frac{1}{2}$ and $\mu_n = -1.91$ are the magnetic moments of protons and neutrons,

respectively, and

$$\ell' = \begin{cases} \ell & \text{if} \quad j = \ell + \frac{1}{2} \\ (-\ell - 1) & \text{if} \quad j = \ell - \frac{1}{2} \end{cases} .$$

Bibliography

[1] A. Bohr and B. R. Mottelson. *Nuclear Structure: Volume I.* World Scientific, 1997.

[2] G. E. Brown and A. D. Jackson. *The nucleon-nucleon interaction.* North-Holland, Netherlands, 1976.

[3] R. B. Wiringa, V. G. J. Stoks, and R. Schiavilla. *Phys. Rev. C*, 51:38–51, Jan 1995.

[4] D. R. Entem and R. Machleidt. *Phys. Rev. C*, 68:041001, Oct 2003.

[5] R. Machleidt and D. R. Entem. *Physics Reports*, 503(1):1 – 75, 2011.

[6] M. Piarulli, L. Girlanda, R. Schiavilla, R. N. Pérez, J. E. Amaro, and E. R. Arriola. *Phys. Rev. C*, 91:024003, Feb 2015.

[7] E. Epelbaum, H.-W. Hammer, and U.-G. Meißner. *Rev. Mod. Phys.*, 81:1773–1825, Dec 2009.

[8] J. Carlson, S. Gandolfi, F. Pederiva, S. C. Pieper, R. Schiavilla, K. E. Schmidt, and R. B. Wiringa. *Rev. Mod. Phys.*, 87:1067–1118, Sep 2015.

[9] M. Piarulli, et al. *Phys. Rev. Lett.*, 120:052503, Feb 2018.

[10] D. Lonardoni, S. Gandolfi, J. E. Lynn, C. Petrie, J. Carlson, K. E. Schmidt, and A. Schwenk. *Phys. Rev. C*, 97:044318, Apr 2018.

[11] G. Hagen, et al. *Nature Phys.*, 12:186, 2016.

[12] S. Bogner, R. Furnstahl, and A. Schwenk. *Progress in Particle and Nuclear Physics*, 65(1):94 – 147, 2010.

[13] V. Somà, C. Barbieri, and T. Duguet. *Phys. Rev. C*, 89:024323, Feb 2014.

[14] T. D. Morris, J. Simonis, S. R. Stroberg, C. Stumpf, G. Hagen, J. D. Holt, G. R. Jansen, T. Papenbrock, R. Roth, and A. Schwenk. *Phys. Rev. Lett.*, 120:152503, Apr 2018.

[15] D. Vautherin and D. M. Brink. *Phys. Rev. C*, 5:626–647, Mar 1972.

[16] K. M. Nollett, S. C. Pieper, R. B. Wiringa, J. Carlson, and G. M. Hale. *Phys. Rev. Lett.*, 99:022502, Jul 2007.

[17] S. Baroni, P. Navrátil, and S. Quaglioni. *Phys. Rev. C*, 87:034326, Mar 2013.

[18] S. Quaglioni and P. Navrátil. *Phys. Rev. C*, 79:044606, Apr 2009.

[19] W. H. Dickhoff and R. J. Charity. *Progress in Particle and Nuclear Physics*, 105:252 – 299, 2019.

[20] W. H. Dickhoff and D. Van Neck. *Many-Body Theory Exposed!, 2nd edition*. World Scientific, New Jersey, 2008.

[21] A. L. Fetter and J. D. Walecka. *Quantum Theory of Many-Particle Systems*. McGraw-Hill, Inc., 1971.

[22] C. Mahaux and R. Sartor. *Adv. Nucl. Phys.*, 20:96, 1991.

[23] A. B. Balantekin, et al. *M. Phys. Lett. A*, 29:1430010, 2014.

[24] A. Akmal, V. R. Pandharipande, and D. G. Ravenhall. *Phys. Rev. C*, 58:1804–1828, Sep 1998.

[25] B. P. Abbott, et al. *Phys. Rev. Lett.*, 119:161101, Oct 2017.

[26] S. Abrahamyan, et al. *Phys. Rev. Lett.*, 108:112502, Mar 2012.

[27] C. J. Horowitz. *Phys. Rev. C*, 57:3430–3436, Jun 1998.

[28] M. C. Atkinson, H. P. Blok, L. Lapikás, R. J. Charity, and W. H. Dickhoff. *Phys. Rev. C*, 98:044627, Oct 2018.

[29] M. H. Mahzoon, M. C. Atkinson, R. J. Charity, and W. H. Dickhoff. *Phys. Rev. Lett.*, 119:222503, 2017.

[30] D. F. Jackson. *Nuclear Reactions*. World Scientific, The Netherlands, 1970.

[31] G. R. Satchler. *Direct Nuclear Reactions*. Clarendon Press, Oxford, 1983.

[32] H. Feshbach. *Ann. Phys.*, 19:287, 1962.

[33] J. D. Jackson. *Classical Electrodynamics*. Wiley, 1999.

[34] F. Perey and B. Buck. *Nuclear Physics*, 32:353 – 380, 1962.

[35] T. de Forest Jr. and J. D. Walecka. *Advances in Physics*, 15(57):1 – 109, 1966.

[36] P. Descouvemont and D. Baye. *Rep. Prog. Phys.*, 73(3):036301, 2010.

[37] E. W. Swokowski. *Calculus with Analytic Geometry*. Prinde, Weber, and Schmidt, Massachusetts, 1979.

[38] C. Bloch. *Nuclear Physics*, 4:503 – 528, 1957.

[39] D. Baye. *Physics Reports*, 565:1 – 107, 2015. The Lagrange-mesh method.

[40] M. Abramowitz and I. A. Stegun. *Handbook of Mathematical Functions*. Dover, New York, 1972.

[41] A. Messiah. *Quantum Mechanics*. John Wiley, New York, 1958.

[42] P. M. Morse and H. Feshbach. *Methods of Theoretical Physics*. McGraw-Hill, New York, 1953.

[43] K. Gottfried and T.-M. Yan. *Quantum Mechanics: Fundamentals*. Springer, New York, 2004.

[44] E. B. Saff and A. D. Snider. *Fundamentals of Complex Analysis with Applications to Engineering and Science*. Pearson Education, Inc., New Jersey, 2003.

[45] G. J. Kramer, et al. *Phys. Lett. B*, 227(2):199 – 203, 1989.

[46] G. Potel, et al. *Eur. Phys. J. A*, 53:178, 2017.

[47] G. J. Kramer. PhD thesis, Universiteit van Amsterdam, Amsterdam, 1990.

[48] W. H. Dickhoff, R. J. Charity, and M. H. Mahzoon. *J. of Phys. G: Nucl. and Part. Phys.*, 44(3):033001, 2017.

[49] A. B. Migdal. *Theory of Finite Fermi Systems and Applications to Atomic Nuclei*. John Wily & Sons, Ltd., 1967.

[50] F. Capuzzi and C. Mahaux. *Ann. Phys.*, 281:223 – 359, 1994.

[51] M. I. Haftel and F. Tabakin. *Phys. Rev. C*, 3:921, 1971.

[52] M. H. Mahzoon. *Implications of a Fully Nonlocal Implementation of the Dispersive Optical Model*. PhD thesis, Washington University in St. Louis, 2015.

[53] A. Deltuva, A. Fonseca, and P. Sauer. *Annual Review of Nuclear and Particle Science*, 58(1):27–49, 2008.

[54] J. W. A. den Herder, H. P. Blok, E. Jans, P. H. M. Keizer, L. Lapikás, E. N. M. Quint, G. van der Steenhoven, and P. K. A. de Witt Huberts. *Nucl. Phys. A*, 490(3):507 – 555, 1988.

[55] P. K. A. de Witt Huberts. *J. Phys. G: Nucl. Part. Phys.*, 16:507, 1990.

[56] A. E. L. Dieperink and P. K. A. de Witt Huberts. *Ann. Rev. Nucl. Part. Sci.*, 40:239, 1990.

[57] I. Sick and P. K. A. de Witt Huberts. *Comm. Nucl. Part. Phys.*, 20:177, 1991.

[58] L. Lapikás. *Nucl. Phys.*, A553:297c, 1993.

[59] V. R. Pandharipande, I. Sick, and P. K. A. de Witt Huberts. *Rev. Mod. Phys.*, 69:981, 1997.

[60] S. Boffi, C. Giusti, F. D. Pacati, and M. Radici. *Electromagnetic Response of Atomic Nuclei*. Oxford, New York, 1996.

[61] C. Giusti, A. Meucci, F. D. Pacati, G. Co', and V. De Donno. *Phys. Rev. C*, 84:024615, Aug 2011.

[62] S. Boffi, C. Giusti, and F. D. Pacati. *Nucl. Phys. A*, 336(3):416 – 426, 1980.

[63] W. H. Dickhoff and C. Barbieri. *Prog. Part. Nucl. Phys.*, 52:377, 2004.

[64] A. M. Mukhamedzhanov and A. S. Kadyrov. *Phys. Rev. C*, 82:051601(R), 2010.

[65] R. J. Furnstahl and A. Schwenk. *J. Phys. G*, 37:064005, 2010.

[66] B. K. Jennings. arXiv:1102.3721, 2011.

[67] R. J. Furnstahl and H. Hammer. *Phys. Lett. B*, 531:203, 2002.

[68] C. Giusti and F. D. Pacati. *Nucl. Phys. A*, 485(3):461 – 480, 1988.

[69] S. Frullani and J. Mougey. *Advances in Nuclear Physics, Volume 14*. Plenum Press, New York, 1984.

[70] M. Goldberger and K. Watson. *Collision Theory*. Wiley, 1964.

[71] J. D. Bjorken and S. D. Drell. *Relativistic Quantum Fields*. McGraw-Hill, 1965.

[72] T. De Forest Jr. *Nucl. Phys. A*, 392(2):232 – 248, 1983.

[73] G. J. Kramer, H. P. Blok, and L. Lapikás. *Nucl. Phys. A*, 679:267, 2001.

[74] C. Giusti and F. D. Pacati. *Nucl. Phys. A*, 473(4):717 – 735, 1987.

[75] M. Brand, K. Allaart, and W. H. Dickhoff. *Nucl. Phys.*, A509:1, 1990.

[76] G. van der Steenhoven, H. P. Blok, J. W. A. den Herder, E. Jans, P. H. M. Keizer, L. Lapikás, E. N. M. Quint, and P. K. A. de Witt Huberts. *Phys. Rev. C*, 32:1787, 1985.

[77] P. Schwandt, H. O. Meyer, W. W. Jacobs, A. D. Bacher, S. E. Vigdor, M. D. Kaitchuck, and T. R. Donoghue. *Phys. Rev. C*, 26:55–64, Jul 1982.

[78] F. G. Perey. In *Direct Interactions and Nuclear Reaction Mechanism*, New York, 1963. Gordon and Breach.

[79] W. H. Press, S. A. Teukolsky, W. T. Vetterling, and B. P. Flannery. *Numerical Recipes in Fortran 90*. Cambridge University Press, 1996.

[80] M. H. Mahzoon, R. J. Charity, W. H. Dickhoff, H. Dussan, and S. J. Waldecker. *Phys. Rev. Lett.*, 112:162503, Apr 2014.

[81] A. Auce, et al. *Phys. Rev. C*, 71:064606, Jun 2005.

[82] J. M. Mueller, et al. *Phys. Rev. C*, 83:064605, Jun 2011.

[83] H. de Vries, C. W. de Jager, and C. de Vries. *Nucl. Data Tables*, 36:495, 1987.

[84] I. Sick, J. B. Bellicard, J. M. Cavedon, B. Frois, M. Huet, P. Leconte, P. X. Ho, and S. Platchkov. *Phys. Lett. B*, 88:245, 1979.

[85] H. Dussan, M. H. Mahzoon, R. J. Charity, W. H. Dickhoff, and A. Polls. *Phys. Rev. C*, 90:061603, Dec 2014.

[86] R. Varner, W. Thompson, T. McAbee, E. Ludwig, and T. Clegg. *Physics Reports*, 201(2):57 – 119, 1991.

[87] J. Lee, et al. *Phys. Rev. Lett.*, 104:112701, 2010.

[88] J. A. Tostevin and A. Gade. *Phys. Rev. C*, 90:057602, Nov 2014.

[89] Ø. Jensen, G. Hagen, M. Hjorth-Jensen, B. A. Brown, and A. Gade. *Phys. Rev. Lett.*, 107:032501, 2011.

[90] T. Wakasa, K. Ogata, and T. Noro. *Prog. Part. Nucl. Phys.*, 96:32, 2017.

[91] L. Atar et al. *Phys. Rev. Lett.*, 120:052501, 2018.

[92] S. Kawase et al. *Prog. Theor. Exp. Phys.*, page 021D01, 2018.

[93] N. B. Nguyen, S. J. Waldecker, F. M. Nunes, R. J. Charity, and W. H. Dickhoff. *Phys. Rev. C*, 84:044611, 2011.

[94] S. Pastore, J. Carlson, V. Cirigliano, W. Dekens, E. Mereghetti, and R. B. Wiringa. *Phys. Rev. C*, 97:014606, Jan 2018.

[95] J. Hyvärinen and J. Suhonen. *Phys. Rev. C*, 91:024613, Feb 2015.

[96] S. Typel and B. A. Brown. *Phys. Rev. C*, 64:027302, Jun 2001.

[97] A. Steiner, M. Prakash, J. Lattimer, and P. Ellis. *Physics Reports*, 411(6):325 – 375, 2005.

[98] X. Roca-Maza, M. Centelles, X. Viñas, and M. Warda. *Phys. Rev. Lett.*, 106:252501, Jun 2011.

[99] C. J. Horowitz and J. Piekarewicz. *Phys. Rev. Lett.*, 86:5647–5650, Jun 2001.

[100] A. W. Steiner, J. M. Lattimer, and E. F. Brown. *The Astrophysical Journal*, 722(1):33, 2010.

[101] B.-A. Li, L.-W. Chen, and C. M. Ko. *Physics Reports*, 464:113 – 281, 2008.

[102] M. B. Tsang, et al. *Phys. Rev. C*, 86:015803, Jul 2012.

[103] I. Angeli and K. Marinova. *Atomic Data and Nuclear Data Tables*, 99(1):69 – 95, 2013.

[104] B. K. Agrawel, S. Shlomo, and V. Kim Au. *Eur. Phys. J. A*, page 525, 2005.

[105] S. S. Avancini, J. R. Marinelli, D. P. Menezes, M. M. W. Moraes, and A. S. Schneider. *Phys. Rev. C*, 76:064318, Dec 2007.

[106] M. Centelles, X. Roca-Maza, X. Viñas, and M. Warda. *Phys. Rev. Lett.*, 102:122502, Mar 2009.

[107] B. D. Anderson, P. R. Bevington, F. H. Cverna, M. W. McNaughton, H. B. Willard, R. J. Barrett, N. S. P. King, and D. J. Ernst. *Phys. Rev. C*, 19:905–912, Mar 1979.

[108] J. Piekarewicz, B. K. Agrawal, G. Colò, W. Nazarewicz, N. Paar, P.-G. Reinhard, X. Roca-Maza, and D. Vretenar. *Phys. Rev. C*, 85:041302, Apr 2012.

[109] S. F. Hicks, S. E. Hicks, G. R. Shen, and M. T. McEllistrem. *Phys. Rev. C*, 41:2560–2570, Jun 1990.

[110] R. Shane, R. Charity, J. Elson, L. Sobotka, M. Devlin, N. Fotiades, and J. Odonnell. *Nuclear Instruments and Methods in Physics Research Section A: Accelerators, Spectrometers, Detectors and Associated Equipment*, 614(3):468 – 474, 2010.

[111] J. A. Harvey, C. H. Johnson, R. F. Carlton, and B. Castel. *Phys. Rev. C*, 32:1114–1117, Sep 1985.

[112] F. Salvat, A. Jablonski, and C. J. Powell. *Computer Physics Communications*, 165(2):157 – 190, 2005.

[113] M. Baldo, A. Polls, A. Rios, H.-J. Schulze, and I. Vidaña. *Phys. Rev. C*, 86:064001, Dec 2012.

[114] A. Rios, A. Polls, and W. H. Dickhoff. *Phys. Rev. C*, 89:044303, Apr 2014.

[115] W. Myers and W. Swiatecki. *Nuclear Physics A*, 601(2):141 – 167, 1996.

[116] J. P. Jeukenne, A. Lejeune, and C. Mahaux. *Physics Reports*, 25(2):83 – 174, 1976.

[117] H. A. Bethe. *Annual Review of Nuclear Science*, 21(1):93–244, 1971.

[118] S. L. Shapiro and S. A. Teukolsky. *Black Holes, White Dwarfs, and Neutron Stars: The Physics of Compact Objects*. Wiley, New York, 1983.

[119] J. M. Lattimer and M. Prakash. *Physics Reports*, 442(1):109 – 165, 2007. The Hans Bethe Centennial Volume 1906-2006.

[120] V. M. Galitski and A. B. Migdal. *Sov. Phys. JETP*, 7:96, 1958.

[121] R. Machleidt, F. Sammarruca, and Y. Song. *Phys. Rev. C*, 53:R1483–R1487, Apr 1996.

[122] Y. Dewulf, W. H. Dickhoff, D. Van Neck, E. R. Stoddard, and M. Waroquier. *Phys. Rev. Lett.*, 90:152501, Apr 2003.

[123] M. Alvioli, C. Ciofi degli Atti, L. P. Kaptari, C. B. Mezzetti, H. Morita, and S. Scopetta. *Phys. Rev. C*, 85:021001, Feb 2012.

[124] K. S. Egiyan, et al. *Phys. Rev. Lett.*, 96:082501, Mar 2006.

[125] R. B. Wiringa, R. Schiavilla, S. C. Pieper, and J. Carlson. *Phys. Rev. C*, 89:024305, Feb 2014.

[126] O. Hen, G. A. Miller, E. Piasetzky, and L. B. Weinstein. *Rev. Mod. Phys.*, 89:045002, Nov 2017.

[127] R. Schiavilla, R. B. Wiringa, S. C. Pieper, and J. Carlson. *Phys. Rev. Lett.*, 98:132501, Mar 2007.

[128] M. Duer, et al. *Nature*, 560(7720):617–621, 2018.

[129] L. Atar, et al. *Phys. Rev. Lett.*, 120:052501, Jan 2018.

[130] J. Ryckebusch, W. Cosyn, S. Stevens, C. Casert, and J. Nys. *Physics Letters B*, 792:21 – 28, 2019.

[131] I. J. Thompson and F. M. Nunes. *Nuclear Reactions for Astrophysics: Principles, Calculations and Applications of Low-Energy Reactions*. Cambridge University Press, New York, 2009.

[132] H. Dussan, S. J. Waldecker, W. H. Dickhoff, H. Müther, and A. Polls. *Phys. Rev. C*, 84:044319, Oct 2011.

[133] S. J. Waldecker, C. Barbieri, and W. H. Dickhoff. *Phys. Rev. C*, 84:034616, Sep 2011.

[134] R. J. Charity, J. M. Mueller, L. G. Sobotka, and W. H. Dickhoff. *Phys. Rev. C*, 76:044314, Oct 2007.

[135] H. Müther and I. Sick. *Phys. Rev. C*, 70:041301, Oct 2004.

[136] U. Meyer-Berkhout, K. W. Ford, and A. E. Green. *Annals of Physics*, 8(1):119 – 171, 1959.

[137] H. Chandra and G. Sauer. *Phys. Rev. C*, 13:245–252, Jan 1976.

[138] B. A. Brown, S. E. Massen, and P. E. Hodgson. *Journal of Physics G: Nuclear Physics*, 5(12):1655–1698, dec 1979.